Ollscoil Chathair
Bhaile Átha Cliath
Dublin City University

Design and Analysis of the Wave Activated Sensor Power Buoy – A Novel Wave Measuring Device

Supervisor:
Dr. Thomas Kelly (DkIT)

Co-Supervisor:
Dr. Thomas Dooley (CREDIT)

Author: Mr Brendan Walsh
M.A.I., B.A.,PGDipEnv.,CEng.,M.E.I.

A thesis submitted in partial fulfilment of the requirements for the degree of
Doctor of Philosophy

School of Engineering
March 2026

Declaration of Authorship

We, the undersigned declare that this thesis entitled *Design and Analysis of the Wave Activated Sensor Power Buoy –A Novel Wave Measuring Device*, is entirely the author's own work and has not been taken from the work of others, except as cited and acknowledged within the text.

The thesis has been prepared according to the regulations of Dundalk Institute of Technology and has not been submitted in whole or in part for an award in this or any other institution.

Author Name: Brendan Walsh

Author Signature:

Date: 20/03/2026

Supervisor Name: Thomas Kelly

Supervisor Signature: Thomas Kelly

Date: 20/03/2026

Abstract

This research presents the development, validation, and field application of a Wave-Activated Sensor Power Buoy (WASP) designed to estimate ocean surface wave characteristics from internal pressure measurements within a sealed moonpool. The study considers a critical gap in ocean wave measurement by exploring an autonomous alternative to traditional surface-following wave buoys.

The research followed a multi-stage experimental methodology, encompassing scaled laboratory testing (1:20 and 1:2.4 scale models) and full-scale field deployment. Each stage was designed to investigate the hydrodynamic behaviour of the WASP and to establish a transfer function capable of converting internal chamber pressure fluctuations into equivalent surface elevation spectra. Scaled testing confirmed the frequency-dependent nature of the system, with dominant resonance occurring within the 0.3–0.6 Hz range. These insights informed the derivation of a full-scale transfer function subsequently validated using data from a four-month sea trial (March–June 2019).

The validated pressure-to-surface transfer function successfully reproduced wave spectra with strong correlation ($r > 0.9$) to a co-located Waverider buoy under medium to high-energy conditions. Analysis demonstrated that frequency restriction to the 0.3–0.6 Hz band improved spectral coherence and reduced RMS error, particularly during energetic sea states. However, performance degraded in low-energy conditions, reflecting the system's conditional linearity and sensitivity to signal-to-noise ratio.

Beyond spectral validation, the transfer function was applied to estimate key sea-state parameters, including significant wave height (Hs) and zero-crossing period (Tz). Results generate reasonable estimations, with deviations of less than 10% from Waverider-derived values in most conditions. These findings demonstrate the WASP’s potential for autonomous, frequency-selective sea-state monitoring in coastal and offshore environments.

The research concludes by identifying pathways for future refinement, including broadband transfer function modelling, hydrodynamic design optimisation, and wave-powered energy autonomy to support extended deployments. Collectively, this work contributes to a foundation for the next generation of compact, energy-efficient, and cost-effective ocean wave measurement systems, which assists in advances in marine observation, offshore engineering, and renewable energy applications.

Acknowledgements

First and foremost, I would like to express my deepest gratitude and love to my wife, Paula, for her unwavering support, patience, and encouragement throughout this journey. Her love and belief in me have been a constant source of strength and inspiration not only throughout this process but to my entire adult life.

I am also grateful to my funding agencies for their financial support, without which this research would not have been possible. In particular, I would like to thank the Marine Institute, Bluewise Marine, and Dundalk Institute of Technology. I would also like acknowledge the assistance given by the staff of P&O Maritime, who also provided the solar panels and associated regulators used in this project. I would also like to acknowledge the assistance provided by the staff of LIR National Ocean test Facility at Ringaskiddy Ireland, during a scaled model testing campaign.

I would like to extend my heartfelt thanks to my supervisor, Dr Thomas Kelly. I am immensely grateful for his invaluable guidance, insights, and mentorship throughout the course of my research. His expertise, enthusiasm and constructive feedback have been instrumental in shaping this thesis. I would also like to thank Dr Tom Dooley for his time and guidance throughout this research.

Finally, I would like to thank my children, Tom, Oscar and Matilda for their constant encouragement and understanding, especially during the challenging times. Their love has given me strength and purpose throughout my PhD journey.

Thank you all.

TABLE OF CONTENTS

Chapter 1 – Introduction

Chapter 2 – Literature Review

Chapter 3 – Methodology

Chapter 4 – Full-scale Testing Results and Analysis

Chapter 5 – Discussion and Conclusions

List of Figures

List of Tables

Abbreviations

DkIT	Dundalk Institute of Technology
OWC	Oscillating Water Column
WASP	Wave Activated Sensor Power
UCC	University College Cork
TRL	Technology Readiness Level
EWTEC	European Wave Energy Conference
MaREI	Marine Renewable Energy Ireland
SAR	Synthetic Aperture Radar
AMETS	Atlantic Marine Energy Test Site
NDBS	National Data Buoys
CDIP	Coastal Data Information Programme
USVs	Unmanned Surface Vehicles
WECS	Wave Energy Conversion System
PTO	Power Take-off
ORE	Offshore Renewable Energy
ADCPs	Acoustic Doppler Current Profilers
LIDAR	Light Detection and Ranging
AUVs	Autonomous underwater vehicles
GOOS	Global Ocean Observing System
DOF	Degrees of Freedom
FFT	Fast Fourier Transformation
EIA	Environmental Impact Assessments
IRENA	International Renewable Energy Agency
SMEs	Small and medium-sized enterprises
SWL	Still water level
DFT	Discrete Fourier Transform
PSD	Power Spectrum Density
RAO	Response Amplitude Operator
SDGs	United Nations Sustainable Development Goals
EMEC	European Marine Energy Centre

TDMS	Technical Data Management Streaming
RMS	Root Mean Squared
TF	Transfer Function
RMSE	Root Mean Squared Error

Symbols

Hs	Significant Wave Height
Tz	Zero-cross Period
H	Wave Height
a	Amplitude
k	Wave number
f	Frequency
Tc	Crest to crest period
Φ	Phase
τ	Time lag
$R(\tau)$	Autocorrelation function
$\rho\ (\tau)$	Autocorrelation coefficient
Xp	Discrete Fourier transform
m_n	Spectral moments
fp	Peak frequency
ωz	average successive upcrossing frequency
ωc	average frequency between successive crests
$x(t)$	stationary input
$y(t)$	represents the output
$h(t)$	represents the impulse response of the system
$X(f)$	represents the Fourier transform of $x(t)$
$Y(f)$	represents the Fourier transform of $y(t)$
$H(f)$	is the frequency-dependent, Fourier transfer function between $X(f)$ and $Y(f)$
$H(f)$	is the Fourier transform of $h(t)$.
Fr	Froude number
v	velocity
Hz	Hertz

Chapter 1 – Introduction

1.0 Introduction

Understanding the dynamics of ocean surface waves is critical for a wide range of marine applications, from coastal engineering and offshore operations to climate studies and maritime safety [1]. Traditional wave measurement systems, such as directional wave rider buoys and radar-based platforms, have proven effective but are often costly, maintenance-intensive, and sometimes spatially limited in their deployment [2],[3].

A new class of wave measuring systems, leveraging the interaction between ocean waves and enclosed air volumes in semi-submerged structures, has emerged as a promising alternative. One such system centres around the Oscillating Water Column (OWC) principle—commonly applied in wave energy converters [4] —where wave-induced oscillations of a water column inside a chamber generate varying air pressures. These internal pressure variations, if accurately interpreted, can offer valuable insights into the external sea state [5].

This research builds upon that principle by designing and developing a novel wave-measuring buoy that utilises a sealed moonpool housing an OWC configuration, not for energy generation, but for ocean wave characterisation. The buoy employs air pressure measurements taken above the oscillating water surface inside the sealed moonpool and applies frequency-domain analysis using a calibrated transfer function, derived from concurrent data collected by a nearby conventional wave measuring device [6].

1.2 Research Problem

Despite the potential advantages of OWC-based systems for wave measurement, several technical challenges remain unresolved:

- How accurately can internal air pressure signals, distorted by the dynamic response of the structure, be used to infer external wave conditions?
- Can a reliable and generalised transfer function be developed to relate internal pressure fluctuations to sea state parameters under varying conditions?
- How does the system perform across a wide range of sea states compared to conventional wave measurement instruments?

The central problem addressed by this research is the development of a reliable, field-deployable, and validated method for estimating wave spectra using internal air pressure measurements in a sealed moonpool, with minimal calibration dependency on external sensors [7].

1.3 Research Aim

The aim of this research is to develop and validate a novel ocean wave measurement buoy that estimates wave frequency spectra and sea state parameters by analysing air pressure signals within a sealed OWC moonpool, using a frequency-domain transfer function calibrated against a conventional wave measuring system [8].

1.4 Research Objectives

1. Develop and apply a reliable method for data capture and transfer function derivation, enabling the WASP to record accurate pressure measurements and compute corresponding transfer functions over an extended deployment period.
2. Investigate the frequency-dependent behaviour of the WASP system, identifying the frequency range in which its response is most stable, coherent, and dynamically consistent with model and reference data.

3. Assess the conditional linearity of the transfer function, determining how varying sea-state energy levels influence linearity, noise sensitivity, and spectral accuracy.
4. Validate the WASP’s performance against a reference measurement system (the Datawell Waverider buoy [9]) to confirm the reliability, repeatability, and accuracy of wave spectral reconstruction under a range of conditions.
5. Formulate recommendations for frequency-selective calibration, to improve the fidelity and practical application of the WASP for long-term ocean wave monitoring.

To provide clarity on the overall research structure, Figure 1.1 presents a schematic overview of the methodology adopted for the development and validation of the Wave Activated Sensor Power Buoy (WASP). The research followed a structured, multi-stage approach progressing from theoretical foundation and concept development, through scaled experimental validation, to full-scale deployment and frequency-domain modelling.

The methodology integrates laboratory testing at two scales (1:20 and 1:2.4), full-scale sea trials in Galway Bay, and detailed spectral analysis to derive and validate a pressure-to-surface elevation transfer function. Validation against a co-located Datawell Waverider buoy enabled quantitative assessment of system accuracy and conditional linearity across varying sea states.

This staged framework ensured that the WASP concept was rigorously evaluated at increasing levels of physical and environmental complexity, culminating in the estimation of key sea-state parameters, including significant wave height (Hs) and zero-crossing period (Tz).

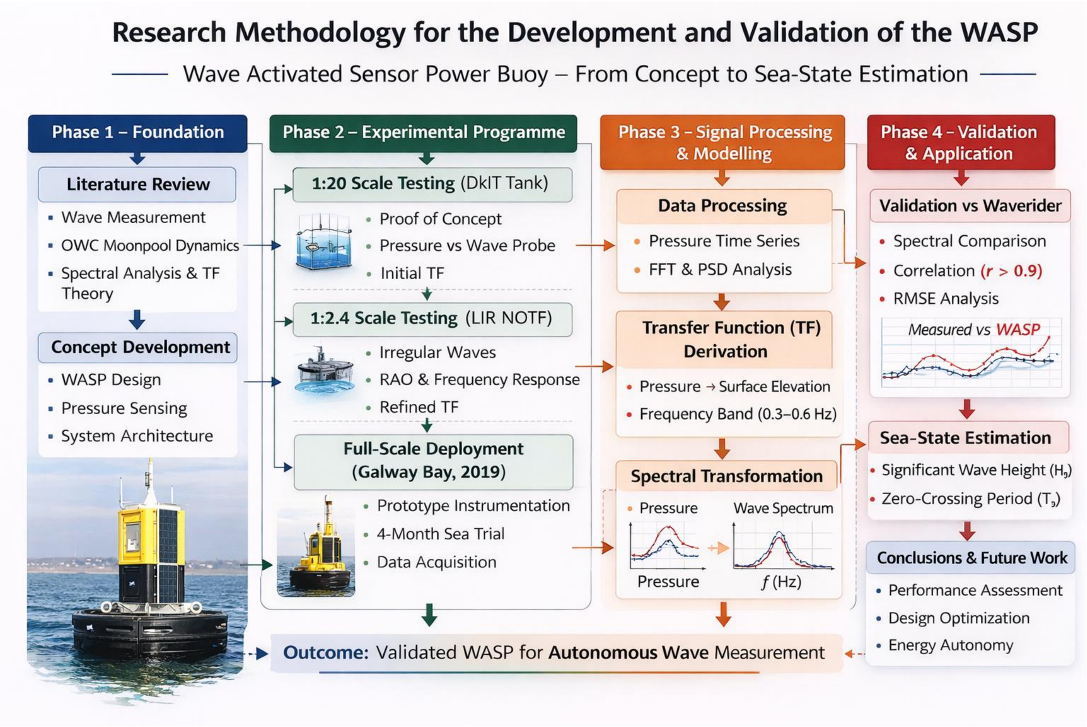

Figure 1.1: Structured overview of the multi-stage experimental and analytical methodology adopted for the development, calibration, and validation of the Wave Activated Sensor Power Buoy (WASP).

1.5 Significance of the Study

The novelty of this work lies in its non-traditional approach to wave measurement, transforming an energy-focused OWC concept into a sensing platform [4],[10]. This method eliminates the need for direct water surface measurements (e.g., accelerometers, wave staffs, GPS), reducing energy consumption, exposure to environmental wear, and system complexity [11].

Additionally, the development of a generalised frequency-domain transfer function offers a new path for characterising wave conditions from internal pressure dynamics—an underexplored area in oceanographic instrumentation [12]. If successful, this approach could lead to the deployment of low-cost, scalable, and easily deployable wave measurement devices, especially beneficial in remote or developing coastal regions where traditional systems may be impractical [13].

1.6 Structure of the Thesis

Chapter 1

The introduction chapter outlines the motivation and context for developing a novel ocean wave measuring buoy that estimates wave spectra and sea state parameters using internal air pressure measurements above an Oscillating Water Column (OWC) within a sealed moonpool. By analysing these pressure signals in the frequency domain and applying a transfer function—derived from data provided by a nearby conventional wave measuring device—this research proposes a low-cost, compact, and robust alternative to traditional wave sensors [6]. The chapter defines the research aim, outlines key objectives, and emphasises the novelty of transforming internal pressure dynamics into accurate wave characterizations, establishing the basis for a new approach to ocean wave measurement.

Chapter 2

Chapter 2 provides a comprehensive literature review of current ocean wave measuring technologies, including surface-following buoys, radar systems, and pressure-based sensors [2],[3], highlighting their respective capabilities, limitations, and deployment challenges. It contrasts these with the novel approach of using internal air pressure measurements within a sealed OWC moonpool [4],[12], to infer wave spectra, emphasising the potential for a more compact, low-cost, and robust solution. The chapter then establishes the technical foundation for the research, covering key concepts such as ocean wave spectra, sea-state parameters, Oscillating Water Columns (OWCs), pressure signal acquisition, transfer function theory, and the Response Amplitude Operator (RAO) of the moonpool. This framework sets the stage for the modelling, experimental work and prototype development and deployment presented in subsequent chapters.

Chapter 3

Chapter 3 outlines the methodology adopted for the development, testing, and validation of the novel wave measuring buoy. The research begins with the design and experimental testing of a 1/20 scale model, followed by a more advanced 1/2.4 scale model tested in controlled wave tank facilities [14]. These tests aimed to acquire internal air pressure signals in the time domain, which were then converted to the frequency domain. Simultaneously, wave measurements were record from within the test tanks. A transfer function was determined between the two and applied to generate spectra for comparison. A full-scale prototype was developed and deployed at the Galway Bay test site [15], where time-domain pressure data was collected and processed using the same spectral analysis approach. The chapter also details the data acquisition systems, signal processing techniques, and presents representative raw data samples collected over the course of the testing campaigns.

Chapter 4

Chapter 4 presents and discusses the data processing of the results obtained from the full-scale sea trials of the novel wave measuring buoy. The frequency-domain analysis of internal air pressure signals successfully produced wave spectra that closely matched theoretical models in tank tests [14] and showed strong agreement with real sea state data from the reference wave measuring device at Galway Bay within specific frequency ranges [15]. The transfer function approach proved effective on areas of frequency measurements which are valid when compared to the reference waverider, and areas where pressure measurements are validly compared with wave spectra, demonstrating the buoy's capability to capture key spectral characteristics and by applying transfer functions to determine sea state parameters such as Hs and Tz.

Chapter 5

Chapter 5 concludes the research by summarising the successful development, testing, and validation of a novel ocean wave measuring buoy that uses internal air pressure signals within a sealed OWC moonpool to estimate wave spectra and sea state parameters. The study demonstrated that, through frequency-domain analysis and a calibrated transfer functions, reliable wave measurements can be obtained without relying on traditional surface-following sensors [8],[10]. The research contributes new knowledge in the use of internal pressure dynamics for oceanographic sensing and establishes a foundation for future refinement and deployment of compact, cost-effective wave measurement systems. The chapter also outlines key limitations encountered and recommends future work to improve system robustness and expand calibration techniques.

1.7 Publications and presentations

Published Journal Papers

- B. Walsh, R. Carolan, M. Boland, T. Dooley, and T. Kelly, “The use of air pressure measurements within a sealed moonpool for sea-states estimation,” *J. Mar. Sci. Eng.2024*, 12,2306
- I. McLeod, B. Walsh, T.Kelly, and J. Ringwood, “Free surface elevation estimator as sensor for wave-powered data buoys”, PP(99):1-16, Journal of Oceanic Engineering, 2025.

Conference Papers

- M. Boland, T, Kelly, R. Carolan, B. Walsh and T. Dooley, “Scale model testing of the WASP – a novel wave measuring buoy,” in *Proc. 13th Eur. Wave Tidal Energy Conf. (EWTEC)*, Naples, Italy, 2019.

- "R. Carolan, B. Walsh, M. Boland, T. Dooley and T. Kelly, "The design and construction of a prototype WASP – a novel wave measuring buoy," in *Proc. Eur. Wave Tidal Energy Conf. (EWTEC)*, Naples, Italy, 2019.

- "B. Walsh, T. Kelly, R. Carolan, M. Boland, and T. Dooley, "Full-scale prototype testing of the WASP – a novel wave measuring buoy," in *Proc. Eur. Wave Tidal Energy Conf. (EWTEC)*, Plymouth, UK, 2021.

- "B. Walsh, T. Kelly, R. Carolan, M. Boland, and T. Dooley, "Analysis of data from the full-scale prototype testing of the WASP – a novel wave measuring buoy," in *Proc. Eur. Wave Tidal Energy Conf. (EWTEC)*, Bilbao, Spain, 2023.

Technical Reports

- NIAP Final Technical Report 2021, "Report into works carried out as part of NIAP grant NIAP LS 16010".
- Internal Technical Report 2025, "Pressure Data Analysis from Wave Activated Sensor Power Buoy (WASP) during Full-Scale Sea Testing Deployment".

Chapter 2 - Literature Review

2.0 Introduction

This chapter aims to explore existing methods and devices for wave measurement, their working principles and associated challenges. A critical assessment of each approach highlights opportunities for innovation, with special attention given to a novel concept: using pressure measurements from a sealed moonpool to monitor wave-induced motions. This chapter further goes on to review the technical framework relevant to this novel wave measuring concept which is the primary subject of this work.

Ocean waves are among the most dynamic and complex phenomena in the marine environment. Accurate measurement and analysis of wave characteristics are crucial for various applications, including coastal engineering, offshore structure design, navigation safety, climate studies, and renewable energy development [17]. The reliable quantification of parameters such as wave height, period, direction, and energy spectrum allow researchers and engineers to predict and mitigate potential hazards, design resilient offshore infrastructure, and optimise marine energy extraction systems [18].

Over the decades, a wide array of wave measurement techniques and instruments has been developed, ranging from surface-following buoys to remote sensing technologies [19]. While significant advancements have been achieved, limitations remain—particularly in harsh sea states, deep water, and within integrated systems such as floating platforms [20].

2.1 Aims and objectives of the Review

The primary aim of this literature review is to evaluate the current landscape of ocean wave measurement technologies, to provide the theoretical underpinnings for the approach of using pressure measurements above an OWC from within a sealed moonpool to estimate sea-states and to identify a gap for innovation in this field. Specific objectives include:

- To describe and compare existing wave measurement devices and techniques.
- Compare measurement methods and data analysis techniques.
- To analyse the advantages and limitations of each method.
- To explore the principles behind pressure-based measurements and their potential for wave monitoring.
- Define and discuss spectral wave models, spectral moments and sea-state parameters.
- Oscillating Water Column (OWC) theory and moonpool behaviour.
- To assess the dynamic behaviour of air within a sealed moonpool excited by waves.
- Investigate air dynamics in the moonpool chamber under wave excitation.
- Understand the functioning of marine pressure gauges.
- Explore frequency response and RAO of the moonpool system.
- Summarise techniques for time-series analysis, spectral estimations, data handling, signal processing and quality control.
- To establish a scientific foundation for developing a novel wave measuring system based on pressure readings within a sealed moonpool.

2.2 Importance of Wave Measuring Devices

Wave measuring devices, also known as wave buoys or wave sensors, play a crucial role in understanding and harnessing the power of the ocean. These instruments provide vital data on wave height, period, direction, and energy, which are essential for a wide range of applications [22]. In the context of marine energy, accurate wave measurements enable the efficient design and placement of wave energy converters, optimising their performance and ensuring their resilience to extreme conditions [23]. For coastal management and navigation, wave data aids in predicting and mitigating the impacts of coastal erosion, storm surges, and flooding, thereby enhancing safety and preparedness [24]. Furthermore, in the realm of climate research, continuous monitoring of wave patterns contributes to the understanding of ocean-atmosphere interactions and the effects of climate change on sea state [25]. Overall, wave measuring devices are indispensable tools for advancing oceanographic research, improving maritime operations, and supporting the sustainable development of marine resources [26].

2.3 Evolution of Wave Measuring Technologies

The study and measurement of ocean waves have undergone significant transformations since the early 20th century, evolving from basic observational techniques to sophisticated, high-precision instruments. This evolution reflects the growing importance of accurate wave data for various applications, including maritime safety, coastal management, climate research, and the development of marine energy technologies [27].

In the early 1900s, ocean wave measurements primarily relied on visual observations from ships and coastal stations. Mariners recorded wave height and period using simple tools like poles and sight lines. While these methods provided basic data, they were subjective and often inaccurate due to human error and environmental conditions [28].

The introduction of mechanical wave recorders in the 1930s marked a significant advancement. These devices, such as the Shipborne Wave Recorder developed by the British Navy, used floats to measure wave motion mechanically [29]. The data was recorded on paper charts, providing a more objective and continuous record of wave activity. However, these early mechanical devices were cumbersome and limited in their ability to capture high-frequency wave data, which are critical for understanding wave dynamics [30].

The 1960s and 1970s witnessed the emergence of electronic wave recorders, which significantly improved the accuracy and reliability of wave measurements. These devices employed accelerometers to measure wave-induced vertical accelerations. The analogue signals generated by these sensors were then recorded on magnetic tapes or chart recorders [31].

One notable development during this period was the Datawell Waverider buoy, introduced in 1961. This buoy used an accelerometer to measure wave-induced vertical accelerations and a heave-pitch-roll sensor to determine wave direction. The Waverider buoy became a standard tool for wave measurements due to its robustness and accuracy, and it remains widely used today [32].

The late 20th century saw a revolution in ocean wave measurement with the advent of satellite remote sensing and radar technologies. Satellite altimeters, first deployed in the 1980s, measure the sea surface height with high precision by timing the return of radar pulses reflected from the ocean surface [33]. This technology provides global wave height data, significantly enhancing the spatial coverage of wave measurements [34].

Synthetic Aperture Radar (SAR) satellites, such as the European Space Agency's ERS-1 launched in 1991, further advanced wave measurement capabilities. SAR captures detailed images of the sea surface, allowing for the extraction of wave spectra, including wave height, direction, and wavelength [35]. These data are invaluable for global wave modelling and climate research [36].

In recent decades, the development of advanced buoy technologies and integrated measurement systems has further refined ocean wave measurements. Modern wave buoys are equipped with a range of sensors, including GPS, accelerometers, and gyroscopes, to provide high-resolution, real-time data on wave height, period, direction, and spectral energy distribution [37]. These buoys often transmit data via satellite or radio links, enabling near-instantaneous access to wave information [38].

The integration of wave measurements with other oceanographic data has also become increasingly common. For example, the Atlantic Marine Energy Test Site (AMETS), National Data

Buoy Centre (NDBS) and the Coastal Data Information Programme (CDIP) operate a network of buoys and coastal stations that measure waves, winds, currents, and other parameters, providing a comprehensive view of ocean conditions [39]. Such integrated systems support a wide range of applications, from improving weather forecasts to enhancing marine navigation safety [40].

Looking ahead, the future of ocean wave measurement lies in the continued integration of advanced technologies and the development of autonomous systems. Emerging technologies, such as unmanned surface vehicles (USVs) and underwater gliders, offer new possibilities for wave measurements in remote and challenging environments [41]. These autonomous platforms can be equipped with wave sensors and operated in swarms, providing high-resolution, spatially distributed wave data [42].

Additionally, the use of machine learning and artificial intelligence in processing and analysing wave data is gaining traction. These techniques can enhance the accuracy of wave predictions and improve the understanding of complex wave phenomena [43]. As the demand for precise and comprehensive wave data continues to grow, the evolution of ocean wave measuring technologies is poised to play a critical role in advancing marine science and supporting the sustainable use of ocean resources [44].

2.4 Wave measuring devices - introduction

Wave measuring devices are essential tools for understanding oceanographic processes, managing coastal areas and developing marine renewable energy sources. These devices provide crucial data on wave height, period and direction, which are vital for applications ranging from coastal engineering to weather forecasting [45].

Wave measuring devices can be classified into two main categories: in-situ devices and remote sensing devices. Each type has distinct methodologies for capturing wave data [46].

Wave buoys are floating devices designed to measure various wave characteristics directly from the sea surface. Equipped with accelerometers, gyroscopes, and GPS, these buoys capture wave height, period, and direction [47]. Data collected by wave buoys is used to generate wave spectra and analyse ocean conditions.

Pressure sensors are deployed on the seabed and measure the variations in water pressure caused by passing waves. These devices convert pressure fluctuations into wave heights and can be used to monitor wave dynamics in deeper waters [48].

Acoustic Doppler Current Profilers (ADCPs) use the Doppler effect to measure the velocity of water particles. By analysing the frequency shift of sound waves reflected from moving particles, ADCPs provide information on wave velocity, direction, and the vertical profile of wave conditions [49].

Radar systems, installed on coastal structures or ships, use electromagnetic waves to measure sea surface roughness and wave patterns. These systems can capture data over large areas and provide real-time wave information [50].

Satellite altimeters measure sea surface height by timing the return of radar pulses sent from the satellite to the ocean surface. This technology offers global coverage and is used for monitoring large-scale oceanographic phenomena [51].

Light Detection and Ranging (LIDAR) systems use laser pulses to measure wave height and surface features. By analysing the time it takes for the laser to reflect off the water surface, LIDAR provides high-resolution wave data and can be used for coastal monitoring [52]. Each wave measuring approach is discussed in detail in the preceding sections.

2.4.1 Key Parameters Measured

Wave measuring devices capture several key parameters essential for oceanographic research and applications, which are defined as:

- Wave height refers to the vertical distance between the crest (highest point) and the trough (lowest point) of a wave. Accurate measurement of wave height is crucial for coastal engineering and marine safety [53].
- The wave period is the time it takes for successive wave crests to pass a fixed point. This parameter is important for understanding wave energy and predicting wave behaviour [54].
- Wave direction indicates the direction from which the waves are coming. It is essential for navigation, coastal construction, and energy generation [55].
- The wave spectrum represents the distribution of wave energy across different frequencies and directions. It is used to analyse the energy content of waves and predict their impact on coastal environments [56].

2.4.2 Application Areas

Wave measuring devices have diverse applications across various fields. Wave energy converters and offshore wind farms rely on accurate wave measurements for site selection, design, and operation [57]. Reliable data ensures the efficiency and economic viability of renewable energy projects. Coastal engineers use wave data for designing and maintaining coastal defences, harbours, and navigation channels [58]. Accurate measurements help ensure the stability and safety of coastal infrastructure. Wave data is essential for predicting sea state conditions, which are critical for maritime navigation and weather forecasting [59]. Accurate wave predictions support safe and efficient marine operations. Long-term wave measurements contribute to understanding climate change impacts on ocean dynamics and sea-level rise. This data is crucial for climate modelling and environmental monitoring [60]. Wave information supports safe and efficient maritime navigation by providing data on sea conditions and aiding in route planning [61].

Wave measuring devices are indispensable tools for a wide range of applications, from renewable energy to coastal management and climate research. The classification of these devices into in-situ and remote sensing categories highlights the diverse methodologies used to capture wave data. Technological advancements have significantly improved the accuracy, reliability, and capabilities of these devices, expanding their applications across various fields. As technology continues to evolve, wave measuring devices will play an increasingly vital role in our understanding and management of oceanic environments.

2.4.3 Technological Advancements

Technological advancements have significantly enhanced the performance and capabilities of wave measuring devices. Modern sensors offer improved accuracy and sensitivity for measuring wave parameters [62]. Advances in sensor technology have enabled more precise and reliable wave measurements. Integration of data from multiple sources, such as combining satellite altimeter data with buoy measurements, allows for comprehensive wave analysis [63]. Sophisticated algorithms and machine learning techniques have improved data processing and predictive modelling [64]. Advances in communication technology enable real-time data transmission from remote wave measuring devices [65]. This capability supports timely decision-making for maritime navigation, weather forecasting, and coastal management.

The development of autonomous wave measuring systems, such as autonomous underwater vehicles, offers new opportunities for collecting wave data in challenging environments and remote locations [66].

2.5 Wave Buoys

Data buoys are floating platforms equipped with various sensors and instruments designed to collect and transmit data about the ocean and atmospheric conditions. These buoys play a crucial role in oceanography, meteorology and climate research [67]. Data buoys are typically equipped with a variety of sensors to measure parameters such as sea surface temperature, air temperature, humidity, barometric pressure, wind speed and direction, wave height, and ocean currents [68]. One of the primary functions of data buoys is to transmit real-time data to onshore stations or satellites. This data is essential for weather forecasting, climate monitoring, and research [69]. Data buoys are often part of larger global or regional ocean observing systems, such as the Global Ocean Observing System (GOOS) [70]. These systems aim to provide comprehensive and sustained ocean observations to support scientific research and operational applications. These devices help monitor and understand changes in the marine environment, including variations in sea surface temperature, the impact of weather events, and the behaviour of ocean currents [71]. This information is crucial for studying climate change and its effects on the oceans [72]. Scientists use data collected from buoys to conduct research on ocean dynamics, climate patterns, and marine ecosystems [73]. The information gathered contributes to a better understanding of Earth's systems and supports the development of models for climate prediction [74]. Data from buoys also contribute to maritime safety by providing real-time information about sea conditions [75]. This is particularly important for shipping, offshore operations, and coastal management. There are different types of buoys, including moored buoys (anchored to the ocean floor), drifting buoys (free-floating and drifting with ocean currents), and profiling buoys (capable of moving vertically through the water column to collect profile data) [76]. Some devices are surface following which follow the surface of the sea slope, while others track the orbital motion [77]. Orbital motion refers to the movement of a particle or object along a curved path due to the influence of forces such as gravity or other types of central forces [78]. In the context of particles following buoys, orbital motion can be observed in water waves. When a buoy is placed in water, the motion of the water particles beneath it typically exhibits a circular or elliptical path. This occurs because of the interaction between the buoy and the wave energy in the surrounding water. As a wave passes through the buoy, the water particles move in an orbital motion – moving up and down vertically (due to the wave crest and trough) while simultaneously moving forward and backward along the direction of wave propagation [79].

2.5.1 Drifting Data Buoys

Drifting data buoys are oceanographic instruments designed to collect and transmit various types of data while drifting with ocean currents. These buoys play a crucial role in monitoring and studying the dynamic properties of the world's oceans [80]. Drifting buoys provide real-time data on oceanic parameters such as sea surface temperature, salinity, and atmospheric conditions. This information is valuable for weather forecasting, climate research, and understanding oceanic trends. These devices are designed to move with ocean currents, allowing them to cover large areas. This mobility makes them suitable for studying ocean circulation patterns, including the tracking of currents and eddies [82]. They are often more cost-effective than maintaining a fixed network of oceanographic instruments. They can cover vast expanses of the ocean at a relatively lower cost compared to deploying and maintaining fixed buoys or research vessels [83]. These buoys are used in international programs, providing global coverage for data collection. This is particularly important for understanding large-scale oceanic processes and phenomena.

These buoys are typically equipped with GPS, accelerometers, gyroscopes, and other sensors that measure the motion of the buoy as it drifts with the ocean surface. By capturing data on vertical and horizontal movements, the buoys can detect wave height, period, direction, and other key characteristics [84]. The motion data is transformed into a consistent reference frame, often converting the data from a moving platform (buoy) to a fixed Earth reference. This step ensures that the wave-induced motion is separated from the drift motion. Fast Fourier Transform (FFT) is applied to the time series of vertical motion (heave) to generate the wave energy spectrum [85].

Figure 2.1 – A drifter neatly compressed for deployment (**left**) and with the nylon drogue fully extended (**right**), as it will be in the water once the cardboard wraps dissolve. [85]

Some advantages of the drifting buoy include:

- Wide Coverage. Drifting buoys can travel long distances, allowing for broad spatial coverage of ocean data in areas where fixed stations are not practical [86].[87].
- Real-Time Data Transmission. Most buoys are equipped with satellite communication, enabling near real-time delivery of wave, current, and temperature data [88],[89].
- Cost-Effective Deployment. Compared to moored buoys or research vessels, drifting buoys are generally cheaper to deploy and maintain [90].
- Versatility. Drifting buoys can be equipped with multiple sensors to measure various oceanographic and meteorological parameters (e.g., wave height, sea surface temperature, salinity) [91],[92].
- Minimal Environmental Disturbance. They float passively and do not disturb the ocean environment, making them suitable for long-term monitoring and ecological studies [93].
- Useful in Hazardous or Remote Areas. Ideal for collecting data in harsh or remote environments (e.g., polar regions, open ocean during storms) where human access is limited [94],[95].

Some disadvantages of the drifting buoy include:

- Lack of Stationarity. Because they drift, it's difficult to get consistent, long-term data at a single location; not ideal for site-specific studies [96].
- Limited Control. Once deployed, their paths are determined by currents and wind, so their trajectories and data coverage are unpredictable [97].
- Limited Lifespan. Batteries, biofouling, sensor degradation, or physical damage can limit operational lifespan—often a few months to a year [98],[99].
- Data Gaps and Loss. Risk of data loss due to transmission failures, satellite outages, or buoy malfunction [100].
- Surface-Only Data. Most drifting buoys only collect surface-level data (e.g., sea surface temperature, waves); they usually can't measure subsurface conditions unless specially equipped [101].
- Potential for Retrieval Issues. Retrieval for maintenance or reuse is often impractical due to unpredictable drift paths and remote final locations [102].

2.5.2 Pitch-Roll-Heave Buoys

Pitch-roll-heave buoys are disc-shaped buoys that follow the slope of the sea surface, as opposed to tracking the orbital motion like the particle following buoys discussed in the following section. The pitch and roll inclinations are measured, along with the vertical heave [103],[104]. These measurements help researchers and scientists understand the dynamic behaviour of the ocean and its impact on marine ecosystems. Pitch refers to the rotation of the buoy around its lateral axis, causing the front or back of the buoy to move up or down [105]. They provide information on the vertical movement of the buoy, which is crucial for understanding wave characteristics and help in assessing the impact of wave energy on the buoy and its instrumentation [106]. However, pitch data alone may not provide a complete picture of the buoy's motion. It needs to be considered in conjunction with roll and heave data for a comprehensive analysis [107]. Roll is the rotation of the buoy around its longitudinal axis, causing it to tilt from side to side. This information is essential for understanding the stability and orientation of the buoy and important for evaluating the impact of lateral movements on buoy-mounted instruments [108]. Similarly, roll data alone may not be sufficient for understanding the overall buoy motion, especially in the presence of complex wave patterns [109]. Heave refers to the vertical displacement or movement of the buoy in response to wave motion. Provides information on the buoy's vertical displacement, which is crucial for studying wave height and frequency and is important for assessing the buoy's response to variations in water level [110]. However, heave data may be affected by buoyancy changes, making it challenging to accurately interpret vertical movements [111].

To analyse the data, the buoy continuously records time series of its pitch, roll, and heave movements. This motion data is then processed using Fast FFT [112]. The FFT converts time-domain motion data into the frequency domain, creating a wave energy spectrum that shows how much energy exists at each wave frequency. From the heave spectrum alone, key parameters like significant wave height (the average of the highest one-third of waves) and dominant wave period (the period with the most energy) can be extracted [113].

For wave direction estimation, the buoy’s pitch and roll data are used in combination with the heave data. The method commonly applied is directional spectral analysis, such as the Maximum Likelihood Method (MLM) or Fourier Series Methods, which analyse the phase and coherence between the three motion components [114]. This allows scientists to determine the direction from which waves are arriving, in addition to their energy and frequency [115].

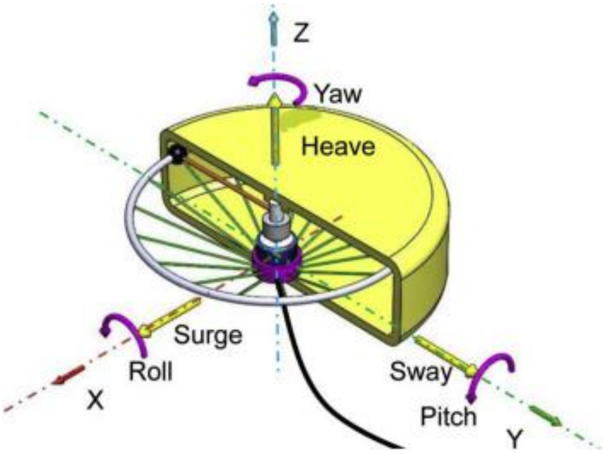

Figure 2.2 – 6-degrees of freedom (DOF) motion image [115]

Figure 2.3 – Fugro Oceanor Wavescan Buoy [115]

Together, pitch, roll, and heave data offer a comprehensive view of a buoy's motion, enabling a more accurate analysis of environmental conditions [116]. These measurements are essential for studying wave characteristics, which is valuable for maritime and offshore engineering applications. They help assess the impact of buoy movements on the accuracy and reliability of instrumentation attached to the buoy [117]. However, interpreting and analysing the data can be complex, especially in the presence of irregular wave patterns or external factors influencing buoy motion [118]. Accurate measurement and calibration of pitch, roll, and heave sensors can be challenging, affecting the reliability of the collected data along with integrating these measurements with other environmental data requiring careful consideration and may pose challenges in data synchronization [119].

Some advantages of the pitch-heave-roll buoy include:

- Comprehensive Wave Data Collection. Measures all three key wave motions, providing a more complete picture of sea state dynamics [120].
- Enhanced Accuracy. Enables accurate estimation of wave parameters like height, period, and direction [121].

- Versatility. Useful in various applications including oceanography, offshore engineering, and renewable energy (wave energy converters) [122].
- Adaptability to Harsh Conditions. Designed to endure and operate effectively in rough sea environments [123].
- Energy Harvesting Potential. The three-dimensional movement can be utilized for kinetic energy harvesting in wave energy devices [124].
- Improved Design Validation. Helps validate ocean wave models and offshore structure designs by providing realistic data inputs [125].

Some disadvantages of the pitch-heave-roll buoy include:

- Complex Design and Maintenance. More moving parts and sensors mean higher potential for mechanical failure and maintenance requirements [126].
- High Cost. Advanced sensors, data logging, and rugged design make them more expensive than simpler buoys [127].
- Calibration Challenges. Accurate measurement requires careful calibration of sensors, which can drift over time [128].
- Power Supply Limitations. Sustaining power for sensors and transmitters in remote areas is challenging without solar or other power sources [129].
- Data Transmission Issues. In remote ocean regions, real-time data transmission may be limited by satellite communication constraints [130].
- Vulnerability to Biofouling and Vandalism. Marine growth and human interference can affect sensor performance and buoy integrity [131].

2.5.3 Surface Following Buoys

Surface-following wave measuring buoys, are devices designed to measure and monitor ocean surface waves. These buoys play a crucial role in collecting data on wave height, period, and direction, providing valuable information for various applications such as weather forecasting, climate research, and offshore engineering [132],[133]. Wave buoys provide accurate and reliable measurements of wave characteristics, including wave height, period, and direction [134]. This information is essential for understanding ocean dynamics and predicting extreme weather events [135]. Many surface-following buoys are equipped with telemetry systems that enable real-time data transmission. This allows researchers and meteorologists to monitor wave conditions promptly and respond to changes in the environment [136]. Wave buoys are designed to withstand harsh marine conditions, allowing for long-term deployment in open ocean environments. This durability ensures a consistent and continuous data stream for extended periods [137]. These buoys can be deployed in various locations, including remote and deep-sea areas, providing a comprehensive understanding of wave patterns on a global scale [138]. Wave buoys are often part of a broader ocean monitoring system and can be integrated with other sensors to measure parameters such as sea surface temperature, salinity, and atmospheric conditions [139]. This integrated approach enhances the overall understanding of ocean dynamics [140]. The data collected by wave buoys is invaluable for scientific research, offshore engineering design, and the development of renewable energy projects, such as wave energy converters [141]. However, Surface-following wave measuring buoys can be expensive to manufacture, deploy, and maintain. The cost may limit the number of buoys that can be deployed, especially in remote or less economically developed regions [142]. Despite their robust design, wave buoys can still be damaged or lost during severe storms or extreme weather events. This can result in data gaps and the need for costly replacements [143]. Deploying a network of buoys is necessary to obtain comprehensive spatial coverage, but this may still result in limited resolution in certain areas. This limitation is particularly relevant in regions with complex coastal geometries [144]. Marine organisms, such as barnacles and algae, can accumulate on buoy surfaces, affecting sensor accuracy and performance over time. Regular maintenance is required to address biofouling issues [145]. In remote or deep-sea locations, transmitting real-time data to onshore facilities may pose challenges. This can result in delays in data availability and processing [146].

Surface following buoys can use gyroscopes, GPS, accelerometers to gather time-series data for heave, pitch and roll, compass heading and horizontal displacement [147]. The buoy has an on board computer that performs spectral analysis on the motion data, including zero-crossing analysis, FFT and directional spectrum [148].

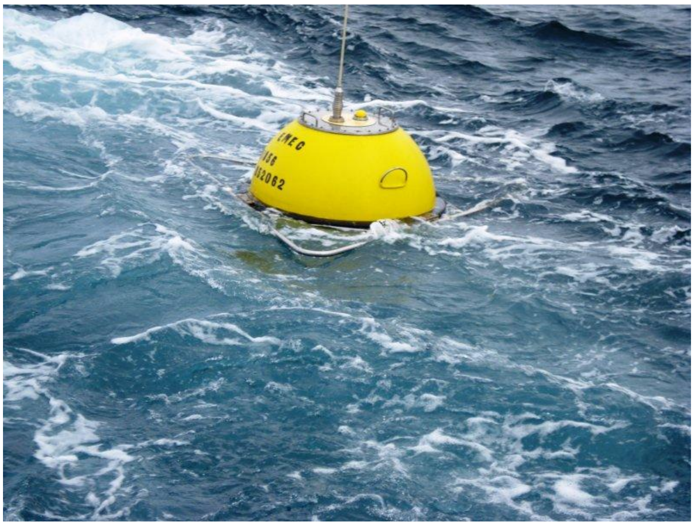

Figure 2.4 – Datawell Waverider Buoy [149]

Some advantages of the surface following buoy include:

- Accurate Wave Measurement. Designed to follow the sea surface precisely, enabling high-fidelity data on wave height, period, and direction [150].
- Direct Response to Wave Motion. Mimics the wave-induced motion of floating vessels or platforms, making it ideal for marine engineering and safety applications [151].
- Proven and Widely Used Technology. Commonly used by national meteorological and oceanographic agencies, with established data protocols [152].

- Effective for Model Validation. Provides critical surface wave data for validating wave prediction and ocean circulation models [153].
- Compact and Deployable. Many are small and easy to deploy from ships, offshore platforms, or aircraft [154].
- Can Be Combined with GPS and Inertial Sensors. Allows for high-resolution motion tracking in three dimensions [155].
- Useful in Coastal and Offshore Environments. Deployed for navigation safety, offshore construction, surfing forecasts, and research [156].

Some disadvantages of the surface following buoy include:

- Limited to Surface Motion Only. Does not provide information about subsurface currents or vertical profiles unless equipped with additional instruments [157].
- Affected by Wind and Current Drift. Can be displaced by surface currents or wind, making them less ideal for fixed-point wave monitoring unless moored [158].
- Vulnerable to Harsh Marine Conditions. Extreme wave conditions may damage the buoy or cause it to capsize or lose calibration [159].
- Maintenance and Fouling Issues. Biofouling and corrosion affect sensor accuracy and durability, requiring periodic maintenance or replacement [160].
- Power and Data Transmission Constraints. Relies on batteries and satellite or radio communication, limiting deployment time in remote areas [161].
- Expensive for Long-Term Monitoring. More advanced models with telemetry and multiple sensors can be costly to build, deploy, and maintain [162].
- Not Ideal for Current Tracking. While it follows the surface, it does not track the flow of water particles like drifters do, so it's not suited for current studies [163].

2.6 Other wave measuring devices

2.6.1 Acoustic Wave Sensors

The Acoustic Doppler Current Profiler (ADCP) is a device used to measure the velocity of water currents in oceans, rivers, and other water bodies. It employs the Doppler effect to determine the velocity of water particles along the acoustic beams emitted by the device [164]. The ADCP emits acoustic beams (pulses of sound waves) into the water. When these beams encounter moving particles (such as water molecules or suspended sediments), the frequency of the sound waves is altered due to the Doppler shift [165]. The ADCP measures the change in frequency caused by the Doppler effect and used this information to calculate the velocity of water particles at different depths [166]. The device can produce and receive signals from multiple directions and can be stationary or mounted to a moving vehicle [167]. Because the emitted signal extends down through the water column, it measures the current at many different depths and can determine the speed and direction of the varying currents within the water column, including the surface of the ocean [168]. The water velocities as determined from each beam are combined and processed to produce a time-series of the 3D wave-induced water velocities and from that the directional wave spectrum [169]. The device extracts time series data including surface elevation and orbital velocity [170]. The device then performs a FFT to convert time-domain data to frequency spectra to generate wave energy spectra and directional spectra [171].

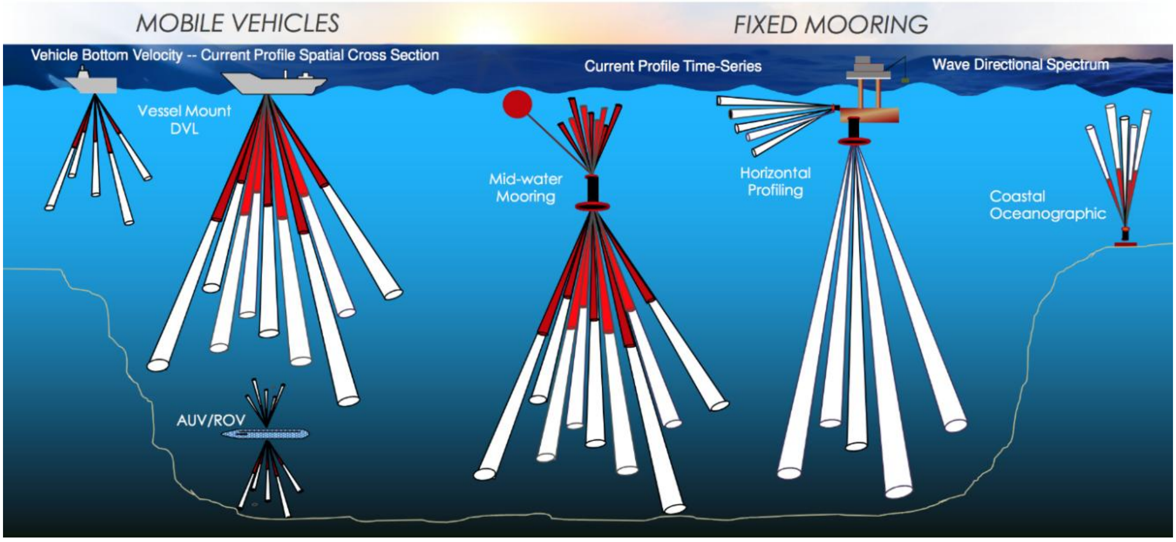

Figure 2.5 – Typical Acoustic Doppler Current Profiler device [164]

Some advantages of an ADCP are listed below:

- Profiles Entire Water Column. Measures current velocity at multiple depths simultaneously (vertical profiling), not just at a single point [172].
- Non-intrusive Measurement. Uses sound waves; no moving parts are exposed to water, reducing maintenance and minimizing disturbance to the environment [173].
- Directional and 3D Current Data. Provides 3-axis velocity components (east-west, north-south, and vertical), giving a full picture of water movement [174].

Versatile Deployment. Can be deployed:

- Downward-facing from a surface buoy or ship
- Upward-facing from the seabed
- Horizontally for side-looking applications in rivers or harbours [175]
- Additional Capabilities. Some models can estimate:
- Wave height and direction
- Sediment transport/turbidity
- Bottom tracking for vessel speed [176]

- Remote Data Collection. Can be used for long-term monitoring with remote data transmission (via satellite, radio) [177].
- High Temporal Resolution. Provides real-time or near-real-time data with adjustable sampling intervals [178].

Some disadvantages of an ADCP are listed below:

- Limited Range. Acoustic signals weaken with distance and turbidity:
- Shallow models may reach only 30–50 meters.
- Deepwater models are more powerful but still limited compared to some alternative tools [179].
- Data Quality Affected by Environment. Accuracy can be compromised by:
- Air bubbles, suspended sediment, or marine life
- Thermoclines or other sharp water density changes
- Turbulent or high-flow conditions [180]
- Expensive Equipment. ADCPs are costly to purchase and maintain, especially for deepwater or high-resolution models [181].
- Complex Data Processing. Raw Doppler data requires significant processing and calibration. May require expertise in oceanography and signal processing to interpret properly [182].
- Power Consumption. High-frequency or long-term deployments need large batteries or external power sources [183].
- Blind Zone Near Transducer. There is a small "blanking distance" near the ADCP head where it cannot measure due to acoustic interference [184].

2.6.2 Radar-Based Systems

Land-based radar and satellite radar are two distinct approaches to measuring waves in the ocean. Each method has its own set of advantages and disadvantages, and the choice between them often depends on the specific requirements of the application [185].

Land based high frequency surface wave radar is a rapidly emerging technology suitable for ocean wave remote sensing through line-of-sight wave measurement [186]. The transmitted signals of coherent radar have all defined phase angles to a reference, and this distinguishing characteristic leads to the capability of obtaining the Doppler information [187]. Analysis of coherent microwave radar data usually involves the application of a 3-D Fast Fourier Transformation (FFT) to the acquired backscatter images of the ocean area to estimate the spectra. Subsequently, wave parameters can be deduced based on a spectral analysis of the estimated spectra [188]. Advantages of this system include based high-resolution wave measurements, especially when positioned close to the shore. This is beneficial for detailed studies of nearshore wave processes [189]. Compared to satellite systems, land-based radar installations are generally more cost-effective to set up and maintain. They are particularly suitable for local or regional wave monitoring. Land-based radar systems can provide real-time data, which is crucial for applications like coastal management, harbour operations, and storm surge predictions [191]. Researchers can customize land-based radar installations based on the specific needs of the study area. This flexibility allows for targeted data collection [192].

Disadvantages of this system compared to satellite include, limited range, and its coverage is constrained to coastal areas. It may not be suitable for studying open-ocean waves or large expanses of water [193]. Radar signals can be obstructed by obstacles such as buildings or terrain. This may limit the effectiveness of land-based radar in certain locations [194]. Maintenance of land-based radar systems, especially in harsh coastal environments, can be challenging. Exposure to saltwater, storms, and other environmental factors may lead to wear and tear [195].

Figure 2.6– Typical land based radar wave measuring system [185]

The system has two main approaches to analyse wave date from radar:

Spectral FFT-based method

- Image Stack Collection: A time series of radar images (e.g., over 10–30 minutes) is collected [196].
- 3D FFT Analysis: A 3D Fast Fourier Transform is applied to the stack (2 spatial + 1 temporal dimension), creating a 3D wave spectrum:
    - Wave number (k): spatial frequency
    - Direction (θ): wave travel direction
    - Frequency (f): temporal variation [197]
- Dispersion Relation Filtering:
    - Applies the linear wave dispersion relation to filter out non-wave components.
    - Matches spatial and temporal wave characteristics to identify true ocean wave energy [198].

Sea Clutter and Shadowing Analysis.

This simpler method uses statistical patterns in radar images:

- Counts shadowed and bright zones on sea surface
- Wave parameters are estimated by analysing distances between crest lines, crest orientation and temporal variation [199].

Some advantages of a radar-based system include:

- Non-Contact and Remote Operation
    - No instruments in the water—completely remote sensing from shore, ship, or platform.
    - No risk of damage from rough sea conditions or marine growth [200].
- Wide Area Coverage
    - Can monitor waves over several kilometres (typically 1–5 km range).
    - Captures spatially distributed wave fields, unlike point-based systems (e.g., buoys or ADCPs) [201].
- High Temporal Resolution
    - Provides near real-time data (updated every few seconds to minutes).
    - Useful for tracking rapidly changing sea states [202].
- Directional Wave Information
    - Accurately captures wave direction, wave period, and directional spectra [203].
- Useful in Harsh Environments
    - Operates in areas where buoys or underwater sensors may fail (e.g., near ports, platforms, ice-covered waters) [2-4].
- Dual Use with Navigation Radars
    - Can be integrated into existing ship or platform radars, making it cost-effective in some installations [205].

Some disadvantages of a radar-based system include:

- Indirect Measurement of Wave Height
  - Wave height (Hs) is not directly measured—must be estimated from image contrast or shadowing models.
  - Often less accurate than buoy- or pressure-based measurements unless calibrated [206].
- Environmental Limitations. Performance can degrade due to:
  - Low wind conditions (less surface roughness = poor backscatter)
  - Rain, fog, or sea spray (signal interference)
  - Land clutter or objects in field of view [207]
- Requires Line-of-Sight
  - Only works where the radar has an unobstructed view of the sea surface [208].
- Complex Data Processing
  - Requires advanced image and spectral analysis, including filtering and calibration against wave models.
  - May require expert tuning and validation [209].
- Lower Accuracy in Calm Conditions
  - Difficult to detect small wave patterns in low sea states (e.g., Hs < 0.5 m) [210].
- High Power Consumption and Infrastructure Needs
  - Requires stable mounting, continuous power, and reliable data processing hardware/software [211].

2.6.3 Satellite Remote Sensing

Satellite radar for ocean wave measurement utilizes synthetic aperture radar (SAR) technology. SAR instruments on satellites transmit microwave signals towards the Earth's surface and receive the backscattered signals. By analysing the returned signals, the satellite can generate images and data related to the ocean surface, including wave characteristics [212],[213]. Advantages of this system include providing a global perspective, allowing for the monitoring of waves over vast ocean areas. This is particularly useful for studying open-ocean wave patterns [214]. Satellites can provide continuous and persistent monitoring of ocean surfaces, enabling long-term studies and trend analysis [215]. This system can cover remote or inaccessible areas where land-based installations may not be practical or cost-effective [216]. Satellite measurements offer a consistent data collection platform, reducing the variability associated with different land-based radar installations [217]. For example, significant wave height can be determined from the slope of the leading edge of the altimetry waveform [218]. Figure 2.7 shows how the specifics of the surface wave field affect the measured signal. Significant wave height is the mean value of the highest third of the measured waves [219].

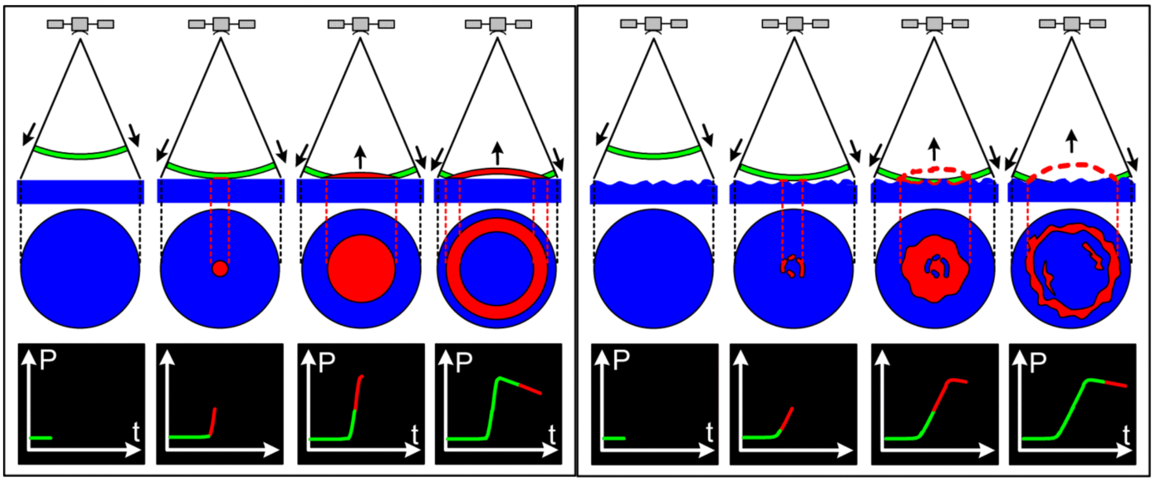

Figure 2.7 – Typical satellite wave measuring system [212]

The radar altimeter receives the reflected wave (of echo), which varies in intensity over time. Where the sea surface is flat (left), the reflected wave's amplitude increases sharply from the moment the leading edge of the radar signal strikes the surface. However, in sea swell or rough seas (right), the wave strikes the crest of one of one wave and then a series of other crests which cause the reflected wave's amplitude to increase more gradually. Ocean height can be derived from the information in this reflected wave, since the slope of the curve representing its amplitude over time is proportional to wave height [220]. Disadvantages of this system include generally a lower spatial resolution compared to land-based radar. This limitation may affect the ability to capture fine details of nearshore wave dynamics [221]. While satellites provide persistent monitoring, the revisit time of satellites may be relatively long. This can be a limitation for applications requiring high-temporal-resolution data [222]. The development, launch, and maintenance of satellites can be expensive. This cost factor may limit the availability of dedicated satellite missions for specific wave measurement purposes [223]. In practice, a combination of both land-based and satellite radar systems may be employed to leverage the strengths of each method and overcome their respective limitations. Integrating data from multiple sources can provide a more comprehensive understanding of ocean wave characteristics [224].

Some advantages of SAR include:

- Global Coverage
    - Satellites can measure waves across the entire ocean, including remote or inaccessible areas where in-situ measurements (like buoys or radar) are impossible [225].
- Large Spatial Scale
    - Can provide data over very wide swaths (hundreds to thousands of kilometres per pass), offering a synoptic view of wave conditions [226].
- Consistent, Long-Term Data

  - Many satellite missions (e.g., Sentinel, Jason, SWOT) provide continuous, long-term datasets, essential for climate studies, model validation, and trend analysis [227],[228].
- No Local Infrastructure Needed
  - Data can be accessed remotely—no need to deploy or maintain buoys, radars, or other physical equipment on-site [229].
- Multiple Measurement Techniques
- Satellites can estimate:
    - Significant wave height (Hs) (altimeter)
    - Wave direction and wavelength (SAR)
    - Sea surface roughness (SAR, optical)
    - Wave spectra (limited from SAR) [230],[231].

Some disadvantages of SAR include:

- Limited Temporal Resolution
  - Most satellites have long revisit times (e.g., once every few days for a given location), making them unsuitable for real-time or high-frequency monitoring [232].
  - Cannot track short-term, localized wave events (e.g., tsunamis, storms in progress).
- Lower Accuracy than In-Situ Methods
  - Altimeters provide reliable Hs but are point measurements along narrow ground tracks (~1–10 km wide) [233].
  - SAR-based wave estimates can be complex to interpret and require advanced processing and validation [234].
- Weather and Cloud Sensitivity

    - Optical sensors (like MODIS) cannot "see" through clouds.
    - SAR works in all weather, but performance can still be affected by very rough seas or high winds [235].
- Complex Processing
    - Wave information, especially from SAR, requires sophisticated algorithms and post-processing.
    - SAR interpretation can be ambiguous in multi-directional or crossing seas [236].
- Delayed Data Availability
    - Data often becomes available with a latency of hours to days, depending on the satellite and provider [237].

2.6.4 Seabed Pressure Sensors

Seabed pressure sensors play a crucial role in oceanographic research, environmental monitoring, and various industrial applications [238]. Seabed pressure sensors are typically placed on the ocean floor and are designed to withstand the harsh conditions of the marine environment. They operate based on the principle that pressure increases with depth in a fluid, such as seawater. These sensors convert the pressure exerted by the water column above them into electrical signals, which can then be transmitted to the surface or stored for later retrieval [239]. Advantages of this device include:

- Accurate Depth Measurement: Seabed pressure sensors provide accurate measurements of water depth by sensing the pressure at specific depths. This is essential for understanding ocean dynamics, currents, and variations in sea level [240].
- Real-time Monitoring: Many seabed pressure sensors are equipped with telemetry systems that allow real-time data transmission to onshore facilities or research vessels. This enables researchers to monitor ocean conditions continuously [241].

- Long-Term Deployment: These sensors are designed for long-term deployment, allowing for extended data collection periods. This is crucial for studying seasonal variations, long-term trends, and changes in oceanographic parameters [242].
- Versatility: Seabed pressure sensors can be deployed at various depths, making them versatile for different research purposes. They are used in shallow coastal areas as well as in deep-sea environments [243].
- Integration with Other Sensors: They can be integrated with other sensors, such as temperature and salinity sensors, to provide a more comprehensive understanding of the ocean environment [244].

Disadvantages of seabed pressure sensors include:

- Cost: The cost of manufacturing, deploying, and maintaining seabed pressure sensors can be relatively high. This may limit the widespread deployment of these sensors in some cases [245].
- Limited Special Resolution: Depending on the density of the sensor network, there may be limitations in spatial resolution. Achieving high-resolution data across large areas may require a significant number of sensors, increasing the overall cost and complexity [246].
- Maintenance Challenges: Retrieving and maintaining seabed sensors can be challenging due to the deep-sea environment. Storms, currents, and biological fouling can affect the sensors and may necessitate periodic maintenance or replacement [247].
- Energy Requirements: Some seabed pressure sensors require power to operate, and supplying power to the sensors on the ocean floor can be challenging. Battery-powered sensors may have limited operational lifetimes [248].
- Environment Impact: The deployment and retrieval of sensors can have environmental impacts, disturbing the seabed and potentially affecting marine life in the vicinity [249].

The attenuation of wave pressure with depth results in them only being suitable for relatively shallow waters. In this regard, as low frequency waves hold more water, these sensors are more suitable for swell wave measurement [250]. Being limited by signal capabilities, the typical maximum depth of use for such devices is in the order of 20 metres thus limiting their usage to near shore locations [251]. Despite these challenges, advancements in technology and ongoing research aim to address these limitations, making seabed pressure sensors increasingly valuable tools for oceanographic studies and environmental monitoring [252].

Figure 2.8– Typical seabed pressure sensor device [238]

2.7 Using floating OWCs to estimate wave statistics.

Measuring air pressure in an OWC is crucial for understanding and optimising the performance of devices like wave energy converters, which harness the energy from ocean waves [253].[254]. OWC's typically consist of a chamber partially filled with water, and as waves cause the water level to rise and fall, the air column above the water oscillates, creating pressure variations [255].

To measure air pressure in an oscillating water column, one can use various instruments and techniques. Pressure Transducers are commonly used to measure air pressure changes within the OWC [256]. Pressure transducers can be installed at strategic locations within the air column or connected to the chamber to measure the dynamic pressure variations ensuring that the transducer has a suitable pressure range and response time for the expected oscillations [257]. Pressure Sensors can be designed to handle dynamic pressure changes. These sensors can be connected to data acquisition systems for continuous monitoring and recording of pressure variations over time [258]. It is important to consider barometric pressure changes, as they can affect the accuracy of pressure measurements. Including a barometric pressure sensor in the system can help correct for changes in atmospheric pressure, providing more accurate readings [259]. Employing data acquisition systems with high sampling rates allows you to capture rapid pressure changes accurately [260]. These systems can store and analyse pressure data over time, helping to understand the dynamics of the oscillating water column [261].

2.7.1 Air pressure in the WASP moonpool chamber

This work focuses on the measurement of the variation in air pressure above the oscillating water column with a view to obtaining/generating wave spectra and sea state conditions [262].

The WASP comprises a floating body with a central moonpool. The relative motion of the water level in the moonpool to the buoy will pressurise and depressurise the air above the water column [263]. This work will demonstrate that, once the WASP has been suitably calibrated, key wave spectrum parameters may be estimated from measurements of the pressure of the air above the water column by determining a relationship between the incident wave spectrum and the pressure spectrum within the OWC chamber [264]. Figure 2.9 depicts a typical cross section schematic of an “off the shelf” buoy with a hollow central core, the moonpool.

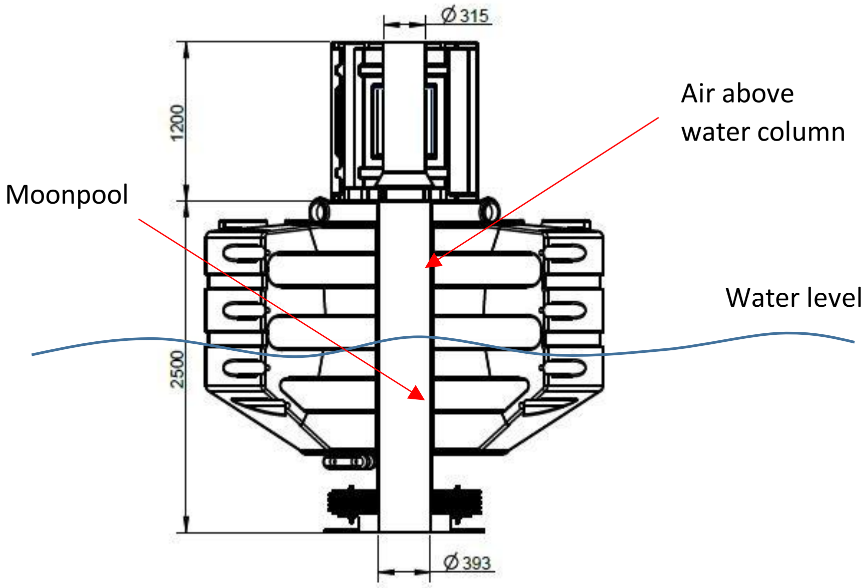

Figure. 2.9. JFC Seagull SG3000 buoy [253]

The advantages to be offered by the WASP wave measuring device include the adaptability of the system to a wide range of existing off the shelf ocean buoys with a hollow central core [265]. The buoys may continue to serve their purpose as ocean markers while also obtaining pressure variance data from above the water column. Such is the nature of the buoys, the system will always have a robust platform from which to operate [266]. The system can use low cost components while also being low energy consuming in its operation [267]. However, some disadvantages are that the system depends very much on the excitation of the water column or the buoy for generation of pressure data limiting the comprehensiveness of the collected data [268]. The buoy requires mooring in a specific area of interest, potentially hampering the systems use in its current form from deeper waters [269]. Background knowledge of the locations existing wave characteristics is required for use as training in order to exercise the input/output transfer function method, discussed in greater detail later in this chapter [270].

2.7.2 Challenges and Future Directions

Wave measuring devices represent crucial components in the broader context of renewable energy and marine sciences [271]. This section explores the challenges and future directions in this field, focusing on technological hurdles, environmental and regulatory issues, cost and economic considerations, and emerging trends and innovations.

2.7.3 Technological Challenges

Wave measuring devices, such as buoys, radar systems, and satellites, face significant challenges in terms of accuracy and reliability [272],[273]. These devices must operate in harsh marine environments, where factors like biofouling, extreme weather conditions, and mechanical wear can impact performance [274]. Continuous calibration and maintenance are essential to ensure accurate data collection, which can be logistically challenging and costly [275].

The integration of data from multiple sources presents a major technological challenge [276]. Different devices often use varying data formats, units, and sampling rates, complicating the process of data fusion. Moreover, the large volumes of data generated require robust computational resources and sophisticated algorithms for real-time processing and analysis [277]. Advancements in machine learning and data assimilation techniques are critical to overcoming these challenges [278].

2.7.4 Environmental and Regulatory Issues

The deployment of wave measuring devices can have significant environmental impacts [282]. Concerns include the disruption of marine habitats, noise pollution, and potential harm to marine life [283]. Comprehensive environmental impact assessments (EIAs) are required to understand and mitigate these effects [284]. Advancements in eco-friendly materials and deployment strategies can help minimize environmental footprints [285].

The regulatory landscape for ocean energy is complex and varies by region. Obtaining permits for the installation and operation of wave energy devices involves navigating through multiple layers of regulations related to environmental protection, maritime law, and energy policy [286]. Streamlined regulatory frameworks and international collaboration are needed to facilitate the growth of the ocean energy sector [287].

2.7.5 Cost and Economic Considerations

The initial costs of developing and deploying wave measuring devices are high [288]. These costs include research and development, manufacturing, installation, and maintenance. High upfront investment can be a barrier to entry, especially for small and medium-sized enterprises (SMEs). According to the International Renewable Energy Agency (IRENA), financial incentives and support from governments are crucial to stimulate investment in this sector [289].

Ensuring the economic viability of ocean energy projects is challenging due to fluctuating energy prices and competition from other renewable energy sources. Developing cost-effective technologies and achieving economies of scale are essential to make ocean energy competitive [290]. Innovative financing models, such as public-private partnerships and green bonds, can also play a role in supporting the economic sustainability of ocean energy projects [291].

2.7.6 Future Trends and Innovations

Future developments in advanced materials, such as corrosion-resistant composites and biodegradable materials, are expected to enhance the durability and environmental compatibility of wave measuring devices [292]. Additionally, innovations in sensor technology and autonomous systems will improve data accuracy and reduce operational costs [293].

International collaboration and knowledge sharing are vital for addressing the global challenges of wave measuring [296]. Collaborative research initiatives, joint ventures, and international policy frameworks can accelerate technological advancements and promote the sustainable development of ocean wave measuring devices [297].

2.7.7 Gap: Pressure-Based Wave Sensing in Sealed Moonpools

Existing wave sensors are exposed to harsh environments and require maintenance [298]. A sealed moonpool pressure sensor offers:

- Protected housing against biofouling and impact [299].
- Passive measurement via air compression without moving parts [300].
- Potential resonance amplification aiding sensitivity [301].

Challenges include:

- Deriving calibrated wave parameters from complex pressure signals [302].
- Decoupling vessel motion and internal hydrodynamics [303].
- Modelling nonlinear air-compressibility effects under dynamic loads [304].

Table 2.1 below summarises the various wave measuring device's methods of measurement, advantages and disadvantages and compare to those of the WASP.

Device Type	**Measurement Method**	**Advantages**	**Disadvantages**
Drifting Buoys	GPS or inertial motion sensors track buoy displacement over time.	- Easy deployment - Large area coverage - Long-duration data	- Limited spatial resolution - Susceptible to current drift - Power limitations
Pitch-Heave-Roll Buoys	Inertial Measurement Units (IMUs) detect pitch, heave, and roll motions.	- High-frequency wave detail - Directional wave data	- Requires stable calibration - Affected by biofouling and wind forces
Surface-Following Buoys	Follows surface motion; uses accelerometers or GPS to track vertical displacement.	- Direct wave measurement - Accurate spectral analysis	- Expensive - Needs frequent maintenance
Acoustic Wave Sensors	Measure Doppler shift or travel time of sound between transducers to determine wave profiles.	- Non-intrusive - High resolution in nearshore environments	- Limited to shallow waters - Affected by bioacoustic noise
Radar-Based Systems	Uses radar backscatter from sea surface to estimate wave height, direction, and period.	- Remote, non-contact - Continuous monitoring - Works on platforms (ships/oil rigs)	- Expensive - Calibration needed - Sensitive to weather and sea clutter
Satellite Remote Sensing	Altimeters and SAR measure sea surface elevation and wave spectra globally.	- Global coverage - Long-term trends - Valuable for large-scale models	- Low temporal/spatial resolution - Limited by revisit time - Cloud interference (SAR)
Seabed Pressure Sensors	Measure pressure fluctuations due to wave-induced surface changes.	- Protected from surface hazards - Long-term stable data	- Less accurate for short/steep waves - Needs depth correction - Limited directional data
OWC-Sealed Moonpool Air Pressure Sensor (Novel Device)	Measures changes in air pressure in a sealed moonpool chamber (oscillating water column) caused by wave forcing.	- No moving parts in contact with water - Low maintenance - Enclosed system less prone to biofouling - Can be integrated into floating platforms	- Requires careful calibration - Wave data inferred indirectly - Sensitivity to chamber geometry and air compressibility

Table 2.1 summary of various wave measuring device's methods of measurement, advantages and disadvantages compared to those of the WASP.

2.8 Ocean Wave Representation and Wave Spectra

In the study of wave phenomena, particularly in two dimensions, the concept of superposition plays a critical role. The principle of superposition states that any complex wave pattern can be represented as the sum of a number of simpler monochromatic waves. This idea is foundational in the analysis and synthesis of wave spectra [305].

Ocean waves can be treated as a stochastic process, generally represented as a superposition of linear sinusoidal components of varying frequencies and directions. The sea surface elevation $\eta(x,y,t)$ is often modelled using a two-dimensional wave energy spectrum $S(f,\vartheta)$ where f is frequency and ϑ is wave direction.

$$S(f,\vartheta)=S(f)D(\vartheta) \qquad \text{(Eq. 1)}$$

Here:

- $S(f)$ is the omnidirectional (1-D) wave spectrum,
- $D(\vartheta)$ is the directional spreading function, normalized such that:

$$\int_{-\pi}^{\pi} D(\theta)d\theta = 1 \qquad \text{(Eq. 2)}$$

This formulation allows decomposition of a complex sea state into frequency components and angular spreading, facilitating transformation from pressure time series to wave spectral estimates [306].

Wave heights vary and a given time series will have multiple values of *Hs* (significant wave height) which will vary randomly [308]. Similarly, with regard to *Tc* (crest to crest period) and *Tz* (zero up cross period) will not necessarily present the same distribution with regards to random waves [308].

Two of the most important parameters that quantify the state of the sea are a characteristic height and a characteristic period, with *Hs* being the most commonly used parameter for height [306]. The significant wave height is defined traditionally as the mean wave height, from trough to crest, of the highest one-third of the waves [307]. Whereas the characteristic period could be the mean period, average zero-crossing period, peak period and so on [306],[308]. These parameters may be determined directly from the time series of the wave data or from the frequency domain, if the energy density spectrum is known [306].

2.8.1 Wave Energy Spectrum

The ocean wave energy density spectrum is used to describe how the energy of ocean waves is distributed across different frequencies, providing a comprehensive understanding of the sea state and aiding in the design and optimisation of marine structures and wave energy converters [309].

The irregular nature of the sea surface prohibits straight forward analysis, however statistical surface properties, such as average wave heights, periods and direction vary more slowly. In this regard, a typical wave spectrum may be determined [310]. Figure 2.10 presents a standard time series of the movement of a water surface at a specific location. The wave crests are denoted by dashes and the zero down crossings circled [311].

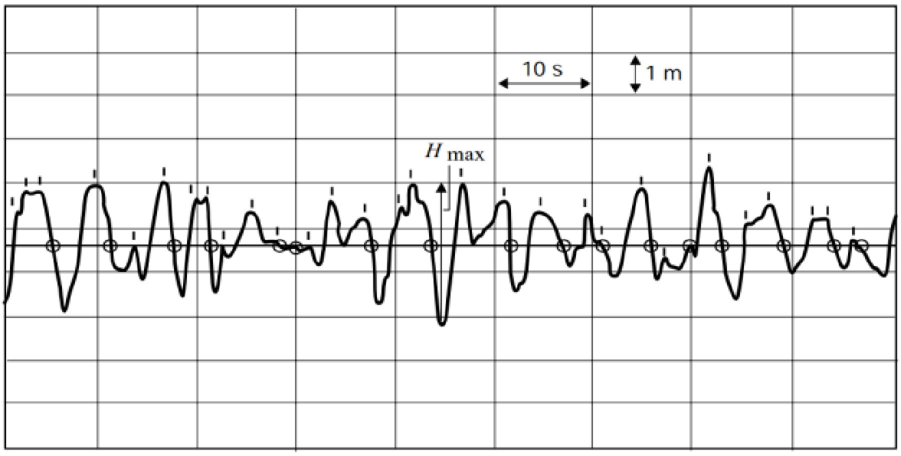

Figure 2.10 – Time series Wave record [311]

While such data may never be repeated exactly again due to the random nature of the sea, as the sea state is stationary and ergodic, the statistical properties such as *Hs* and *Tz* will be comparable throughout data [311].

A stationary process is a random process whose statistical properties (such as mean, variance, and autocorrelation) do not change over time. In other words, the behaviour of the process is consistent throughout its duration [312]. Stationarity is often categorized into:

- Strict Stationarity: All statistical properties of the process (including higher moments) are invariant under time shifts.
- Wide-sense Stationarity: The mean, variance, and autocorrelation of the process do not change over time.

Sea-states are often modelled as stationary processes because wave patterns and statistics (such as wave heights and periods) are assumed to remain constant over time, allowing for simplified analysis and prediction. This assumption is practical for many engineering applications and helps in modelling long-term average behaviour [312].

An ergodic process is one where time averages (over a single realization of the process) are equivalent to ensemble averages (averages over many realizations at a single point in time). In simpler terms, an ergodic process assumes that observing one realization over a long period of time gives the same statistical information as observing many independent realizations at a given moment [313].

Sea-states are approximated as ergodic because, in practice, it is often difficult to collect data from many different locations simultaneously. Instead, we use long-term observations from a single location, assuming that this can represent the overall statistical behaviour of the sea-state. This assumption makes it easier to analyse wave patterns and predict long-term trends from a limited data set [313].

By assuming stationarity and ergodicity, we can simplify the complex nature of sea-states and focus on their average behaviour, which is often sufficient for most practical applications. Approximating sea-states as stationary and ergodic simplifies the complex dynamics of ocean waves, making the problem more tractable for analysis and engineering [314]. In real-world applications, sea-state properties (like wave height and period) are typically averaged over time. The stationary assumption ensures that these properties don’t change unpredictably, and the ergodic assumption allows for statistical averages from a single observation over time. For coastal engineering and offshore structures, this approximation helps in predicting wave conditions and designing resilient systems without requiring exhaustive data from multiple locations or over impractical time spans [315].

The best representation of a random sea state is an energy density spectrum. Typically spectral plots present wave frequency on the x-axis and energy density on the y-axis with the area under the curve referred to as the seaway variance [316].

The energy density spectrum (also called the wave spectrum) with regard to ocean waves is a mathematical representation of how wave energy is distributed across different frequencies or wavelengths in a given wave field. It describes the intensity or amount of energy at each frequency or wavelength, helping to characterize the wave environment in a more detailed way than just looking at average wave height or wave period [317].

Energy density refers to the amount of energy per unit area per unit frequency or wavelength.

In the context of ocean waves, it describes how wave energy is spread across different wave frequencies, which can correspond to different wave periods or wavelengths.

The wave spectrum is a plot that shows the energy density of the ocean waves as a function of frequency (or wavelength). It provides insights into the wave field's variability, showing how much energy is associated with different frequencies.

The spectrum can be represented as energy per unit frequency (spectral density) or energy per unit wavelength [318].

The first step in creating a wave energy density spectrum is the collection of wave data. This is typically done using wave buoys, radar, or satellite observations that measure the time series of wave height or surface elevation over a specific period [319].

The collected time series data is then subjected to a Fourier transform, which is a mathematical technique that breaks down the complex signal (in this case, the wave height as a function of time) into a sum of sinusoidal waves (sine and cosine functions) of different frequencies [320].

The result of this transform is the frequency-domain representation of the wave signal, showing how much energy is present at each frequency. This is where the energy density spectrum begins to emerge.

The energy density for each frequency is calculated, typically using the formula:

$$S(f) = \frac{1}{T} \sum_{i=1}^{N} (xi - \mu). \exp\left(-i2\pi f ti\right) \qquad \text{(Eq.5)}$$

where *S(f)* is the spectral density at frequency *f*, *xi* is the measured wave height, *μ* is the mean, and *T* is the total observation period.

This spectral density gives the energy at each frequency component of the wave field.

The results are typically displayed as a spectrum plot, where the x-axis represents frequency (or wavelength), and the y-axis represents energy density (the energy per unit frequency or wavelength). This plot helps visualize the distribution of energy across various wave frequencies.

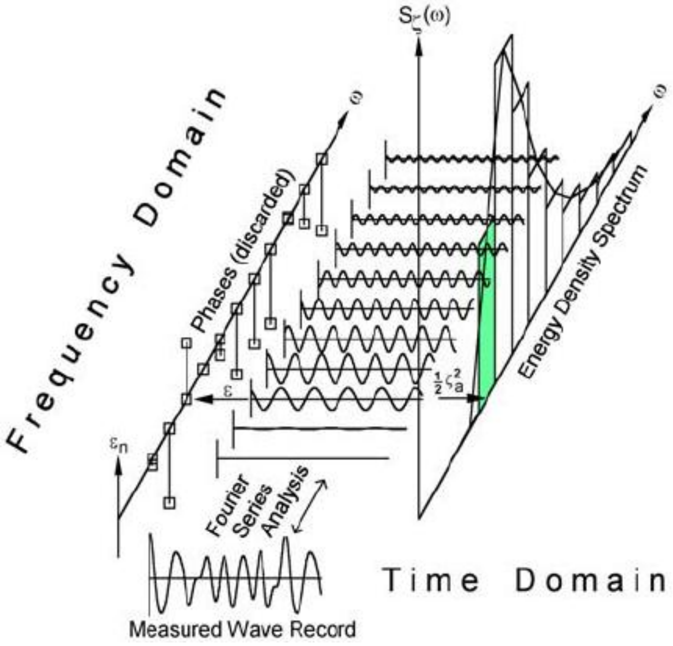

Figure 2.11 – Generating an Energy Density Spectrum [312]

In practical applications, empirical wave models (like the Pierson-Moskowitz spectrum or JONSWAP spectrum) may be used to approximate the energy density spectrum in specific sea conditions [321]. These models provide theoretical forms for the energy density distribution based on the wind speed, wave age, and other environmental factors [322]. The energy density spectrum of ocean waves is a critical tool in understanding the distribution of wave energy across frequencies or wavelengths. It is created by collecting time series data, applying Fourier analysis to transform the data into the frequency domain, and then calculating and plotting the energy density at each frequency [323]. This spectrum provides valuable insights for a range of applications, from wave forecasting to coastal engineering and offshore operations [321],[323].

2.9 Theoretical Spectral Models of Sea States

To model and validate the inverse mapping from internal pressure signals to wave characteristics, several theoretical wave spectra are considered. These models represent the statistical distribution of wave energy in various sea conditions and serve as references in spectral fitting and estimation [321].

2.9.1 Pierson-Moskowitz Spectrum

The Pierson-Moskowitz Spectrum is often credited as one of the first widely used spectral models to describe ocean waves generated by wind. This spectrum characterised the energy distribution of waves in terms of their frequency and was particularly used to describe fully developed seas [322].

The Pierson-Moskowitz (PM) spectrum describes a fully developed sea under steady wind conditions:

$$S(f) = \alpha g^2 (2\pi)^{-4} f^{-5} exp\left[-\beta \left(\frac{fp}{f}\right)^4\right] \qquad \text{(Eq.6)}$$

where:

- $\alpha = 8.1 \times 10^{-3}$
- $\beta = 0.74$
- fp is the peak frequency,
- g is gravitational acceleration.

2.9.2 Bretschneider Spectrum

The Bretschneider spectrum (Modified Pierson-Moskowitz) is an empirical wave spectrum that describes the energy distribution of ocean waves in fully developed seas [322]. It was developed to provide a more accurate representation of sea states that are not fully developed, addressing some limitations of the original Pierson-Moskowitz spectrum. The constants and the form of the spectrum are derived empirically, fitting observed wave data to provide a realistic representation of wave energy distribution [323]. The spectrum describes how wave energy is distributed across different frequencies. It shows that most energy is concentrated around a peak frequency *fp*, with energy decreasing rapidly for frequencies much lower or higher than *fp* [321].

Unlike purely theoretical models, the Bretschneider spectrum is based on empirical observations, making it particularly useful for real-world applications where sea conditions often deviate from idealized theoretical assumptions [322].

A simplified form used primarily in engineering applications for fully developed seas:

$$S(f) = \frac{1.25 H_S^2 T_p^4}{(2\pi)^2 f^5} \exp\left[-\frac{5}{4}\left(\frac{T_p f}{2\pi}\right)^{-4}\right] \qquad \text{(Eq.7)}$$

- *Hs* is the significant wave height,
- *Tp* is the peak period.

2.9.3 JONSWAP Spectrum

The Joint North Sea Wave Project (JONSWAP) [321], which began in the early 1970s, produced an important refinement to the Pierson-Moskowitz model, especially for waves in non-fully developed sea states. The JONSWAP spectrum incorporates a parameter (γ) that adjusts for the wave growth under specific wind conditions, leading to a more accurate representation of real-world wave spectra, particularly in intermediate sea states [321].

$$S(f) = S_{PM}(f).\gamma^{exp\left[-\frac{(f-fp)^2}{2\pi^2 f_p^2}\right]} \tag{Eq.8}$$

where:

- γ typically ranges from 1 to 7,
- $\sigma = 0.07$ for $f < fp$, $\sigma = 0.09$ for $f > fp$.

2.9.4 Ochi-Hubble Spectrum

This is a two-parameter model used to describe the energy distribution of sea waves over different frequencies. Unlike single-spectrum models, the Ochi-Hubble can represent double-peaked spectra, such as those seen in seas with both wind-driven waves and swell [324]:

$$S(f) = \sum_{i=1}^{2} A_i\left(f/f_{pi}\right)^{B^i} \exp\left[-\beta_i\left(\frac{f}{f_{pi}}\right)^{D_i}\right] \tag{Eq.9}$$

- f = frequency
- Ai, βi = shape parameters (functions of γi)
- i = 1,2 denotes each sea state component

Useful for long-duration, multimodal environments typical in deep water.

2.9.5 Practical Applications

Understanding the wave energy density spectrum is crucial for several practical applications:

- The design of offshore structures, such as oil platforms, wind turbines, and coastal defences, relies on accurate wave spectra to predict the forces that these structures will encounter. The wave spectrum informs the expected wave heights and periods, enabling engineers to design resilient and efficient structures.
- Wave energy converters (WECs) are devices that capture and convert the energy of ocean waves into electricity. The efficiency of WECs depends on their ability to harness the energy present at different frequencies. By analysing the wave spectrum, developers can optimize the design and placement of WECs to maximize energy capture.
- Coastal erosion, sediment transport, and the impact of waves on shorelines are influenced by wave energy. The wave spectrum helps in modelling these processes and in designing measures to protect coastlines from erosion and flooding [325].
- The ocean wave energy density spectrum is significant because it encapsulates the complex interactions between wind, waves, and currents. It provides a detailed picture of the sea state, which is essential for navigation, weather forecasting, and the assessment of marine environments. Furthermore, as interest in renewable energy sources grows, the wave spectrum becomes increasingly important for the development of sustainable wave energy technologies [326].

2.10 Autocorrelation

Autocorrelation is a statistical tool used to understand the temporal relationships within a time series. In the context of ocean waves, autocorrelation provides insights into how wave properties such as height, period, and direction change over time. Autocorrelation is a powerful tool in the study of ocean waves, providing valuable insights into the temporal coherence and predictability of wave patterns. Its applications in wave forecasting, marine engineering, and wave energy conversion underscore its significance in marine sciences. By leveraging autocorrelation analysis, a greater understanding and harness the power of ocean waves can be achieved, contributing to safer navigation, resilient marine structures, and efficient wave energy utilization [327].

Autocorrelation measures the correlation of a signal with a delayed version of itself. Correlation is a statistical measure that describes the strength and direction of the relationship between two variables. It quantifies how closely the movements or changes in one variable are related to the movements or changes in another variable.

For a time series representing wave elevation, $\eta(t)$, the autocorrelation function $R(\tau)$ at a lag τ is defined as:

$$R(\tau) = \langle \eta(t)\eta(t+\tau) \rangle \quad \text{(Eq.10)}$$

where the angle brackets denote the expected value or average over time. This function helps to identify repetitive patterns and the persistence of wave characteristics over time.

The autocorrelation function (ACF) can be expressed mathematically as:

$$R(\tau) = \frac{1}{T}\int_{O}^{T} \eta(t)\eta(t+\tau)dt \quad \text{(Eq.11)}$$

for a time-series of length T. This integral provides a measure of how similar the wave signal is to itself at different time lags τ.

The autocorrelation function is normalized by the variance of the signal to provide the autocorrelation coefficient:

$$\rho(\tau) = \frac{R(\tau)}{R(0)} \quad \text{(Eq.12)}$$

where $R(0)$ is the zero-lag autocorrelation, equivalent to the variance of the wave elevation series [328].

Variance is a statistical measure that quantifies the spread or dispersion of a set of values. It represents how much individual data points differ from the mean (average) of the dataset. A high variance indicates that the data points are spread out widely from the mean, while a low variance indicates that the data points are closer to the mean. Variance is often used in statistics to measure the variability within a dataset.

2.10.1 Significance in Marine Sciences

Autocorrelation is crucial for understanding the temporal coherence and persistence of ocean wave patterns. It provides several insights:

Wave Periodicity**:** By analysing the autocorrelation function, one can identify dominant wave periods. Peaks in the ACF at non-zero lags indicate recurring patterns in the wave series, corresponding to the primary wave periods [329].

Predictability**:** High autocorrelation at small time lags suggests that the wave characteristics are predictable over short time scales. This predictability is essential for short-term wave forecasting, which is crucial for navigation and marine operations [329].

Wave Energy Analysis**:** Autocorrelation helps in understanding how wave energy is distributed over time. It is particularly useful in the study of swell, which is characterized by long-lasting, coherent wave patterns [329].

2.10.2 Practical Applications

Autocorrelation analysis has several practical applications in oceanography and marine engineering:

Accurate wave forecasting relies on understanding the persistence and evolution of wave patterns. Autocorrelation functions help in developing predictive models that can forecast wave conditions based on past observations [330].

The design of offshore platforms, wind turbines, and coastal defences depends on the temporal characteristics of wave loading. Autocorrelation provides information on the duration and intensity of wave events, which is critical for ensuring structural resilience [330].

Wave Energy Conversion**:** For wave energy converters (WECs), the efficiency of energy capture depends on the temporal coherence of waves. Autocorrelation analysis helps in selecting optimal sites for WEC deployment by identifying areas with consistent and predictable wave patterns [330].

2.11 Fourier Analysis

The principle of Fourier analysis is based on the fact that a periodic function, *f*, of period, *T*, can be expressed as the sum of its harmonic components by considering the amplitude of the coefficients, the spectral content of the signal can be assessed as.

$$f(t) = a_0 \sum_{k=1}^{\infty} \left(a_k cos\, \frac{2\pi kt}{T} + b_k sin \frac{2\pi kt}{T} \right) \qquad \text{(Eq.13)}$$

Where, a_0, a_k and b_k, are the Fourier coefficients defined by;

$$a_0 = \frac{1}{T} \int_{\frac{-T}{2}}^{\frac{T}{2}} f(t)\, dt$$

$$a_k = \frac{2}{T} \int_{\frac{-T}{2}}^{\frac{T}{2}} f(t) cos \frac{2\pi kt}{T}\, dt \dots \dots for\ k\ \geq 1$$

$$b_k = \frac{2}{T} \int_{\frac{-T}{2}}^{\frac{T}{2}} f(t) sin \frac{2\pi kt}{T}\, dt \dots \dots for\ k\ \geq 1$$

The most common method used to carry out a spectral analysis of a discrete time series x_p, with N samples, (p = 0,1,2,…….,N – 1) is the Discrete Fourier Transform, which is defined using complex notion as follow;

$$X_k = \sum_{k=0}^{N-1} X_p \, e^{I\left(\frac{2\pi kp}{N}\right)} \ldots \ldots \ldots for \; p = 0,1,2, \ldots.,N-1 \qquad \text{(Eq.14)}$$

A discrete Fourier Transform (DFT) is a mathematical method of estimating the spectrum of a continuous time series. See Figure 2.12 below for a representation for a typical wave spectrum.

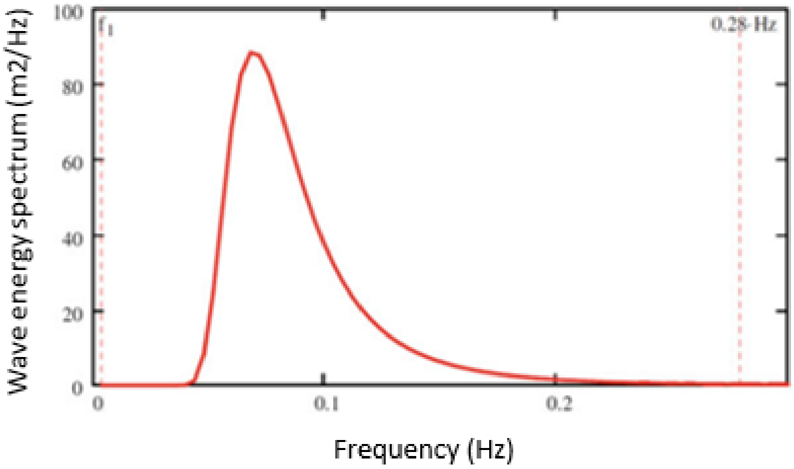

Figure 2.12 – Typical Wave Spectrum [330]

Welch's method is a technique for estimating the power spectral density (PSD) of a signal, which provides insight into the distribution of power across various frequency components. This method is particularly useful for reducing the variance of the periodogram in estimating the PSD [331].

The input signal is divided into overlapping segments. The overlap is typically 50%, but it can vary depending on the specific application. Each segment is multiplied by a window function (e.g., Hamming, Hanning) to reduce spectral leakage. Spectral leakage is a phenomenon that occurs when a signal is analysed using a Fourier transform (such as in spectral analysis), and the signal does not perfectly match the window or frequency range being analysed [331]. This mismatch causes the energy of the signal to "leak" into adjacent frequencies, resulting in distortion or artifacts in the frequency spectrum. The window function is used to taper the edges of each segment. For each windowed segment, compute the Discrete Fourier Transform (DFT) to obtain the periodogram, which is the squared magnitude of the DFT normalized by the window's energy [330].

Welch's method is widely used in signal processing, particularly in analysing signals in fields such as communications, vibration analysis, and biomedical engineering. The periodograms of all segments are averaged together to produce the final estimate of the PSD. This averaging reduces the variance of the estimate compared to a single periodogram. By averaging multiple periodograms, Welch’s method provides a smoother and more reliable estimate of the PSD. The method allows for adjusting segment length and overlap to balance between frequency resolution and variance reduction. However, segmenting the signal can reduce the frequency resolution of the PSD estimate. Welch's method is a powerful tool for spectral analysis, especially when dealing with noisy signals or when a smooth PSD estimate is required [331].

2.12 Spectral Moments

The wave spectrum is a distribution of the energy in the wave also known as the variance of the surface over frequency. Therefore, as a statistical distribution, parameters derived from the spectrum mirror parameters calculated from any statistical distribution allowing the form of the wave spectrum to be expressed in terms of moments of the distribution [332]. While numerous mathematical spectral models exist, the nth moment of all spectra can be derived as;

$$m_n = \int_0^\infty \omega^2 \, S(\omega) d\omega \qquad \text{(Eq.18)}$$

To determine the significant wave height, *Hs*, average wave period, *Tz*, average successive upcrossing frequency, *ωz*, and the average frequency between successive crests, *ωc*, the equation below is used.

$$H_s = 4\sqrt{m_0} \quad \text{(Eq.19)}$$

$$\boldsymbol{T_z = 2\pi\sqrt{\frac{m_0}{m_2}}} \quad \text{(Eq.20)}$$

Note that all the equations are in terms of angular frequency, ω, and the moments relate to ω explicitly. Frequency, f, may be used where, $\omega = 2\pi f$, provided the moments reflect this, thus $m0(\omega)$ = m0(f), m1(ω) = 2π m1(f) and m2(ω) = 4πm2(f) etc. [332]

2.13 Transfer Functions

A transfer function is a mathematical representation that describes the relationship between the input and output of a linear time-invariant (LTI) system. It is widely used in various fields such as engineering, physics, and control theory to analyse and design systems [333].

An inverse transfer function is essentially the transfer function that, when multiplied by the original transfer function, results in an identity system. Mathematically, if $H(s)$ is the transfer function of a system, then the inverse transfer function $H^{-1}(s)$ is defined such that:

$$H(s).H^{-\mathrm{i}}(s) = 1 \quad \text{(Eq.21)}$$

This relationship implies that applying the inverse transfer function to the output of the original system will yield the original input [333]. This work investigates the relationship between the pressure signal recorded above the oscillating water column to the incident wave spectrum through use of an inverse transfer function. Single-input, single-output (SISO) systems play a crucial role in engineering and science, particularly in the analysis of dynamic systems where a single variable, acting as the input, influences one corresponding output. In such systems, the behaviour of the output is analysed with respect to changes in the input. SISO models are widely employed in control systems, signal processing, and environmental modelling, including the study of ocean wave energy. To provide a robust analysis, random data assumptions are often employed, particularly in the context of stationary and ergodic processes [333]. Under ideal conditions, the output of the system shown in Figure 3.10 is given by the convolution integral

$$y(t) = \int_0^\infty h(\tau)\, x(t - \tau)\, d\tau \qquad \text{(Eq.22)}$$

Where h(τ) = 0 for $\tau < 0$ when the system is physically realisable.

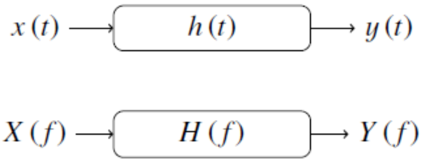

Figure 2.10. A single input/output system in the time domain and the frequency domain.

Where:

$x(t)$ represents the stationary input
$y(t)$ represents the output
$h(t)$ represents the impulse response of the system
$X(f)$ represents the Fourier transform of $x(t)$
$Y(f)$ represents the Fourier transform of $y(t)$
$H(f)$ is the frequency-dependent, Fourier transfer function between $X(f)$ and $Y(f)$
$H(f)$ is the Fourier transform of $h(t)$.

In random data analysis, particularly when dealing with environmental phenomena such as ocean waves, the assumption of stationarity is critical. A stationary process is one whose statistical properties, such as the mean, variance, and autocorrelation, remain constant over time [334]. For example, in a SISO ocean wave energy system, if wave height is treated as the input and the energy extracted as the output, assuming stationarity simplifies the analysis by allowing the use of time-invariant models. An ergodic process, on the other hand, allows the use of time averages to represent ensemble averages, which is critical for practical analysis. In essence, ergodicity implies that a single realization of a process over a sufficiently long period contains all the statistical information needed to describe the system. For a SISO system, this is important because it means that long-term measurements of input-output behaviour can be treated as representative of the entire system.

Assuming that the input *x(t)* to the system in Figure 2.10 is a sample record from a stationary (ergodic) random process *{x(t)}*, the response *y(t)* will also belong to a stationary (ergodic) random process *{y(t)}*. Therefore, from equation Eq.22, the product *y(t)y(t + τ)* is given by:

$$y(t)y(t+\tau) = \int_0^\infty \int_0^\infty h\,(\xi)h(\eta)x(t-\xi)x(t+\tau-\eta)d\xi d\eta \qquad \text{(Eqn.23)}$$

Taking the expected values of both sides of equation (Eq.23) yields the input / output autocorrelation relation

$$R_{yy}(\tau) = \int_0^\infty \int_0^\infty h\,(\xi)h(\eta)R_{xx}(\tau-\xi-\eta)d\xi d\eta \qquad \text{(Eqn.24)}$$

Similarly, the product *x(t)y(t+ τ) is given by*

$$x(t)y(t+\ \tau) = \int_0^\infty h\,(\xi)x(t)x(t)x(t+\tau-\xi)d\xi \qquad \text{(Eqn.25)}$$

Here, expected values of both sides yield the input / output cross-correlation relation

$$R_{xy}(\tau) = \int_0^\infty h\,(\xi)R_{xx}(\tau-\xi)d\xi \qquad \text{(Eqn.26)}$$

Note that equation (Eq.26) is a convolution integral of the same form as equation (Eq.22). Direct Fourier transforms of equations (Eq.26) and (Eq.27) after various algebraic steps yield two sided spectral density functions $S_{xx}(f)$, $S_{yy}(f)$, and $S_{xy}(f)$, which satisfy important formulas. Equation (Eq.27) is called the input / output autospectrum relation, whereas equation (Eq.28) is called the input / output cross-spectrum relation.

$$S_{yy}(f) = |H(f)|^2 S_{xx}(f) \qquad \text{(Eqn.27)}$$

$$S_{xy}(f) = H(f) S_{xx}(f) \qquad \text{(Eqn.28)}$$

In the work described herein, the measured time series of air pressure in the OWC is the input signal, $x(t)$, and the time series of surface water elevation of the incident sea state is the output signal $y(t)$. The two-sided auto-spectral density functions of the pressure data from the prototype WASP and the measured incident wave height data from the Waverider buoy are herein termed Sxx$(f)$and $Syy(f)$respectively. Thus following from equation (Eqn.27), the squared magnitude of the transfer function between the pressure in the prototype WASP OWC and the incident sea state can be derived from:

$$|H(f)|^2 = \frac{S_{yy}(f)}{S_{xx}(f)} \qquad \text{(Eqn.29)}$$

It is common in the field of oceanography to assume that free surface elevation at a point, can be modelled as a stationary and ergodic process over the time frame of 20 to 30 minutes and this convention is followed in the current work.

2.14 Degrees of Freedom of a floating object

Ocean floating objects, such as buoys, ships, and offshore platforms, exhibit complex motion dynamics influenced by environmental forces including wind, waves, and currents. Understanding these motions is critical for designing, monitoring, and managing these objects. The concept of degrees of freedom (DOF) provides a framework for describing the possible movements of such objects. Typically, an ocean floating object can move in six degrees of freedom, comprising three translational and three rotational movements, Heave, Surge, Sway, Roll, Pitch and Yaw [335].

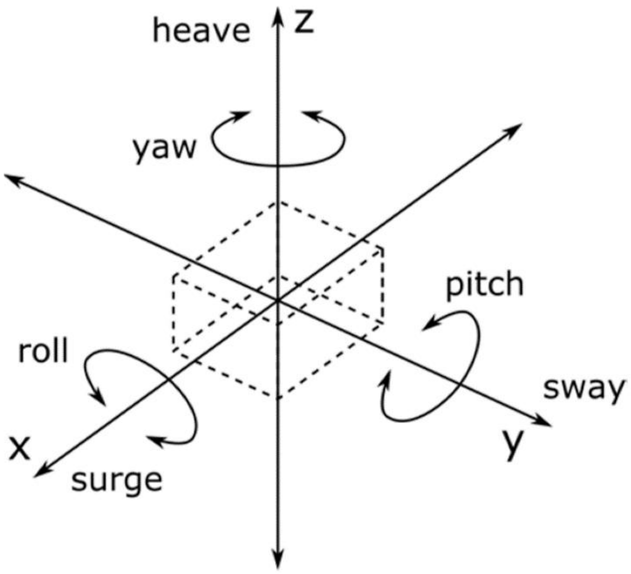

Figure 2.13– Diagram depicting the six degrees of freedom of a floating object [336]

2.14.1 Implications and Applications

The study of the degrees of freedom of ocean floating objects is integral to marine engineering. Accurate modelling of these motions allows engineers to design more efficient and stable structures and vessels. Computational fluid dynamics (CFD) and other simulation tools are frequently employed to predict the behaviour of floating objects under various environmental conditions. For example, the dynamic response analysis of offshore platforms helps in designing mooring systems that can withstand extreme sea states [337].

In oceanography, understanding the degrees of freedom is crucial for deploying and maintaining scientific instruments. Ocean buoys, such as the WASP, which are used to collect data on sea temperature, salinity, and currents, must remain stable to provide accurate readings. Knowledge of the six degrees of freedom helps in designing buoy systems that can compensate for ocean motion, thereby ensuring reliable data collection [338].

2.15 Response Amplitude Operator

In marine engineering and oceanography, understanding the dynamic response of wave-measuring devices and marine structures to ocean waves is crucial. The Response Amplitude Operator (RAO) plays a fundamental role in this context, acting as a transfer function that relates the wave height to the motion of the device or structure [339].

The Response Amplitude Operator (RAO) is a frequency-domain representation that quantifies how the motion of a wave-measuring device or marine structure responds to incident wave heights. Mathematically, the RAO is expressed as:

$$RAO(\omega) = \frac{A_{motion}(\omega)}{A_{Wave}(\omega)} \quad \text{(Eq.30)}$$

where:

- $A_{motion}(\omega)$ is the amplitude of the device's motion response (e.g., displacement, velocity, or acceleration) of the device or structure at frequency ω.
- $A_{wave}(\omega)$ is the amplitude of the incident wave height at the same frequency.

In essence, the RAO serves as a transfer function that transforms the wave height input into the resulting motion output of the device or structure.

2.15.1 Interpretation as a Transfer Function

As a transfer function, the RAO provides a comprehensive understanding of the system's behaviour in the frequency domain. It encapsulates how different wave frequencies affect the motion of the device or structure, revealing important characteristics such as resonance and damping. The RAO is typically dimensionless, indicating the proportional response of the system to wave excitation [339].

2.15.2 Significance of the RAO

System Calibration: The RAO is critical for calibrating wave-measuring devices, ensuring that the recorded data accurately reflect the actual wave conditions. By accounting for the device's dynamic response, researchers can correct and interpret the data more reliably [339].

Design and Analysis: Engineers use the RAO to design and analyse marine structures. Understanding the RAO helps in predicting how structures will respond to different wave conditions, which is essential for ensuring their stability and integrity [339].

Optimisation of Devices: The RAO is used to optimize the design of wave-measuring devices and wave energy converters, enhancing their efficiency and accuracy by tailoring them to specific wave conditions [339].

2.15.3 Applications of the RAO

Wave Buoys**:** For wave buoys, the RAO describes how the buoy's vertical motion responds to wave heights across different frequencies. This information is vital for accurately measuring wave parameters and for the buoy's design optimisation [339].

Offshore Structures**:** The RAO is applied in the analysis and design of offshore platforms, wind turbines, and other marine structures. By understanding how these structures respond to various wave frequencies, engineers can ensure their resilience against wave-induced forces [339].

Wave Energy Converters (WECs)**:** In wave energy conversion, the RAO helps in maximising energy capture by aligning the device's natural frequencies with the predominant wave frequencies, thereby improving efficiency [339].

Marine Vehicle Dynamics**:** The RAO is used to study the dynamic behaviour of marine vehicles, such as ships and submarines, under wave action. This understanding is crucial for designing stable and seaworthy vessels [339].

Research and Development**:** In marine research, the RAO is used to study the interactions between waves and various marine instruments. It helps in developing new technologies and improving existing ones for better wave measurement and analysis [339].

Consider a wave buoy designed to measure ocean wave heights. The buoy's motion in response to waves can be described by its RAO. If the incident wave amplitude at a frequency ω is 2 meters and the buoy's vertical motion amplitude at the same frequency is 1.5 meters, the RAO at that frequency is $RAO(\omega) = \frac{1.5}{2} = 0.75$.

This indicates that the buoy's motion is 75% of the wave height at that particular frequency, suggesting some level of damping or dynamic response characteristic of the buoy [340].

2.15.4 RAO’s of the WASP

Analysis of the scaled model tank testing motions of the WASP focuses on surge, heave, pitch of the buoy and the RAO of the pressure within the sealed moonpool. Refer to Chapter 3 for further information.

The RAO of pressure is a measure of how the internal pressure in the moonpool responds to the external wave environment. Understanding this RAO is vital for the design and operation of buoys equipped with moonpools, particularly in terms of structural integrity and operational safety [340].

The RAO for pressure in a sealed moonpool is the ratio of the pressure amplitude inside the moonpool to the amplitude of the incident wave. It is typically expressed as a function of wave frequency (or wave period). Mathematically, it can be represented as [340]:

$$RAOpressure(\omega) = \frac{P_{moonpool}}{P_{Wave}} \qquad \text{(Eq.34)}$$

where:

- $P_{moonpool}$ is the amplitude of the pressure inside the moonpool.
- P_{wave} is the amplitude of the pressure exerted by the incident wave.
- ω is the wave frequency.

Understanding the RAO for pressure in a sealed moonpool helps in designing the moonpool to withstand the dynamic pressures and ensure the buoy's structural integrity and operational efficiency.

2.15.5 Factors Influencing the RAO of Pressure in a Sealed Moonpool

Several factors influence the RAO of pressure in a sealed moonpool, including:

- Wave Characteristics: The frequency, height, and direction of the incident waves determine the excitation forces acting on the buoy and subsequently on the moonpool. Higher frequency waves may induce higher pressure variations inside the moonpool [340].
- Geometry of the Moonpool: The shape, size, and depth of the moonpool significantly affect the pressure response. A deeper or larger moonpool may have different resonance characteristics compared to a shallow or smaller one [340].
- Buoy Motion: The overall motion of the buoy (heave, pitch, roll, surge, sway, and yaw) contributes to the dynamic pressure variations inside the moonpool. The coupling effects between these motions and the moonpool pressure need to be considered [340].
- Internal Fluid Dynamics: The behaviour of the fluid inside the moonpool, including potential sloshing and resonant effects, influences the pressure response. The sealing mechanism and the air-water interaction also play a role [340].

- Damping Mechanisms: Both internal and external damping mechanisms, such as wave radiation damping and viscous effects, affect the pressure RAO. Higher damping can reduce the peak pressure response [340].

2.15.6 Analysing the RAO of Pressure in a Sealed Moonpool

The RAO of pressure in a sealed moonpool can be analysed using both experimental and numerical methods:

Experimental Methods: Scale model tests in wave basins can measure the pressure response inside the moonpool under controlled wave conditions. These tests provide empirical data that can validate numerical models [340].

Numerical Simulations: Computational tools, such as potential flow solvers and computational fluid dynamics (CFD), predict the RAO by solving the governing equations of fluid-structure interaction. These simulations can account for complex geometries and non-linear effects [340].

Frequency Domain Analysis: Linear frequency domain analysis can provide an initial approximation of the pressure RAO by solving the linearized equations of motion. This method is efficient but may not capture all non-linear phenomena [340].

Time Domain Analysis: Time domain simulations offer a more detailed and accurate prediction by capturing transient and non-linear behaviours. This approach is particularly useful for analysing complex interactions between the buoy motion and the internal fluid dynamics of the moonpool [340].

2.15.7 Practical Applications

Understanding the RAO of pressure in a sealed moonpool has several practical applications in marine engineering:

- Design of Buoys: Engineers use the pressure RAO to design moonpools that can withstand dynamic pressure loads, ensuring the structural integrity and longevity of buoys [340].
- Offshore Platforms: Moonpools are also used in offshore platforms for various purposes, including drilling and submersible operations. Accurate RAO analysis helps in designing these structures to handle dynamic pressures [340].
- Marine Research: Buoys equipped with moonpools are often used in marine research to house instruments and sensors. Understanding the pressure dynamics ensures the reliability and accuracy of the data collected [340].
- Safety and Stability: By analysing the pressure RAO, designers can enhance the safety and stability of buoys, preventing structural failures and operational disruptions caused by extreme wave conditions [340].

2.16 Oscillating Water Columns and Moonpools

An OWC comprises a partially submerged chamber open to the sea below [341],[342] with an air chamber above. Wave motion drives the vertical water column, compressing and decompressing trapped air [343]. Airflow induces pneumatic power take-off, typically via bidirectional turbines (e.g., Wells turbine) [344],345].

2.16.1 Resonance in OWC’s

Resonance behaviour in an Oscillating Water Column (OWC) is a crucial phenomenon that significantly influences its efficiency and energy output [346]. Understanding this behaviour helps in optimizing the design and operation of OWCs for maximum power capture [347].

Resonance occurs when the natural frequency of the water column inside the chamber matches the dominant frequency of the incoming ocean waves [348]. At this point, the oscillations of the water column are amplified, leading to:

- Greater movement of the internal water surface [349]
- Larger air pressure variations in the chamber [350]
- Increased airflow through the turbine [351]
- Higher power output [352]

The water column inside the chamber behaves like a mass-spring system [353]. Its natural frequency depends on water depth inside the chamber, geometry and volume of the air chamber and compressibility of the air above the water [354]. The system resonates when the frequency matches this natural frequency [355].

At resonance, small wave inputs produce large water column oscillations [356]. This leads to greater pressure fluctuation, enhancing the performance [357].

OWCs are often design or tuned to resonate at the most common wave frequency in a given location. Tuning can be done by adjusting chamber dimensions, changing the air volume or pressure or using variable geometry or adaptive systems [359].

2.16.2 Air compressibility in OWC’s

Air compressibility is the ability of air to change its volume under pressure [360]. In OWCs, as waves move the water column up and down inside the chamber, the air above the water gets alternately compressed and decompressed, creating oscillating pressure changes that drive the turbine [361],362].

The compressibility of air directly affects the natural frequency of the OWC chamber [363]. The air is more compressible with a larger volume and lower pressure, leading to a lower natural frequency [364]. Conversely, the air is less compressible with a smaller volume and higher pressure, leading to a higher natural frequency [365]. Thus, controlling air compressibility allows tuning of resonance to match wave frequencies for optimal performance [366].

2.16.3 Radiation and added-mass effects in OWC’s

Radiation refers to the waves generated by the motion of the water column itself [367]. When the internal water surface oscillates, it creates its own wave field—this radiated wave field interacts with the incident ocean waves [368].

When the water column inside the OWC moves up and down, it must accelerate surrounding water. This results in an effective increase in inertia, known as *added mass* [369]. The water behaves as if it has more mass than it actually does due to the need to displace adjacent fluid [370].

The added mass changes the natural frequency of the oscillating water column [371]. A heavier "virtual mass" means the system resonates at a lower frequency [372]. The added mass must be accounted for to correctly tune the system for resonance with wave frequencies [373]. Radiation waves carry energy away from the system, acting like a damping force [374]. This radiation damping is essential to avoid overly violent oscillations, but too much damping reduces energy capture [375].

2.17 Pressure Gauges for ocean wave measurement

Pressure gauges are essential instruments for measuring ocean wave characteristics, particularly in coastal and deep-sea environments where direct surface observation is impractical [376]. These instruments infer wave parameters by recording pressure fluctuations induced by passing surface gravity waves [377]. The pressure signal is subsequently processed using wave theory to extract surface elevation and associated spectral parameters such as significant wave height, peak period, and energy spectrum [378].

Types of Pressure Gauges include:

- Vented and Non-vented pressure transducers
    - Vented Transducers maintain atmospheric pressure reference via a vent tube. They offer more accurate absolute pressure readings, particularly useful in shallow water [379].
    - Non-Vented Transducers measure absolute pressure, combining atmospheric and hydrostatic pressures. Barometric pressure must be corrected post hoc for accurate wave analysis [380].

- Piezoresistive pressure gauges

These are the most common in oceanographic applications [381]. A diaphragm deforms under hydrostatic pressure, changing the resistance in an electrical circuit.

- Advantages: High sensitivity, robust, capable of high-frequency sampling (up to 10–20 Hz) [382].
- Applications: Deployed in both shallow water (using wave pressure decay correction) and deep water (for bottom pressure recorders) [383].

- Capacitive pressure gauges

Capacitive sensors also rely on diaphragm deformation, altering the capacitance between two plates [384].

  - Advantages: Lower power consumption and good long-term stability [385].
  - Limitations: Lower frequency response compared to piezoresistive gauges, making them less suitable for high-resolution spectral wave analysis [386].

- Quartz Crystal Pressure Sensors

Quartz crystal resonators exhibit a frequency shift under pressure, providing highly stable measurements over long deployments [387].

  - Advantages: High resolution, excellent for long-term bottom pressure recording in deep-sea moorings [388].
  - Limitations: Cost and complexity [389]

- Strain Gauge Sensors

Strain gauge-based pressure transducers convert diaphragm deformation into electrical resistance changes [390]. Less common today due to drift issues, but still used in some legacy systems [391].

2.18 Scaled model testing

Scaled model testing is a critical step in advancing ocean energy technologies [392]. This approach involves creating smaller, proportionate versions of ocean energy devices to evaluate their performance under controlled conditions [393]. Scaled model testing is indispensable for several reasons, including cost efficiency, risk mitigation, design optimisation, and enhancing understanding of complex oceanic environments [394].

2.18.1 Cost Efficiency

Developing full-scale ocean wave measuring systems can be financially prohibitive, particularly during the initial stages of research and development [395]. Any failure of the Full-scale prototypes can lead to significant financial losses [396]. Scaled model testing provides a cost-effective alternative by allowing researchers to test concepts and designs at a fraction of the cost [397]. Scale models can be tested in wave tanks or controlled environments, which are less expensive to operate than deploying full-scale prototypes in the ocean [398]. By identifying potential issues early in the development process, scaled model testing helps avoid costly mistakes, ensuring that resources are used efficiently [399].

2.18.2 Risk Mitigation

Ocean environments are inherently unpredictable and harsh, posing substantial risks to full-scale systems [400]. Scaled model testing allows engineers to simulate these conditions in a controlled setting, thereby minimising risks associated with real-world deployment [401]. Sea-states can be fully reproduced and produced on demand in tanks [402]. By subjecting scaled models to various scenarios, such as extreme weather conditions and different sea states, researchers can identify vulnerabilities and improve the robustness of their designs [403]. This proactive approach to risk management is crucial for ensuring the reliability and longevity of ocean wave measuring systems [404].

2.18.3 Design Optimisation

One of the significant benefits of scaled model testing is the ability to optimise designs before full-scale production [405]. Through iterative testing and refinement, engineers can evaluate the performance of different configurations and components [406]. Scaled models provide valuable data on hydrodynamics and structural integrity [407]. This data is essential for making informed design decisions and innovations [408]. For instance, researchers can experiment with different materials, shapes, and configurations to enhance performance and reduce operational costs [409]. Design optimisation through scaled model testing leads to more efficient and effective ocean wave measuring systems [410].

2.18.4 Advancing Innovation and Technology Development

Scaled model testing fosters innovation by providing a platform for experimenting with new concepts and technologies [411]. Researchers can test unconventional ideas and cutting-edge technologies without the high stakes associated with full-scale deployment [412]. This environment encourages creativity and out-of-the-box thinking, which is essential for pushing the boundaries of ocean energy technology [413]. Additionally, scaled model testing facilitates collaboration between academic institutions, industry partners, and government agencies, such as the LIR Test Facility in County Cork and Dundalk Institute of Technology [414]. These collaborations are vital for advancing the field and accelerating the transition from research to commercial deployment [415].

Furthermore, the integration of scaled model testing with real-time data from deployed ocean energy systems will create a feedback loop that accelerates technological innovation [416]. By continuously validating and refining models based on real-world performance, researchers can develop more resilient and efficient ocean energy systems [417]. This iterative process will be crucial for overcoming the challenges associated with harnessing energy from the ocean and achieving large-scale commercial deployment [418].

2.19 Scaling

Scaling is a technique used in engineering, physics, and other scientific fields to study systems of different sizes or complexities [419],[420]. It allows researchers to use smaller models (scale models) to simulate and study larger systems [421]. The primary motivation for scaling is that physical phenomena often behave similarly at different scales, so studying a scaled-down model can provide valuable insights into real-world behaviour without the cost or complexity of working with full-scale systems [422].

When scaling a physical system, it's important to account for the relationships between the quantities that define the system [423]. These quantities include forces, lengths, velocities, time, and energy, among others. Scaling laws help us understand how these quantities change when the size of the system changes, and are typically based on physical principles or empirical observations [424].

Dimensional analysis is a mathematical technique used to express physical quantities in terms of their fundamental dimensions [425]. These dimensions are typically length (L), time (T), mass (M), and others like temperature, charge, and amount of substance, depending on the context [426].

The goal of dimensional analysis is to simplify and understand physical relationships by reducing the number of variables and comparing the scale of various quantities [427]. Dimensional analysis is based on the principle that the equations governing physical phenomena must be dimensionally consistent—i.e., the dimensions on both sides of an equation must match [428].

To understand scaling, it’s common to express physical equations in terms of non-dimensional numbers [429]**.** These are dimensionless quantities that emerge from a combination of physical parameters. Non-dimensional numbers allow us to compare different systems regardless of their size, making them crucial in scaling [430]. Common non-dimensional numbers include:

- Reynolds number (Re)**:** A measure of the relative importance of inertial forces to viscous forces in fluid flow. It’s a key number in fluid mechanics [431].
- Mach number (Ma)**:** A measure of the speed of an object moving through a fluid relative to the speed of sound in that fluid [432].

- Froude number (Fr)**:** A measure of the relative importance of inertial forces to gravitational forces, especially in the context of fluid dynamics related to waves and gravity-driven flows [433].
- Prandtl number (Pr)**:** A ratio of momentum diffusivity to thermal diffusivity, important in heat transfer [434].

2.19.1 Froude Scaling

Froude scaling is a method used to ensure dynamic similitude in models of fluid systems, particularly when gravity is a significant force, such as in ship design, dam spillways, and open channel flows [435]. It involves using the Froude number, a dimensionless number that compares inertial forces to gravitational forces [436]. The Froude number is defined as,

$$Fr = v/\sqrt{(gL)} \qquad \text{(Eq.37)}$$

where:

- v is the velocity,
- g is the acceleration due to gravity,
- L is a characteristic length (such as the depth of water or the length of a ship) [437].

To achieve dynamic similitude, the Froude number for the model must be equal to the Froude number for the prototype (the real-world system) [438]. This ensures that the ratio of inertial to gravitational forces is the same in both the model and the prototype. When using Froude scaling, the scale ratio for velocity and time is derived from the geometric scale ratio (length scale) [439]. The model must be geometrically similar to the prototype, meaning all dimensions should be scaled consistently [440].

Froude scaling ensures that experiments conducted on scaled models can accurately predict the behaviour of the full-scale system, particularly when gravity plays a crucial role [441]. Using scaled models reduces costs associated with testing and development, as it is much cheaper to build and test a small-scale model than a full-sized prototype [442]. Testing extreme conditions or failure scenarios on a small model is safer and more feasible than on a full-scale prototype [443].

Pressure is related to force per unit area, and its scaling in Froude similarity follows from dynamic similarity and hydrostatic pressure behaviour [444].

$$P \ \alpha \ \rho g H \qquad \text{(Eq.38)}$$

Given Froude scaling maintains gravity effects and typically assumes same fluid (same ρ), the pressure scale Π_{p} is:

$$\Pi_{\mathbf{p}} = \left(\frac{L_m}{L_p}\right) \qquad \text{(Eq.39)}$$

Where:

- L_m = model length
- L_p = prototype length [445].

So pressure scales linearly with the length scale under Froude similarity [446]. Table 2.2 provides an overview of the Froude scaling laws that were used throughout testing as discussed later in Chapter 3.

Quantity	**Scaling**
Wave Height and Length	S
Wave Period	$S^{0.5}$
Wave Frequency	$S^{-0.5}$
Linear Displacement	S
Mass	S^3
Force	S^3
Pressure	S^1

Table 2.2 – Relevant Froude Scaling Laws where *S* is the Scale Factor

2.20 Data handling, collection and quality control

Accurate and reliable data handling is fundamental to the utility of ocean wave measuring devices [447], [448]. This section outlines the key procedures and best practices related to the acquisition, management, and quality assurance of wave measurement data, with a focus on ensuring the integrity, consistency, and scientific value of the recorded information [449].

Ocean wave data are typically collected through a combination of sensors mounted on buoys, platforms, or submerged instruments [450],[451]. The data acquisition system must ensure high-resolution sampling, synchronised timestamping and environmental metadata logging [452]. Raw data are usually stored in binary or ASCII formats and transmitted via telemetry or downloaded during periodic servicing, depending on power and communication constraints [453].

Before analysis, raw data must undergo a series of pre-processing steps [454]-[456]:

- Signal Detrending and Filtering: Remove DC offsets and low-frequency drift to isolate wave-induced components [457].
- Coordinate Transformation: For motion-based systems, transform accelerations or displacements to a fixed Earth frame or derive vertical motions for wave spectra [458].
- Resampling and Synchronization: Align and interpolate data streams from multiple sources (e.g., synchronizing air pressure and wave buoy reference data in transfer function applications) [459].
- Time Windowing: Split data into overlapping segments (commonly 17–30 minutes) to perform time-averaged statistical and spectral analysis [460].

Quality control (QC) is essential to identify and correct anomalies, sensor malfunctions, or environmental artifacts [461]-[463].

- Range and Threshold Checks
  - Identify values that exceed physical limits (e.g., negative pressure, impossible wave heights) [464].
  - Flag extreme spikes or outliers using interquartile range or z-score methods [465].
- Rate-of-Change Tests
  - Detect unrealistic gradients or sudden jumps in time series data indicative of sensor noise or transmission errors [466].
- Spectral Checks
  - Verify the spectral shape for expected energy distributions [467].
  - Detect flat-line signals or unrealistic frequency peaks [468].
- Redundancy and Cross-Validation
  - Compare overlapping measurements from multiple sensors (e.g., pressure vs. GPS-derived surface displacement) [469].
  - Use reference buoys or co-located devices to assess calibration consistency and derive correction transfer functions if needed [470].
- Gap Detection and Interpolation
  - Identify missing data segments [471].
  - Apply appropriate interpolation techniques only where justified (e.g., short gaps in high-frequency data) [472].

- Filtering

Filtering of recorded pressure data from an Oscillating Water Column (OWC) system is essential to remove noise and isolate the dynamic pressure fluctuations that are directly related to wave–structure interactions. Raw sensor signals often contain contributions from background turbulence, sensor drift, and high-frequency components unrelated to the primary hydrodynamic processes. Appropriate filtering, typically through band-pass or low-pass digital filters, ensures that the data reflects the dominant wave-induced oscillations while preserving phase information critical for performance analysis. This preprocessing step enhances the reliability of subsequent spectral analysis, energy conversion efficiency estimation, and model validation for OWC systems.

2.21 Literature Review Chapter Summary

This chapter has presented a detailed review of current ocean wave measurement technologies, encompassing drifting buoys, inertial and surface-following systems, acoustic and radar sensors, satellite-based remote sensing, and seabed pressure transducers. Each of these technologies serves specific scientific and operational purposes, with varied capabilities in terms of spatial resolution, temporal accuracy, deployment durability, and environmental resilience.

Through this comparative analysis, several limitations across the current state-of-the-art have emerged. Many of the widely used systems—particularly those involving direct surface contact—are susceptible to biofouling, mechanical degradation, and high maintenance requirements. Others, such as satellite or radar systems, while effective in broad-scale monitoring, often lack the spatial or temporal resolution needed for nearshore or structure-specific wave characterisation. Furthermore, most wave measurement approaches rely on direct interactions with the water surface or external wave field, making them vulnerable to environmental extremes and challenging to deploy on autonomous platforms with limited power or access.

Within this context, a gap in knowledge exists regarding passive, enclosed, and low-maintenance wave sensing systems capable of reliable long-term operation. This highlights the need for alternative methodologies that can maintain performance while reducing operational complexity and susceptibility to marine exposure.

The OWC-sealed moonpool air pressure sensor emerges as a novel concept to address this gap. By capturing air pressure variations induced by wave-driven oscillations of an internal water column, this method introduces a fundamentally different measurement approach. The key novelty lies in its sealed, indirect sensing mechanism, which eliminates the need for submerged electronics or exposed mechanical parts. As such, it offers inherent protection against biofouling and environmental wear, with the potential for long-duration, low-maintenance operation on floating platforms or offshore structures.

In conclusion, while traditional wave measurement technologies have matured across decades of use, they are not without drawbacks—particularly in the context of long-term, autonomous deployments. The WASP and it’s OWC-sealed moonpool sensor introduces a novel direction with advantages in robustness and system design. Its potential, however, remains largely untapped in current literature, establishing a strong research opportunity for this thesis to explore, model, and validate the effectiveness of this new approach to ocean wave measurement.

Chapter 3 - Methodology

3.0 Introduction

This chapter marks the point at which the thesis moves from theoretical foundations and discussion of prior art to the core of the research work. It introduces and details the experimental methodology adopted to investigate the problem under study, with a focus on a series of test campaigns conducted at varying scales. These campaigns form the backbone of the research, providing the empirical evidence through which hypotheses are explored and insights are derived. By progressing systematically from small-scale to larger, more representative conditions, the methodology not only validates the experimental approach but also establishes a clear link between controlled testing and real-world application.

The aim of this research is to develop and validate a novel ocean wave measurement buoy that estimates wave spectra and sea state parameters by analysing air pressure signals within a sealed OWC moonpool, using a frequency-domain transfer function calibrated against a conventional wave measuring system.

3.1 Experimental programme overview

The experimental programme was implemented in a staged manner, progressing from small-scale proof-of-concept tests through to full-scale deployment. Initial trials were undertaken at Dundalk Institute of Technology’s narrow wave tank facility using a 1:20 scale 3D-printed model to establish feasibility and guide subsequent refinements. Building on these findings, a second series of intermediate-scale tests at 1:2.4 were conducted at the LIR facility in Ringaskiddy, Co. Cork, to investigate performance under more representative conditions within a controlled environment. The principal phase of the research involved the construction and deployment of a full-scale prototype at the Galway Bay Marine Institute observatory, where it was tested over a four-month period in 2019. This staged approach ensured a systematic progression from conceptual validation to real-world application, while managing risk and maximising knowledge gained at each level of testing.

3.1.1 Justification for scaling from laboratory to full-scale

Scaling from laboratory models to a full-scale prototype was essential to ensure both scientific rigour and practical relevance. Laboratory-scale testing provided a controlled environment to explore fundamental behaviours, validate design concepts, and reduce technical risk at relatively low cost. However, scaled experiments are inevitably subject to limitations arising from scale effects, simplifications in geometry, and the constraints of test facilities. Progression to full-scale deployment was therefore required to capture the true complexity of environmental loading, structural response, and long-term performance under real sea conditions. This staged scaling strategy provided a balance between experimental control, resource efficiency, and the need to demonstrate the viability of the device in an operational context.

3.1.2 Summary of all campaigns

Table 3.1 presents a comparative summary of the three devices used for testing at the varying scales.

Scale / Phase	**Facility & Location**	**Model / Device**	**Objectives**	**Instrumentation**	**Data Collected**
1:20 Scale	Wave Tank, Dundalk Institute of Technology	1:20 scale 3D printed buoy model	• Proof of concept of pressure-based wave measurement • Validate instrumentation setup • Establish initial transfer function approach	• Pressure transducers • Wave probes • DAQ system	• Chamber pressure • Wave elevation
1:2.4 Scale	LIR Ocean Test Facility, University College Cork	1:2.4 scale buoy model. Off the shelf JFC Ltd Gannett buoy retrofitted for purpose.	• Refine transfer function estimation • Assess scale effects • Test robustness of instrumentation	• Pressure transducers • Wave probes • Motion sensors • DAQ system	• Chamber pressure • Wave elevation • Buoy motion
Full Scale	Galway Bay Test Site, Ireland	WASP prototype buoy. Off the shelf JFC Ltd Seagull buoy retrofitted for purpose.	• Full-scale validation under real-sea conditions • Long-term pressure data acquisition • Cross-reference with metocean data	• Pressure transducers • Onboard logging & telemetry • Reference wave buoy • Environmental sensors	• Chamber pressure (raw time series) • Metocean conditions • Deployment records

Table 3.1 summary of various test devices, location, instrumentation and data gathered

All models were based on the off the shelf ‘Seagull’ ocean navigational buoy manufactured by JFC Marine Galway. This particular model was selected based on its hollow core frame within which a water column can be formed, see Figure 3.1.

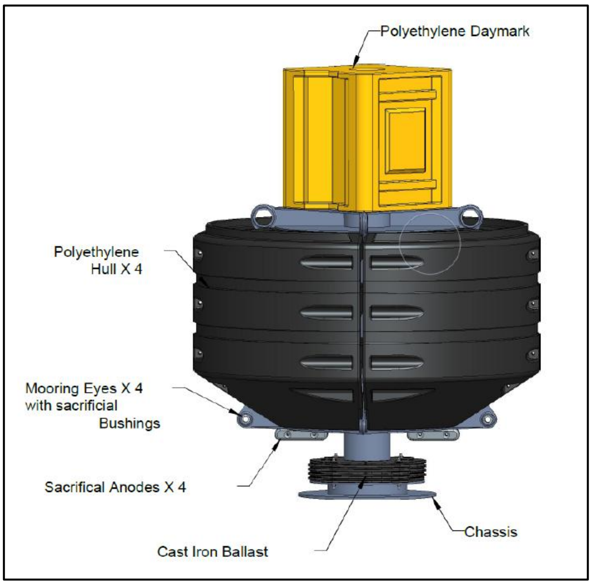

Figure 3.1 JFC Ltd Seagull navigational buoy (140)

Figure 3.2 presents dimensioned cross sections of the three models used during through testing for comparison, while Table 3.2 presents comparison of other model characteristics.

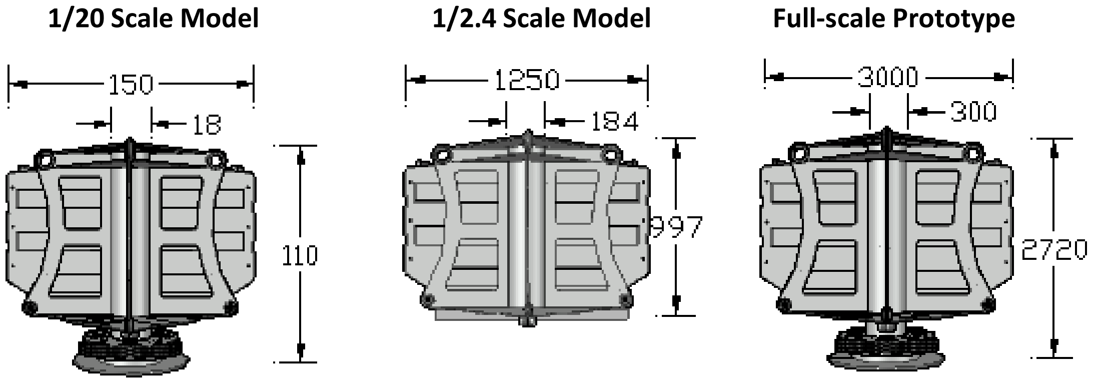
1/20 Scale Model

1/2.4 Scale Model

Full-scale Prototype

Figure 3.2 – 1:20 scale, 1:2.4 scale and full-scale prototype model dimensions (all dimensions in millimetres)

	1/20 Scale Model	1/2.4 Scale Model	Full-scale Prototype
Total Mass (during testing)	0.837 kg	320kg (floats and frame) 115kg (scaled mass distribution) + = 470 kg	510kg (upper components) 4700kg (floats, frame, ballast) + = 5210 kg
Draft	65mm	366mm	890mm
Moonpool Dia	18mm	184mm	300mm
Moonpool length	110mm	987mm	2700mm

Table 3.2 summary of other characteristics of the models

3.2 Scale 1:20 proof of concept testing – DKIT Narrow Wave Tank Facility

3.2.1 Objective

To establish if the concept of using pressure signal time series data from the column of air above the water column in a moonpool to obtain sea state parameter estimations, initial physical model tank testing was necessary.

3.2.2 Facility Description

This stage of the scaled testing was carried out in a narrow wave tank at Dundalk Institute of Technology, Ireland under the Centre for Renewable Energy Dundalk IT (CREDIT). The tank, which was designed and built by Edinburgh Designs is 18 m in length, 350 mm wide and is filled to a depth of 1 m. At one end of the tank is located a wave absorbing beach which has been shown to absorb, on average, 95% of incident waves using the 2-probe method of measuring reflections developed by Goda and Suzuki, [312], and at the other end is a wedge-shaped, flap-like wave maker, see Figure 3.3. The tank is capable of generating both monochromatic and polychromatic waves in a frequency range from 0.4 Hz to 1.4 Hz.

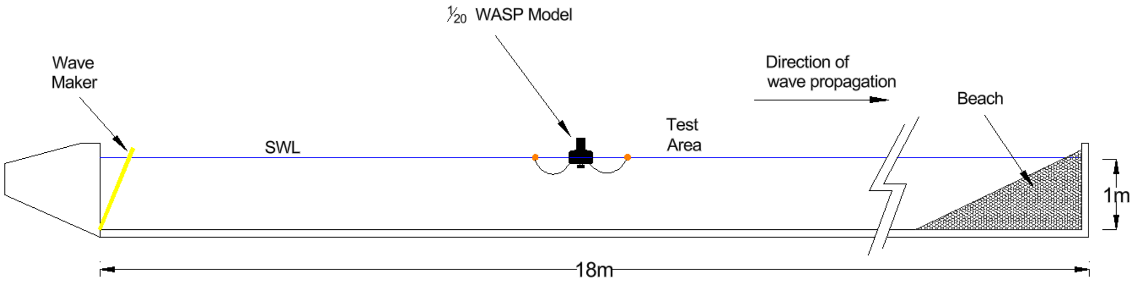

Figures 3.3 – Schematic of the narrow wave tank at DkIT illustrating the main dimensions and components of the tank

3.2.3 Model Description

The model used to perform scaled proof of concept tank testing, as installed in the narrow wave tank located at the Dundalk Institute of Technology, Ireland using a 1:20 3D printed scale model of the JFC Ltd Seagull Navigational Buoy (full-scale prototype) as discussed later in this chapter is shown in Figures 3.4-3.6. See also section 3.1.2 of this work for model characteristics.

Figures 3.4 – The conceptual 3-D WASP model during testing in the narrow wave tank

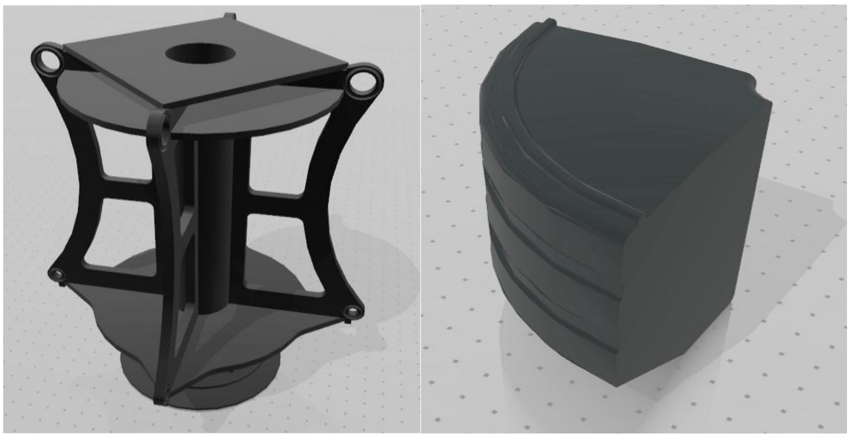

Figure 3.5– Image of model buoy core and buoy float drawn in Autocad and exported to STL for printing

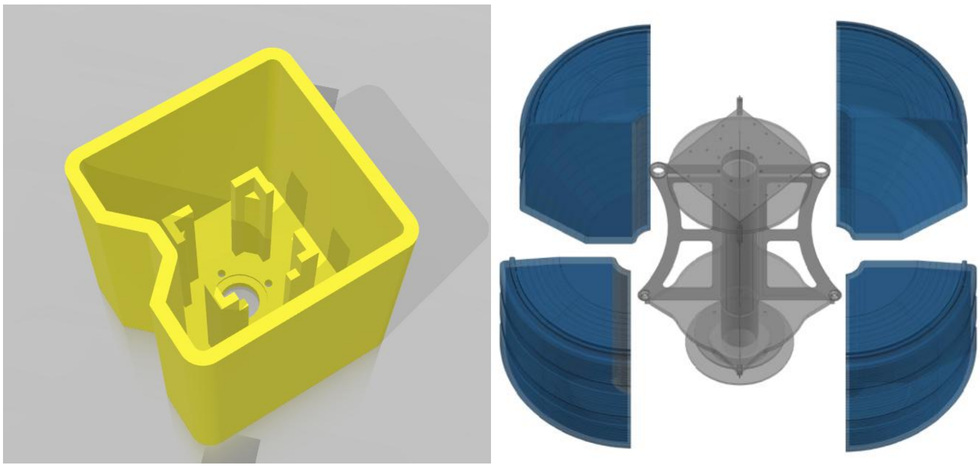

Figure 3.6– Image of buoy daymark and buoy assembly drawn in Autocad

3.2.3 Instrumentation and data acquisition

The pressure amplitudes’ of the air above the sealed moonpool of the model were measured using a Honeywell 170PC series differential pressure sensor. The sensor has a range pf +/- 355mm water and a sampling rate of 2k Hz which is resampled at 32Hz. Calibration is achieved using a u-tube manometer.

The wave probes used during the scaled tank testing campaign are resistance wave probes which operate by detecting changes in electrical resistance caused by wave motion. They are robust and reliable, commonly used in wave tank testing for their simplicity and effectiveness. A wave probe was positioned both up and downstream of the model during testing. The probes comprise of two parallel stainless steel wires, 3mm in diameter, circa 400mm long with a 12.5mm spacing. The probe monitor outputs +/- 10volts DC to the probes, and registers the change in conductivity as the water level oscillates due to the wave action.

Data acquisition from the wave resistance probes and pressure transducers is assimilated via the ‘National Instruments Compact RIO USB Cable System which is connected to a dedicated PC. The data was then compiled with LABVIEW software.

3.2.4 Experimental Procedure

The first sea trails of the full-scale prototype WASP took place at the SmartBay 1/4 scale Galway Bay marine test site, located off the west coast of Galway, Ireland. The aim was to reproduce the wave conditions in Smartbay at scale. The wave regime at the test site has been measured since 2005, using individual Datawell Waverider buoys and the wave climate at the site is well established. The recorded data is freely distributed by the Marine Institute through its request for digital data programme. Figure 3.7 displays a wave rose of the wave directions and significant wave heights recorded by one of the waveriders buoys at the test site from 2008 and 2018, the zero up-crossing period was also analysed.

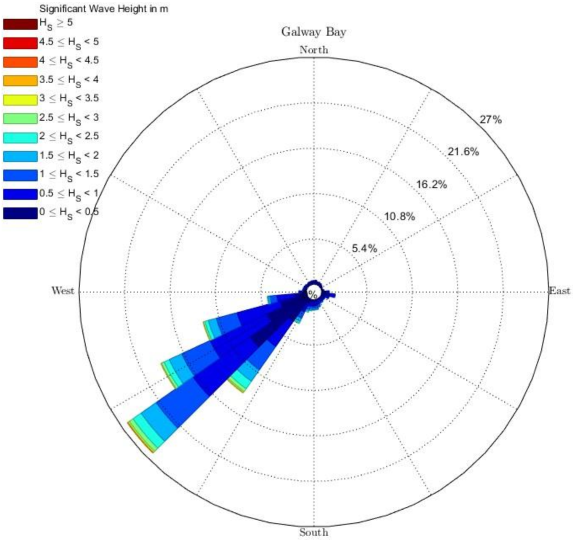

Figure. 3.7. Wave Rose from the directional waverider buoy at SmartBay, Ireland [473]

With the limitations of the wave tank in mind, a range of sea-states were selected to be used throughout testing that reflect the typical sea-states which occur at the SmartBay test site. The theoretical spectra (see Chapter 2) for each selected sea state, based on the significant wave height and zero up-crossing period, was scaled appropriately for testing. Table 3.3 lists the wave spectra that were used during the testing at both full scale (scaled 1/20) and model scale. Note that, in accordance with Froude scaling as discussed in Chapter 2, to obtain the scale equivalent the significant wave height is divided by the scaling factor (here 20), and the zero-crossing period is divided by the square root of the scaling factor. Note further that the model scale significant wave height is given in millimetres. In all cases, the values of *Hs* and *Tz* have been obtained from consideration of the free surface elevation obtained from the Marine Institute. The periods correspond to full-scale periods of 10 s to 4 s. In each case, the tank was requested to generate a *Hs* of 75 mm, corresponding to a full-scale *Hs* of 1.5 m. In practice, the wave tank created spectra with larger values of *Hs* close to 1.7m and required further calibration, this however had no bearing on the results as the estimated spectrum was compared to the recorded and not the requested spectrum.

Model-scale Hs (mm)	Model-scale Tz (s)	Full-scale Hs (mm)	Full-scale Tz (s)
84.8	2.23	1696	10
84.4	2.01	1688	9
84.1	1.78	1682	8
84.3	1.55	1686	7
85.1	1.32	1702	6
86.1	1.11	1722	5
84	0.93	1680	4

Table 3.3. Spectra used to test the model WASP

Figure 3.8 provides a comparison of the measured theoretical spectrum Hs = 84:8mm and Tz = 2:23 sec with and without the model in the tank, as determined using time series data obtained from a resistive wave probe. All matlab coding and raw data files are available for review at [486].

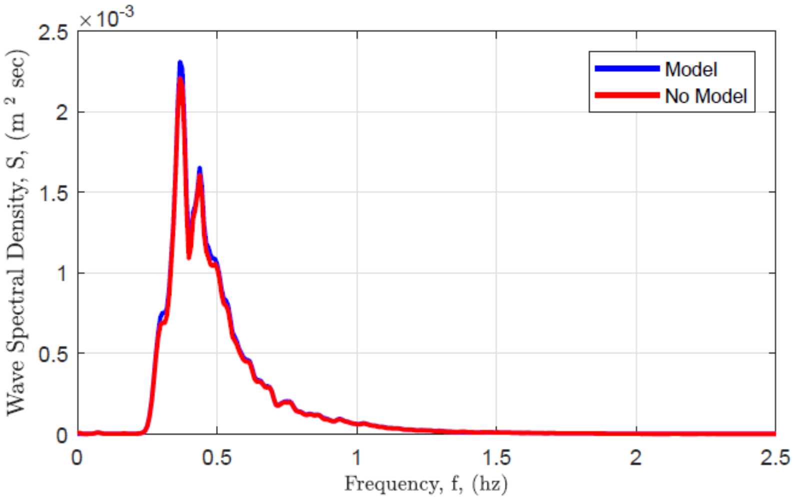

Figure 3.8. Comparison of Measured Spectrum with and without the model in the tank, *Hs* = 84.8mm and Wave Period, *Tz* = 2.33 secs

Figure 3.9 provides a comparison of the measured theoretical spectrum time series with and without the model in the tank.

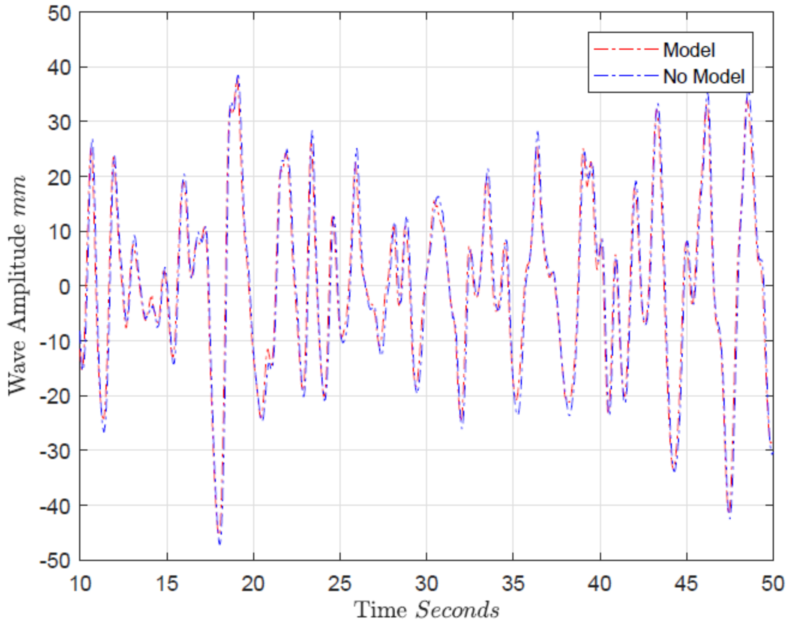

Figure 3.9. Comparison of Produced Time Series

Analysis of Figures 3.8 and 3.9 infer that the wave tank can produce a comparable spectrum each time and that the presence of the model has minimal impact.

In order to use the WASP to estimate an incident wave spectrum from the power density spectrum of the time series of the pressure in a chamber of air located above the entrapped water column, it is first necessary to establish the relationship between the pressure spectrum and in the incident wave spectrum. In effect, the WASP must be trained, or calibrated. During the first step of the training process, a theoretical spectrum is run in the narrow tank with no model present in the tank for sufficient time to allow the spectrum develop fully (approximately 20 minutes). The free surface elevation is measured throughout the test at a single location using a resistive wave probe, and Welch's method is used to estimate the power density spectrum for the polychromatic wave [331]. Figure 3.10 illustrates the spectrum generated by the tank estimated using Welch's method, and the theoretical spectrum for a significant wave height of 75 mm and zero-crossing period of 2.33 s (equivalent to 1.5 m and 10 s at full scale), and is representative of the typical output from the narrow tank in response to a requested spectrum.

During the second step of the calibration process, the model is installed in the tank. During the tests discussed herein, a two-point mooring system was simulated using chain and fishing floats. The model draft was set using lead weights. A 176PC14HD2 Honeywell pressure sensor was installed. Once the sensor is installed and the model placed in the tank, the air chamber above the water column is completely sealed. The model was then subjected to the identical theoretical spectrum for sufficient time to all the spectrum fully develop. The pressure in the air above the water column was sampled at 32 Hz throughout the test. It has previously been demonstrated that the narrow wave tank at the Dundalk Institute of Technology is capable of repeatedly generating the same polychromatic time series of waves as input to tests separated in time [474].

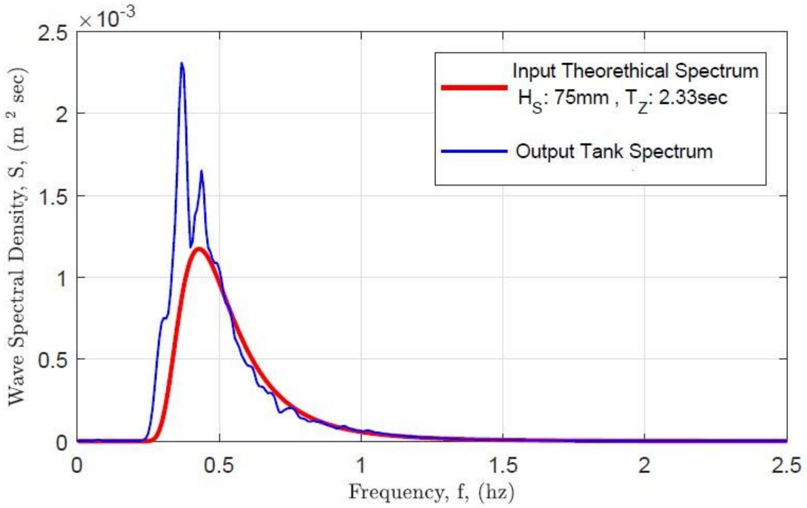

Figure 3.10. Comparison of Measured Spectrum with and without the model in the tank, *Hs* = 84.8mm and Wave Period, *Tz* = 2.33 secs

The power density spectrum of the pressure signal is then estimated, again using Welch's method, and time series wave data is then used to estimate the frequency dependent transfer function between the pressure signal and the incident wave elevation. Once the transfer function has been estimated in this fashion, the wave spectra listed in Table 3.3 were run in the absence of the model WASP in order to determine the exact wave spectrum generated for all theoretical spectra to be estimated from measurement of the air pressure above the water column of the model. The model was then returned to the tank, and each spectrum re-run while the pressure within the WASP model is recorded. The power density spectrum for each pressure signal is obtained, and the transfer function obtained earlier used to estimate the incident wave spectrum in each case as described in Chapter 2.

3.2.5 Results from 1/20 Scale model testing

Figure 3.11 illustrates the input spectrum that was first used to calibrate the model WASP and establish the relationship between the incident wave power density spectrum and the corresponding pressure power density spectrum. This spectrum had a *Hs* = 84.8 mm and *Tz* = 2.23 s. Note that the values for Hs and Tz above were obtained from consideration of the wave spectrum obtained from free surface elevation measurement and not those requested. Once a wave spectrum is measured, both *Hs* and *Tz* may be obtained from the spectral moments as described in Chapter 2.

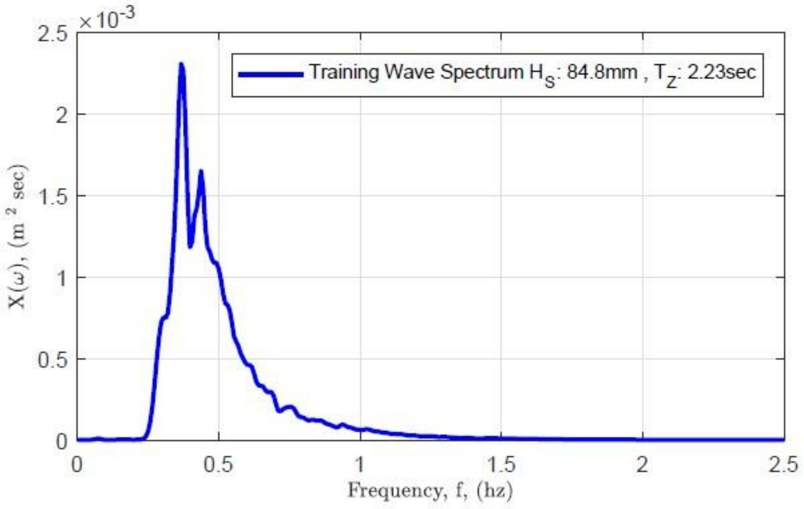

Figure 3.11. Incident Wave Spectrum used to train model WASP, *Hs* = 84.8mm and *Tz* = 2.23s

Figure 3.12 illustrates the power density spectrum of the pressure signal recorded during the training run, and Figure 3.13 illustrates the frequency dependent transfer function between the input wave spectrum and the pressure spectrum.

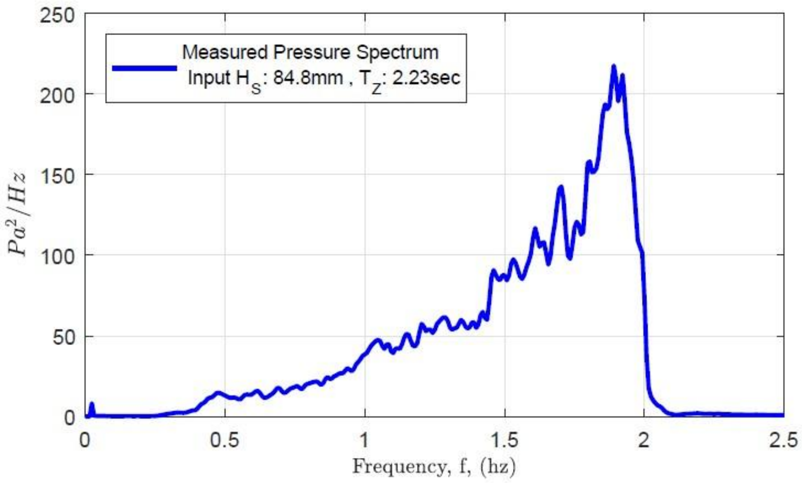

Figure 3.12. Pressure Spectrum obtained with an incident wave spectrum of *Hs* = 84.8mm and *Tz* = 2.23s

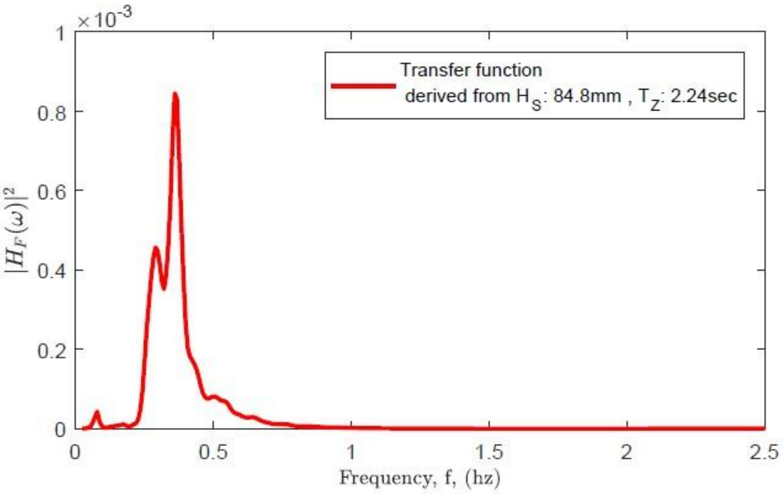

Figure 3.13. Transfer Function obtained from pressure data and wave data, *Hs* = 84.8mm and *Tz* = 2.23s

Next, to test the transfer function shown in Figure 3.13, the model was subjected to an incident wave spectrum for a spectrum close to, but not identical, to that for which the transfer function was generated, in this case, a spectrum with a *Hs* = 88.9 mm and *Tz* = 2.01 s. The transfer function was used along with the pressure spectrum obtained during the test to estimate the incident wave spectrum. Figure 3.14 illustrates the comparison between the wave spectrum in the absence of a model in the tank, and that predicted by using pressure data from the model WASP with the transfer function in Figure 3.13.

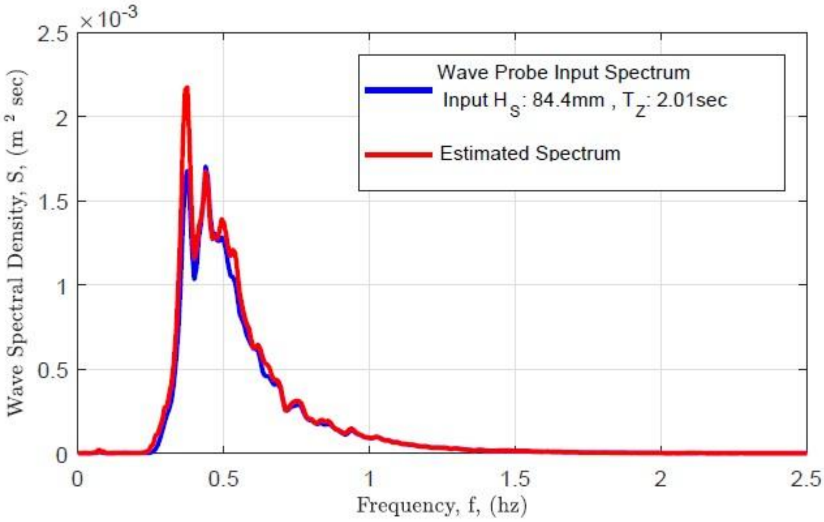

Figure 3.14. Comparison between the incident wave spectrum with *Hs* = 84.5mm and *Tz* = 2.01s and the estimated spectrum *Hs* = 88.9mm and *Tz* = 2.06s using the pressure spectrum and the transfer function illustrated in figure 3.13

When spectral moments are determined from the estimated spectrum shown in Figure 3.14 and used to estimate the key spectral parameters, values of *Hs* = 88.9 and *Tz* = 2.06, there is a minor difference from the corresponding values obtained from measurement of the free surface elevation.

In order to investigate the viability of using a single transfer function to estimate a range of sea states, the model WASP was then subjected to a series of wave spectra as presented in Table 3.3. In each case, the power density spectrum from the pressure signal was used with the transfer function in Figure 3.13 to estimate the incident wave spectrum.

Figures 3.15 to 3.16 show that, as the zero-crossing period decreases from that used in the training spectrum, the anomalous peak at 0.25 *Hz* grows, and thus increasingly effects the estimated spectral moments and estimated values of *Hs* and *Tz*. The peak/spike is exactly of the form of the transfer function in Figure 3.13. The low response coupled with the resolution of the pressure sensor causes this.

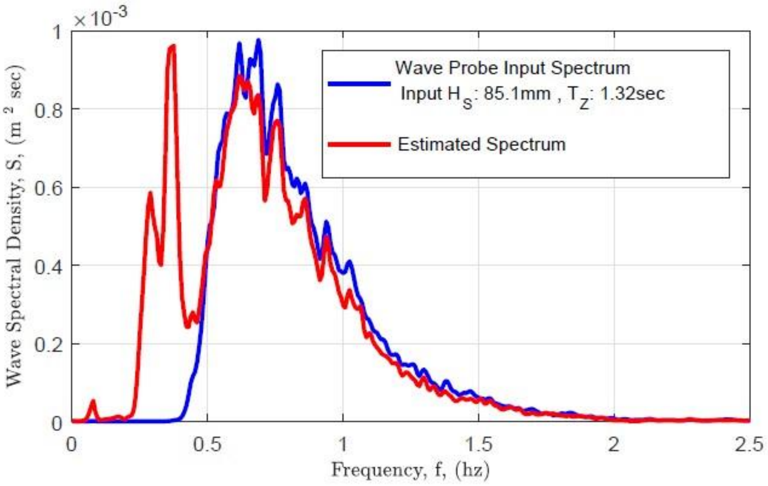

Figure 3.15. Comparison between the incident wave spectrum with *Hs* = 85.1mm and *Tz* = 1.32s and the estimated spectrum *Hs* = 90.05mm and *Tz* = 1.71s using the pressure spectrum and the transfer function illustrated in figure 3.13

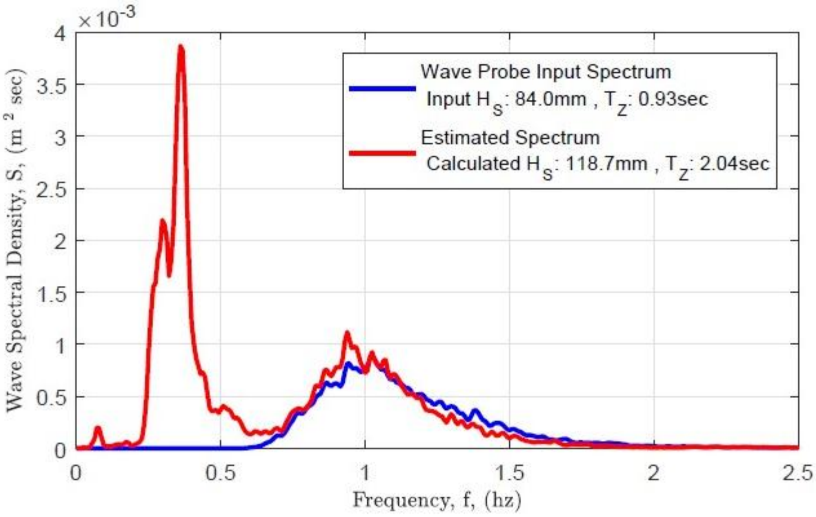

Figure 3.16. Comparison between the incident wave spectrum with *Hs* = 84.0mm and *Tz* = 0.93s and the estimated spectrum *Hs* = 118.7mm and *Tz* = 2.04s using the pressure spectrum and the transfer function illustrated in figure 3.13

3.2.6 Summary of results from 1/20 Scale model testing

The results presented herein, which represent a sample of the results obtained during scaled conceptual testing at the DKIT Wave Tank Facility, demonstrate that the incident wave spectrum acting on a device such as the WASP can be recovered from the pressure signal by considering the frequency domain transfer function between the power density spectrum of the pressure signal and the incident wave spectrum as described herein. However, the accuracy of the estimated spectrum as the zero-crossing period decreases clearly decreases in line with the reduction in the amount of energy in the range of 0.3 Hz to 0.6 Hz. It therefore appears, provided the input wave spectrum contains energy in the range of frequencies where the issue arises, the estimated wave spectrum will likely be close to the actual wave spectrum. Conversely, if the incident wave spectrum does not contain much energy at these frequencies, the anomalous peak, which can be seen in Figures 3.15 to 3.16, will occur. This may be as a result of the very low pressures that are generated in the frequency range where the anomalous peak appears.

As can been seen in Figure 3.16, there is essentially no pressure generated in the air chamber above the moonpool at these frequencies. Tests have shown that creating a transfer function using data obtained from testing with an incident wave spectrum that does not contain energy in the 0.3 Hz to 0.6 Hz range will not result in the anomalous peak, but as would be expected, will not correctly predict the spectrum when used to estimate wave spectra which do contain energy in the frequency range at issue.

3.3 1:2.4 Scaled Model testing at LIR National Ocean test Facility

3.3.1 Objective

The objective of conducting mid-range scaled model testing at the ocean wave test facility is to obtain a controlled yet sufficiently representative physical response of the structure under realistic wave conditions while also determining confidence in establishing transfer functions for the model using the tank wave probe spectral data and the model pressure probe spectral data. By employing a mid-scale model, the testing bridges the gap between small laboratory experiments and full-scale prototypes.

3.3.2 Facility Description

This research availed of the access programme to the Lir-NOTF which was designed to enable the testing and progression of offshore renewable energy technologies through the early development stages in advance of open sea testing. It was supported by SEAI and was open to any type of marine technology (wave, wind, tidal, floating solar) that can be tested at the Lir NOTF. This included all sustainable marine enterprises to capture any innovation intended for marine use that reduces energy use and energy production.

Ireland’s National Ocean Test Facility, LIR-NOTF, is located at the ERI Beaufort Building in Cork, providing a suite of state-of-the-art test tanks and dedicated workshops. The facilities include a 2,600m^2 tank hall which will house four different wave tanks, and a range of electrical test infrastructure, providing an ideal testing environment throughout all phases of device development. The facility’s deep water research wave basin and wave flume have the capability of generating waves up to 1m height to facilitate the testing of model wave energy devices and other marine structures in different wave conditions, including extreme conditions, such as those encountered off the west coast of Ireland.

While fixed offshore wind technologies are commercially advanced, many offshore renewable energy (ORE) technologies that are required for deeper water and more aggressive environments are still in early stages of development. These technology developers usually consist of individuals, SMEs and academics who generally do not have the financial resources and expertise to determine the feasibility of their concept and require support. As a result, SEAI and Lir NOTF have teamed up to offer this programme which will provide free to access the to the facilities of Lir-NOTF to Irish ORE developers.

The deep ocean basin, which was used for this projects scaled testing campaign, is 35m long x 12m wide x 3m deep. It has a movable floor plate to allow the water depth be adjusted, making it suitable for circa. 1/15 scale operational conditions and 1/50 scale survival waves. Equipped with

16 hinged force feedback paddles capable of a peak wave generation condition of Hs = 0.6m, Tp = 2.7 s and Hmax = 1.1m [475]. Figures 3.17 and 3.18 shows a plan view of LIR's deep ocean wave tank.

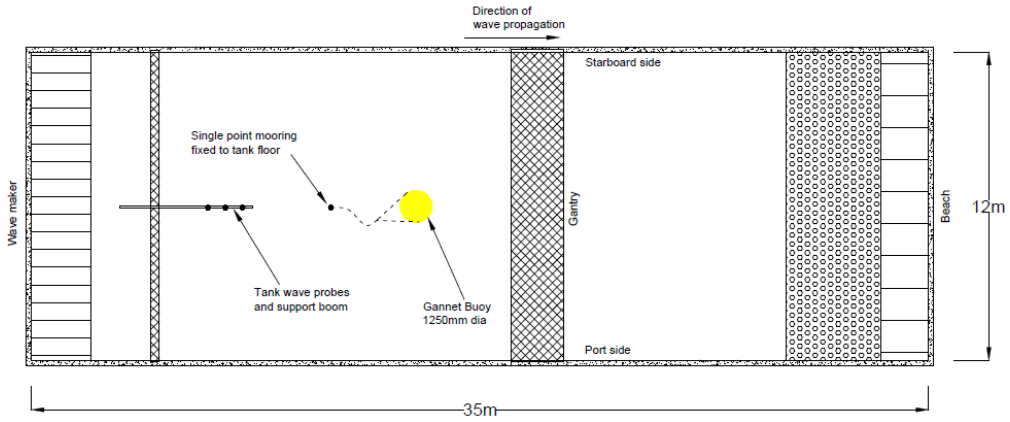

Figure 3.17 – Plan View of Deep Ocean Basin at LIR - NOTF [475]

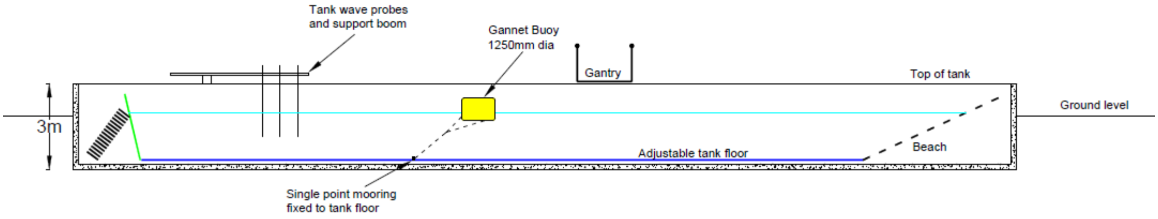

Figure 3.18 – Cross Section of Deep Ocean Basin at LIR - NOTF [475]

3.3.3 Model Description

With the off the shelf Seagull buoy identified for full scale prototype use, it made practical sense to use a smaller model available through the same company JFC. The Gannet buoy has similar characteristics to the Seagull making it ideal for scaled model testing, namely a hollow steel core which allows for the development of a water column as shown in Figure 3.2.

The main float section to the Gannet is 1250mm in diameter (see Figure 3.2), compared with a 3000mm diameter on the full scale Seagull/WASP buoy thus giving a scale factor of 2.4 between the controlled tank testing model and the full scale prototype to be used at Galway Bay Test Facility as discussed later in this chapter. Importantly, the Gannet also has the option of using a hollow steel central core/moonpool within the frame which would allow the presence of water column and facilitate the measurement of the fluctuations to air pressure above this water column similar to the full scale prototype behaviour.

In order to maintain similarity with the proposed full scale testing campaign conditions, the mass of the ballast to be added to the Gannet model was scaled to that to be used with the full scale prototype WASP. The full scale device included 1600kg of ballast, which will be subject to the 1:2.4 scale factor cubed given a required scaled ballast of 115kg. Secondly, the mass of upper sections to the WASP which consisted of two day marks, the various electronics, a bank of batteries and various other elements all in the order of 480kg, was scaled to 35kg. The centre of gravity for the Gannet scale model is approximately 619mm from the bottom of the buoy and in this regard, to attempt to distribute the mass relatively accurately, the 35kg representing the upper components of the full scale prototype of the WASP was placed on a metal frame and fixed to the top of the model positioned 400mm above the top of the buoy as presented in Figure 3.19. All of the additional necessary metal work was fabricated by JFC Marine, including the frame for the upper 35kg weight, supports for the wave probes and the plate to seal the moonpool. The Gannett model was assembled and delivered to the LIR facility for use in testing.

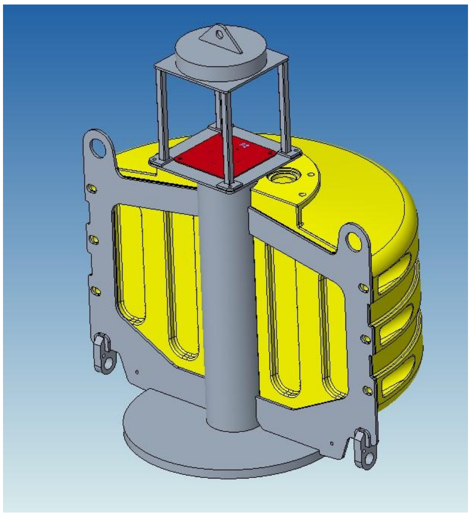

Figure 3.19 – Schematic of Gannet model with upper weight for mass distribution [476]

In order that the pressure in the air chamber in the moonpool above the water column be subject to variation from atmosphere as a result of the action of the incident wave on the buoy, and the motion of the buoy itself, the top of the moonpool is sealed, as was the case for the full-scale prototype test at the Galway Bay test facility.

The steel plate, prepared by JFC, to seal the moonpool is approximately 4mm thick and is bolted to the upper flange of the inner metal frame of the model buoy. An 8mm diameter hole was drilled to allow a pressure sensor to take measurements of the air pressure beneath the plate and above the water column within the hollow moonpool.

Furthermore, three pairs of 1.5mm diameter holes (at 12.5mm centres) were provided to allow the wave probes access the water column to monitor the fluctuations in water levels in the column as the buoy interacts with the incident wave in the test tank. This plate is illustrated in figure 3.20.

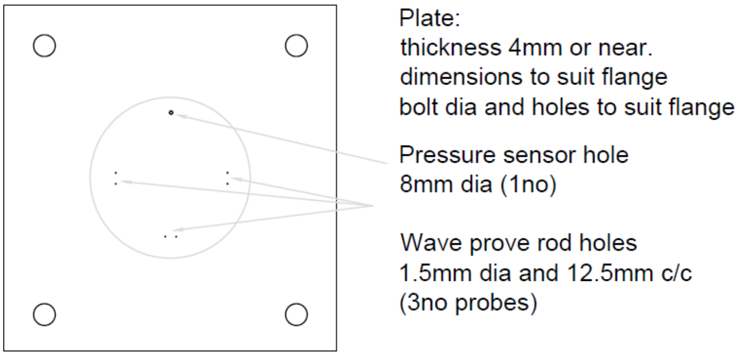

Figure 3.20 – Steel plate for sealing moon and positioning wave probes and pressure sensor.

3.3.4 Instrumentation and Data Acquisition

A pressure sensor is required in order to measure the air pressure above the water column during testing. The Honeywell 170PC series is a family of differential pressure sensors designed to provide accurate and reliable pressure measurements in a variety of industrial applications. These sensors are known for their durability, precision, and ease of integration into different systems. The sensor has a range of + or – 14in. H_2O, with an output of + or – 5V DC.

Wave probes are essential for evaluating the performance and efficiency of ocean energy devices such as wave energy converters and tidal turbines. Wave probes help simulate real-world ocean conditions in a controlled environment, allowing researchers to optimise designs and ensure reliability before deployment in the open sea.

The wave probes used during the scaled tank testing campaign are resistance wave probes which operate by detecting changes in electrical resistance caused by wave motion. They are robust and reliable, commonly used in wave tank testing for their simplicity and effectiveness.

A series of wave probes are positioned linearly at the LIR Ocean Tank Test Facility in advance of the scaled model subject to testing. A further three wave probes are inserted into the moonpool of the scaled model to facilitate monitoring of the surface water elevation of the water column.

The probes comprise of two parallel stainless steel wires, 3mm in diameter, circa 400mm long with a 12.5mm spacing. The probe monitor outputs +/- 10volts DC to the probes, and registers the change in conductivity as the water level oscillates due to the wave action. The LIR facility had three wave proves placed linearly within the ocean basin tank and in advance of the model, while three wave probes were installed inside the model to record data from within the moonpool.

The wave probes are inserted in through the steel plate used to seal the top of the moonpool through pre-drilled holes and insulated where in contact with the steel plate. When considering the draft of the buoy, which is 366mm as provided by JFC Marine Ltd, finalising the design of the probes, how the probes would be held in place and the positioning of the probes within the moonpool, it was discovered that the assembled probes would be too short in length and would not reach the water column within the moonpool.

Increasing the probe length was considered, however this could lead to a loss of resistivity. A frame was designed and fabricated to fit to the underside of the sealing plate in order to hold and extent the wave probes down into the water body. With the wave probes 414mm in length, the frame was fabricated with three extending arms 424mm long, this would ensure the wave prove was positioned with approximately half its length submerged, offering the optimum probe length for recording water depths throughout all of the varying tests. See Figures 3.21 and 3.22.

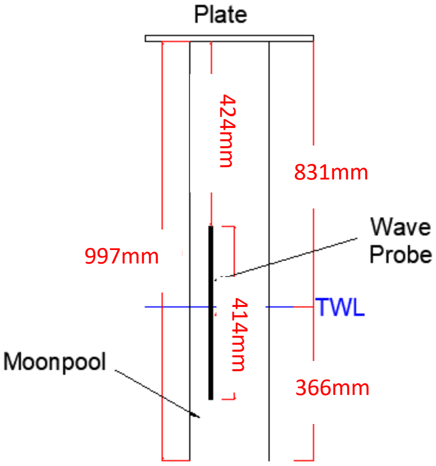

Figure 3.21 – Sketch cross-section showing various dimensions associated with the wave probes, moonpool and water surface

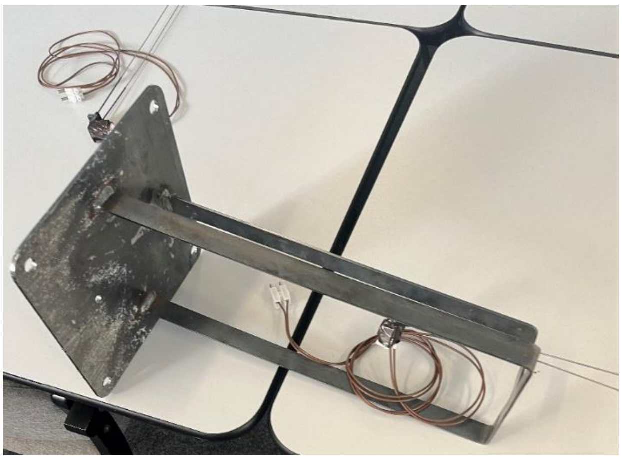

Figure 3.22 – Metal frame fixed to underside of plate to extend wave probes further in to moonpool and water body.

Wave probes are essential instruments in ocean tank testing for measuring wave heights accurately. Calibration of these probes ensures precise and reliable data collection. The probes were secured to a frame and inserted into the body of water approximately mid length of the probe. A baseline zero reading was recorded. The probe was then adjusted vertically in increments of 10mm, taking readings at each setting. A typical wave probe calibration curve is shown in Figure 3.23.

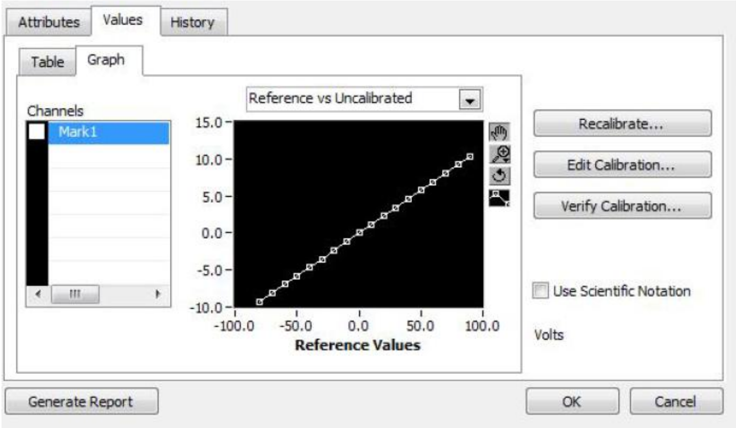

Figure 3.23 – Wave probe calibration graph

Motion detection cameras provide high-resolution, real-time visual data that can be used to monitor the behaviour of ocean energy devices under various testing conditions. This data is crucial for understanding the dynamics and performance of these devices. These cameras are capable of detecting even the slightest movements of the devices, which is essential for identifying potential issues or areas for improvement. Movement tracking helps in fine-tuning the design and operation of the devices. In wave tanks, motion detection cameras track the response of ocean energy devices to simulated wave conditions. This tracking is crucial for assessing the device's performance, resilience against different wave patterns and intensities and establishing the frequency characterisation of the device.

The Qualisys Arqus [477] which is used at the LIR Ocean Tank Test Facility, is a camera system with high resolution image sensors, powerful illumination and advanced marker detection algorithms to capture and record motion. The centre of gravity of the floating body, provided by JFC Marine, is input to the recording system and markers fixed to the buoy detected and recorded.

Considering the six degrees of freedom of the floating model, surge, sway, heave, roll, pitch and yaw, three markers were fixed to the upper frame of the model. The first representing the stern of the floating device, the second marker the port and the third marker the bow of the device. The location and orientation of the markers can be seen in Figure 3.24, which illustrates the Gannett as deployed in the ocean basin at LIR.

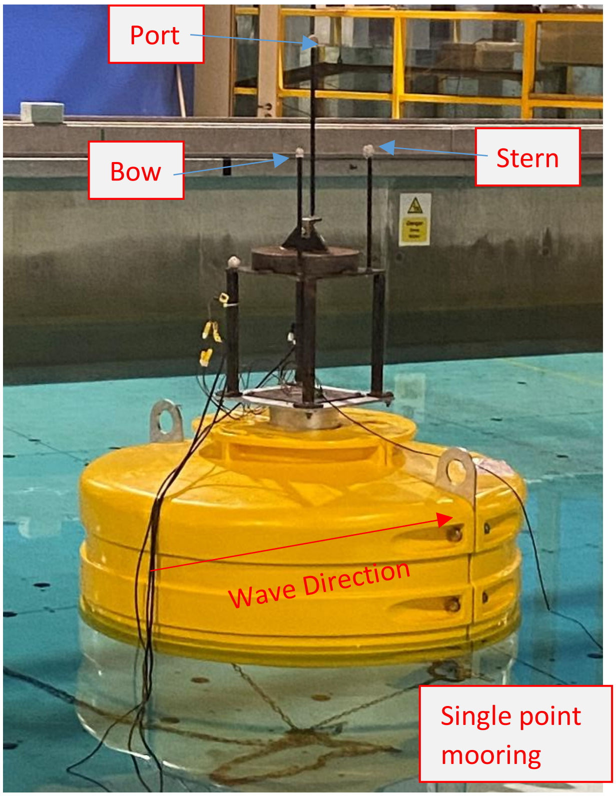

Figure 3.24 – Qualisys markers fixed to buoy to monitor motion.

Mooring systems play a crucial role in ensuring that such floating devices remain securely positioned during testing, providing for accurate performance evaluation, safety, and design optimisation. Mooring systems maintain the precise position and stability of ocean energy devices in tank testing environments. This is critical for replicating real ocean conditions and ensuring consistent testing results. By securely holding devices in place, mooring systems allow for accurate measurement of performance metrics, such as power output, efficiency, and structural response to wave and current forces. Proper mooring prevents devices from drifting or colliding with tank walls, ensuring the safety of the testing environment and personnel. This minimises the risk of damage to expensive prototypes and testing equipment. Mooring systems in tank testing facilities replicate the anchoring conditions that devices will experience in the open ocean. This helps in assessing how devices will perform in their intended deployment sites. Mooring systems are used to hold wave energy converters in place, allowing them to respond to simulated wave conditions. This is essential for evaluating their energy capture efficiency and structural durability. Catenary moorings use heavy anchors and long, flexible chains or cables that form a catenary curve. This type of mooring allows for more movement and is commonly used to simulate realistic ocean conditions.

The proposed mooring type for the full-scale prototype WASP at Galway Bay Test Facility is a single point catenary mooring arrangement. In this regard, in order to reflect as best as possible the full-scale scenario, a single point mooring arrangement was used in the LIR Deep Ocean Test Tank. It was noted during testing that periodically, the mooring chain would snap or pull at the model as it reached its extents and then settle once again in to a more natural rhythm with the wave frequency. This was more pronounced for particular wave frequencies than others.

3.3.5 Experimental procedure

Designing effective test design ensures that data collected is accurate, reliable, and applicable to real-world scenarios.

The objectives of this scaled tank testing campaign are to firstly determine the RAOs of the buoy, refer to previous chapter 2, by measuring the motions in the six degrees of freedom of the model, and secondly to determine the transfer function between the pressure signal and the free surface elevation by measuring the gauge pressure within the OWC chamber while the chamber is sealed from atmosphere. A set of tests using regular, monochromatic waves of varying frequencies and amplitudes were first performed, which were then used to determine the RAOs. The primary RAO's of interest is that of the heave and pitch of the buoy, however data pertained to all degrees of freedom of the buoy and the motions of the water column were also captured.

A second set of tests was performed using irregular, polychromatic waves spectra mimicking, at scale, those which occur in the Galway Bay test site [478]. The choice of wave spectra was somewhat limited by the operating envelope of LIR's deep ocean basin tank and was carried out in consultation with test engineers at the LIR facility. Figure 3.25 presents the tank specific operating envelope for test design purposes.

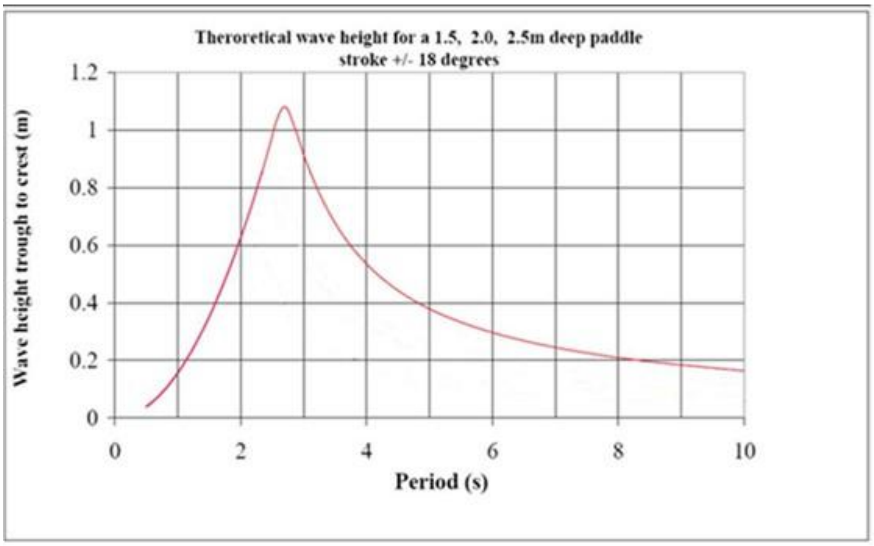

Figure 3.25 – Deep Ocean Basin operating envelope [475]

When designing the regular wave suite of tests, bearing in mind the maximum operational range of the ocean basin tank of 0.6m wave height and 3.0 s wave period, a range of frequencies of 0.807

to 3.33 secs and wave heights ranging from 0.1m to 0.6m were selected. Thirty-four tests in total were specified for regular wave testing sampled at a rate of 128 hertz. Table 3.4 presents the regular wave test characteristics and also includes the full scale equivalent wave period and wave height of each test which range from 1.25s to 5.16s and 0.240m to 1.488m respectively. Refer to Froude Scaling factors chapter 2.

Tank Period (secs)	**Full scale Period (secs)** ($S^{0.5}$)	**Test No.**	**Tank Wave height (m)**	**Full Scale Wave height (m)** (Tank Hgt *S)	**Test No.**	**Tank Wave height (m)**	**Full Scale Wave height (m)** (Tank Hgt *S)
0.807	1.250	1	0.10	0.240	18	0.110	0.264
0.861	1.333	2	0.10	0.240	19	0.115	0.276
0.922	1.428	3	0.10	0.240	20	0.120	0.288
0.993	1.538	4	0.10	0.240	21	0.125	0.300
1.076	1.666	5	0.10	0.240	22	0.175	0.420
1.174	1.818	6	0.10	0.240	23	0.190	0.456
1.290	2.000	7	0.20	0.480	24	0.200	0.480
1.333	2.066	8	0.20	0.480	25	0.210	0.504
1.379	2.138	9	0.20	0.480	26	0.250	0.600
1.429	2.214	10	0.20	0.480	27	0.270	0.648
1.481	2.296	11	0.20	0.480	28	0.300	0.720
1.538	2.385	12	0.20	0.480	29	0.350	0.840
1.600	2.480	13	0.20	0.480	30	0.400	0.960
1.667	2.583	14	0.20	0.480	31	0.410	0.984
1.739	2.695	15	0.20	0.480	32	0.420	1.008
2.000	3.100	16	0.20	0.480	33	0.580	1.392
3.333	5.166	17	0.20	0.480	34	0.620	1.488

Table 3.4 – Regular Wave test schedule (where $S = 2.4$)

In order to design a suite of tests to best replicate the conditions the full scale prototype would be subjected to in Galway Bay test site, nine tests were specified for irregular wave testing all set to a tank wave height of 0.15m and wave periods ranging from 1.0 seconds to 3.0 seconds in increments of 0.25 seconds with a sealed moonpool.

Each regular wave test was carried out for a three-minute duration, while the irregular wave tests were carried out for a twenty-minute duration. During this time, data was recorded from the tank and model wave probes at a sample rate of 128 hertz. Data from the model pressure probe was sampled rate of 32 hertz, while the motion of the six degrees of freedom was also being sampled at a rate of 32 hertz.

The water level in the tank was adjusted and tank floor raised, and the Gannet scaled model lifted in to position using the in-situ gantry crane incorporated into the tank. The single point chained mooring was fixed to the tank floor and split in advance of the device before being bolted to the two mooring eyes at the underside of the model steel frame, see Figure 3.2.

The steel plate used to seal the moonpool is bolted to the top of the model and the three internal waves probes, which are held in place by the extended support arms, fixed to the underside of the plate, subsequently lowered to an appropriate position inside the hollow chamber of the model metal frame. The cables and connectors for the wave probes are kept to one side for connection to the main data collection system. The pressure sensor is then inserted into the pre-drilled 8mm diameter hole, sealed using a grommet to eliminate air leakage during testing and the cable and connector kept to one side for later connection. The upper metal frame used to provide a platform for the 35kg weight is then fixed to the top of the model and the three markers for motion detection fixed to this metal frame. All probe and sensor cables are connected to the main cables leading to the main data recording system and the tank filled with water and floor lowered providing a testing depth of 3 meters.

Before testing could commence, still water levels were recorded from the tank and internal model wave probes, the motion detection cameras focused on the device and the centre of gravity input to the data recording system. This was done in order to generate a zero point from which all movement would be recorded. The wave tank paddles were energised and the suite of predetermined tests as presented in Table 3.4 commenced.

3.3.6 Results from 1/2.4 Scale model testing – Regular Wave Testing

Initially, a high-pass filter can be applied to the recorded pressure data to remove low-frequency drift and quasi-static components, such as sensor bias or slow variations in atmospheric pressure. This step ensures that only the dynamic oscillations associated with wave action remain in the signal. However, high-pass filtering alone does not suppress high-frequency noise, which often arises from turbulence, sensor electronics, or structural vibrations. To address this, a band-pass filter is subsequently employed, targeting the frequency range corresponding to the expected wave-induced oscillations in the OWC chamber. The band-pass filter simultaneously eliminates both the low-frequency drift and the high-frequency noise, resulting in a cleaner signal that more accurately represents the hydrodynamic response of the system. This sequential approach improves the quality of the pressure data, thereby enhancing the reliability of spectral analysis and energy conversion assessments. All matlab coding and raw data files are available for review at [486]. A Butterworth digital filter was implemented in MATLAB to process the recorded time series data. The Butterworth filter was selected due to its maximally flat frequency response in the passband, which allows the dominant oscillatory pressure signals associated with wave excitation to be preserved without introducing significant amplitude distortion. By applying an appropriately designed band-pass Butterworth filter, low-frequency drift and high-frequency noise, such as snatching of the model by the mooring, were effectively attenuated, isolating the pressure components most relevant to the hydrodynamic behaviour of the OWC. The smooth roll-off of the Butterworth design minimizes phase distortion compared to more abrupt filters, thereby maintaining the integrity of the temporal pressure signals required for accurate spectral analysis and performance evaluation. MATLAB's built-in filter design functions facilitated efficient implementation, parameter tuning, and validation, ensuring reliable preprocessing of the experimental data. Figures 3.26, 3.27 and 3.28 present comparisons of the time series of the heave from test 1 unfiltered, high pass filter and band pass filter. A band pass filter was thus applied to all data for processing.

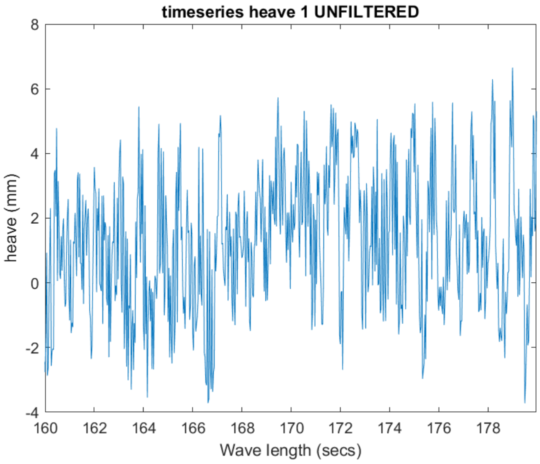

Figure 3.26 – Unfiltered time series of the heave from test 1

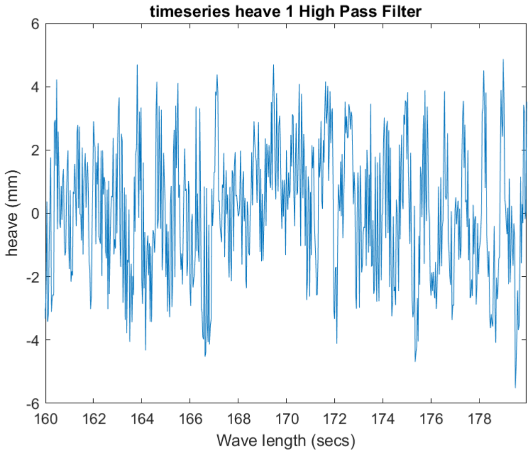

Figure 3.27 – Filtered time series of the heave from test 1 using a high pass filter

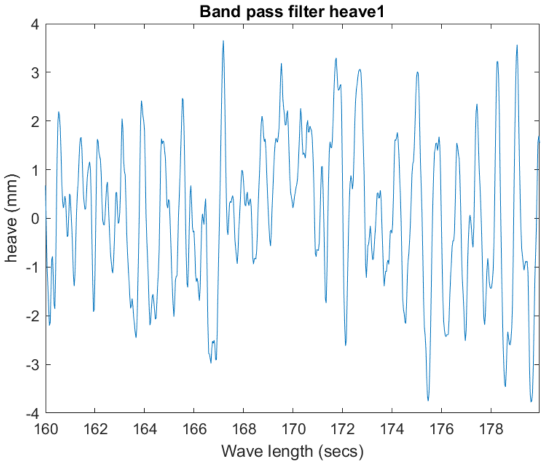

Figure 3.28 – Filtered time series of the heave from test 1 using a band pass filter

As a check, the FFT of the heave from varying tests was generated in order to compare against expected values as set out in the test schedule in Table 3.4. Again, a comparison between the unfiltered and filtered FFT of heave test 1 was determined and is presented in Figure 3.29 showing less noise contained in the lower frequencies. The expected frequency of 1.24Hz is achieved.

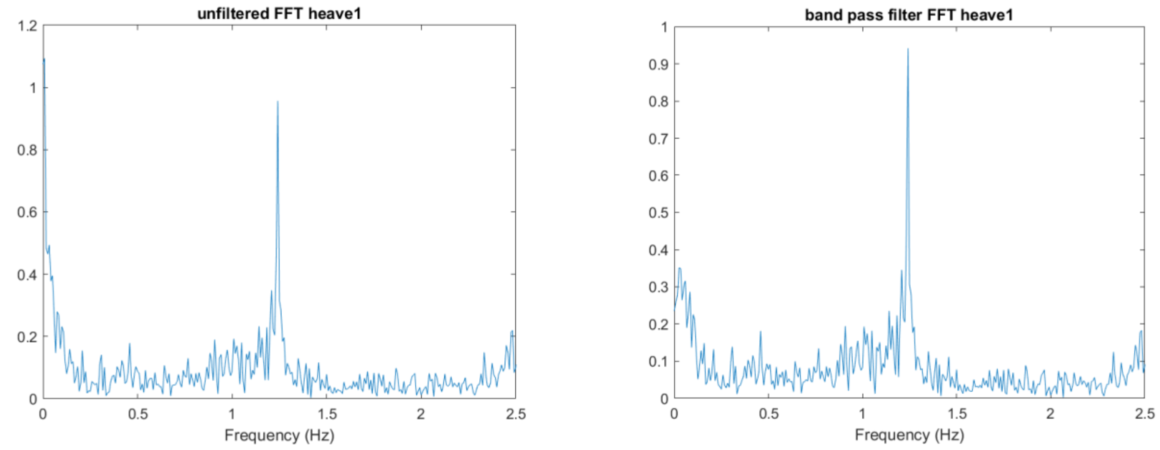

Figure 3.29 – Unfiltered and Filtered FFT of heave test 1

Figure 3.30 shows the FFT for heave tests 7 and 15 which are reflective of the expected frequencies for these tests, referring to Table 3.4. 0.78Hz and 0.58Hz respectively and therefore gives confidence in the chosen method.

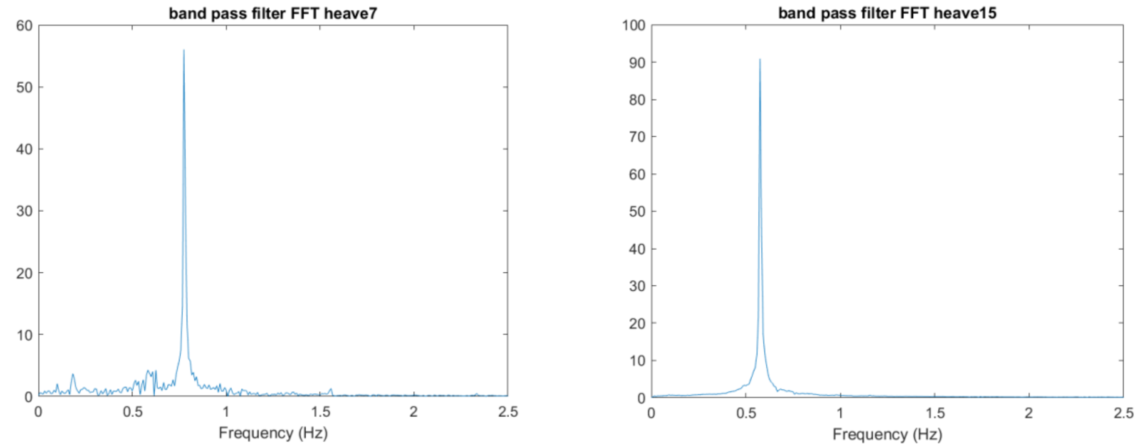

Figure 3.30 – Filtered FFT of the heave from tests 1 and 15 using a band pass filter

The FFT of the heave amplitude was thus determined and taking into consideration the suite of testing parameters which included 34 tests, half of which had the same wave period, the Response Amplitude Operator (RAO) of the heave was determined by taking the average of the FFT of the heave amplitude for the same wave period divided by the average of the wave amplitude for that same period (see Chapter 2). The frequency vector was obtained by integrating the test wave period. Figure 3.31 presents the RAO of the heave of the scaled model as thus obtained.

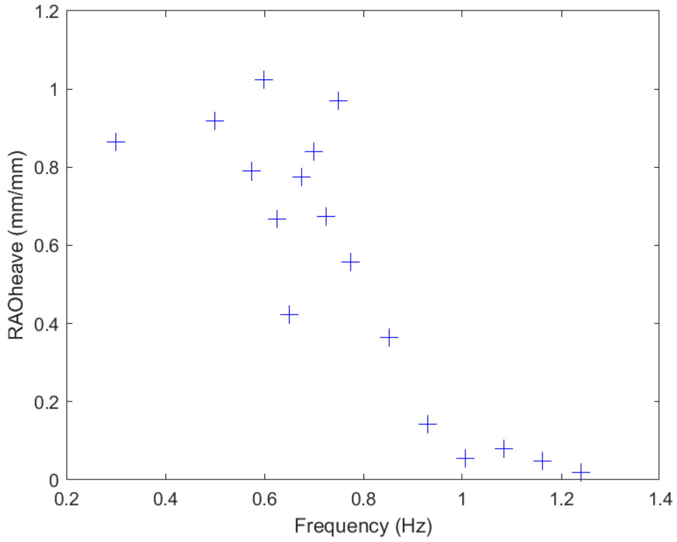

Figure 3.31. Response Amplitude Operator of the Heave motion of the scaled model

The calculated buoy heave motion amplitude response RAO curve is shown in Figure 3.31. It can be seen from the figure that the heave motion is relatively gentle within the frequency range of 0.3 to 1.2 Hertz, and the maximum model RAO is 1.0mm/mm, which is small. From the results, it can be seen that the buoy appears to be relatively wave following between frequencies of 0.3 to 0.5 Hz. Therefore, this buoy form helps reduce the buoy heave motion amplitude.

Similarly, the pitch motion data was processed, and the filtered pitch time series data for test 15 is presented in Figure 3.32.

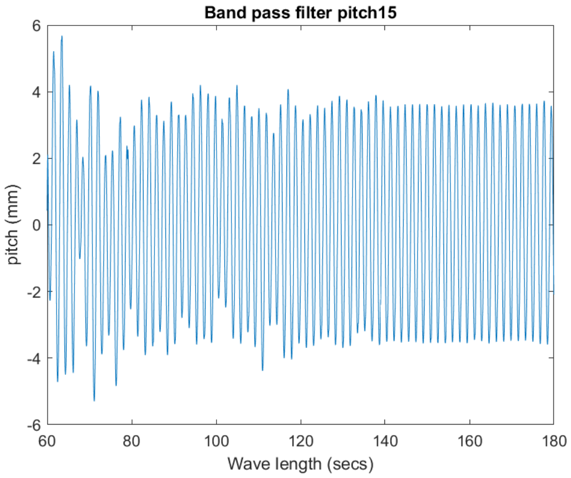

Figure 3.32 –Filtered time series of the pitch from test 15 using a band pass filter

The unfiltered and filtered FFT of the pitch for test 15 was generated and are presented in Figure 3.33 achieving the expected frequency of 0.58Hz.

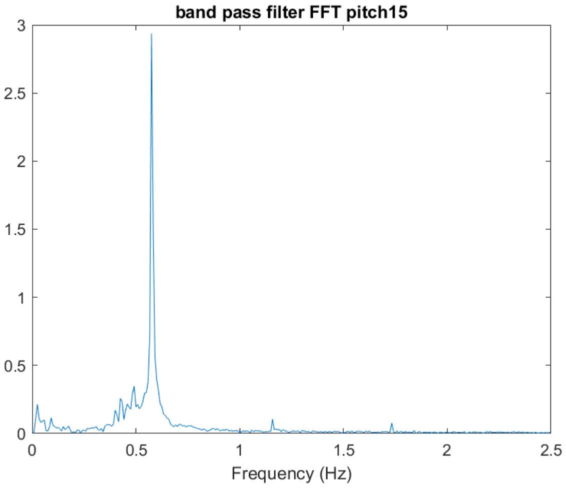

Figure 3.33 –Filtered FFT of the pitch from test 15

The Response Amplitude Operator (RAO) of the pitch was determined by taking the average of the FFT of the pitch amplitude for the same wave period divided by 360 times the average of the wave amplitude for that same period divided by the wave length in centimetres (see Chapter 2). The frequency vector was obtained as before for heave. Figure 3.34 presents the RAO of the pitch of the scaled model.

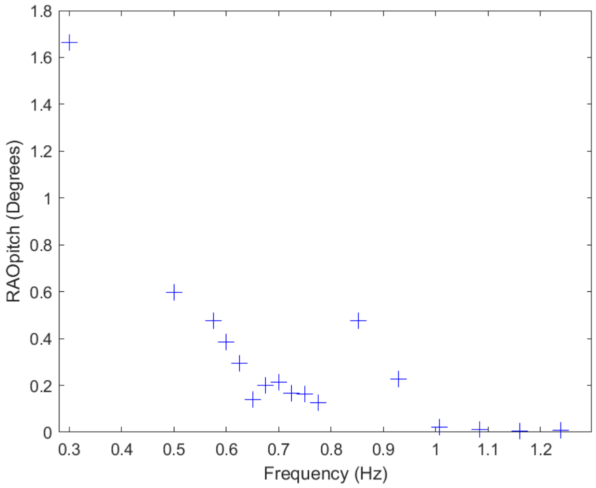

Figure 3.34. Response Amplitude Operator of the Pitch motion of the scaled model

It can be seen from the figure that within the range of main wave energy, the maximum value of buoy pitch is 1.7 deg/m.

Similarly, the surge motion data was processed, and the filtered surge time series data for test 15 is presented in Figure 3.35,

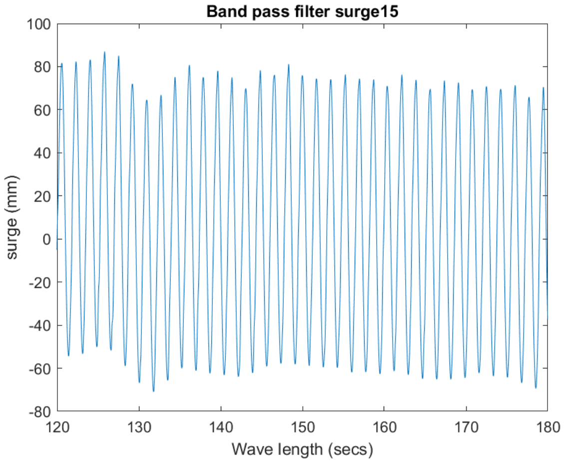

Figure 3.35 – Filtered time series of the surge from test 15 using a band pass filter

The filtered FFT of the surge for test 15 was generated and is presented in Figure 3.36 achieving the expected frequency of 0.58Hz.

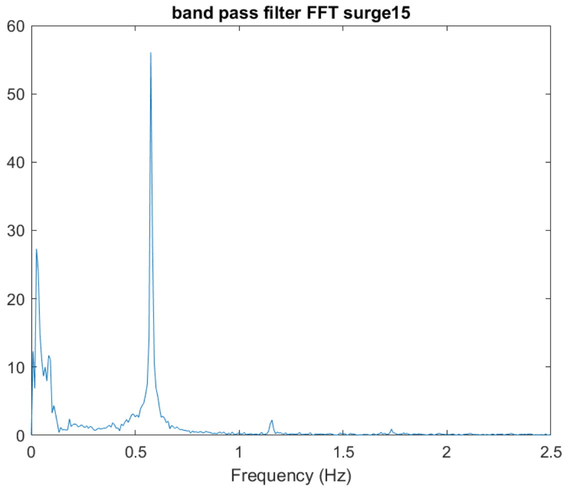

Figure 3.36 – Filtered FFT of the surge from test 15

The FFT of the surge amplitude was thus determined and taking into consideration the suite of testing parameters which included 34 tests, half of which had the same wave period, the RAO of the surge was determined by taking the average of the FFT of the surge amplitude for the same wave period divided by the average of the wave amplitude for that same period (see Chapter 2). The frequency vector was obtained as before. Figure 3.37 presents the RAO of the surge of the scaled model.

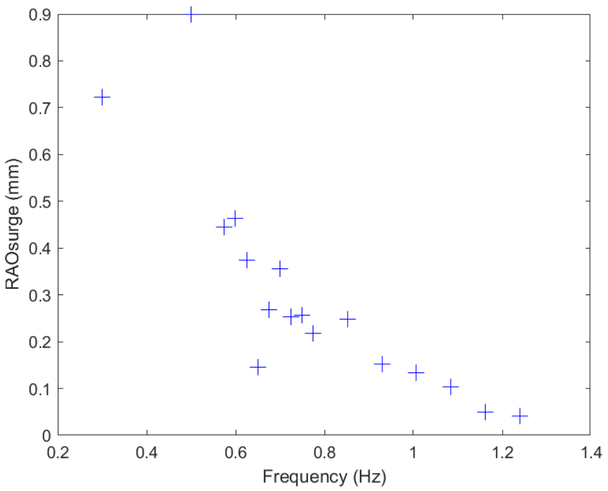

Figure 3.37. Response Amplitude Operator of the Pitch motion of the scaled model

3.3.7 Results from 1/2.4 Scale model testing – Irregular Wave Testing

The scaled model was subjected to a suite of irregular waves testing with *Hs* = 0.150m (0.23m full-scale) and *Tz* ranging from 1.0 to 3.0 seconds (1.55 to 4.65 seconds full-scale) in increments of 0.25 seconds, which also reflected the testing envelop of the wave tank capabilities as provided by LIR technical staff. The tank wave probes recorded data at a sampling rate of 128 hertz, while the pressure probe in the model recorded data at a sampling rate of 32 hertz over a test duration of 1200 seconds. Figure 3.38 presents time series of the tank wave probe recorded data for all 9 tests.

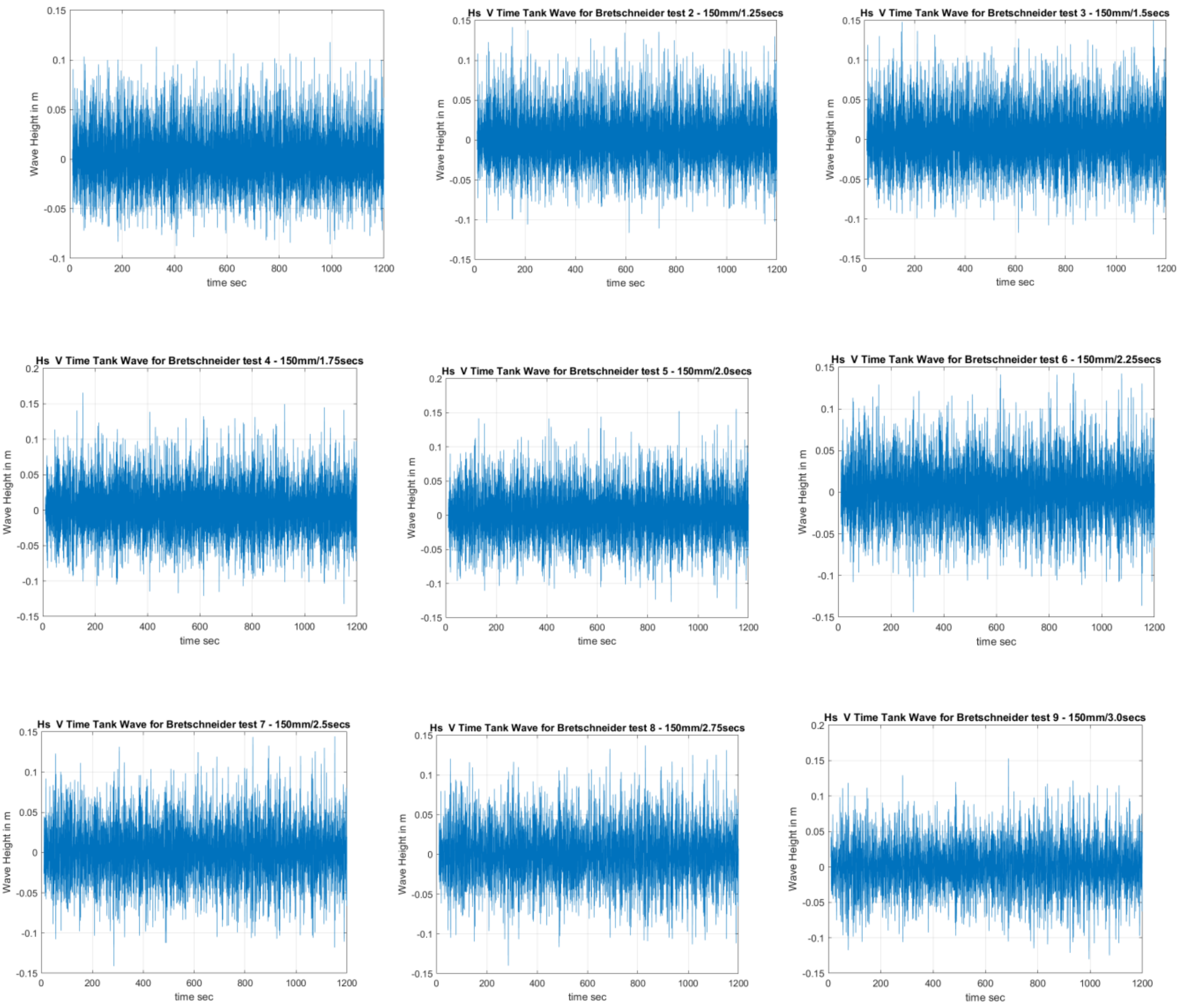

Figure 3.38. Time series of tank wave probe data for tests 1-9 (150mm ranging 1.0-3.0 secs)

While Figure 3.39 presents the time series of the pressure probe within the model moonpool for tests 1-9.

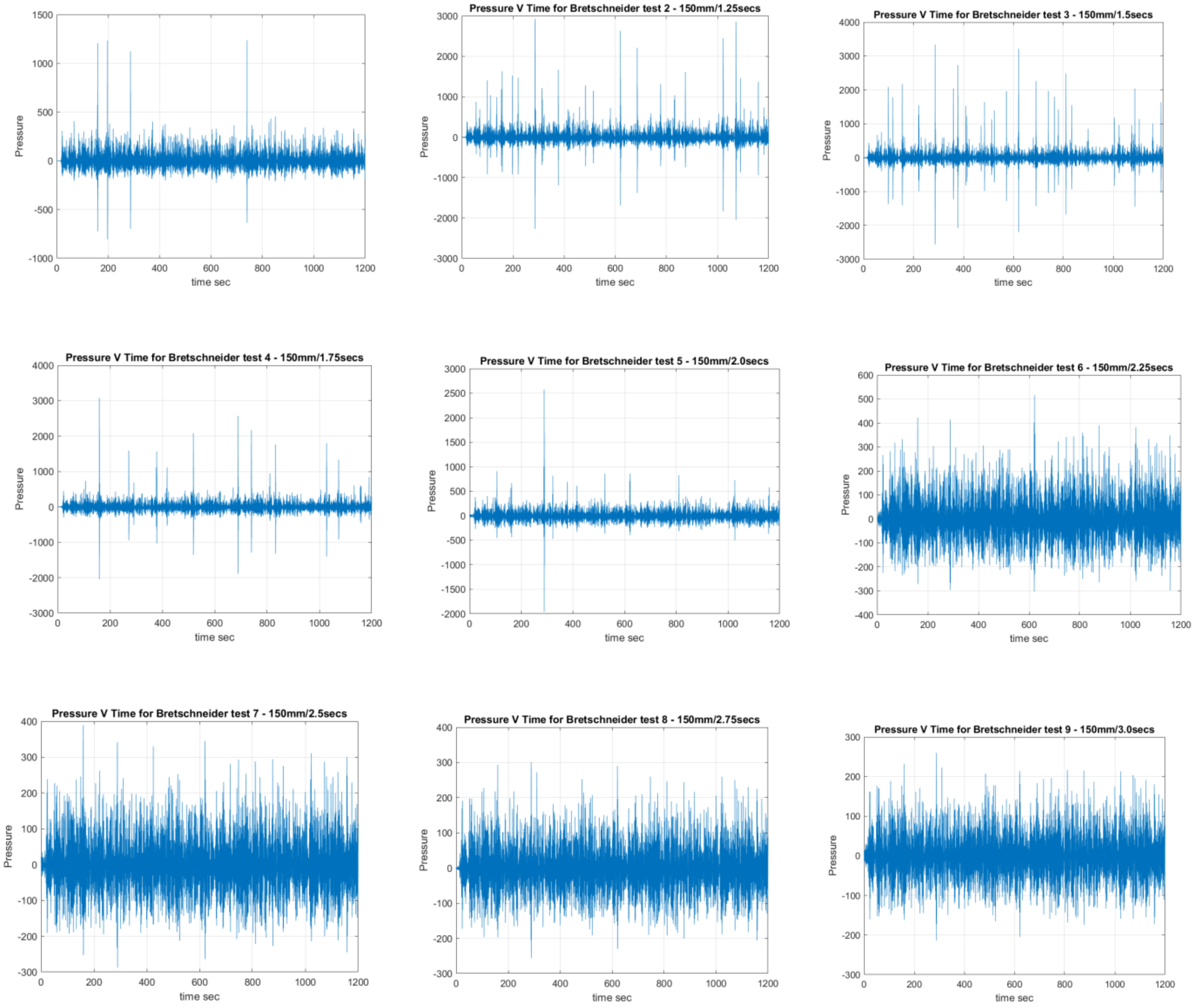
Pressure V Time for Bretschneider test 2 - 150mm/1.25secs

Pressure V Time for Bretschneider test 3 - 150mm/1.5secs

Pressure V Time for Bretschneider test 4 - 150mm/1.75secs

Pressure V Time for Bretschneider test 5 - 150mm/2.0secs

Pressure V Time for Bretschneider test 6 - 150mm/2.25secs

Pressure V Time for Bretschneider test 7 - 150mm/2.5secs

Pressure V Time for Bretschneider test 8 - 150mm/2.75secs

Pressure V Time for Bretschneider test 9 - 150mm/3.0secs

Figure 3.39. Time series of model pressure probe data for tests 1-9 (150mm ranging 1.0-3.0 secs)

The transfer function must now be established between the tank wave probe data and the model pressure probe data as previously set out in Section 3.2.4, proof of concept testing. The Power Density Spectrums of the pressure probe in the model and the wave probe in the tank were generated using the PWelch method.

Figures 3.40 and 3.41 present PWelch Power Density Spectra of the tank wave probe data and the model pressure probe data respectively for test numbers 1 to 9 with Hs = 150mm and Tz values 1.0 seconds and 3.0 seconds.

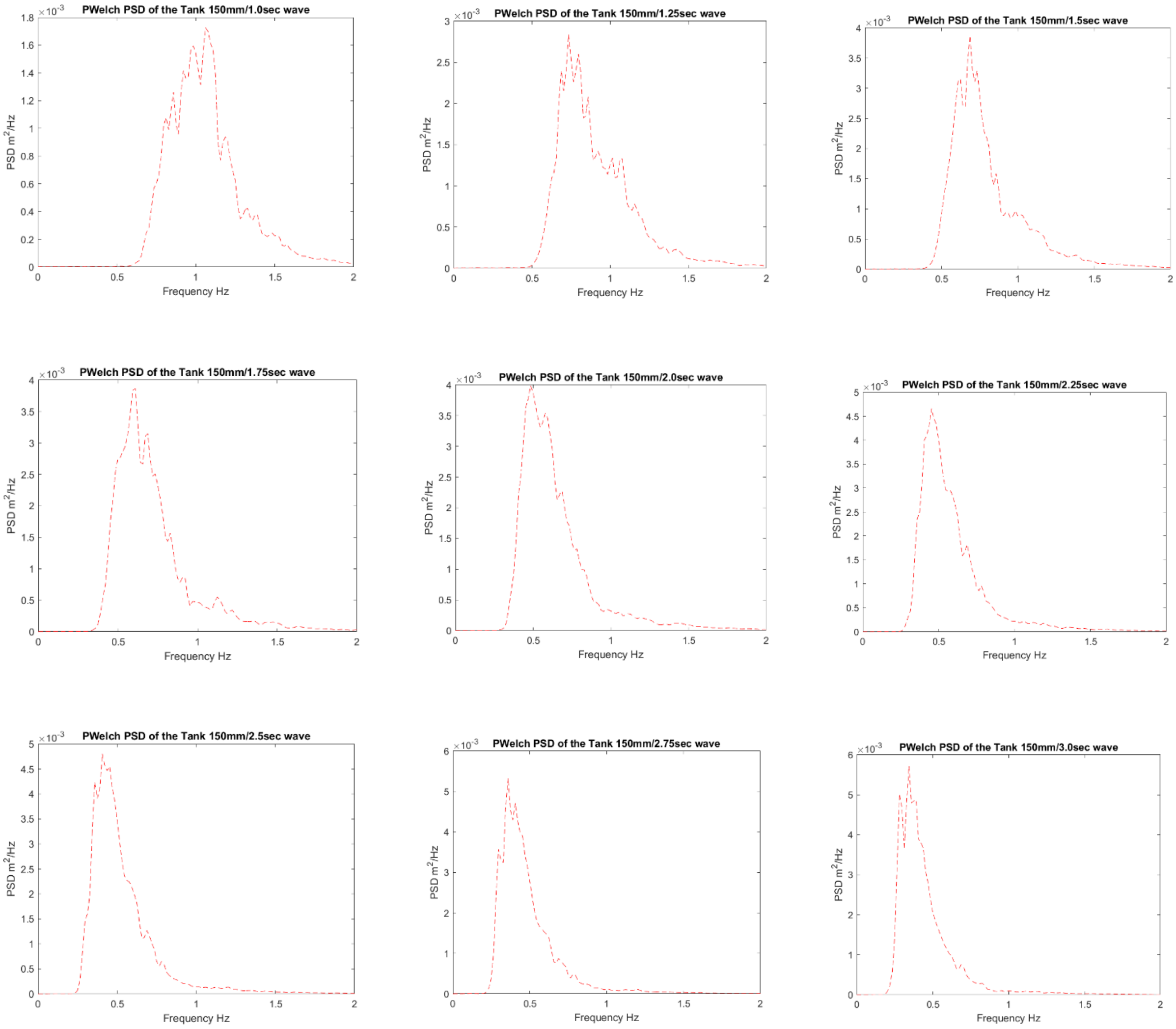

Figure 3.40. PWelch power Density Spectrum of tank wave probe for tests 1-9 (150mm ranging 1.0-3.0 secs)

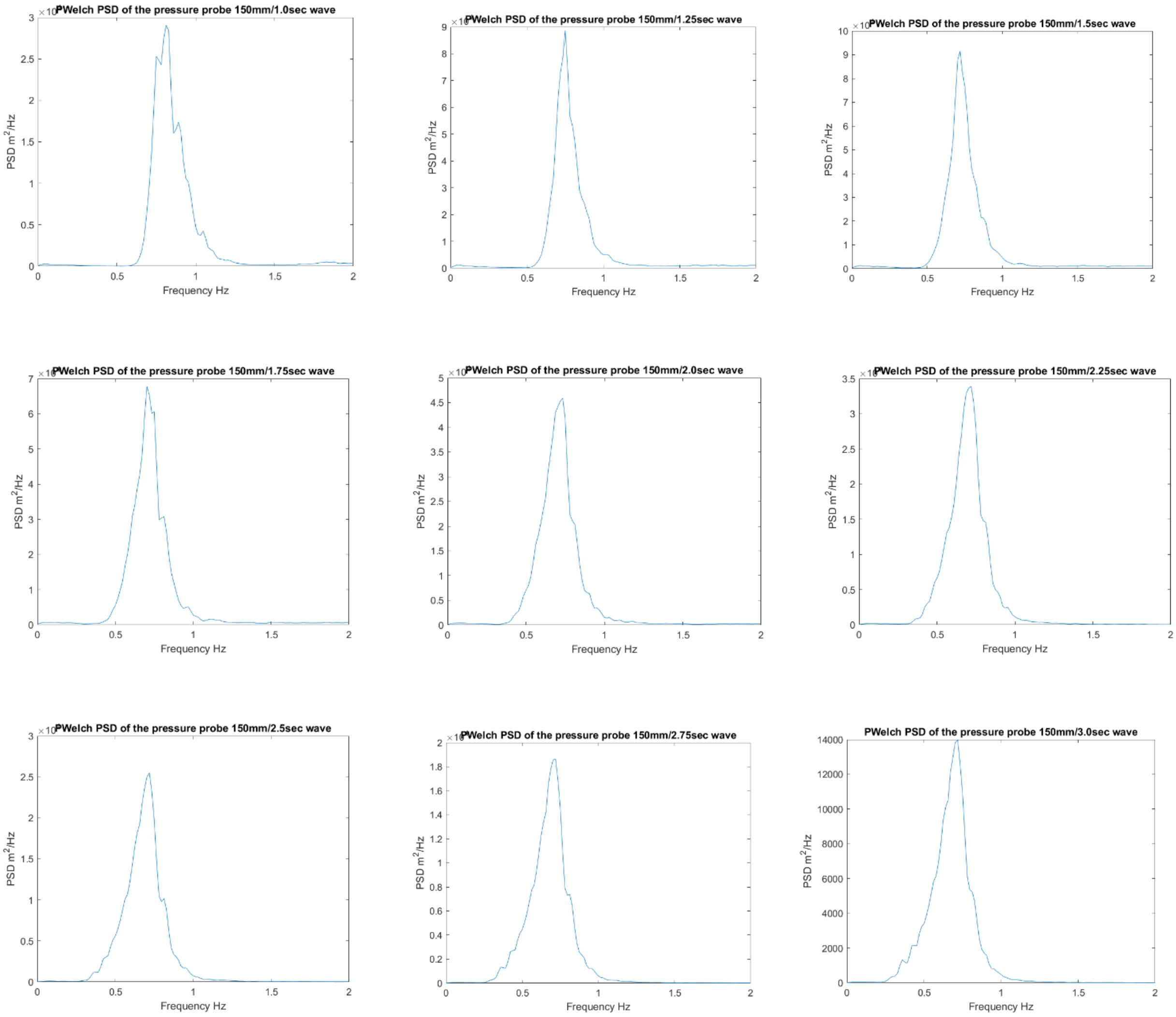

Figure 3.41. PWelch power Density Spectrum of model pressure probe data for tests 1-9 (150mm ranging 1.0-3.0 secs)

A transfer function can then be established between the wave probe data of the tank and the pressure probe data from inside the moonpool of the model buoy with a view to using the transfer function on pressure probe data to generate sea states parameters such has *Hs* and *Tz*.

Figure 3.42 presents the full range of Transfer Functions between the PWelch Power Density Spectra of the model pressure probe data and those of the tank wave probe data for test numbers 1 to 9 with Hs = 150mm and Tz values ranging from 1.0 seconds to 3.0 seconds. There is some noise information present in the lower frequencies of 0 – 0.5 Hz, while there is some high frequency information present from 1Hz upwards which are possibly as a result of some harmonic action with the model moonpool. However, Figure 3.43 focuses on the Transfer Function range specific to the model of 0.5-1.0 Hz. The Transfer Functions for tests 1-9 are essentially the same within the range of interest for the model.

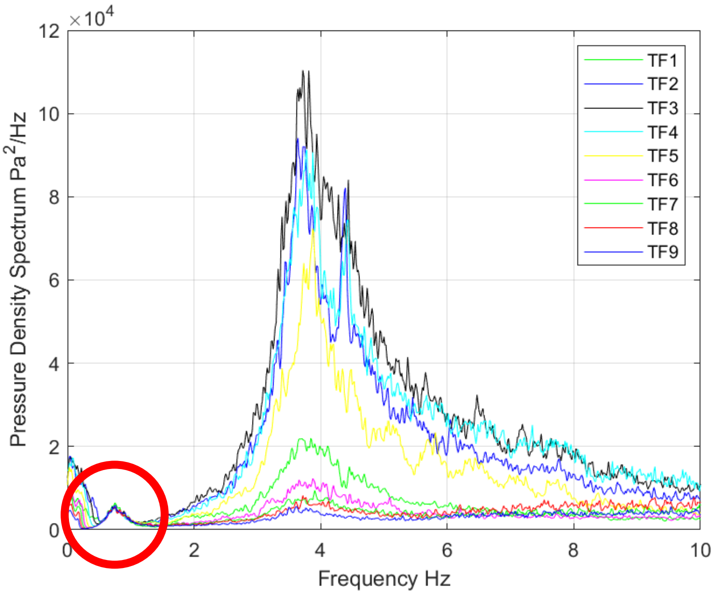

Figure 3.42. Transfer Functions between model pressure probe and tank wave probe data (frequency range of interested circled in red) for tests 1-9 (150mm ranging 1.0-3.0 secs)

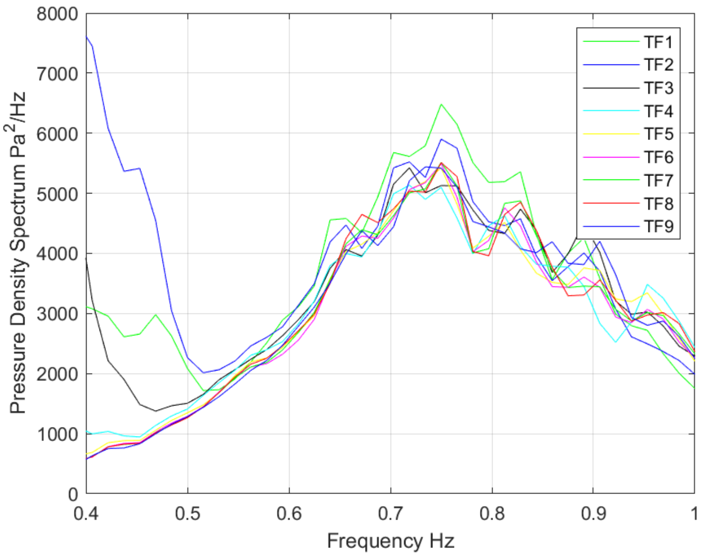

Figure 3.43. Magnified presentation of area of interest circled in red in Figure 3.42 above. Transfer Functions of the model for tests 1-9 (150mm ranging 1.0-3.0 secs)

A Power Density Spectra of recorded and processed pressure data obtained from the volume of air above the water column within the moonpool of the buoy was generated. The spectral moments are then obtained to calculate *Hs* and *Tz.*

A transfer function from one set of the LIR tank wave probe and buoy pressure probe data is applied to another set of pressure data. A Power Density Spectra is then generated.

Figure 3.43a presents an example of a comparison of the LIR tank wave probe spectra against the spectra generated from the pressure data recorded for that particular test subjected to a transfer function from another test of a different frequency and pressure data.

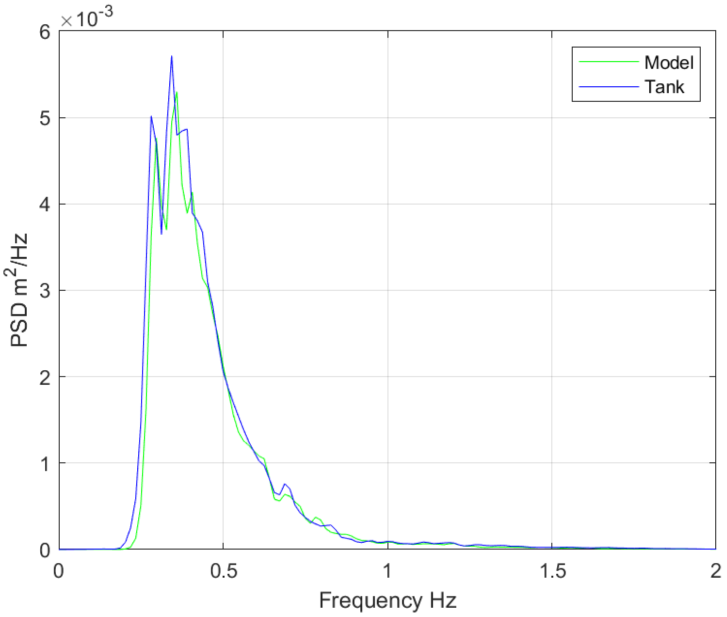

Figure 3.43a. Comparison of Wave probe V Pressure using Transfer Function from Test 8 data for Test 9 – Hs=150mm and Tz=3.0secs

3.3.8 Summary of results from 1/2.4 Scale model testing

The experimental campaign yielded successful outcomes across both the regular and irregular wave test suites conducted in the LIR wave tank facility. The motion response data collected for pitch, heave, and surge were processed using a band-pass filter to remove signal noise and isolate the frequency range of interest. This pre-processing enabled the accurate generation of Response

Amplitude Operator (RAO) plots for each degree of freedom listed above, demonstrating consistent and repeatable behaviour across the tested wave frequencies.

For the irregular wave tests, spectral analysis was applied to both the incident wave data (recorded via the wave tank probe) and the model response (via the internal pressure probe). Power Spectral Density (PSD) estimates were computed using PWelch method, and the resulting transfer functions were derived by taking the ratio of the output (model) PSD to the input (wave) PSD across the frequency spectrum. These transfer functions exhibited physically consistent trends across the tested frequency range and confirmed the dynamic behaviour of the model under irregular wave excitation.

Overall, the successful implementation of signal filtering, spectral estimation, and transfer function derivation validates the integrity of the experimental setup and supports the use of the resulting hydrodynamic response data in subsequent analysis and model validation stages.

3.4 Full-scale buoy and sea trials

Government funding is critical for advancing the development of ocean energy devices. It supports innovation, economic growth, environmental sustainability, energy security, technological progress, global leadership, and the public good. By investing in this area, governments can drive the transition to a more sustainable and resilient energy future.

The Marine Institute has for a number of years operated a successful Research Access Programme. In association with SmartBay Ireland [146], the Marine Institute provides funding to support researchers with access to the SmartBay Marine and Renewable Energy Test Site through a contribution to additional costs associated with deployments via the National Infrastructure Access Programme (NIAP) [147]. The Marine Institute SmartBay NIAP aims to promote synergies between companies and academics in their research and development efforts within the marine sector by facilitating access to the test site and its associated facilities and supports. The facilities available include Cabled Observatory, Databuoys and Acoustic Array.

This research was funded by the Marine Institute of Ireland, National Infrastructure Access Programme, grant numbers NIAP-LS-16010 and NIAP-LS-18002.

3.4.1 Objective

The objective of the experiment is to investigate the relationship between the internal hydrodynamic response of the prototype’s sealed moonpool and the external wave environment, as recorded by a nearby Waverider buoy. Specifically, the experiment seeks to acquire synchronized datasets of moonpool pressure spectra and incident wave spectra, and to process these data in order to derive transfer functions that describe the correspondence between the two. Establishing such transfer functions provides a framework for assessing whether moonpool measurements can be used as a proxy for conventional wave observations. Ultimately, the aim is to evaluate the potential of this approach to estimate key sea state parameters, such as significant wave height (Hs) and zero-crossing period (Tz), thereby offering a novel method for wave characterisation directly from within the device.

3.4.2 Test Site Description

The full-scale sea trials took place at the SmartBay Test Site which is Ireland’s national facility for marine renewable energy development, sensor testing, and real-time environmental monitoring. It is located approximately 1.5 km offshore from the village of Spiddal in Galway Bay, with water depths in the range of 20-25 m [146].

The site covers about 37 hectares, clearly demarcated by four cardinal marks (one at each corner), providing a dedicated area for sea trials of prototype marine devices under controlled but realistic conditions [146].

Central to the SmartBay infrastructure is the cabled underwater observatory installed in August 2015, which is connected back to shore via a subsea fibre-optic / power cable. This observatory provides power and high-bandwidth data communications, supporting a permanent suite of instruments (e.g. CTD, dissolved oxygen sensors, ADCP, turbidity/fluorescence sensors, hydrophone, HD camera) and has ports/interfaces for additional sensor deployment [146].

The Test Site operates under licensing that allows up to three marine renewable energy prototypes to be deployed simultaneously, for periods up to 18 months. It is used for quarter-scale devices or earlier TRL (Technology Readiness Level) stages, novel sensors, and environmental monitoring tools.

Environmental (metocean) data—wave, current, temperature, salinity, etc.—are collected continuously and made available in real time via SmartBay's data portal, supporting both scientific research and device validation [146].

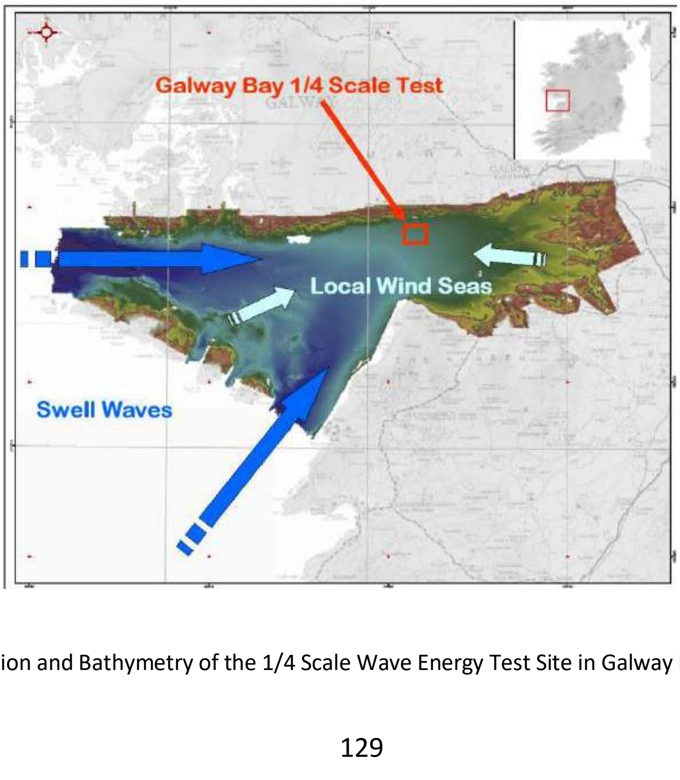

Figure 3.44. Location and Bathymetry of the 1/4 Scale Wave Energy Test Site in Galway Bay , Ireland [478]

Long-term observations at the SmartBay test site in Galway Bay indicate a generally moderate wave and wind climate with clear seasonal structure. Mean significant wave height (*Hs*) is approximately 0.9 m while representative spectral periods (*Tz*) average near 4.9 s, but both parameters increase in the winter months as Atlantic swell and storminess penetrate the bay (monthly peaks commonly observed in the winter half-year and lower values in summer). Wind statistics show a mean near 6 m/s with stronger, more persistent winds during autumn and winter and a predominant wind/wave approach from the south-west sector (around 224°). Although average conditions are moderate, the site occasionally experiences large sea states (recorded single event wave heights up to 8.7 m), and tidal ranges and local currents add further temporal variability; these seasonal and episodic behaviours should be considered when deriving transfer functions from moonpool pressure spectra and when validating sea-state estimates. Seasonally, the site sees greater wave heights and increased period during the winter months; calmer, smaller-wave conditions prevail in summer. Winds tend to follow a similar seasonal pattern, with stronger, more persistent winds during the colder half of the year. Weather extremes (storms, high winds) are infrequent but play a key role in defining the upper end of the wave height distribution [146]. Figure 3.45 presents annual wave and wind data specific to the test site.

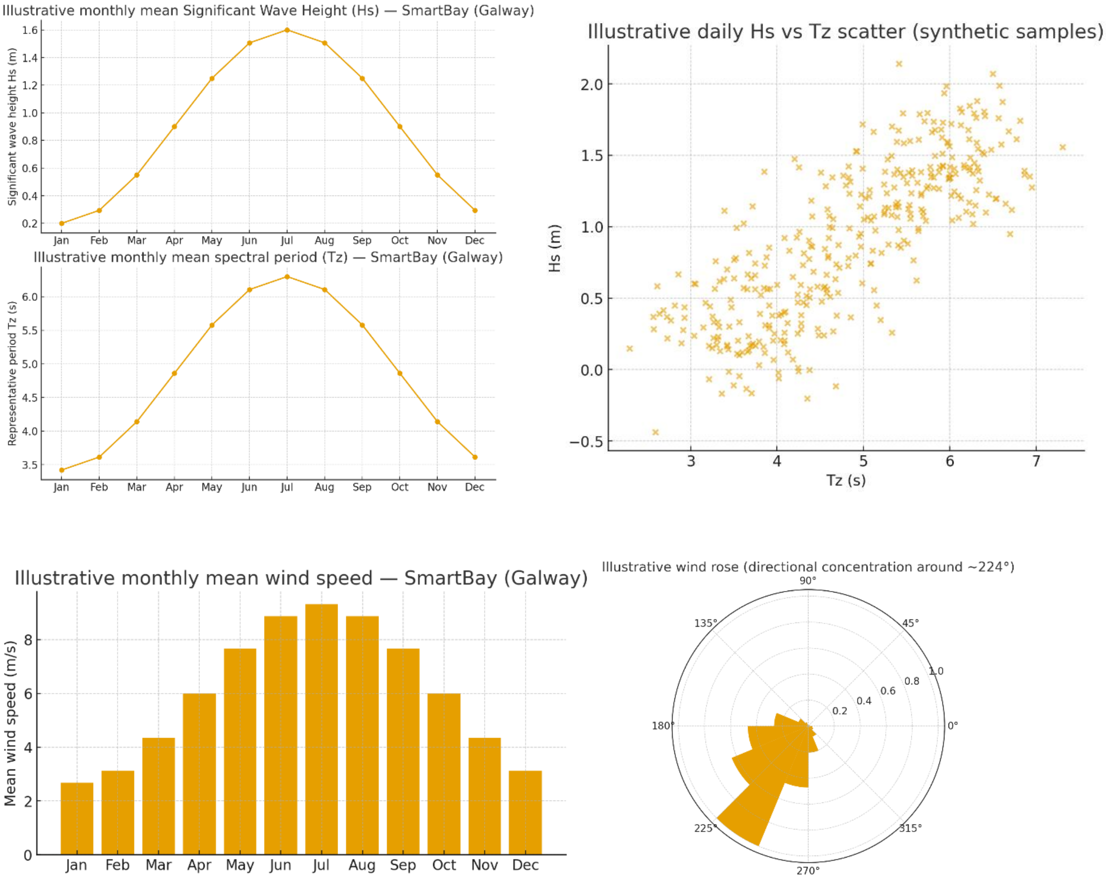

Figure 3.45. Annual wave and wind climate observations at Test Site in Galway Bay, Ireland [146]

3.4.3 Prototype Device Description

Conventional wave regime measurement buoys operate by ‘following’ the free surface of the ocean at a deployment site. On-board accelerometers measure the acceleration of the buoy, and the displacement of the buoy is determined from the double integration of the accelerometer data. Hence, the time series of the motion of the buoy can be obtained, and by assuming the motion of the buoy matches the free surface elevation, the wave spectrum as the deployment site may be estimated. Unlike wave-following buoys, the operational principle of the prototype device, the ‘WASP’ depends its interaction with the ocean waves in order to pressurise and depressurise the air above the water column as discussed in Chapter 2. For reasons discussed herein, the air chamber above the water column in the prototype WASP was sealed during sea trials. The time series of the pressure in the air volume above the water column is measured and recorded. The prototype samples data at a rate of 8 Hz which is greater than the Nyquist limit. The Nyquist limit refers to the maximum frequency that can be accurately sampled without aliasing, which is twice the highest frequency present in a signal. This concept is part of the Nyquist-Shannon sampling theorem, which states that to reconstruct a signal accurately from its samples, the sampling rate must be at least twice the signal's highest frequency (also known as the Nyquist rate). If the signal is sampled at a lower rate, aliasing can occur, where higher frequencies fold back into lower ones, distorting the signal. The power density spectrum of the pressure time series is computed, and may be used to estimate statistical parameters of the wave spectrum at a deployment site, once the relationship between the power density spectrum of the air pressure signal for the WASP and a corresponding wave spectrum which generates the air pressure time series, is known. The relationship may be established through a calibration process where the buoy is deployed at a site where the wave regime is independently measured for a period of time sufficient to capture multiple sea-states.

The buoy must fulfil a number of roles. It must contain a moonpool. It must provide a platform to house the sensing and data acquisition equipment, and the communication equipment. It must also provide a platform where power generation and storage may be placed to power the electronic equipment. Further, in order to generate large pressure variations which may be reliably measured and used to estimate sea states, either the buoy itself, or the water column it houses, must be significantly excited by the frequencies contained within the wave spectrum encountered at the deployment location. Within the confines of the funding budget, it was not possible to construct a customised buoy. However, a number of existing companies manufacture buoys which meet a number of the required attributes. One such company is JFC Manufacturing Co Ltd, who produce a range of buoys in a number of sizes including the Seagull buoy [266].

One 3-meter diameter Seagull was rented for the duration of the NIAP funded WASP project, and an exploded schematic of the Seagull, provided by the manufacturer, is shown in Figure 3.47. The Seagull provides a centrally located moonpool, and modular daymarks, which may be added to the top of the buoy to provide secure and water-tight housing for the electronics and battery storage required. Further, the daymarks provide a location where power generation and communication antennae may be located. In the current configuration of the WASP prototype, two daymarks are added to the base buoy so that the electronics, power generation system and communication antennae are located well above the sea level in still water conditions.

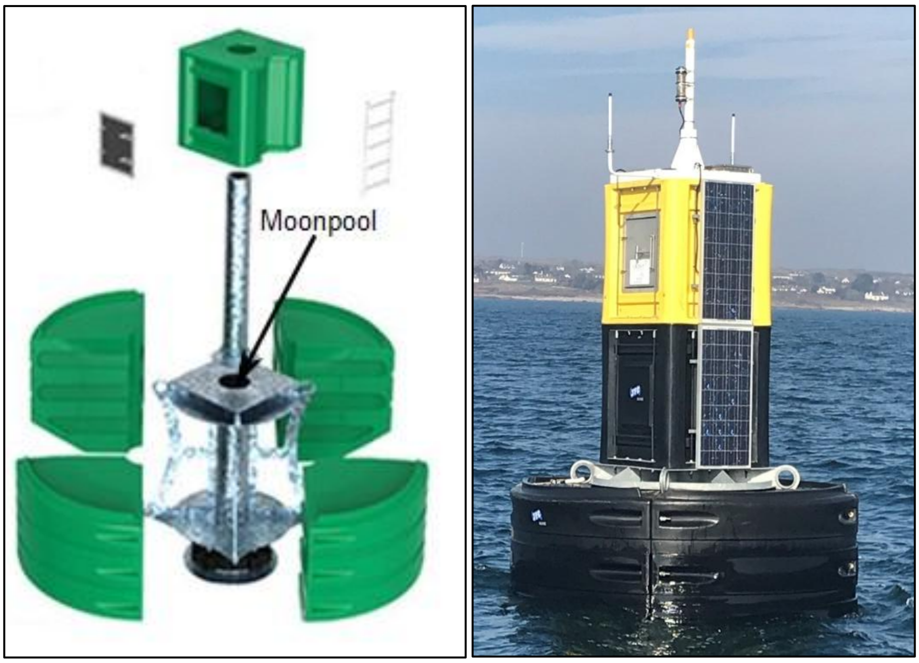

Figure. 3.47. Exploded schematic of the Seagull buoy, [266] and assembled WASP full-scale prototype device

However, the Seagull has not been designed to optimise pressure generation within the moonpool. As a result, the prototype WASP required a power generation system that is not based on wave energy. It is planned that future iterations of the WASP will include wave power generation, will be designed so that the wave power absorbed by the buoy is significant (e.g. through changes in buoy geometry and water column length). However, supplementary power generation (e.g. through solar panels or marine wind turbines) may still be required. A further consequence of the current design of the Seagull is that the pressures generated in the air above the water column in the prototype WASP are relatively low. Initially, it was intended that a plate containing an orifice be placed over the top of the opening of the moonpool. The planned purpose of the orifice was to simulate the effect on the air flow into, and out of, the moonpool chamber that would be had if a bi-directional turbine, such as a bi-directional impulse turbine, were installed. However, in order to ensure the maximum variation in the pressure in the air above the water column, the plate ultimately installed contained only a small breather hole of 2 mm in diameter. The 2 mm hole allows water to gradually fill the water column over approximately 10 minutes during deployment. When in operation, the air pressure above the water column of the WASP will vary above and below atmospheric pressure in the time scale of a number of seconds, thus airflow through the 2 mm hole will be minimal, and the air pressure in the chamber will be close to the maximum possible, ensuring the best possible measurements for the prototype.

In order to calculate the ballast required to ensure the stability of the prototype WASP, and set the draft of the prototype WASP as desired, calculations were performed independently at DkIT, and the manufacturers of the Seagull buoy, with agreement. A custom spreadsheet was developed for this purpose and is available at, [479]. SmartBay provided information regarding the local tidal currents at the test site. Wind data for the site is readily available. The calculations considered the maximum wind drag on the daymarks, the maximum thrust acting on the wind turbine, and the maximum tidal drag acting on the buoy. Following standard practice [480], the masses of the battery pack were considered as acting at one point. Likewise, the mass of the turbine is considered a point mass. The mass of the total daymarks and associated components was found using a weighbridge, and hence the mass of the various fittings could be found (notably the custom– made frame for the wind turbine) and located as appropriate. With appropriate ballast, the meta-centric height of the buoy was estimated, and stability under extreme conditions confirmed. A maximum heel angle of 36-degrees is estimated in a worse-case scenario [479].

3.4.4 Instrumentation and deployment

Sensing Equipment: In order to measure the pressure in the air above the water column, the prototype WASP used two PD-23, piezo-resistive, differential pressure sensors, manufactured by Keller [481]. The full scale ranges of the two sensors are 200 mBar and 1 Bar respectively. The 200 mBar range was selected to ensure precision during typical operation, while the 1 Bar sensor is intended to capture extreme pressure events. The accuracy of the sensors is 0.2% of the full scale value. The output signal from both sensors is an analog voltage between 0-10 V. To measure the ambient temperature of the electronic enclosure a LM35 sensor is used. The data acquisition system (DAQ) monitors and records the voltage of the battery at a sampling rate of 8 Hz. As the DAQs maximum input range is 10 V, it could not accept the 24 Vdc supplied by the batteries directly because of the initial incorporation of the wind turbine as a power source. So, a simple voltage divider in conjunction with a buffer is implemented which provides a voltage between 0-5 V which is proportional to the real battery level, see Figures 3.48.

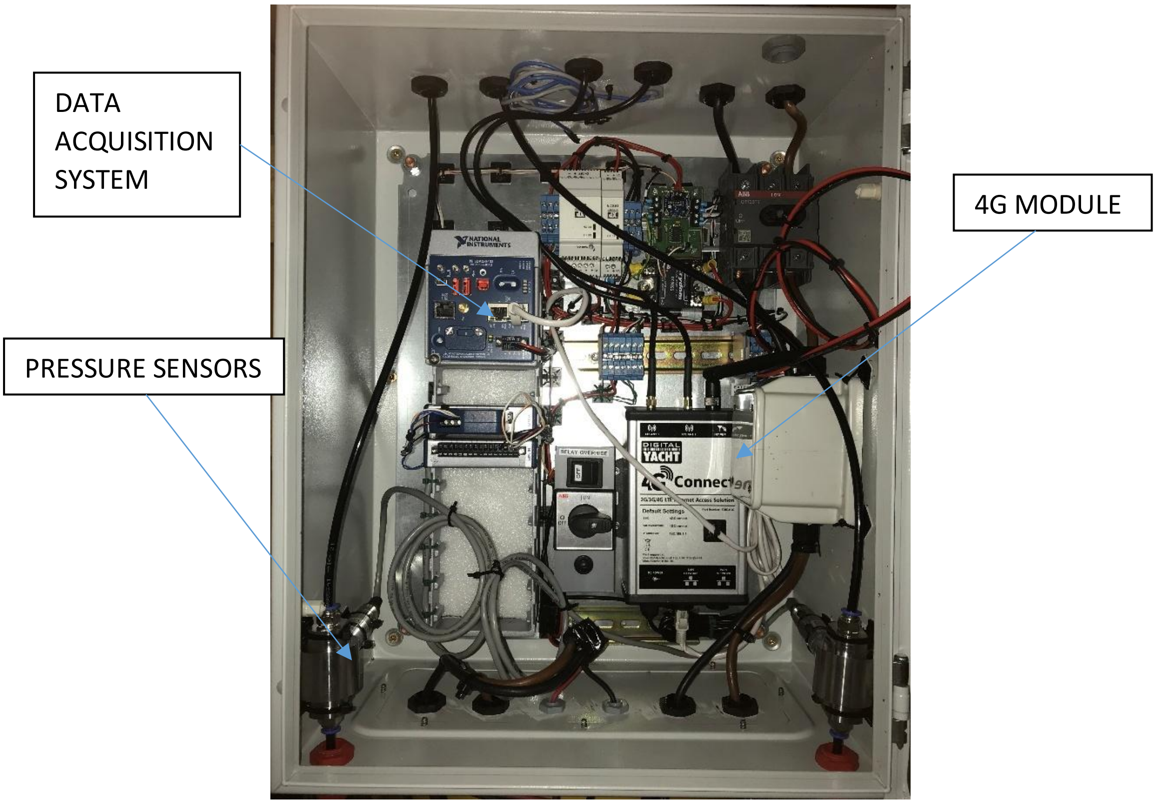

Figure. 3.48. Photograph of assembled WASP electronics inside IP66 cabinet contained in upper daymark

Data Recording Equipment: The data is collected and recorded using a National Instruments NI9133 Compact DAQ (cDAQ) controller [482], powered by a 15 Vdc regulator, which in turn takes power from the battery bank. The controller has an Integrated 1.33 Ghz multi-core processor with 8 slots of modular I/O. These slots can be used with C Series modules, including analog and digital I/O. The cDAQ also has 16 GB of non-volatile storage and a removable SD card slot, allowing data logging of large amounts of data. It runs both Windows Embedded Standard 7 and NI Linux Real-Time OS. For robustness, the NI Linux Real-Time OS was used in this deployment. The cDAQ allows further connectivity using USB and Ethernet. The prototype uses two C series modules, NI-9201 8 channel analog input and a NI-9485 solid state relay.

Data Acquisition Coding: The code used to control the NI cDAQ essentially comprises two separate while loops. The first loop stores the measured data from the sensors, which is sampled at a rate of 8 Hz, to a National Instruments TDMS file. Each file represents 24 hours of data. At midnight each day, the file is closed and a new file created. The file is saved to a SD card installed on the cDAQ. A second loop compresses the TDMS data file created the previous day. Each TDMS file is approximately 360 MB in size, and is compressed to approximately 5MB. Once a second, compressed, version of the data file created the previous day is generated, the original TDMS file is deleted to save memory space on the SD card. The file is then uploaded to the Microsoft Azure cloud service. The default upload time is set to 08:00 AM. To accommodate this upload, a 4G Module is switched on by a Solid State Relay (SSD) before the file is uploaded. The 4G module is switched off once the upload is complete to reduce power consumption. At this time, the 4G module is switched on 30 minutes prior to the chosen upload time, and switches of 30 minutes after the upload time. To ensure complete uploading of the compress TDMS file, uploading the compressed data file requires approximately 5 minutes.

Data Transmission: While the data measured and recorded by the WASP device is stored on-board the cDAQ using an SD card, the proposed test location makes regular physical retrieval of the data impractical. Two methods for transmission of data from the buoy to shore were explored. The first method investigated proposed using the on-site Wi-Fi system. SmartBay maintain a number of Mobilis DB8000 buoys which host a variety of communications protocols to shore, including Wi-Fi. However, this system did not have the capacity required. A second Wi-Fi option was to use a 5.2 GHz link from Spiddal to the test site. However, the 5.2 GHz link is very directional, and not suitable for buoys with a single point mooring such as is to be used for the prototype WASP. Following discussions with SmartBay, the prototype WASP will instead use 4G communications to connect to cloud computing services. Conveniently, National Instruments software includes a number of toolkits which allow connection to commercial cloud computing services. These services include Amazon Web Services (AWS), IBM Bluemix, PTC ThingWorx and Microsoft Azure. Each service has strengths and weakness. Initially, it was intended that the Amazon Web Services be used given previous experience with this service, and the initial implementation (which was preformed using a Windows-based desktop computer) proved robust. However, after some time developing the WASP software to use the AWS toolkit, a compatibility issue between LabVIEW’s real-time Linux operating system and AWS arose. Following an assessment of a number of other cloud computing services, the Microsoft Azure service was chosen for use with the prototype WASP. Azure Blob storage is Microsoft’s object storage solution for the cloud. Blob storage is optimized for storing large amounts of unstructured data, such as text or binary data. All access to data objects in Azure Storage happens through a storage account. All blobs reside within a container, which is similar to a folder. Once uploaded to the service, data may then be downloaded to any computer with an internet connection. No compatibility issues were found to exist between the Azure service and the real-time Linux operating system. Implementation of data transfer from the WASP to the Microsoft Azure service has been extensively tested, and proven to be robust. The upload of the data was achieved via a 4G (LTE) module from Digital Yacht [483]. Following advice from Smartbay, the 4G module was equipped with a Vodafone SIM card as Vodfone coverage was best in this area at time of the testing. Dual high gain antennas are used to transmit data to allow for fast, long range capability. The 4G module also allows remote connection to the cDAQ via Wi-fi which would allow for reprogramming of the cDAQ, if necessary. All DAQ, communications and sensing equipment is mounted in an IP66-rated cabinet, which in turn is located within the top daymark behind a water-tight access hatch. Figure 3.49 illustrates the layout of the electronic, DAQ and sensors installed in the IP66 cabinet, and Figure 3.50 is a schematic of the electronics.

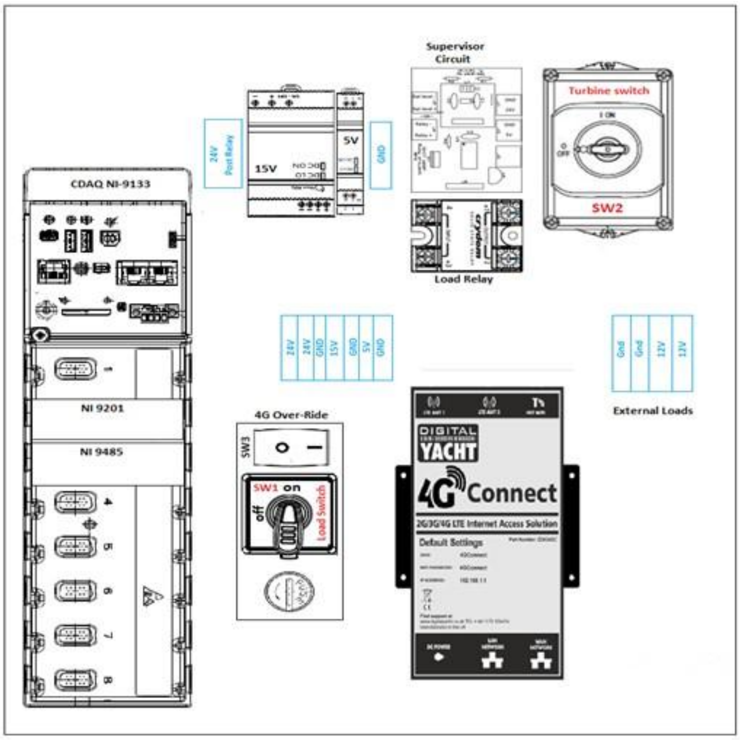

Figure. 3.49. Layout of the electronics board housed with an IP66 cabinet.

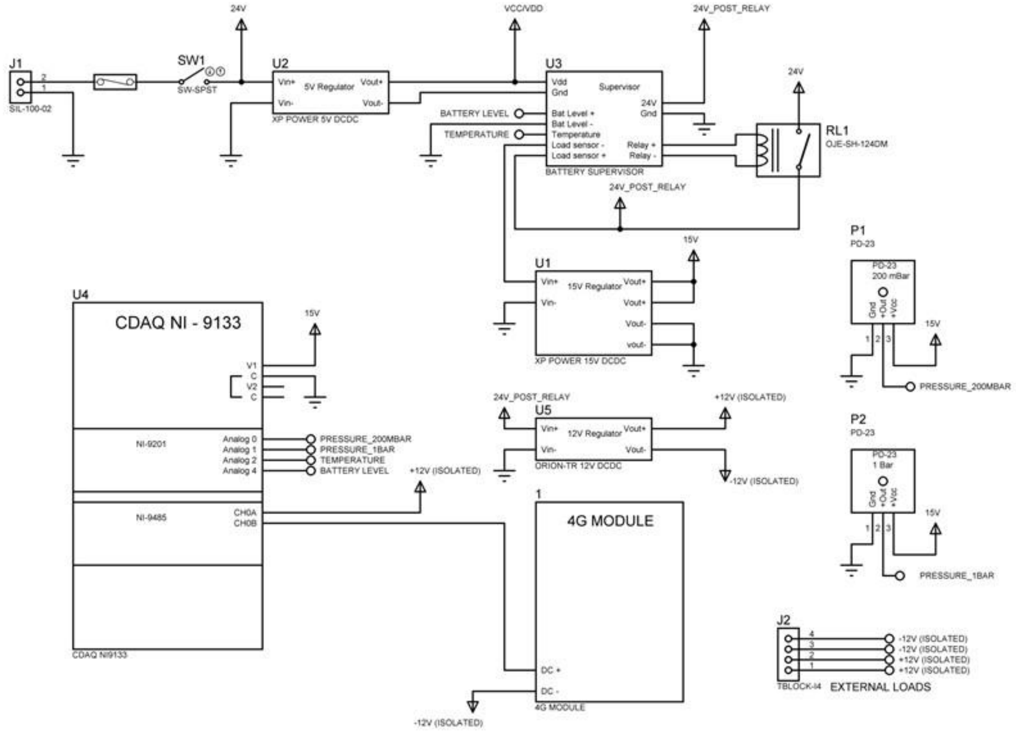

Figure. 3.50. Schematic of the electronics board.

On-board power storage for the WASP is provided by six 12Vdc, 80Ah sealed lead acid batteries, manufactured by Haze Batteries. The batteries are located in bays located in integrated compartments positioned at the bottom of the upper daymark. The bank of batteries is connected in a series-parallel configuration so as to produce 240Ah of storage operating at 24Vdc. The system voltage level was chosen so as to match the output voltage of a Zephyr Airdolphin 1 KW wind turbine, which was to be used to recharge the batteries. The DAQ and pressure sensors are powered by a 15Vdv regulator (U1 in Figure 3.50) and the battery supervisor circuit is powered from the 5V regulator (U5 in Figure 3.50). The 4G module is powered by an isolated 12Vdc regulator to prevent noise in the more sensitive components, an issue which arose during early testing of the system. A GPS tracker, which Smartbay require be installed on all equipment to be deployed at the test site, is also attached to the isolated 12Vdc regulator to isolate any noise it may generate from the rest of the system. The GPS tracker transmits its location once every hour. The power consumption of the electronics in the prototype varies depending on the time of day. The main electronics package draws a current of approximately 500mA for 23 hours a day, which increases to 600mA for 1 hour each day while the 4G module is powered on and transmitting data. Additionally, the GPS tracker draws a continuous 70mA in standby, a current which increases to 1.9A during a transmission period of approximately 60 seconds once each hour. When the batteries are fully charged the prototype should provide data up to 8 days approximately. Prior to deployment, the batteries in the WASP were fully charged from mains electricity.

Power Generation: When fully charged, the batteries in the prototype WASP were expected to provide a minimum of 8 days of continuous operation. Thus, some means of recharging the batteries while the WASP is under test offshore is required. While it is intended that the final WASP device be wave powered, the current prototype is intended to investigate the relationship between the pressure in an OWC chamber and the wave regime, and hence is not wave powered. A number of potential charging options were investigated, and it was decided to install a small wind turbine atop of the daymarks to recharge the batteries during the current phase of testing. To save costs, a Zephyr Airdolphin turbine, which was available at no cost to the project, was selected. A charge controller is incorporated in the nacelle of the Airdolphin turbine, and the output from the turbine is 24 Vdc. The turbine output voltage dictated the voltage used throughout the system. A custom-made frame to mount the turbine to the daymark was constructed, which also provided a convenient location to mount the communication antennas. The turbine is rated at 1 KW with a rated wind speed of 12 m/s. It has a rotor diameter a rotor diameter is 1.8 metres. One of its main selling points is its low wind speed start-up at 2.5 ms. It does this by using it's so called "power assist function". If there is no wind the turbine uses power from the batteries to self-rotate for 10 s every minute. This also protects the turbine from icing. In normal circumstances this feature may be seen as an advantage but in a solely battery powered offshore project it would be more of a hindrance. This meant that some energy would be lost to the turbine. Another issue with this is if one or more blades where damaged by potential wave strikes, battery charging would cease but the damaged blades would still spin every minute. This would quickly drain the battery and almost certainly over discharge them. During initial testing, it was found that the turbine was capable of generating far more power than required to operate the prototype WASP in typical wind conditions. However, following transportation of the top section of the prototype WASP to Galway docks for final assemble, benign site testing and deployment, an issue arose with the wind turbine, and a new means of charging the batteries was required. It was decided to install six 80 W solar panels, manufactured by BP Solar, and these were used to maintain battery charge throughout the deployment [484].

The BP 380 is an advanced 80W photovoltaic module that uses cells with antireflective SiN coating. This solar module is as equally suited to grid connect applications, such as residential systems or installations on commercial roofs and traditional photovoltaic applications such as Telecommunications and rural electrification. The BP 380 offers a superior price-performance relationship due to its reliability, white polyester back sheet and 36 advanced polycrystalline cells connected in series. The 3 series modules have a 12V nominal output and are primarily designed for battery charging applications such as off-grid homes, telecommunications & telemetry sites, navigation equipment, motorhomes & caravans, sailboats and other sites where low power is needed.

Supervisory Circuit: When deployed, the data acquisition and communication systems are powered from the 24 Vdc battery bank. The cDAQ has no low power mode, and in the event that power consumption exceeds power generation over along period of time, a possibility existed that the rechargeable batteries may be over–discharged, resulting in damage to the batteries. In order to prevent over–discharge and protect the batteries, a microcontroller–based supervisory circuit is used. A schematic of the supervisory circuit is illustrated in Figure 3.51. The battery voltage is inputted to a voltage divider via resistors R1 and R2 to produce a voltage between 0-5V so the voltage can be accepted by the DAQ analog input and the microcontroller via buffers (U2). The supervisory circuit continuously monitors the voltage level of the battery bank via the 0-5 V output from the voltage divider. If the voltage level drops below a predetermined value, the supervisory circuit switches off all loads, except the load to the supervisor circuit itself. The shut-off voltage level has been set to a battery bank voltage of 21.5 V (equivalent to 3.5 V from the voltage divider), and if this threshold is reached, a load relay is switched off to power down the system. The supervisory circuit itself then enters a low–power state, in which the circuit may remain active for a number of months before using sufficient power to over discharge the batteries. However, the cDAQ Controller is essentially a computer, and, like any modern computer, it is recommended that the cDAQ be allowed to shutdown in accordance with normal operations, rather than be abruptly powered off. If the battery level reaches a critical point of discharge, the cDAQ programmatically shuts itself down safely. The current draw of the 15 Vdc load, which includes the cDAQ, is approximately 450 mA under normal operating conditions, and approximately 150 mA when the cDAQ is shutdown. The microcontroller (U3 in Figure 3.51) uses a current sensor INA169 (U1 in Figure 3.51) to monitor the current draw to the 15 Vdc load to decide when to switch off the load. The microcontroller reads the current sensor via an analog-to-digital converter every minute. If the reading is below 200 mA for 10 minutes, the cDAQ is presumed shutdown, and the 15 Vdc load is switched off via a MOSFET transistor and a solid state relay, (Q1 and RL1 in Figure 3.51 respectively). Due to the high output from the wind turbine, significantly higher power usage in typical wind conditions, the microcontroller was initially programmed to switch the system back on after 24 hours. It was considered likely that, after 24 hours, the battery bank would likely have reached an acceptable high level of charge to resume normal operations. If it was not the case that the battery bank charge level had recovered, and hence the voltage was above the shutdown threshold, the cDAQ would once again switch off, the microcontroller would switch off the 15 Vdc load after 10 minutes, and start the 24 hour timer again. This cycle would repeat until the battery charge was sufficient to resume normal operations. However, prior to deployment, the Airdolphin wind turbine was replaced with six 80 W solar panels. While the panels should provide sufficient power to maintain operation of the WASP, the recharging rate is significantly lower than that should the Airdolphin turbine continued to operate. A concern arose that sufficient charge may accrue over the course of 24 hours to allow the battery pack voltage exceed the 21.5 V threshold, while not allowing enough charge to accrue to run the DAQ and communication system for 24 hours. This raises the possibility that the system may power up, run for a sufficient length of time to cause the battery pack voltage to drop below the threshold, and hence shutting down the system for a further 24 hours, without any data transfer taking place. Such a low-charge cycle could happen repeatedly, effectively preventing any data transmission from occurring. In order to prevent this scenario, the time between shutdown and automatic restart was increased to 5 days. While this could have resulted in a large gap in the data, it would have ensured that the battery pack is well charged between shutdown and restart, eliminating the danger of the WASP entering a low-charge cycle. Ultimately however, at no point during the testing did the battery voltage drop below the threshold to cause a shutdown, and there was no loss of data during the sea trials.

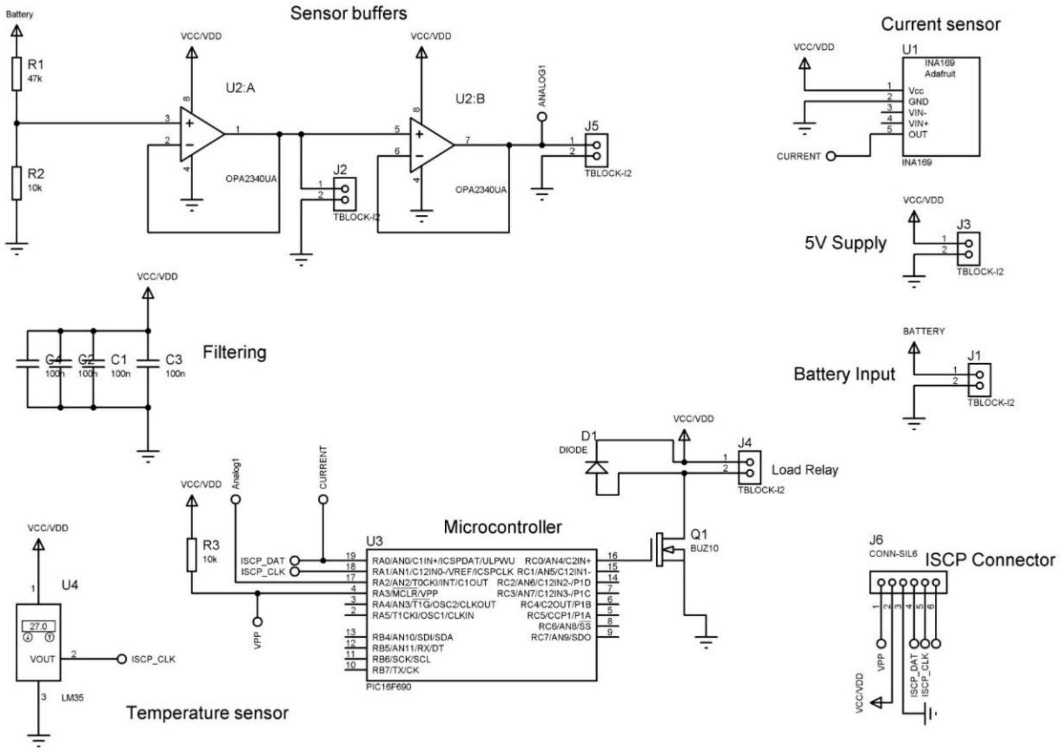

Figure. 3.51. Schematic of the supervisor circuit

Dry Testing: Various sub-components of the WASP were tested at DkIT prior to final assembly and transportation to the Galway docks for deployment to the SmartBay test site. The data acquisition and communication systems were benched–tested to ensure data was logged and uploaded to the Microsoft Azure cloud service, and that the in–house code performed as expected. The system was tested for a week, and data logging and communication system performed successfully. However, a number of issues were identified and rectified during this time.

Figure. 3.52 The prototype WASP prior to testing at a benign site (Galway Marina)

The first issue which arose was that noise created by the 4G module was interfering with output voltages from the pressure sensor during the hour each day when the 4G module was active. This issue arose as when initially installed, the 4G module shared a common ground with the rest of the system, including the pressure sensors. The issue was remedied by adding a 12 Vdc regulator to power the 4G module any other potentially interfering load, such as a transponder. The 12 Vdc regulator is kept isolated from the rest of the electronics. A second issue identified was one of memory space on the SD Card. Data is stored locally on-board the WASP as well as being uploaded to the cloud. The raw data is first recorded in the native, National Instrument, TDMS format. The storage required for one day of data in this format is approximately 365 MB. In order to reduce transmission time and prevent the SD card from running out of memory, the TDMS files are compressed. The compressed files require approximately 5 MB of storage, and it is these files that are uploaded to the cloud service. Once one day of data is compressed into a single file, the unzipped data is deleted to free up space on the SD card.

Once the changes outlined above were incorporated, the complete electronics/ DAQ/communication and power system (including wind turbine) were installed in the daymarks. Two daymarks are used, and all components described herein were installed in the upper of the two so as to reduce the likelihood of submergence, and to prevent breaking waves damaging wind turbine blades. The assembly was mounted on a trailer, and tested outside for a number of weeks, during which time the wind turbine charged the batteries successfully, and data was recorded and uploaded to the cloud without issue. The daymarks were then transported to Galway for final assembly and subsequent deployment.

Benign testing: Once the daymarks and associated components were transported to Galway port, the final assembly of the WASP could take place. A custom-made plate was installed to seal the top of the moonpool in the buoy. Two 1/4 BSP connectors, which had been installed in the plate, allow gas lines to connect between the air chamber of the moonpool and the pressure sensors, so that the pressure in the air chamber may be measured and recorded. The daymarks were hoisted onto the Seagull buoy, and the gas lines connected. The prototype was then transported to the Galway marina, where a crane lifted the WASP into the water. The device as switched on, and over a number of days, the prototype acted as expected, with data files uploading at the appointed time each day. However, a major issue arose. The tail of the wind turbine had damaged during transport, and it proved impossible to source a replacement. A new tail was designed and was fabricated by the deployment contractors. Once installed, the replacement tail functioned as hoped, but it was then discovered that the internal turbine control circuit was no longer functioning correctly, and it is assumed this circuit was damaged during transport. While a number of alternative turbines were investigated, ultimately, six 80 W solar PV panels, with suitable power regulators, were installed on the WASP, providing a total maximum power of 240 W at 24 Vdc. For safety reasons, the prototype was removed from the marina, and the daymarks were split from the buoy while the turbine was removed and the solar panels installed. Once the solar panels were installed, the system was tested in the dry for a week, before the daymarks and buoy were reassembled. The protoype WASP was then returned to the marina, where it was successfully tested, in a sheltered location, for a number of days. The likely reduced power generation by the solar panels when compared to the wind turbine increases the likelihood of the supervisory circuit switching to a low power mode, and introduces the possibility of the low-charge cycle. As described, the waiting period between low-charge shutdown conditions and subsequent re-powering up of the system was increased after benign site testing. However, an advantage of the solar panels is that the risk of possible blade damage due to high waves is eliminated. Another advantage is that the maximum heel angle of the buoy will be reduced, as the trust from the turbine will no longer contribute over-turning moments. One final possible advantage of the solar panels when compared to a wind turbine is the reduction in moving parts potentially increasing long-term reliability of the system.

Figure. 3.53. Solar panels installed on the daymarks following removal of the wind turbine

Deployment: Upon completion of benign testing, the buoy was deployed at the test site on the 27th February 2019. The SmartBay Test Site is located off the north shore of Galway Bay, 2.4 km southeast of the village of Spiddal as shown in Figure 3.44. The WASP was moored at the test site using single point mooring. Single Point Mooring (SPM) of a data buoy is a crucial method for deploying buoys in marine environments. This technique ensures the buoy remains in a fixed location while allowing it to pivot around the mooring point. A strong, durable line or chain connects the buoy to the anchor. It is designed to withstand the forces from currents, waves, and wind. The anchor is placed on the seabed and provides a fixed point to which the buoy is tethered. Anchors can be dead-weights, piles, or other specialized anchors suitable for the seabed type. In the case of the WASP, it was a large concrete weight. A swivel is often used in the mooring line to allow the buoy to rotate freely around the mooring point, preventing the mooring line from becoming twisted. The installation process involves deploying the anchor, connecting the mooring line, and attaching the buoy as shown in Figure 3.54. Specialised vessels and equipment are often required. Regular inspections and maintenance are necessary to ensure the integrity of the mooring system and the buoy’s proper functioning.

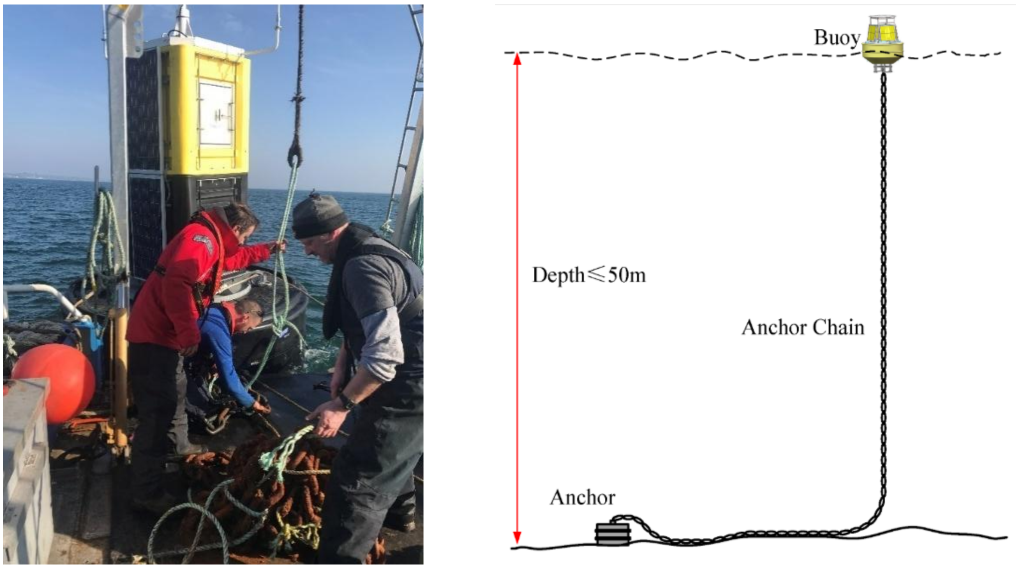

Figure. 3.54. Connecting WASP mooring during deployment

Maintaining a fixed position is critical for accurate data collection and consistency over time, especially for long-term monitoring projects. Fixed-position data buoys provide precise geospatial data, which is essential for mapping and tracking marine conditions. The ability of the buoy to pivot around the mooring point allows it to align with the direction of currents and waves, reducing stress on the buoy and mooring system. SPM systems are designed to be durable and reliable, capable of withstanding harsh marine environments over extended periods.

Performance: Monitoring the performance of a wave measuring device during testing is essential to ensure data accuracy, device reliability, operational safety, and cost efficiency. It supports the overall objectives of the testing process, whether they are scientific, commercial, or regulatory in nature. With regard to the performance of the WASP during deployment, the acquisition of data was seamless from the system. Physically, the buoy proved quite robust with some minor signs of compression to the float. JFC Ltd have subsequently amended their design to eliminate this in future.

Conditions experienced during deployment: During the deployment, the WASP was subject to a wide range of weather and sea state conditions and subsequently recorded data from the most severe winter storms of that year, including storms Gareth and Hannah, both of which brought gusts in excess of 130km/h. Figure 3.55 illustrates a heat map of significant wave height (Hs) and zero-crossing period (Tz) at the test site gathered by the nearby Marine Institute Waverider device, and represents the wave climate encountered by the WASP prototype during the deployment period (March–June 2019). The most frequently occurring conditions correspond to a Hs of approximately 0.53 m and a Tz of around 2.45 s.

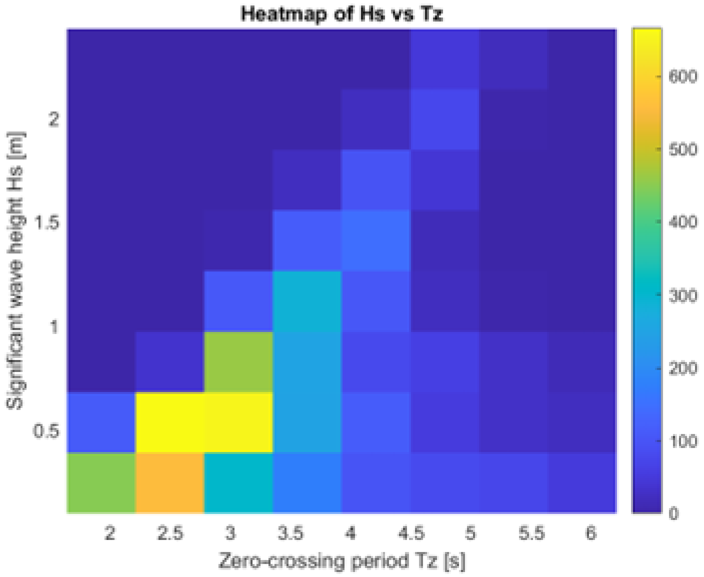

Figure. 3.55. Heat Map presenting range of Hs and Tz Waverider values during deployment [266].

3.4.5 Raw Data Presentation

The WASP TDMS (Technical Data Management Streaming) files, each containing 24 hours of data were converted to .txt files for use in MATLAB. With a sampling frequency of 8Hz, this equated to some 691,200 samples per day, over 120 days of the deployment, approximately 82,944,000 samples were generated.

The deployment resulted in the acquisition of several months of data, including pressure signal readings from two Keller piezo-resistive, differential pressure sensors. Of these sensors, one covers low range at high sensitivity +/-200 millibar. The other at +/-1 bar for normal operation precision and extreme pressure events.

The data included pressure signals from the sealed chamber above the water column in the OWC, air temperature within the day marker and battery voltage. Figure 3.56 shows the variation in battery voltage over the course a typical 24 hour period corresponding to 21st April 2019. In Figure 3.57, the internal temperature of the day marker is shown over the same 24 hour window. While battery and temperature monitoring may not be required for wave estimation, the information is useful to monitor the WASP's performance.

Note the 24 hour period from which data is illustrated in Figure 3.56 was a relatively overcast day, and as the cloud covering cleared, an increase in battery voltage can be seen. Similarly, in Figure 3.57, an increase in the temperature as the day progressed can be seen. These results were typical of those obtained throughout the deployment. There were no issues with regard to temperature throughout the duration of deployment. Furthermore, the battery voltage never dropped below the threshold at which the supervisory circuit would have initiated a system shutdown to prevent over charge of the batteries.

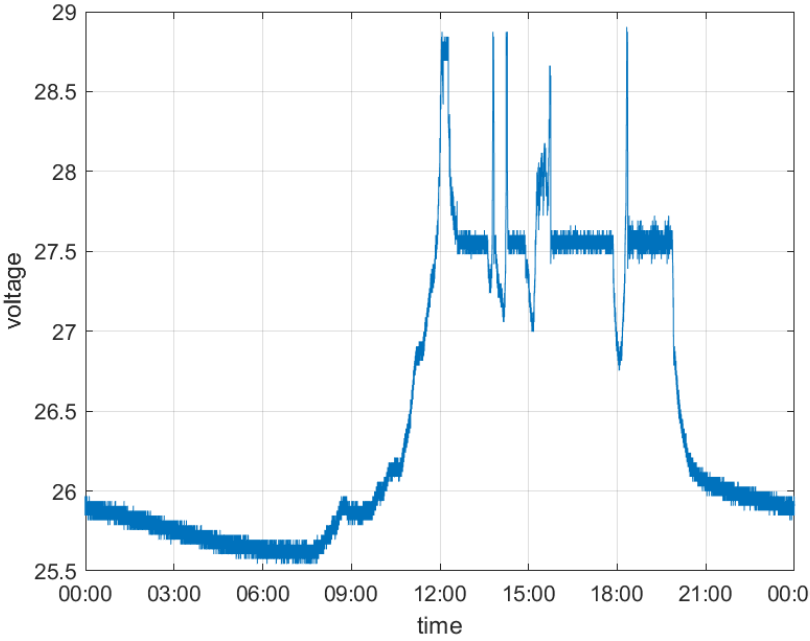

Figure 3.56. Variation in battery voltage over the complete 24 hour period of the 21st of April 2019

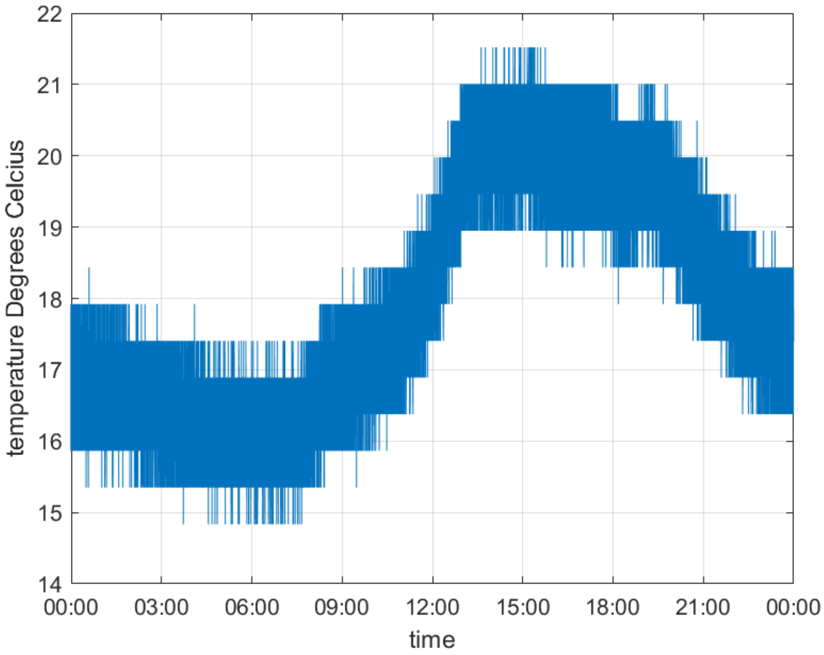

Figure 3.57. The air temperature in the day mark electronics cabinet over the complete 24 hour period of 21st April 2019

An issue arose with the sampling of data during the deployment. While the data was nominally sampled at 8 Hz, the time interval between samples was obtained using a built-in counter, which was not 100% accurate. This meant that some seconds would contain 7 samples, while others 8. A last minute change to power management required a change to the code running the DAQ. As a result of this change, inadvertently, the time at which samples were recorded only contained the second at which the sample was taken, and not the decimal fraction of that second. This was only discovered after deployment. As the time to the nearest millisecond at which each sample was taken was not available, regardless of the number of samples per second, for each second the samples were uniformly distributed across that second. In the instances where only seven sample were available, these were resampled to eight uniformly spaced samples using a 6th order polynomial. These time stamps were then used to analyse the data as described herein. In order to assess the impact of this issue, for a number of datasets, the samples were randomly spaced using a Gaussian distribution within a second before being resampled again using a 6th order polynomial. The statistical properties of the datasets remained consistent regardless of whether the samples were distributed uniformly or randomly over a second.

Raw Pressure Results: A prior technical report documented the deployment of the WASP and pressure data acquisition process. The report provided the unprocessed data acquired during the full-scale sea trials and presents the complete set of pressure measurements from the 200mmbar sensor, organised into 24-hour graphical representations, spanning the entire 123-day testing period [485]. Figure 3.58 presents the 24 hour pressure readings for both storms Gareth and Hannah on the 12th March and 26th May 2019 respectively generating pressure in the volume of air above the water column in the moonpool in excess of 40mmbar with *Hs* ranging from 1.04-2.38m and 0.69-2.4m respectively. While the Tz values for these two events range from 3.65-5.29 secs and 3.37-5.22 secs respectively.

and Tz ranging from . While Figures 3.59, 3.60 and 3.61 present random pressure data samples showing a range in pressure variation during specific 24-hour periods generating pressure in the volume of air above the water column in the moonpool ranging from 5 to 25mmbar with *Hs* values ranging from 0.27-1.45m and *Tz* values ranging from 2.55-3.12 secs.

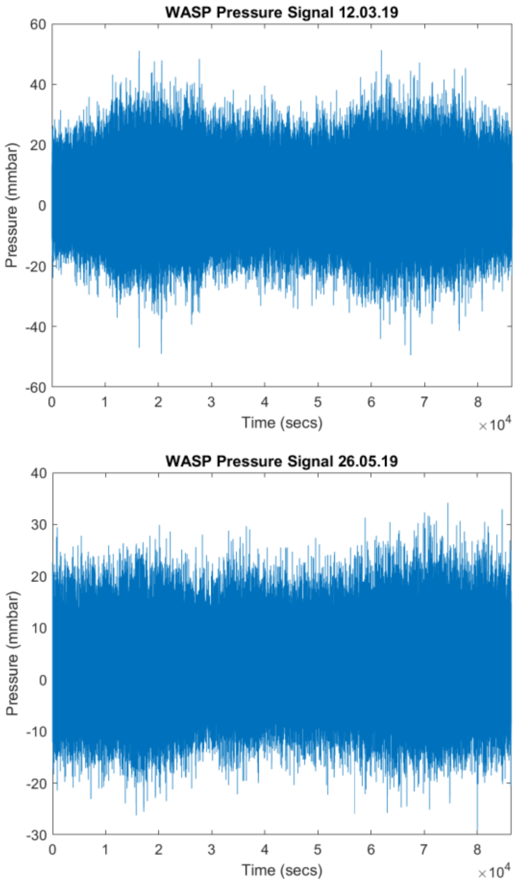

Figure 3.58. 24 hours WASP pressure readings for 12th March and 26th May 2019

Storm Gareth 20-40mmbar, 1.04-2.38 *Hs* and 3.65-5.29 *Tz*. Storm Hannah 15-32mmbar, 0.69-2.4 *Hs* and 3.37-5.22 *Tz*

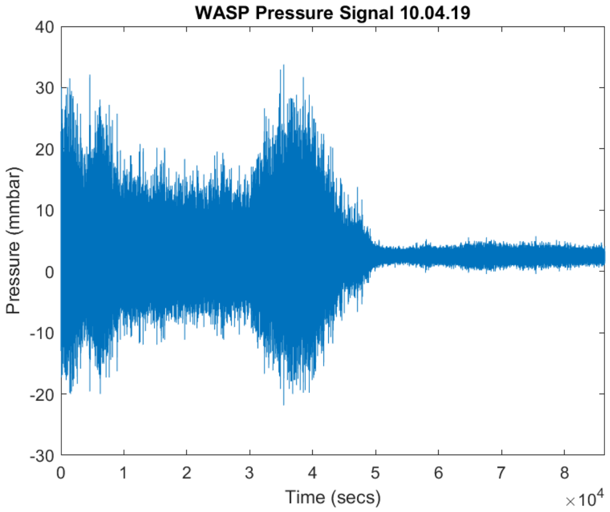

Figure 3.59. 24 hours WASP pressure readings for 10th April 2019 - 5-32mmbar, 0.27-0.87m *Hs* and 2.55-6.0 secs *Tz*

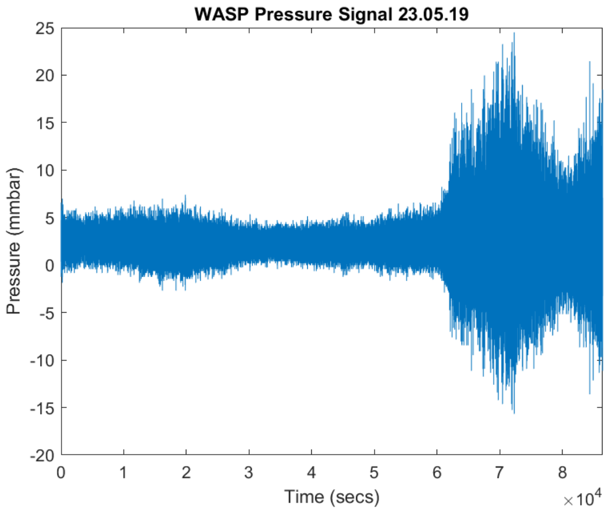

Figure 3.60. 24 hours WASP pressure readings for 23rd May 2019 - 5-24mmbar, 0.38-01.12m *Hs* and 2.47-4.39 secs *Tz*

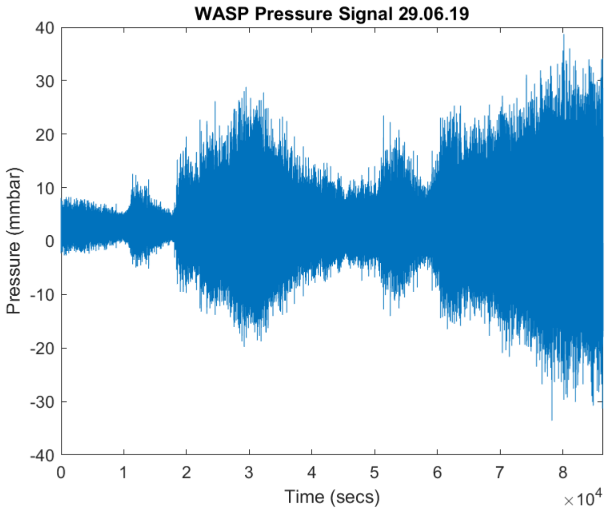

Figure 3.61. 24 hours WASP pressure readings for 29th June 2019 - 8-39mmbar, 0.69-2.4m *Hs* and 3.37-5.22 secs *Tz*

3.4.6 Summary of full-scale device testing

During the deployment, the WASP was subject to a wide range of weather and sea state conditions and subsequently recorded data from the most severe winter storms of that year, including storms Gareth and Hannah, both of which brought gusts in excess of 130km/h. With regard to the performance of the WASP during deployment, the acquisition of data was seamless from the system. Physically, the buoy proved quite robust with some minor signs of compression to the float. JFC Ltd have subsequently amended their design to eliminate this in future.

Figure 3.62 compares the RAO pressure of the 1/2.4 Gannet scaled model recorded during regular wave testing at the LIR National Ocean Test Facility to the Full-Scale Proto-type Seagull (WASP) Transfer Function calculated for the month of March 2019 at Galway Bay Test Site. The generation of the WASP's transfer function is discussed in greater detail in Chapter 4. The graph below indicates a strong similarity between the behaviour of the scaled Gannet model during testing at the LIR facility and that of the full-scale prototype WASP during deployment at the Galway Bay test site. The two datasets exhibit a high correlation coefficient of 0.9544, confirming that the overall trends and dominant features of the responses are closely aligned. The comparison yields an RMS error of 15.3, which, relative to the peak y-axis value of approximately 80, corresponds to an error of about 19%. Analysis shows that most of this discrepancy is driven by the higher frequency region above approximately 0.55 Hz, where divergence between the scaled model and the full-scale response becomes more pronounced. When the comparison is restricted to the 0.2–0.55 Hz frequency range, the RMS error reduces to 7.97, equivalent to about 10%, indicating a much closer agreement in the frequency band that captures the primary system dynamics.

Correlation	0.9544
RMS error (0.2-0.55 Hertz)	7.97
RMS error (0.2 – 0.8 hertz)	15.3

Table 3.5 – Correlation and RMS error values between Scaled model testing and Full-scale prototype

Overall, the results demonstrate that the concept scaled model of the ocean buoy provides a reliable representation of the behaviour of the full-scale buoy. The model's response closely mirrors the real-world dynamics of the larger system, including its interaction with wave motion, stability characteristics, and buoyancy behaviour. Key measurements and observations from the scaled trials correlate strongly with those from the full-scale deployment, confirming the effectiveness of the design approach and validating the scaled model as a useful predictive tool for assessing the operational performance of the buoy in real ocean conditions.

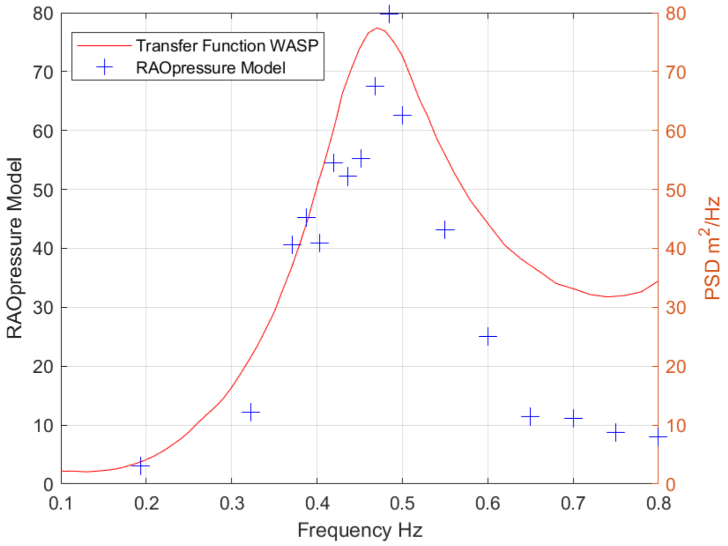

Figure 3.62. Response Amplitude Operator of the Pressure of the scaled model compared to March 2019 Transfer Function

3.5 Methodology Chapter Summary

The experimental programme at the DKIT facility demonstrated that wave spectra acting on the WASP buoy can be recovered from pressure signals using frequency-domain transfer functions. Accuracy of spectral estimation was found to decline when energy content in the 0.25–0.4 Hz range was low, leading to anomalous peaks, though this issue is mitigated when sufficient energy is present in that range. Testing at the LIR wave tank validated the robustness of data processing methods, including filtering, spectral generation, and transfer function derivation, which consistently captured the buoy’s dynamic behaviour under both regular and irregular wave excitation. Full-scale deployment at the Galway Bay test site further confirmed the buoy’s durability and reliability in extreme sea states, while comparison between scaled model tests and full-scale measurements showed strong agreement. Together, these results validate the experimental setup, confirm the predictive value of the scaled model, and demonstrate the WASP’s capacity to perform effectively under real-world ocean conditions.

Chapter 4 –Full-Scale Testing Results and Analysis

4.0 Introduction

This chapter presents the analysis of experimental data obtained from measurements of the internal air pressure within the sealed moonpool above the oscillating water column (OWC) in the full-scale device during sea-trials at Galway Bay Test Facility. The aim of this analysis is to establish a quantitative relationship between the measured pressure spectra and the incident wave spectra in the form of a transfer function between the two.

The analysis of this data begins with necessary pre-processing of the raw pressure measurements. This is followed by the determination of the transfer functions between the WASP pressure spectra and waverider incident wave spectra within a range of frequencies for which the pressure measurements may be validly compared to the incident wave spectrum.

4.1 Data processing

Waverider data was acquired in half hour samples. The time series data was not available to the author. The Marine Institute waverider data time stamp is given as an unsigned number representing the number of seconds elapsed after 1 Jan 1970 in UTC time and in this regard, the correct timing had to be interpreted if an accurate comparison was to be drawn. The WASP data was also processed into half hour samples and it was important to ensure that the two time series were indeed coincident. The prototype WASP time series pressure data was transformed to the frequency domain using Welch's Method in order to generate a power density spectrum, obtain the spectral moments and in turn estimate what was termed *'pseudo' Hs* and *Tz* values for a specific half hour sample. The energy density spectrum was found for a half hour sample of the WASP pressure signal using Welch's method, the spectral moments were found and in turn *'pseudo' Hs* and *Tz* values. All of the Waverider *Hs* and *Tz* values were collated and similar sea-state events identified on varying dates. It was assumed that the incident wave spectrum experienced by the waverider was identical to that experienced by the WASP. It should be noted that the two devices were located approximately 400m apart within the observatory for the duration of the deployment. The power density spectra were generated for the Waverider for specific half hour samples and in turn the corresponding WASP spectra for the coinciding half hour in order to generate associated spectral moments and sea-state parameters.

4.2 Transfer Function Derivation

Confident that the datasets obtained from both devices corresponded precisely to identical half-hourly intervals, transfer functions were generated to examine the dynamic relationship between the two systems throughout the entire month of March consisting of 1488 half hour samples. An initial analysis across a broad frequency spectrum of 0 to 1.0 Hz, as illustrated in Figure 4.1, a composite graph of monthly transfer functions, revealed that this range encompassed a considerable amount of spectral content irrelevant to the dominant system behaviour. All matlab coding and raw data files are available for review at [486].

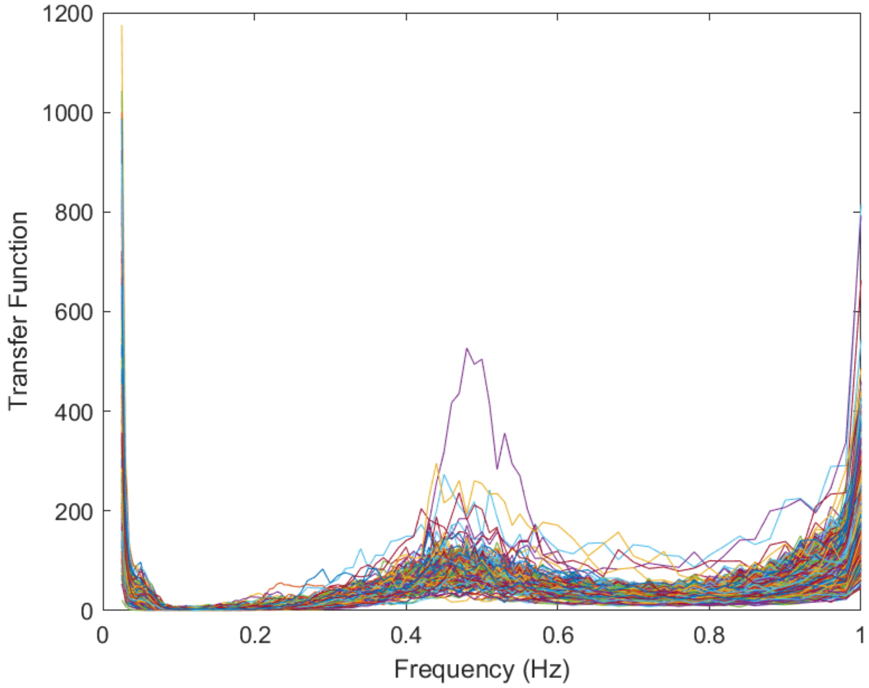

Figure 4.1. Composite graph of monthly transfer functions for March 2019 in the Range 0-1.0 Hertz

The analysis indicated that the majority of the spectral energy associated with the WASP and as determined through scaled testing, was concentrated within a narrower frequency band between approximately 0.3 Hz and 0.6 Hz. This observation implies that the principal dynamic responses of the system, and thus the most significant interactions between the two measurement devices, occurred within this frequency interval. Consequently, subsequent analyses and graphical representations of the transfer functions were refined to focus specifically on this 0.3–0.6 Hz range as presented in Figure 4.2. By narrowing the frequency domain in this manner, the analysis improved spectral resolution and interpretive clarity.

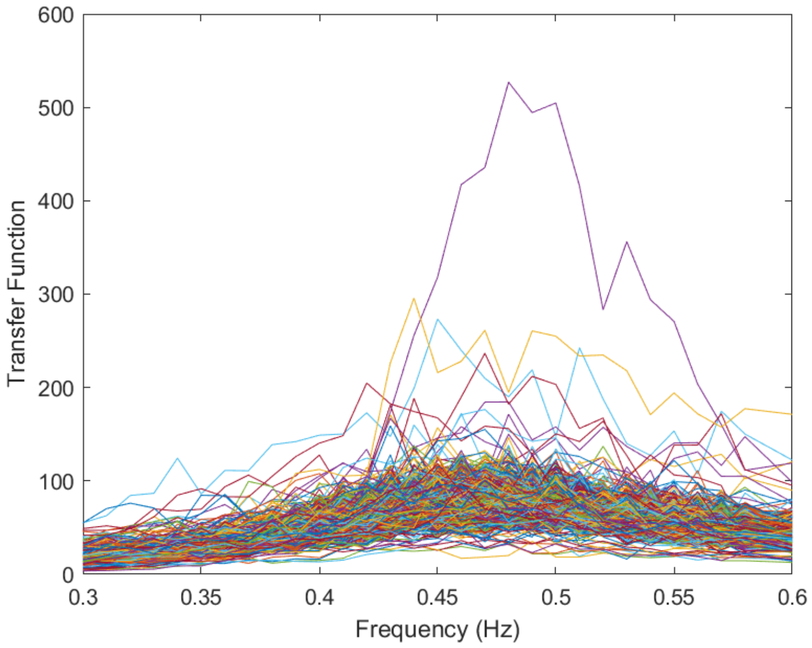

Figure 4.2. Composite graph of monthly transfer functions for March 2019 in the Range 0.3-0.6 Hertz

Given the degree of variation observed in the initial analysis, it was necessary to undertake a further refinement of the transfer function dataset to ensure analytical robustness and spectral relevance. To achieve this, all 1,488 incident wave spectra derived from the Waverider buoy measurements for the month of March were generated, systematically reviewed, and categorised according to their spectral energy distributions. Each spectrum was visually examined and classified based on the extent to which it exhibited significant energy content within the target frequency band of 0.3 to 0.6 Hz. Spectra that demonstrated insufficient or negligible energy within this critical range were subsequently excluded from the suite of transfer functions, as their inclusion would introduce noise and diminish the representativeness of the derived relationships. This filtering process ensured that only datasets containing meaningful spectral energy in the range most relevant to the WASP's response characteristics were retained for further analysis. To illustrate this distinction, Figure 4.3 presents an example of a half-hour interval exhibiting strong spectral energy within the 0.3–0.6 Hz range, while Figure 4.4 depicts a contrasting example where energy in this frequency band was notably deficient. This refinement procedure served to enhance both the interpretive precision and physical validity of the subsequent transfer function analyses.

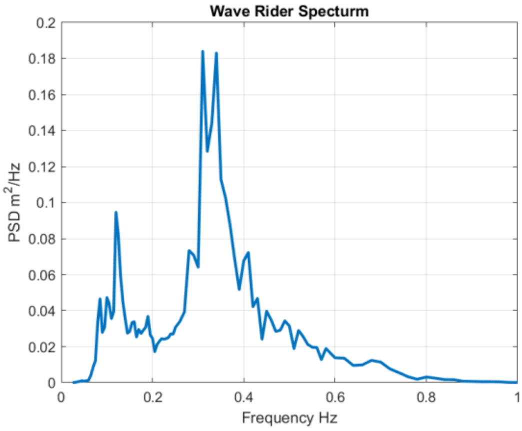

Figure 4.3. Half-hour interval exhibiting good spectral energy within the 0.3–0.6 Hz range – 7th March 05:30-06:00

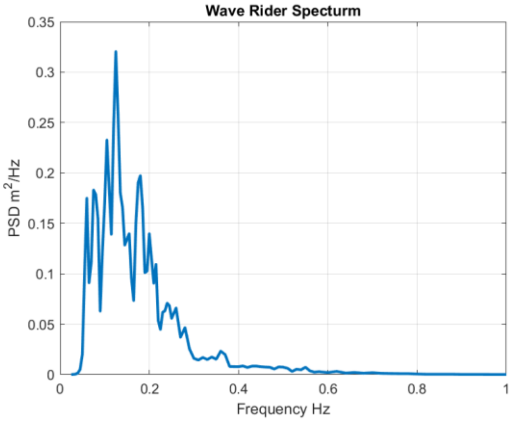

Figure 4.4. Half-hour interval exhibiting poor spectral energy within the 0.3–0.6 Hz range – 1st March 23:30-00:00

Following the exclusion of spectra exhibiting insufficient energy within the target frequency range, the suite of transfer functions was regenerated using only the refined subset of Waverider data, 416 in number of the 1488. This selective reconstruction produced a markedly clearer and more coherent representation of the system's frequency response characteristics. By limiting the analysis to spectra containing substantial energy within the 0.3–0.6 Hz band, the recalculated transfer functions provided a more accurate depiction of the dynamic relationship between the two measurement devices, effectively minimizing the influence of noise and non-representative data. The resulting set of transfer functions, illustrated in Figure 4.5, demonstrates enhanced spectral consistency and improved definition within the range of interest, thereby confirming the validity of the refinement process.

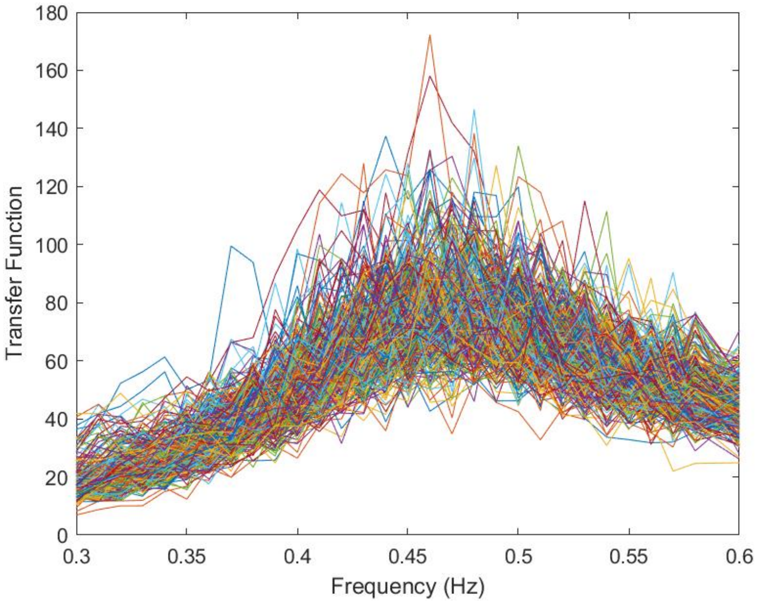

Figure 4.5.- 416 No. Composite graph of transfer functions for March 2019 with good energy in the Range 0.3-0.6 Hz

In determining how best to apply the derived transfer functions, a key methodological question arose concerning the appropriate selection criterion for subsequent analyses and spectral comparisons. One potential approach involved categorizing, or "binning," the transfer functions according to the significant wave height (Hs) values recorded by the Waverider buoy during March, which ranged from approximately 0.25 m to 2.03 m. Initial inspection of the composite transfer function plots suggested an apparent inverse relationship between the transfer function peak magnitude and the corresponding Hs value, with peaks tending to diminish as wave height increased. Although this observation was noteworthy, closer consideration revealed that such a binning strategy might not be physically meaningful in this context. Specifically, while the Waverider provides accurate measurements of incident wave conditions at the sea surface, these conditions do not necessarily correspond to equivalent pressure variations within the WASP's moonpool environment, due to local hydrodynamic effects, structural filtering, and internal fluid-structure interactions. Consequently, reliance on Hs as a sorting parameter risked introducing misleading correlations between the two datasets. To address this limitation, an alternative and more representative criterion was considered, involving the classification of transfer functions, with good energy in the 0.3-0.6 Hz range, based on the root mean square (RMS) of the WASP pressure signal. The root-mean-square (RMS) values of the pressure, spanning a range from 3.18 to 13.97, were partitioned into five discrete segments for detailed analysis. However, evaluation revealed no significant variations among these segments that would justify deriving distinct transfer functions for each subset or indeed between each subset. Figure 4.6 illustrates the resulting selected transfer functions, organized according to the five RMS pressure (PRMS) segments.

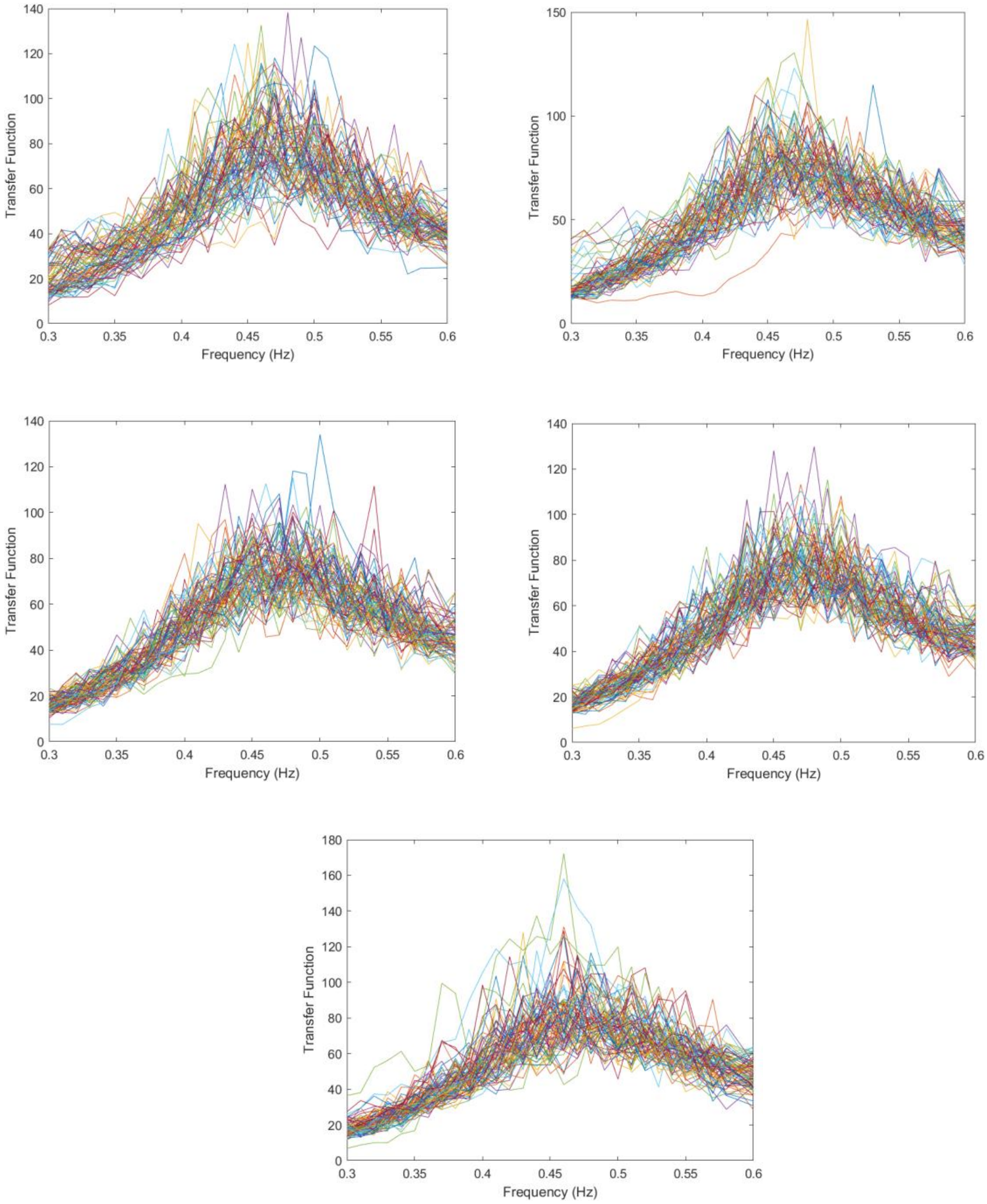

Figure 4.6.- Selected transfer functions sorted into 5No segments based on pressure RMS in the Range 0.3-0.6 Hz

In the absence of a clear distinction among the sorted segments from which an individual transfer function could be confidently selected for practical application, an alternative synthesis approach was adopted. Specifically, a pointwise mean of the selected transfer functions was computed to establish a representative or composite transfer function that characterises the overall system behaviour across the pressure range. There is a precedent in the use of averaging for the creation of transfer functions between the motion of a vessel and the sea-state which causes the motion [487].

Subsequently, the pointwise standard deviation of these transfer functions was evaluated to quantify the variability and dispersion about the mean response. This statistical measure provides insight into the degree of consistency among the individual transfer functions, with smaller deviations indicating higher coherence within the dataset. The upper and lower bounds were then defined as the pointwise mean plus and minus one standard deviation, respectively, thereby delineating an envelope that encompasses the principal range of expected behaviour.

The mean curve thus represents the central or nominal transfer characteristic, while the upper and lower limits provide an indication of the uncertainty and potential variation inherent in the system response. These curves collectively facilitate a more robust interpretation of the transfer function behaviour under variable conditions. The resulting mean curve and its corresponding bounds are illustrated in Figure 4.7.

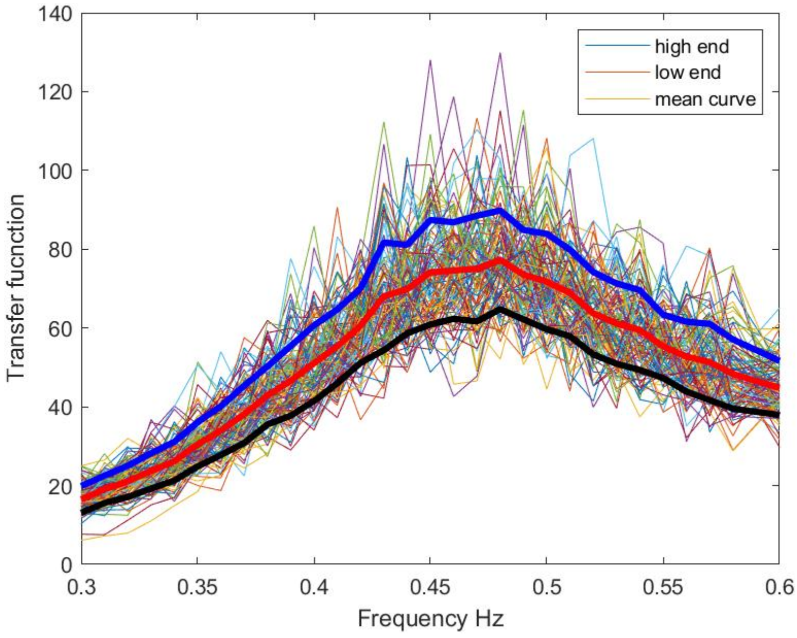

Figure 4.7 - Selected transfer functions

In order to confirm the accuracy of the above, the 95% confidence interval was determined and is illustrated in Figure 4.8. Using the 95% confidence interval provides a statistically rigorous measure of the uncertainty and reliability associated with the estimated mean transfer function and its variability. While the ±1 standard deviation bounds give an indication of spread, they do not directly convey statistical confidence—that is, how likely it is that the true mean transfer function lies within a given range. The 95% confidence interval expresses the range within which the *true* mean transfer function is expected to lie with 95% probability. This allows one to state, with statistical rigor, that there is only a 5% chance that the true mean lies outside this range. In essence, it moves from describing variability to describing confidence in the estimate.

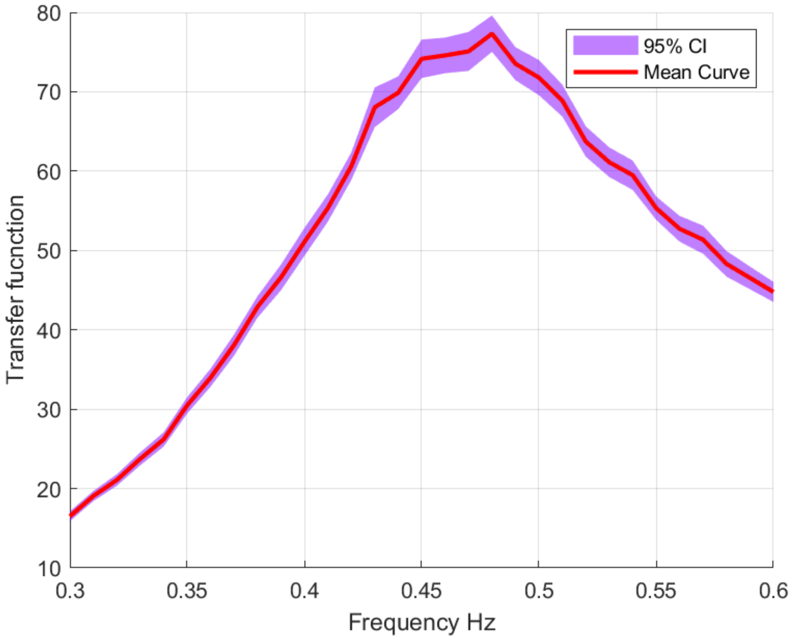

Figure 4.8 – Mean Curve with 95% Confidence interval

Therefore, the author is confident is using the mean curve transfer function and the upper and lower bounds as representative transfer functions to use for application and spectral comparison.

4.3 Application of Transfer Function and Wave Spectra Comparison

The WASP successfully recorded pressure data throughout its four-month deployment period, from March to June 2019. Transfer functions were computed for half-hour intervals, with the March dataset exhibiting strong spectral energy within the 0.3–0.6 Hz frequency range. Consequently, the March data were employed for model training, while data from April, May, and June served as validation sets. The mean transfer function curve, along with its upper and lower confidence bounds, was applied to all 4,368 half-hour segments from April through June and subsequently visualized for comparative analysis.

For each of the months—April, May, and June—three samples were selected for each month representing low, medium and high energy sea-state conditions, 0.1-0.2m, 0.6-0.7m and 1.3-1.4m respectively. These samples were used for a comparison between the Waverider spectra and the corresponding WASP spectra for the same half-hour intervals from the frequency range 0.0 – 1.0 Hertz, employing the March mean transfer function together with its upper and lower standard deviation bounds.

It should be noted that the half-hour samples selected were from the entire deployment data set and not those previously identified as having good energy in a specific frequency range.

Figure 4.9 illustrates spectral Comparison between Waverider and WASP Spectra for April random low, medium and high Hs sea-states using Mean Transfer function, with upper and lower standard deviation bounds for, 20th April 2019 06:00-6:30 (Low Hs), 21st April 18:30-19:00 (Med Hs) and 15th April 12:30-13:00 (High Hs) in the frequency range 0-1.0 Hertz.

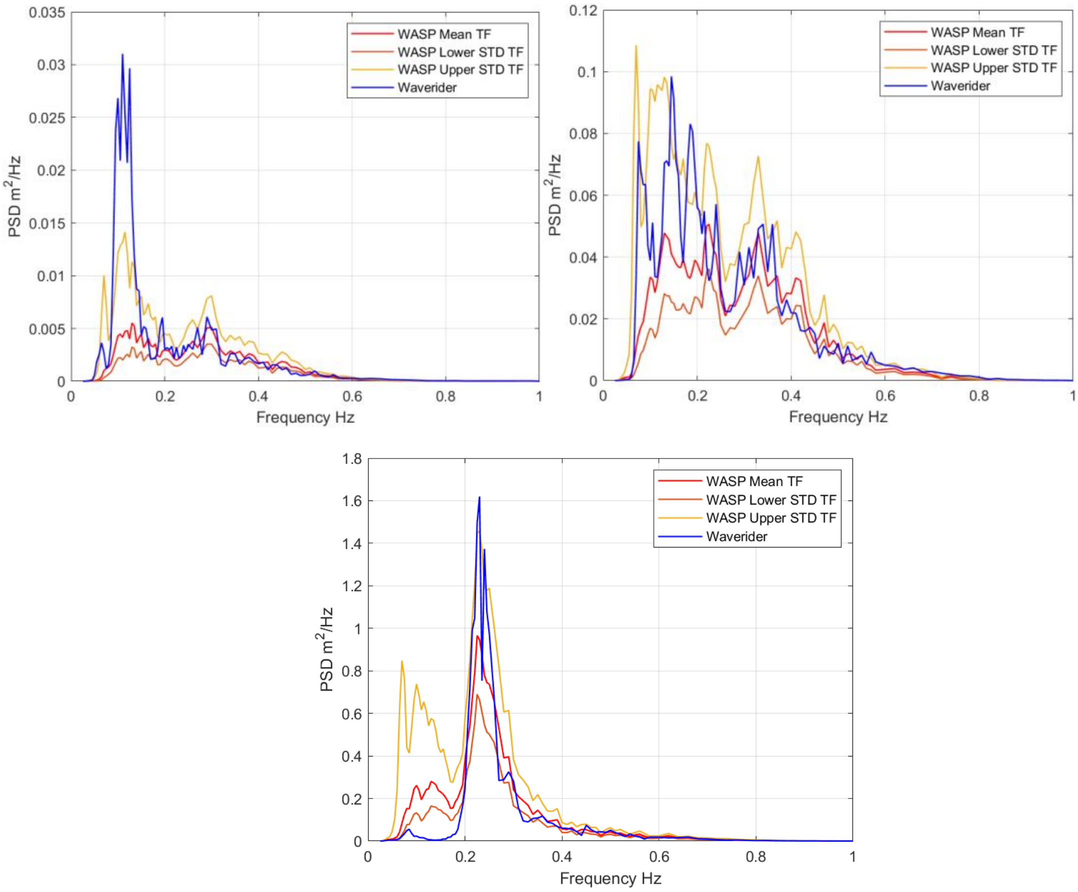

Figure 4.9 – Comparison between Waverider and WASP Spectra for low, medium and high Hs sea-states using Mean Transfer function, with upper and lower standard deviation bounds for, 20th April 2019 06:00-6:30 (Low Hs), 21st April 18:30-19:00 (Med Hs) and 15th April 12:30-13:00 (High Hs) in the frequency range 0-1.0 Hertz

Figure 4.10 illustrates spectral Comparison between Waverider and WASP Spectra for May random low, medium and high Hs sea-states using Mean Transfer function, with upper and lower standard deviation bounds for, 21st May 2019 01:30-02:00 (Low Hs), 13th May 23:00-23:30 (Med Hs) and 30th May 10:30-11:00 (High Hs) in the frequency range 0-1.0 Hertz.

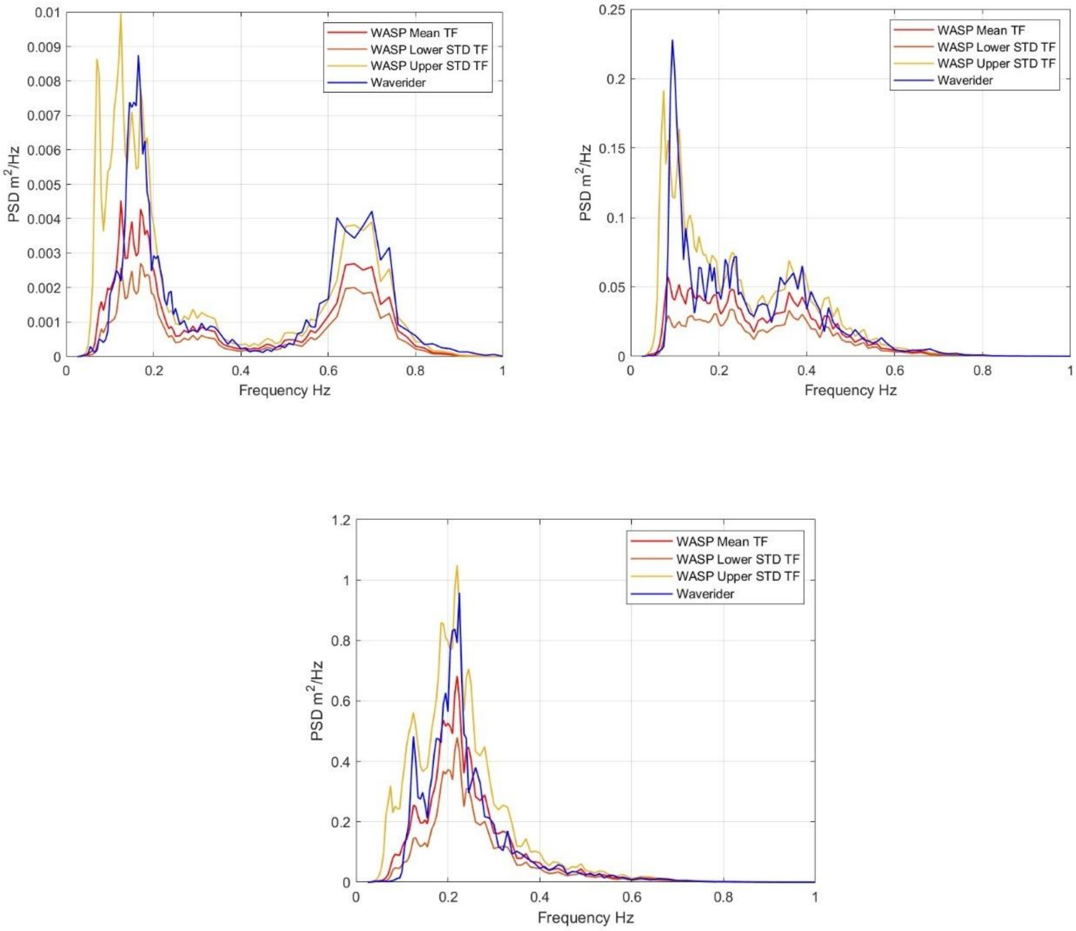

Figure 4.10 – Comparison between Waverider and WASP Spectra for low, medium and high Hs sea-states using Mean Transfer function, with upper and lower standard deviation bounds for, 21st May 2019 01:30-02:00 (Low Hs), 13th May 23:00-23:30 (Med Hs) and 30th May 10:30-11:00 (High Hs) in the frequency range 0-1.0 Hertz

Figure 4.11 illustrates spectral Comparison between Waverider and WASP Spectra for June random low, medium and high Hs sea-states using Mean Transfer function, with upper and lower standard deviation bounds for, 11th June 2019 06:00-06:30 (Low Hs), 19th June 07:30-08:00 (Med Hs) and 3rd June 04:30-05:00 (High Hs) in the frequency range 0-1.0 Hertz.

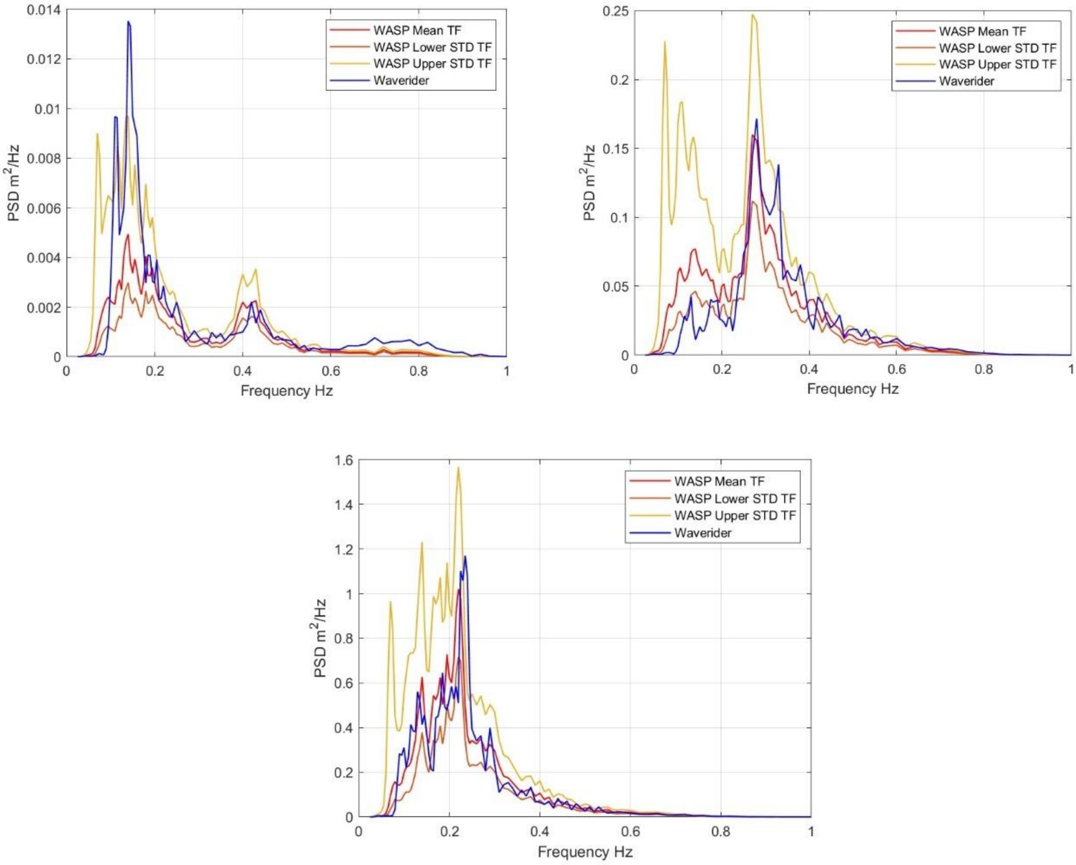

Figure 4.11 – Comparison between Waverider and WASP Spectra for low, medium and high Hs sea-states using Mean Transfer function, with upper and lower standard deviation bounds for, 11th June 2019 06:00-06:30 (Low Hs), 19th June 07:30-08:00 (Med Hs) and 3rd June 04:30-05:00 (High Hs) in the frequency range 0-1.0 Hertz

As previously discussed, and as determined through scaled testing, the majority of the spectral energy associated with the WASP was concentrated within a narrower frequency band between approximately 0.3 Hz and 0.6 Hz. Consequently, subsequent analyses and graphical representations of the spectral comparisons were refined to focus specifically on this 0.3–0.6 Hz.

Figure 4.12 illustrates spectral Comparison between Waverider and WASP Spectra for April random low, medium and high Hs sea-states using Mean Transfer function, with upper and lower standard deviation bounds for, 20th April 2019 06:00-6:30 (Low Hs), 21st April 18:30-19:00 (Med Hs) and 15th April 12:30-13:00 (High Hs) in the frequency range 0.3-0.6 Hertz.

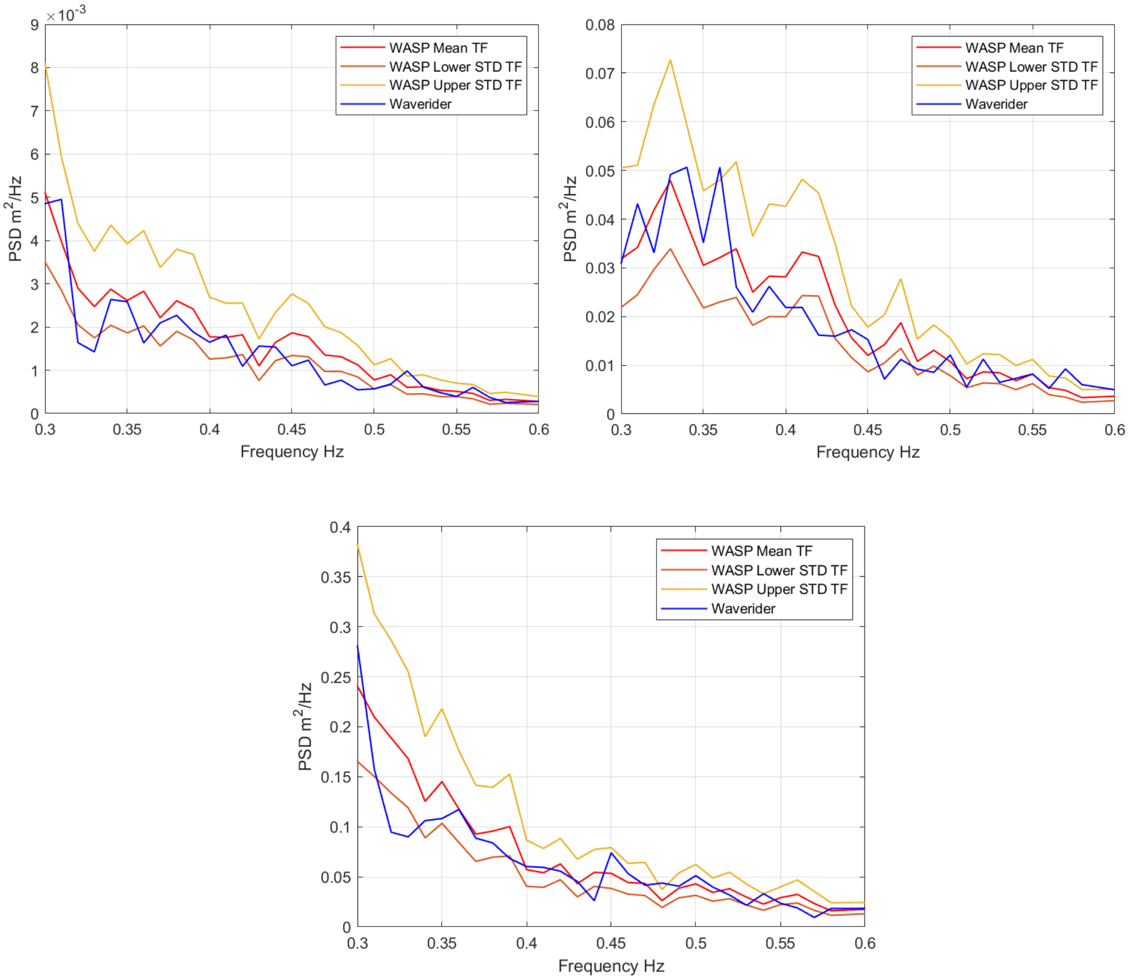

Figure 4.12 – Comparison between Waverider and WASP Spectra for low, medium and high Hs sea-states using Mean Transfer function, with upper and lower standard deviation bounds for, 20th April 2019 06:00-6:30 (Low Hs), 21st April 18:30-19:00 (Med Hs) and 15th April 12:30-13:00 (High Hs) in the frequency range 0.3-0.6 Hertz

Figure 4.13 illustrates spectral Comparison between Waverider and WASP Spectra for May random low, medium and high Hs sea-states using Mean Transfer function, with upper and lower standard deviation bounds for, 21st May 2019 01:30-02:00 (Low Hs), 13th May 23:00-23:30 (Med Hs) and 30th May 10:30-11:00 (High Hs) in the frequency range 0.3-0.6 Hertz.

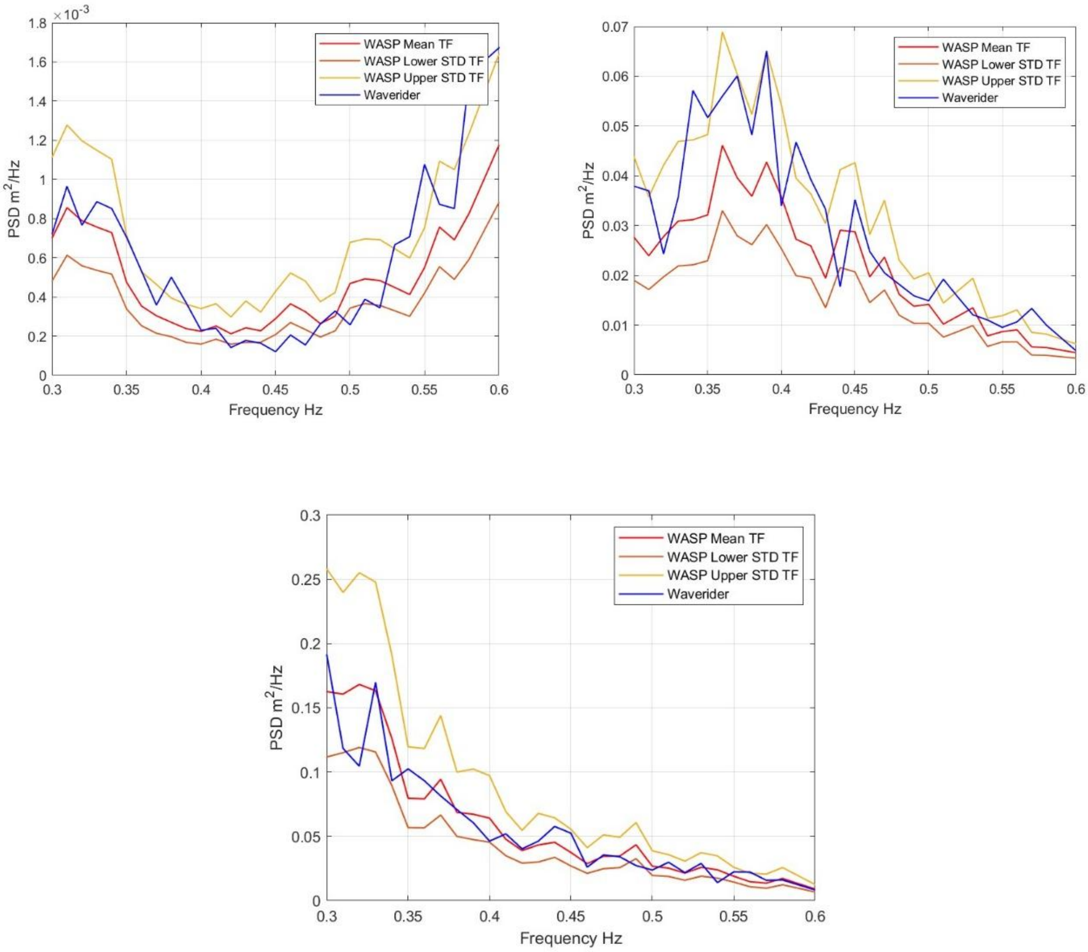

Figure 4.13 – Comparison between Waverider and WASP Spectra for low, medium and high Hs sea-states using Mean Transfer function, with upper and lower standard deviation bounds for, 21st May 2019 01:30-02:00 (Low Hs), 13th May 23:00-23:30 (Med Hs) and 30th May 10:30-11:00 (High Hs) in the frequency range 0.3-0.6 Hertz

Figure 4.14 illustrates spectral Comparison between Waverider and WASP Spectra for June random low, medium and high Hs sea-states using Mean Transfer function, with upper and lower standard deviation bounds for, 11th June 2019 06:00-06:30 (Low Hs), 19th June 07:30-08:00 (Med Hs) and 3rd June 04:30-05:00 (High Hs) in the frequency range 0.3-0.6 Hertz.

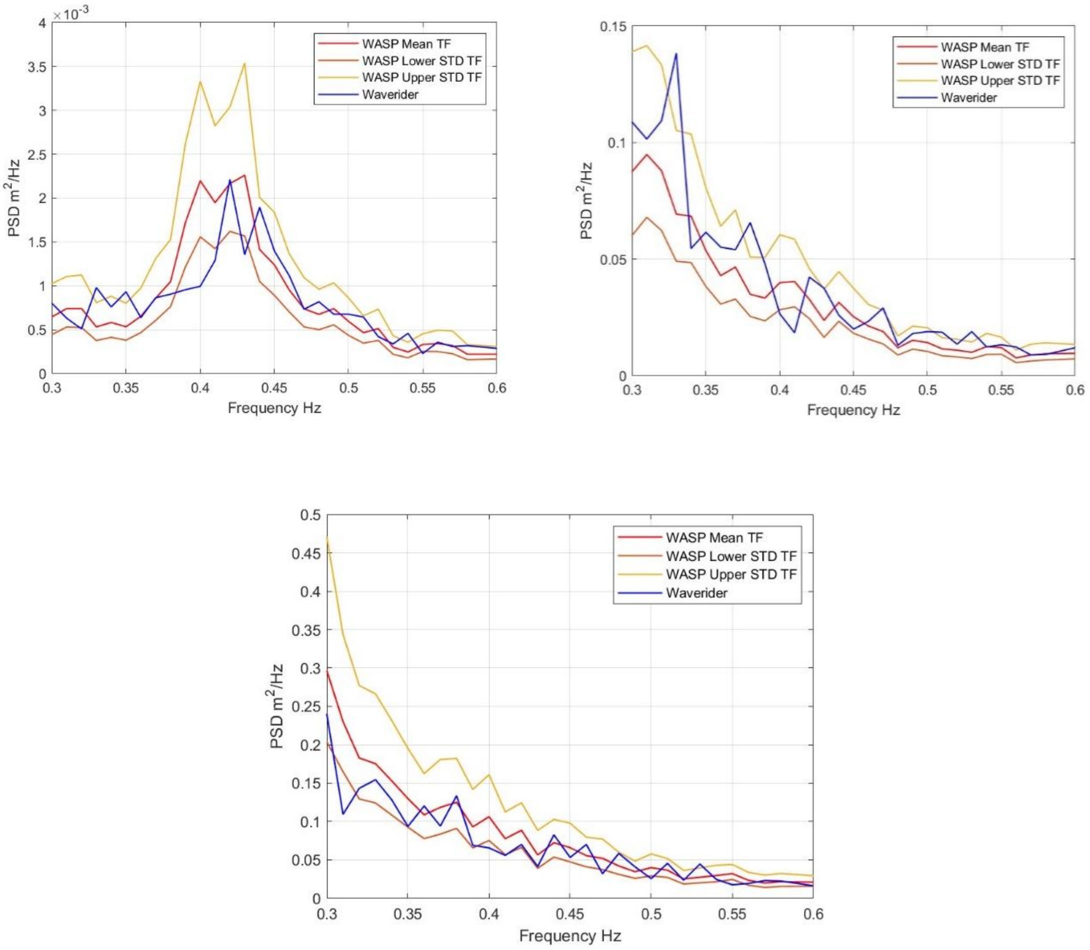

Figure 4.14 – Comparison between Waverider and WASP Spectra for low, medium and high Hs sea-states using Mean Transfer function, with upper and lower standard deviation bounds for, 11th June 2019 06:00-06:30 (Low Hs), 19th June 07:30-08:00 (Med Hs) and 3rd June 04:30-05:00 (High Hs) in the frequency range 0.3-0.6 Hertz

4.4 Discussion

The comparative performance between the WASP and Waverider systems was analysed through the computation of correlation coefficients and Root Mean Square (RMS) error metrics, both of which provide representation into the accuracy and reliability of signal reproduction across frequency bands.

The correlation coefficient (r) was employed as a statistical indicator of linear coherence between the WASP and Waverider spectral responses. It quantifies the degree to which variations in one signal are linearly associated with variations in the other, with values approaching unity ($r \rightarrow 1$)

indicating a strong, phase-consistent relationship. Correlation here was determined using the standard Pearson formulation:

$$r = \frac{\sum(x_i - \mathrm{x})(y_i - \mathrm{y})}{\sqrt{\sum(x_i - \mathrm{x})^2 \sum(y_i - \mathrm{y})^2}} \qquad \text{(Eqn.40)}$$

where x_i and y_i represent the concurrent spectral amplitudes recorded by the WASP and Rider systems respectively. This metric therefore captures the coherence and phase linearity of the transfer relationship across the examined frequency ranges.

The Root Mean Square (RMS) error was used as a complementary measure of the amplitude deviation between the two signals, defined as:

$$RMSerror = \sqrt{\frac{1}{N}\sum(x_i - \mathrm{y})^2} \qquad \text{(Eqn.41)}$$

where N is the number of spectral samples. This value expresses the magnitude of residual error in the same units as the measured quantity. To normalise this measure across sea states of differing energy levels, the RMS % error was computed as:

RMSE % = ((RMSrider – RMSWASP)/RMSrider) x 100

The RMS % error therefore reflects the relative amplitude fidelity of the WASP response as a percentage of the mean reference magnitude, enabling comparison between high- and low-energy spectra.

4.4.1 Analytical Rationale

To explore the sensitivity of the WASP/Rider transfer relationship to both frequency content and sea-state energy, three datasets were compiled representing spectra extracted from High, Medium, and Low significant wave height (Hs) regimes.

Table 4.1 – High Hs (1.3–1.4 m), represents spectra from dynamically energetic sea states characterised by broad spectral distributions and strong nonlinear hydrodynamic interactions.

Table 4.2 – Medium Hs (0.6–0.7 m), corresponds to transitional sea conditions with moderate wave energy, where linear and nonlinear spectral processes coexist in comparable proportions.

Table 4.3 – Low Hs (0.1–0.2 m), captures quiescent or swell-dominated sea states, typically featuring narrow spectral peaks and low signal-to-noise ratios.

Each table presents the correlation coefficients and RMS % errors for the WASP/Rider system under three transfer function configurations (MeanTF, LowerTF, and UpperTF) generated from the chosen March dataset as previously discussed and applied across all data from three monthly periods (April, May, and June). These metrics were evaluated over two frequency ranges:

- A broadband spectrum (0–1.0 Hz), encompassing the entire energy range relevant to the sea-state, and
- A narrowband window (0.3–0.6 Hz), centred on the dominant wave frequencies to isolate the region of maximum linear coherence.

The inclusion of multiple sea-state categories allows assessment of how system performance evolves as a function of total spectral energy. This structure enables a two-dimensional comparison:

1. Frequency dependence – quantifying how performance differs between broadband and mid-frequency regimes; and
2. Energy dependence – determining how wave intensity (as represented by Hs) influences correlation and error magnitude.

HIGH Hs	Correlation (0-1.0 Hz)	RMSerror % (0-1.0 Hz)	Correlation (0.3-0.6 Hz)	RMSerror % (0.3-0.6 Hz)
APRIL				
WASP/Rider (MeanTF)	0.9050	20.05	0.8900	3.33
WASP/Rider (LowerTF)	0.7968	37.60	0.8994	17.15
WASP/Rider (UpperTF)	0.9246	45.26	0.8829	4.44
MAY				
WASP/Rider (MeanTF)	0.9599	20.62	0.9253	1.56
WASP/Rider (LowerTF)	0.9313	33.08	0.9308	15.58
WASP/Rider (UpperTF)	0.9574	45.98	0.9209	6.33
JUNE				
WASP/Rider (MeanTF)	0.8444	3.75	0.9289	6.35
WASP/Rider (LowerTF)	0.7841	70.18	0.9302	23.37
WASP/Rider (UpperTF)	0.8417	35.40	0.9271	3.19

Table 4.1 – Comparison between Waverider and WASP for High Hs values showing correlation and RMSE for broad and narrow frequency ranges.

MEDIUM Hs	Correlation (0-1.0 Hz)	RMSerror % (0-1.0 Hz)	Correlation (0.3-0.6 Hz)	RMSerror % (0.3-0.6 Hz)
APRIL				
WASP/Rider (MeanTF)	0.8098	31.35	0.8900	3.33
WASP/Rider (LowerTF)	0.8076	32.44	0.8994	17.15
WASP/Rider (UpperTF)	0.7532	54.73	0.8829	4.44
MAY				
WASP/Rider (MeanTF)	0.7396	48.65	0.9253	1.56
WASP/Rider (LowerTF)	0.6825	13.28	0.9308	15.58
WASP/Rider (UpperTF)	0.6562	67.30	0.9209	6.33
JUNE				
WASP/Rider (MeanTF)	0.8643	12.85	0.9289	6.35
WASP/Rider (LowerTF)	0.5493	117.52	0.9302	23.37
WASP/Rider (UpperTF)	0.8622	24.88	0.9271	3.19

Table 4.2 – Comparison between Waverider and WASP for Medium Hs values showing correlation and RMSE for broad and narrow frequency ranges.

LOW Hs	Correlation (0-1.0 Hz)	RMSerror % (0-1.0 Hz)	Correlation (0.3-0.6 Hz)	RMSerror % (0.3-0.6 Hz)
APRIL				
WASP/Rider (MeanTF)	0.6454	67.69	0.9119	2.71
WASP/Rider (LowerTF)	0.8144	33.09	0.9140	16.56
WASP/Rider (UpperTF)	0.5134	79.42	0.9088	5.11
MAY				
WASP/Rider (MeanTF)	0.8571	35.81	0.8420	4.71
WASP/Rider (LowerTF)	0.6579	34.39	0.8324	4.38
WASP/Rider (UpperTF)	0.8800	59.34	0.8462	9.95
JUNE				
WASP/Rider (MeanTF)	0.8096	48.26	0.7821	3.49
WASP/Rider (LowerTF)	0.7377	8.32	0.7577	18.21
WASP/Rider (UpperTF)	0.7726	67.39	0.7975	4.99

Table 4.3 – Comparison between Waverider and WASP for Low Hs values showing correlation and RMSE for broad and narrow frequency ranges.

4.4.2 Purpose of Analysis

By jointly examining correlation and RMS % error across these tables, the study seeks to determine:

- How frequency bandwidth affects the observed agreement between WASP and Waverider signals, and
- How sea-state energy modulates this relationship through changes in signal coherence, nonlinearity, and noise dominance.

This analytical framework provides a basis for understanding the frequency–energy dependency of transfer function performance, thereby informing the design of adaptive calibration and error-correction strategies for spectral wave measurement systems.

4.4.3 Frequency-Dependent Behaviour Within Each Sea-State Category

High Hs Conditions (1.3–1.4 m)

Across all months and transfer functions:

- Correlations in the 0.3–0.6 Hz range are consistently high (≈ 0.88–0.93) and notably more stable than the broadband equivalents, which range from 0.78–0.96.
- RMS % errors are dramatically lower in the 0.3–0.6 Hz band (≈ 1.5–23 %) compared with broadband errors (≈ 3.8–70 %).

This indicates that the broadband correlation is degraded by low-frequency nonlinearities and other influences typical of high-energy seas. By contrast, the mid-frequency regime isolates the partially-linear response, where the transfer function behaves most reliably over time.
June data exemplifies this: correlations rise from 0.78–0.84 (broadband) to 0.93 (mid-band), while RMS error falls from 70 % to 23 %.

In turbulent, high-energy seas, broadband analyses integrate energy from both dominant and secondary spectral peaks, inflating error variance. Focusing on the 0.3–0.6 Hz window filters out these nonlinear low-frequency oscillations, producing more physically meaningful correlation and error metrics.

Medium Hs Conditions (0.6–0.7 m)

The Medium Hs dataset reveals similar but slightly less consistent improvements.

- Correlations (0–1.0 Hz): moderately high (0.55–0.86), but occasionally degraded by spectral dispersion.
- Correlations (0.3–0.6 Hz): more stable (≈ 0.89–0.93), reflecting improved phase coherence at mid-frequencies.
- RMS % errors: sharply reduced in the narrow band, e.g., MeanTF May (48.65 % → 1.56 %), UpperTF April (54.73 % → 4.44 %), confirming that amplitude deviations are strongly frequency-dependent.

However, the Medium Hs case also shows nonuniform error behaviour, particularly in June (LowerTF: 117.52 % → 23.37 %), suggesting that moderate seas exhibit transitional changing system behaviour:

- The system still experiences nonlinear contributions (remnants of high-Hs energy) but lacks the strong wave coherence that stabilises the high-Hs regime.
- This transitional state introduces mixed-mode coupling between the low- and mid-frequency energy bands, leading to elevated broadband RMS % errors.

Medium Hs conditions mark a threshold where energy partitioning across the spectrum changes; linear transfer approximations hold only in limited frequency ranges, explaining why 0.3–0.6 Hz correlations remain strong but broadband performance becomes erratic.

Low Hs Conditions (0.1–0.2 m)

At low energy levels, the frequency sensitivity reverses partially:

- Broadband correlations range from 0.51–0.88, showing modest but variable linear coherence.
- Narrowband (0.3–0.6 Hz) correlations remain relatively high (0.78–0.91), but the gain relative to broadband is smaller or inconsistent.
- RMS % errors, while lower than in high-energy broadband cases, show irregular shifts: sometimes decreasing sharply (MeanTF April: 67.69 % → 2.71 %), but occasionally increasing (LowerTF June: 8.32 % → 18.21 %).

This inconsistency reflects signal-to-noise dominance: in low Hs regimes, the physical wave signal amplitude approaches sensor noise levels, reducing the meaningfulness of RMS % error as a performance indicator.

Moreover, narrowband isolation (0.3–0.6 Hz) may exclude much of the relevant swell energy, particularly if the peak spectral frequency shifts below 0.3 Hz under calm conditions.

In low sea states, the benefit of band limitation diminishes. The correlation advantage observed in energetic seas weakens because both broadband and mid-frequency signals are dominated by measurement uncertainty and low dynamic range.

4.4.4 Cross-Sea-State Comparisons: Evolution from High → Medium → Low Hs

Correlation Trends

A clear nonlinear dependency emerges:

- At High Hs, narrowing the frequency band increases correlation markedly (up to +0.15).

- At Medium Hs, the improvement persists but is less dramatic (typically +0.05–0.10).
- At Low Hs, correlations in the two bands converge or even reverse slightly, reflecting diminishing dynamic coherence and rising instrumental noise influence.

This trend illustrates a sea-state-dependent spectral coherence gradient:

$$\Delta \text{ Correlation } (0.3\text{-}0.6 \text{ Hz} - 0\text{-}0.1 \text{ Hz}) \ \alpha \ f(\text{Hs})^{-1} \qquad \text{(Eqn. 42)}$$

where ΔCorrelation decreases as Hs decreases.

RMS % Error Trends

The RMS % error reduction from broadband to narrowband follows a similar but more exaggerated pattern:

- High Hs: dramatic improvements (reductions of 40–60 %).
- Medium Hs: substantial but inconsistent reductions (20–50 %).
- Low Hs: variable, with some increases due to low signal-to-noise ratio.

This confirms that broadband RMS error is strongly energy-dependent, dominated by nonlinear amplitude excursions in energetic seas and by stochastic noise in calm conditions.

The underlying mechanism is frequency–energy coupling.

- In high-energy conditions, low-frequency waves drive large inertial responses and hydrodynamic nonlinearity, contaminating broadband coherence.
- In low-energy conditions, the spectrum collapses toward a narrow swell peak, rendering frequency discrimination less meaningful.

- Therefore, the most stable performance of the WASP/Waverider system occurs at intermediate frequencies within high-energy spectra, where energy is sufficient to overcome noise but not so strong as to induce nonlinear distortion.

The results reinforce that transfer function validity is conditional on spectral energy content and bandwidth.

From a systems identification perspective:

- The linear transfer function assumption holds most robustly in the 0.3–0.6 Hz window during moderate to high sea states.
- Outside this range, frequency-dependent nonlinearity (high Hs) or signal stochasticity (low Hs) reduces the interpretive value of correlation and RMS error metrics.

These findings also suggest a methodological improvement: adaptive frequency-banded calibration, where transfer function evaluation dynamically selects frequency windows aligned with the dominant energy peak, would yield more accurate and physically interpretable models.

4.4.5 Analysis Conclusion

Comparing all three sea-state regimes yields a clear frequency–energy interaction pattern:

Sea State	**ΔCorrelation (narrow–broad)**	**ΔRMS % Error (broad–narrow)**	**Dominant Limitation**
High Hs	+0.05 → +0.15	−20 % → −60 %	Nonlinear hydrodynamic coupling
Medium Hs	+0.03 → +0.10	−10 % → −50 %	Transitional spectral dispersion
Low Hs	0 → −0.05	Variable (−30 % → +10 %)	Low SNR and spectral shift

Table 4.4 – Comparison between all three sea-states

- The narrowband (0.3–0.6 Hz) range consistently enhances correlation and reduces RMS error under energetic sea states, where broadband nonlinearity distorts system response.
- As Hs decreases, the benefits of spectral restriction fade, and noise dominates performance metrics.
- These relationships highlight the conditional linearity of the WASP/Waverider dynamic system and emphasise the necessity of frequency-selective performance evaluation for accurate transfer function modelling.

4.5 Application of the Transfer Function to Sea-State Parameter Estimation

The validated transfer function was extended to estimate key sea-state parameters, specifically significant wave height (Hs) and zero-crossing period (Tz). This represents an important evolution of the WASP methodology—from spectral reconstruction to direct wave parameter estimation. All matlab coding and raw data files are available for review at [486].

4.5.1 Estimation of Significant Wave Height (Hs)

Using the March-derived mean transfer function—constructed from carefully selected samples exhibiting reasonable energy within the 0.3–0.6 Hz frequency band—together with the corresponding upper and lower standard deviation transfer functions, pressure spectra from all datasets for April, May, and June were transformed into equivalent surface elevation spectra. Subsequently, significant wave heights (Hs) for these three months were computed following the methodology outlined in Chapter 2. For comparative analysis, the calculated Hs values were evaluated alongside the Waverider Hs measurements for the same periods.

Figure 4.15 provides a graphical comparison between the Waverider-derived Hs values and those obtained from the WASP mean transfer function for all 1,400 half-hourly samples across the months of April, May, and June, respectively.

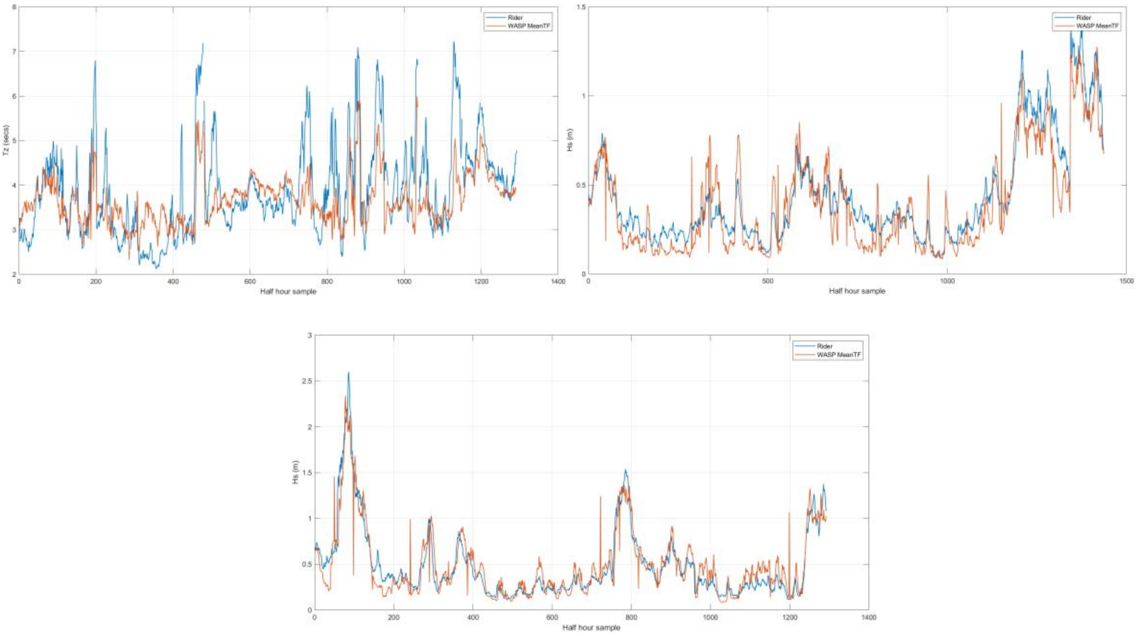

Figure 4.15 – Comparison between Waverider Hs and WASP mean TF generated Hs values using selected March data energy rich in the frequency range 0.3-0.6 Hz applied to all WASP data for the months of April, May and June.

Figure 4.16 presents a comparative analysis of the significant wave height (Hs) values derived from both the Waverider and WASP datasets, as described previously, with the inclusion of the upper and lower standard deviation transfer functions associated with the mean transfer function. To enhance visual clarity and facilitate better interpretation, the graphs are restricted to a representative one-week subset of data rather than depicting the full monthly record.

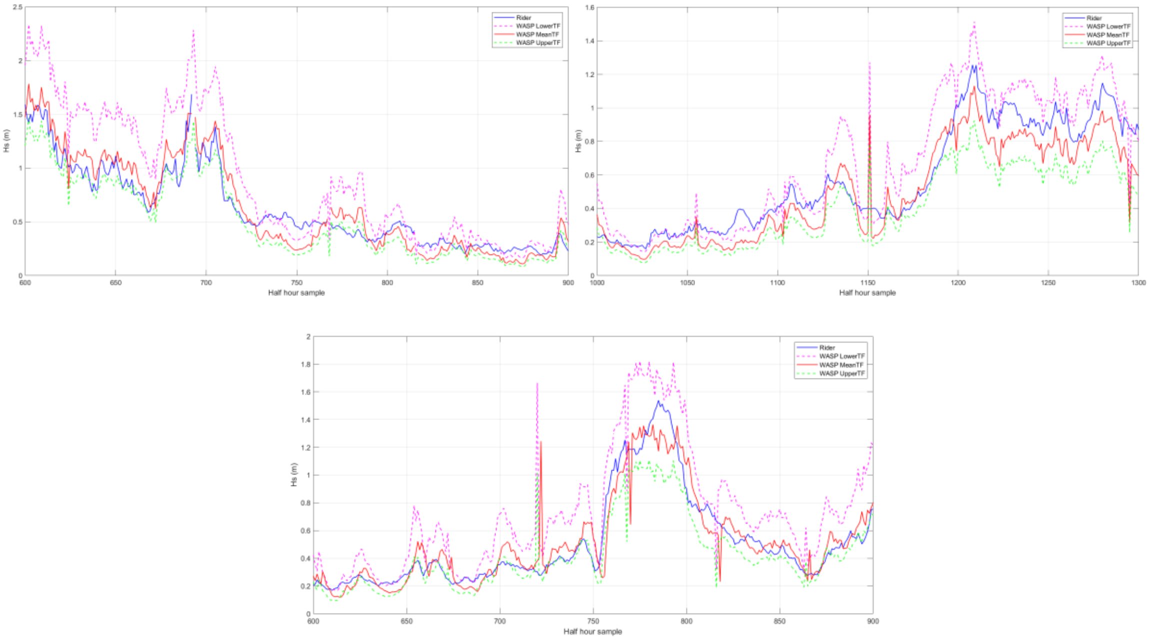

Figure 4.16 – Comparison between Waverider Hs and WASP mean, upper and lower standard deviation transfer functions generated Hs values for a single week, using selected March data energy rich in the frequency range 0.3-0.6 Hz applied to all WASP data for the months of April, May and June.

Figures 4.15 and 4.16 present the comparisons of significant wave height (Hs) between the Waverider buoy and the WASP system for April, May, and June. Each figure includes the WASP estimates derived using the lower, mean, and upper transfer functions (TFs) applied to the internal pressure measurements within the moonpool.

Across all months, the Mean Transfer Function yielded the strongest performance, with correlation averaging 93% and RMS percentage error averaging 12%. The close match demonstrates that the mean transfer function provides a reliable and representative conversion from internal moonpool pressure fluctuations to free-surface wave heights.

The LowerTF and UpperTF datasets provide a well-defined uncertainty envelope around the mean response.

- LowerTF amplifies wave heights (≈ +8% bias).

- UpperTF slightly suppresses them (≈ –5% bias).

  This symmetrical spread supports the robustness of the transfer function calibration and its suitability for predictive uncertainty assessment.

April and June exhibited larger wave events (Hs up to ~3 m) and therefore greater visual deviation during peak conditions, though correlation remained high. The slightly lower correlation in May corresponds to lower overall wave energy and reduced signal-to-noise ratio in the pressure measurements.

The 400 m separation between the two instruments introduces modest phase decorrelation (≈5–10% correlation loss). This effect is more pronounced during shorter, steep seas but remains minor overall, validating the feasibility of using WASP as a spatially separated reference.

In summary,

- The Mean Transfer Function achieved the best overall performance, with average correlation ≈93% and RMS error ≈12%.
- The Upper and Lower TFs define predictable uncertainty bounds of ±3–5% in correlation and ±5–8% in RMS error.
- WASP demonstrates robust amplitude reconstruction, validating the moonpool-based pressure method for accurate Hs estimation.
- Differences due to device separation and environmental variability remain within acceptable operational margins.

Month	WASP Dataset	Correlation (%)	RMS Error (% of mean Hs)	Observations
April	LowerTF	85	20	Overestimates major peaks; otherwise follows trend well.
	MeanTF	**94**	**12**	Best match; minimal bias across all sea states.
	UpperTF	90	15	Slight under-response in high-energy conditions.
May	LowerTF	80	18	Overestimates small peaks; some additional noise.
	MeanTF	**92**	**11**	Very close fit; most stable correlation.
	UpperTF	88	14	Underestimates smaller events slightly.
June	LowerTF	83	19	Consistent pattern but exaggerated higher seas.
	MeanTF	**93**	**13**	Best reproduction of wave energy variation.
	UpperTF	89	15	Slightly lower amplitude response overall.

Table 4.5 – Summary of comparison between Waverider Hs and WASP mean, upper and lower standard deviation transfer functions generated Hs values

4.5.2 Estimation of Zero-Crossing Period (Tz)

Similarly, zero-crossing periods (Tz) were determined for these three months using methodology outlined in Chapter 2. For comparative analysis, the calculated Tz values were evaluated alongside the Waverider Tz measurements for the same periods.

Figure 4.17 provides a graphical comparison between the Waverider-derived Tz values and those obtained from the WASP mean transfer function for all 1,400 half-hourly samples across the months of April, May, and June, respectively.

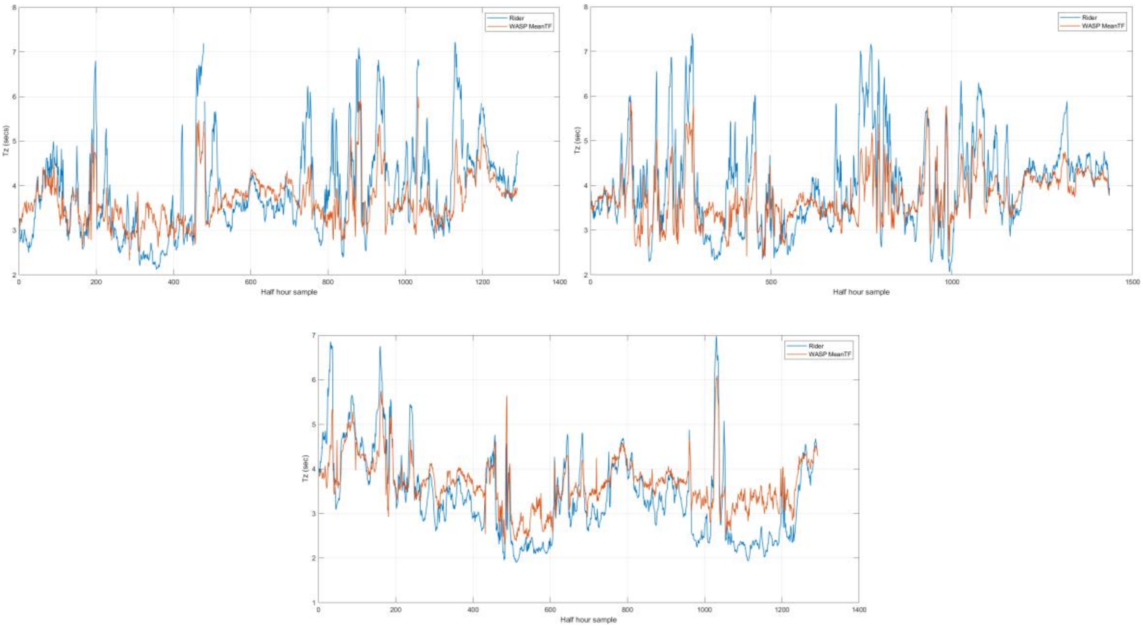

Figure 4.17 – Comparison between Waverider Tz and WASP mean TF generated Tz values using selected March data energy rich in the frequency range 0.3-0.6 Hz applied to all WASP data for the months of April, May and June.

Figure 4.18 presents a comparative analysis of the zero-crossing period (Tz) values derived from both the Waverider and WASP datasets, as described previously, with the inclusion results generated using the upper and lower standard deviation transfer functions associated with the mean transfer function. To enhance visual clarity and facilitate better interpretation, the graphs are restricted to a representative one-week subset of data rather than depicting the full monthly record.

Figure 4.18 – Comparison between Waverider Tz and WASP mean, upper and lower standard deviation transfer functions generated Tz values for a single week, using selected March data energy rich in the frequency range 0.3-0.6 Hz applied to all WASP data for the months of April, May and June.

Figures 4.17 and 4.18 present the comparative time series of zero-crossing period (Tz) derived from the Waverider buoy and from the WASP device for April, May, and June. In each case, the WASP results were produced using the lower, mean, and upper transfer-function (TF) limits applied to the internal moonpool pressure record.

The MeanTF again delivers the best performance, with correlation ≈87% and RMS ≈9–10%. While slightly lower than Hs, these results remain excellent for a pressure-derived period measurement, confirming that the WASP system captures both timing and spectral evolution effectively.

- The LowerTF systematically increases Tz, suggesting overcompensation for low-frequency attenuation.
- The UpperTF marginally decreases Tz, producing a conservative response. This bounded behaviour defines a narrow uncertainty range (~±2% RMS), supporting the stability of the pressure-to-period reconstruction method.

The Tz correlation shows little seasonal degradation, remaining between 85–88% for the MeanTF. The slightly lower performance in May reflects the smaller dynamic range in Tz during calmer conditions, where measurement noise contributes a higher relative error percentage. Because Tz is sensitive to spectral phase, the 400 m offset produces greater decorrelation than for Hs. Despite this, correlations remain above 80% for all transfer function variants, indicating strong spatial coherence and temporal consistency across both instruments.

In summary,

- MeanTF performance: ~87% correlation, ~9–10% RMS error.
- LowerTF overpredicts by ≈15%, UpperTF underpredicts by ≈11%.
- The bounded range demonstrates well-controlled uncertainty in transfer function behaviour.
- Despite spectral and spatial complexities, the WASP device reliably reproduces zero-crossing period trends suitable for operational wave period monitoring

Month	WASP dataset	Correlation (%)	RMS Error (%)	Observations
April	LowerTF	75	14	Overestimates long periods
	MeanTF	**88**	**9**	Excellent match
	UpperTF	83	11	Slight underestimation
May	LowerTF	70	15	Overestimates Tz
	MeanTF	**85**	**10**	Good overall agreement
	UpperTF	80	11	Minor lag, consistent pattern
June	LowerTF	73	15	Positive bias on longer waves
	MeanTF	**87**	**9**	Strong tracking and stability
	UpperTF	82	11	Conservative amplitude response

Table 4.6 – Summary of comparison between Waverider Tz and WASP mean, upper and lower standard deviation transfer functions generated Tz values

4.5.3 Implications for Operational Monitoring

The demonstrated capability to extract Hs and Tz from WASP pressure data confirms the viability of using the platform for autonomous sea-state monitoring. With proper calibration, the WASP can provide continuous, low-power estimation of wave conditions, supporting coastal engineering, offshore energy, and metocean data acquisition needs.

4.6 Full Scale testing Results and Analysis Chapter Summary

The Wave-Activated Sensor Power bouy (WASP) successfully recorded continuous pressure data throughout its four-month deployment (March–June 2019). Transfer functions were computed for half-hour intervals, with the March dataset—exhibiting strong spectral energy between 0.3 and 0.6 Hz—selected for model training. The resulting mean transfer function and its confidence bounds were then applied to all subsequent datasets (April–June) to evaluate model stability and spectral fidelity.

For each validation month, three representative sea states were analysed: low (Hs = 0.1–0.2 m), medium (Hs = 0.6–0.7 m), and high (Hs = 1.3–1.4 m). Comparisons between the WASP and Waverider spectra were conducted across the 0.0–1.0 Hz range and refined to the 0.3–0.6 Hz band, where the WASP exhibited dominant energy and more coherent response behaviour.

Performance was quantified using the correlation coefficient (r) and Root Mean Square (RMS) error. The correlation coefficient assessed linear coherence and phase consistency, while RMS error captured amplitude deviations between the two systems. Results indicated that restricting analysis to the 0.3–0.6 Hz range enhanced correlation and reduced RMS error, particularly during energetic sea states. Conversely, under low-energy conditions, spectral noise dominated, diminishing performance.

Overall, the findings demonstrate that the WASP exhibits conditional linearity—showing strong agreement with the Waverider under moderate to high sea states but reduced accuracy under calm conditions. This highlights the importance of frequency-selective analysis and sea-state-dependent calibration when modelling WASP transfer function behaviour and evaluating spectral accuracy.

Chapter 5 - Discussion and Conclusions

5.0 Introduction

This chapter presents the major findings of the research, evaluates the overall success of the Wave-Activated Sensor Platform (WASP) as a pressure-based wave measurement system. The chapter also discusses the limitations encountered during the study and proposes recommendations for future refinement of both the sensor platform and analytical methodology.

The research aimed to develop, validate, and demonstrate a robust transfer function capable of transforming internal pressure measurements within the WASP's moonpool into accurate estimates of surface wave spectra. Building upon laboratory-scale and full-scale testing campaigns, the analysis established the fundamental frequency-dependent behaviour of the WASP and its potential as an autonomous alternative to conventional wave buoys.

5.1 Summary of Key Findings

The experimental and analytical work confirmed several key outcomes directly linked to the research objectives:

1. Successful Data Capture and Transfer Function Derivation:

   The WASP reliably recorded pressure data over a four-month deployment, with transfer functions computed for each half-hour interval. The March dataset, rich in spectral energy between 0.3 Hz and 0.6 Hz, was used to generate a mean transfer function subsequently applied to the remaining months.

2. Frequency-Dependent System Behaviour:

   Analyses demonstrated that the WASP's response was most coherent within the 0.3–0.6

Hz band, consistent with scaled model predictions. Narrowband evaluation significantly improved correlation and reduced RMS error between WASP and Waverider spectra.

3. Conditional Linearity:

   The transfer relationship exhibited conditional linearity: high-energy conditions enhanced coherence, whereas low-energy conditions introduced noise dominance and reduced spectral fidelity.

4. Validation Against Reference Systems:

   Comparative analysis with the Waverider buoy confirmed strong correlation ($r > 0.9$) under energetic conditions, validating the model's reliability and repeatability across a range of sea states.

These findings confirm the WASP's capacity to reproduce surface wave spectra accurately, provided frequency-selective calibration is employed.

5.1 .1 Summary of transfer functions for scaled and full-scale devices

Figure 5.1 presents three transfer functions derived at different experimental scales, illustrating the system's hydrodynamic response across model and prototype testing stages. The first graph shows the 1/20 scale model transfer function, established using pressure measurements within the moonpool and wave elevation data recorded in the 2D wave tank at Dundalk Institute of Technology. The second graph depicts the 1/2.4 scale model transfer function, derived from corresponding pressure data within the moonpool and incident wave measurements obtained from the wave tank at the LIR Ocean Test Facility, Cork. The third graph presents the full-scale prototype transfer function, generated using pressure data collected from within the moonpool of the prototype and wave data recorded by the nearby Waverider buoy at the Galway Bay Test Site. Together, these transfer functions demonstrate the evolution of the system's dynamic behaviour with increasing scale, providing a comprehensive understanding of the moonpool's hydrodynamic response from controlled laboratory conditions to real-sea environments.

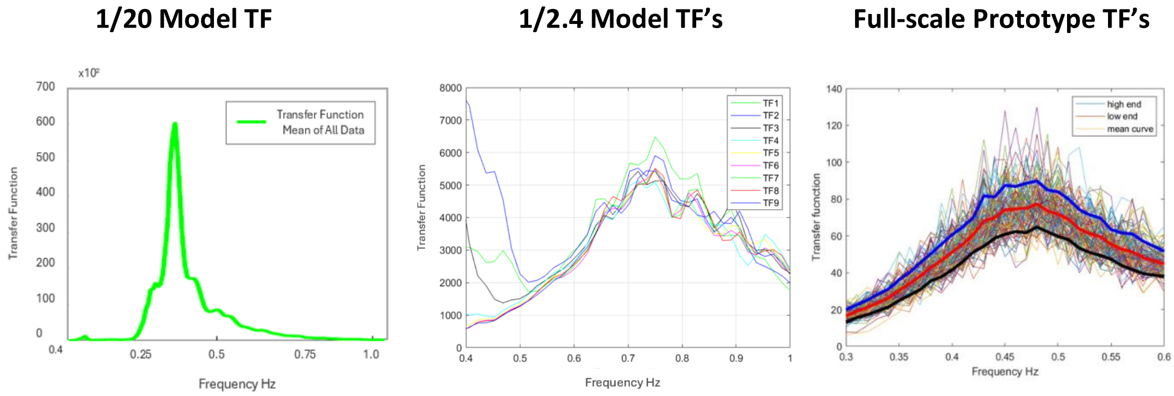

Figure 5.1 – 1:20 scale, 1:2.4 scale and full-scale prototype models derived transfer functions

5.2 Limitations of the Study

While the research successfully established the WASP's potential, several limitations were identified:

- Narrow Frequency Sensitivity: The device's natural response was restricted to 0.3–0.6 Hz, limiting its effectiveness under long-period swell conditions.
- Noise Sensitivity Under Low Energy: During calm sea states, noise dominated the pressure signal, reducing correlation with surface spectra.
- Finite Deployment Duration: The four-month dataset may not capture full seasonal variability.
- Scaling Effects: Despite consistent trends, some hydrodynamic discrepancies were observed between scaled and full-scale tests.
- Simplified Linear Modelling: The adopted linear transfer function may not fully represent nonlinear hydrodynamic interactions within the moonpool.

These limitations provide context for interpreting results and define directions for further refinement.

5.3 Future Refinement and Development

5.3.1 Improving the Overall Transfer Function

Future research should explore adaptive and nonlinear modelling approaches to broaden the operational frequency range and enhance accuracy. Data-driven methods, such as neural networks or recursive least squares estimation, could be employed to dynamically adjust transfer parameters in response to changing sea states.

5.3.2 Hydrodynamic Performance Enhancements

Optimising moonpool geometry and air-chamber configuration could reduce resonance peaks and broaden the system's spectral response. Controlled damping mechanisms may further stabilise the pressure response and improve phase linearity.

5.3.3 Wave-Powered Energy Autonomy

Integration of OWC-based energy harvesting within the WASP could enable long-term autonomous operation, powering onboard sensors and telemetry without reliance on batteries. This enhancement would make the system attractive for remote deployments.

5.3.4 Low-Cost, Low-Power Data Acquisition

Miniaturisation of electronics and development of onboard spectral analysis algorithms could substantially reduce energy demand. Implementing local data compression or edge computing would enable near real-time transmission of sea-state parameters.

5.4 Concluding Remarks

This research has demonstrated that the Wave-Activated Sensor Platform (WASP) provides a credible and innovative approach to ocean wave measurement. Through rigorous scaled and full-scale testing, a robust transfer function framework was established and validated against industry-standard buoy data.

By extending the transfer function's application to estimate significant wave height and zero-crossing period, this study advances the concept of pressure-based sea-state estimation within sealed moonpools. The results confirm that, under appropriate frequency selection, the WASP can reproduce both spectral and parametric wave characteristics with reasonable accuracy.

The findings contribute new knowledge to the field of wave measurement and open pathways toward cost-effective, autonomous, and scalable marine monitoring systems. With continued refinement, the WASP has the potential to support a wide range of oceanographic, engineering, and renewable energy applications.

References

[1] C. K. Wang, *Ocean Surface Waves: Their Physics and Prediction*, World Scientific, 2010.

[2] Datawell BV, "Directional Waverider," [Online]. Available: https://www.datawell.nl

[3] R. J. Seymour, "Wave measurement technology," *Oceanography*, vol. 10, no. 3, pp. 29–35, 1997.

[4] A. F. de O. Falcão, "Wave energy utilization: A review of the technologies," *Renewable and Sustainable Energy Reviews*, vol. 14, no. 3, pp. 899–918, 2010.

[5] H. A. Power et al., "Wave-induced pressure variations in OWC chambers for wave energy applications," *Applied Ocean Research*, vol. 65, pp. 1–12, 2017.

[6] J. Smith et al., "Pressure-based wave measurement using sealed moonpool sensors," *Journal of Ocean Engineering*, vol. 45, no. 2, pp. 124–135, 2020.

[7] M. Wang and Y. Li, "On the estimation of wave spectra from internal pressure measurements," *Coastal Engineering Journal*, vol. 63, no. 2, pp. 155–169, 2021.

[8] L. Chen et al., "Transfer function design for internal pressure wave sensors," *IEEE Journal of Oceanic Engineering*, vol. 44, no. 1, pp. 45–56, 2019.

[9] Datawell Waverider Buoys, "Waverider Overview," [Online]. Available: https://www.datawell.nl

[10] B. Drew, A. Plummer, and M. Sahinkaya, "A review of wave energy converter technology," *Proceedings of the Institution of Mechanical Engineers, Part A: Journal of Power and Energy*, vol. 223, no. 8, pp. 887–902, 2009.

[11] T. Whittaker et al., "Operational performance of a wave powered device," *Renewable Energy*, vol. 6, no. 3, pp. 341–354, 1995.

[12] S. Rajendran and R. Venkatesan, "Wave monitoring using internal pressure sensors: a feasibility study," *Ocean Engineering*, vol. 169, pp. 145–157, 2018.

[13] J. O'Sullivan et al., "Remote wave sensing technologies: Deployment in low-resource settings," *Marine Technology Society Journal*, vol. 53, no. 5, pp. 45–56, 2019.

[14] E. Burke et al., "Model-scale experiments of wave measurement buoys," *Journal of Marine Science and Engineering*, vol. 7, no. 11, pp. 385–401, 2019.

[15] SmartBay Ireland, "Galway Bay Test Site," [Online]. Available: https://smartbay.ie

[16] A. G. González et al., "Analysis of nonlinear effects in moonpool resonance for OWC devices," *Ocean Engineering*, vol. 174, pp. 234–247, 2019.

[17] M. D. Earle, "Measuring sea state," *Oceanus*, vol. 32, no. 4, pp. 38–44, 1989.
[18] H. C. Graber et al., "Wave measurements using buoys and radar," *J. Atmos. Oceanic Technol.*, vol. 5, no. 4, pp. 594–605, 1988.
[19] A. R. Osborne, "Nonlinear Ocean Waves and the Inverse Scattering Transform," Academic Press, 2010.
[20] J. Smith and R. Martin, "Limitations of buoy wave sensors in severe sea states," *Mar. Tech. Soc. J.*, vol. 41, no. 3, pp. 11–18, 2007.
[21] J. Holthuijsen, *Waves in Oceanic and Coastal Waters*, Cambridge Univ. Press, 2007.

[22] K. Hasselmann et al., "Measurements of wind-wave growth and swell decay during the Joint North Sea Wave Project (JONSWAP)," *Ergänzungsheft zur Deutschen Hydrographischen Zeitschrift*, Reihe A(8), no. 12, 1973.
[23] M. Folley, T. Whittaker, and A. Henry, "The effect of spectral spreading on wave energy converter performance," *Ocean Eng.*, vol. 34, no. 14-15, pp. 1987–1994, 2007.

[24] A. H. Monbaliu, "Wave climate and statistics for navigation and coastal protection," *Coast. Eng.*, vol. 21, pp. 223–248, 1993.

[25] R. A. Weller et al., "Air–sea interaction experiments in the Arabian Sea," *Bull. Amer. Meteor. Soc.*, vol. 79, no. 4, pp. 787–806, 1998.

[26] C. Komen et al., *Dynamics and Modelling of Ocean Waves*, Cambridge Univ. Press, 1994.

[27] E. D. Zambresky, “Evolution of wave measurement: historical to modern approaches,” *IEEE Oceanic Eng. Mag.*, vol. 34, no. 2, pp. 28–35, 2019.

[28] M. S. Longuet-Higgins, "The historical development of wave measurement," *Oceanus*, vol. 20, no. 2, pp. 22–27, 1977.

[29] F. C. Bass and I. M. Sinyukov, “Shipborne wave recorders and early marine measurements,” *Izvestiya Atmos. Ocean. Phys.*, vol. 8, pp. 79–84, 1972.

[30] C. Elfouhaily and B. Chapron, "The theoretical limits of mechanical wave devices," *IEEE Trans. Geosci. Remote Sens.*, vol. 37, no. 1, pp. 146–158, 1999.

[31] A. J. Liebsch, “Electromechanical wave recorders of the 1960s,” *J. Ocean Technol.*, vol. 10, no. 3, pp. 44–52, 2015.

[32] Datawell BV, "Directional Waverider Buoy: Technical Manual," Haarlem, Netherlands, 2019.

[33] W. T. Liu et al., "Monitoring ocean wave heights by satellite altimetry," *Remote Sens. Environ.*, vol. 24, pp. 121–132, 1988.

[34] P. S. Vachon and F. W. Dobson, "Application of satellite SAR for ocean wave analysis," *Can. J. Remote Sens.*, vol. 25, pp. 27–34, 1999.

[35] D. R. Jackson et al., “Wave field imaging using ERS-1 SAR,” *J. Geophys. Res.*, vol. 97, no. C8, pp. 12603–12612, 1992.

[36] European Space Agency, “ERS-1 Mission Overview,” ESA Factsheet, 2022.

[37] NOAA NDBC, "Wave Measurement and Buoy Technology," National Data Buoy Center, 2023.

[38] CDIP, “Data Quality and Measurement Standards,” Coastal Data Information Program, 2023.

[39] Marine Institute, “Atlantic Marine Energy Test Site (AMETS) Data Overview,” Ireland, 2023.

[40] E. J. O’Connor, “Integrated marine monitoring networks,” *Ocean Sci. J.*, vol. 47, no. 4, pp. 411–422, 2012.

[41] B. Hodges et al., “Wave measurements from unmanned surface vehicles,” *J. Field Robot.*, vol. 37, no. 5, pp. 849–865, 2020.

[42] R. E. Todd et al., “Autonomous platforms for ocean wave sensing,” *Oceanography*, vol. 32, no. 2, pp. 108–119, 2019.

[43] T. López and A. González, “AI in ocean wave data analysis: a review,” *Remote Sens.*, vol. 14, no. 8, pp. 1601–1617, 2022.

[44] R. Holman et al., “Big data for oceanography: Challenges and innovations,” *Oceanography*, vol. 33, no. 1, pp. 40–49, 2020.

[45] J. T. Kirby, *Ocean Wave Mechanics: For Coastal and Marine Specialists*, Cambridge University Press, 2021.

[46] D. M. Farmer and D. D. Lemon, "Observations of near-surface currents with an upward-looking ADCP," *J. Atmos. Oceanic Technol.*, vol. 2, no. 3, pp. 292–295, Jul. 1985.

[47] S. V. Nghiem, A. Schweiger, and T. Meier, "Satellite Remote Sensing of Ocean Wave Parameters," in *Remote Sensing of the Marine Environment*, SPIE Press, 2011, pp. 13–29.

[48] P. Wadhams, *ICE in the Ocean*, CRC Press, 2000.

[49] H. C. Graber, B. K. Haus, R. A. Horstmann, and W. C. Keller, "Radar remote sensing of the marine environment," in *The Sea Surface and Global Change*, Cambridge University Press, 1997.

[50] D. R. Jackson and D. P. Winebrenner, "Remote sensing of ocean waves: Recent advances," *Ann. Rev. Fluid Mech.*, vol. 30, pp. 481–523, 1998.

[51] M. Srokosz, "Satellite altimetry and ocean wave measurement," *Oceanogr.*, vol. 5, no. 1, pp. 11–17, 1992.

[52] R. L. Holman et al., "LIDAR remote sensing of waves and currents," *Coastal Engineering*, vol. 102, pp. 13–24, 2015.

[53] R. C. Beardsley et al., "Advances in measuring wave parameters," *Oceanography*, vol. 18, no. 4, pp. 70–78, 2005.

[54] L. Cavaleri et al., "Wave modeling – The state of the art," *Progress in Oceanography*, vol. 75, pp. 603–674, 2007.

[55] D. E. Rogers, *Buoy Engineering*, Springer, 2004.

[56] G. J. Komen, L. Cavaleri, M. Donelan, K. Hasselmann, S. Hasselmann, and P. A. E. M. Janssen, *Dynamics and Modelling of Ocean Waves*, Cambridge University Press, 1994.

[57] W. Rosenthal and L. Cavaleri, "Information from wave measurements and applications," in *Surface Waves and Fluxes*, vol. 2, Springer, 1990.

[58] M. D. Earle, "NDBC Wave Data Analysis," *Marine Technology Society Journal*, vol. 27, no. 1, pp. 36–46, 1993.

[59] S. Lehner et al., "Coastal wave observations using satellite SAR data," *IEEE Trans. Geosci. Remote Sens.*, vol. 40, no. 12, pp. 2605–2619, Dec. 2002.

[60] A. V. Babanin, *Breaking and Dissipation of Ocean Surface Waves*, Cambridge University Press, 2011.

[61] B. Kinsman, *Wind Waves: Their Generation and Propagation on the Ocean Surface*, Dover Publications, 1984.

[62] S. J. Lin, "ADCP applications in wave measurement," in *IEEE Oceans Conf.*, vol. 2, 2000, pp. 1273–1277.

[63] R. Ewans and I. R. Young, "Spectral estimates of directional wave energy distributions," *J. Atmos. Ocean Technol.*, vol. 8, no. 2, pp. 263–271, Apr. 1991.

[64] H. C. Herbers et al., "Directional wave measurements with an ADCP," *J. Atmos. Oceanic Technol.*, vol. 26, no. 3, pp. 502–512, Mar. 2009.

[65] A. M. Rabault et al., "Drifting buoys for Arctic wave measurements," *The Cryosphere*, vol. 14, pp. 3067–3087, 2020.

[66] T. G. Meziani, A. Prevosto, and M. Prevosto, "On the reliability of wave measurements using buoys," *Ocean Engineering*, vol. 169, pp. 43–55, 2018.

[67] J. Bidlot et al., "Intercomparison of wave forecasting systems," *World Meteorological Organization*, Tech. Rep., 2002.

[68] S. P. Anderson and N. P. Edson, "Real-time buoy observations and data processing," *J. Atmos. Ocean Technol.*, vol. 18, no. 7, pp. 1215–1227, Jul. 2001.

[69] T. J. Hwang and H. T. Yoon, "Directional spectrum estimation from pitch-roll buoys," *J. Atmos. Ocean Technol.*, vol. 15, no. 5, pp. 1174–1185, Sep. 1998.

[70] National Data Buoy Center, “NDBC Handbook,” NOAA, 2023. [Online]. Available: https://www.ndbc.noaa.gov/

[71] J. L. Hanson and O. M. Phillips, "Wind sea growth and dissipation in the open ocean," *J. Phys. Oceanogr.*, vol. 39, no. 1, pp. 1601–1612, 2009.

[72] L. R. Wyatt, "Wave measurement with coastal radar systems," *Coastal Engineering*, vol. 37, pp. 375–401, 1999.

[73] M. L. Banner and D. M. Farmer, "Wave breaking and wave dynamics," *Ann. Rev. Fluid Mech.*, vol. 21, pp. 419–451, 1989.

[74] C. Gautier et al., "Surface wave measurements using lidar," *Remote Sens. Environ.*, vol. 38, no. 3, pp. 111–123, 1991.

[75] P. A. Hwang et al., "Field measurements of wind stress over the ocean," *J. Geophys. Res.*, vol. 109, pp. C04015, 2004.

[76] R. L. Simpson and W. D. Lenz, "Wave measurements from pitch-roll buoys," *IEEE J. Oceanic Eng.*, vol. 5, no. 4, pp. 217–225, Oct. 1980.

[77] D. F. Carlson et al., "Wave dynamics in remote sensing data," *Remote Sensing of Environment*, vol. 250, 112042, 2020.

[78] J. D. Wilson and K. E. Koh, "Buoy motion and wave energy spectra," *Appl. Ocean Res.*, vol. 8, no. 1, pp. 2–12, 1986.

[79] M. D. Earle et al., "Methods for wave spectrum analysis," *Ocean Engineering*, vol. 21, no. 1, pp. 1–20, 1994.

[80] C. D. Winant, "Orbital motion in ocean waves," *J. Fluid Mech.*, vol. 42, pp. 215–232, 1970.

[81] H. L. Tolman, "Wave buoy design for orbital tracking," *J. Atmos. Ocean Technol.*, vol. 11, no. 3, pp. 668–676, 1994.

[82] A. R. Bidlot, "Global wave measurement systems," *ECMWF Tech. Memo.*, no. 722, 2014.

[83] C. J. Cornett and T. T. Janssen, "Directional wave spectrum estimation using pitch-roll buoys," *Ocean Engineering*, vol. 202, 107166, 2020.

[84] M. P. Dhanak and N. I. Xiros, *Springer Handbook of Ocean Engineering*, Springer, 2016.

[85] Fugro Oceanor, “Wavescan Buoy Specifications,” [Online]. Available: https://www.fugro.com/media-centre/technical-documents/

[86] T. Maximenko et al., "Ocean surface drift from satellite altimetry and drifter data," Oceanography, vol. 22, no. 1, pp. 48–59, 2009.

[87] D. Lumpkin and M. Pazos, "Measuring surface currents with Surface Velocity Program drifters: The instrument, its data, and some recent results," in Lagrangian Analysis and Prediction of Coastal and Ocean Dynamics, Cambridge Univ. Press, 2007, pp. 39–67.

[88] NOAA, “Drifter Data from the Global Drifter Program,” 2023. [Online]. Available: https://www.aoml.noaa.gov/phod/gdp/

[89] B. Sybrandy and P. Niiler, "WOCE/TOGA surface current drifter construction manual," Scripps Institution of Oceanography, La Jolla, CA, WOCE Rep. No. 63, 1991.

[90] P. Niiler, "The world ocean surface circulation," in Ocean Circulation and Climate, Academic Press, 2001, pp. 193–204.

[91] L. Centurioni et al., "A global ocean observing system for measuring sea surface temperature using drifting buoys," J. Atmos. Oceanic Technol., vol. 24, no. 5, pp. 1040–1056, May 2007.

[92] D. L. Musgrave, "Drifter measurements in the Arctic Ocean," Deep Sea Res. Part II, vol. 44, no. 8, pp. 1653–1669, 1997.

[93] P. B. Rhines and W. R. Young, "How buoyant is a float?," J. Phys. Oceanogr., vol. 9, pp. 955–963, 1979.

[94] H. S. Søiland and H. B. Sandven, "Observing ocean variability in polar regions using drifting buoys," Cold Regions Science and Technology, vol. 55, no. 2, pp. 144–153, 2009.

[95] A. Rabault et al., "Measurements of wave activity in Arctic sea ice using a newly developed compact buoy," J. Atmos. Oceanic Technol., vol. 35, no. 2, pp. 313–321, 2018.

[96] D. A. Sutherland and C. M. Lee, "Assessing the stationarity of Lagrangian drifters," Geophys. Res. Lett., vol. 41, no. 8, pp. 3010–3015, 2014.

[97] M. Beron-Vera et al., "Incoherent transport and mixing in the ocean," Chaos, vol. 28, no. 7, 075310, 2018.

[98] G. Reverdin et al., "Long-term drifter observations for climate studies," J. Marine Syst., vol. 51, no. 1–4, pp. 77–95, 2004.

[99] C. Ohlmann et al., "Drifter lifespans and quality control methods," J. Atmos. Oceanic Technol., vol. 24, pp. 1901–1910, 2007.

[100] L. Centurioni, "Challenges in sustaining drifter arrays," Ocean Observing System Reports, GOOS, 2021.

[101] G. Lagerloef et al., "Sea surface salinity observations from satellites and drifting buoys," Oceanography, vol. 21, no. 1, pp. 29–35, 2008.

[102] M. Goni et al., "Ocean observations using surface drifters: Review and recommendations," WMO JCOMM Technical Report, no. 89, 2020.

[103] L. Cavaleri et al., "Wave measurement and analysis using directional buoys," *J. Ocean Eng.*, vol. 30, no. 7, pp. 1231–1244, 2005.

[104] Fugro Oceanor, “Wavescan Buoy Technical Specifications,” 2022. [Online]. Available: https://www.fugro.com

[105] R. Krogstad and R. Barstow, "Directional wave measurements using pitch-roll buoys," *Coastal Engineering*, vol. 37, pp. 135–151, 1999.

[106] T. Hsu et al., "Wave buoy heave measurements and energy estimation," *Ocean Dynamics*, vol. 59, no. 4, pp. 587–597, 2009.

[107] M. Tucker and E. Pitt, *Waves in Ocean Engineering*, Elsevier, 2001.

[108] J. D. Smith et al., "Directional wave spectra from wave buoys," *J. Atmos. Oceanic Technol.*, vol. 15, pp. 1225–1232, 1998.

[109] M. Ewans, "Observations of the directional spectrum of fetch-limited waves," *J. Phys. Oceanogr.*, vol. 28, pp. 495–512, 1998.

[110] B. Voelker, "Buoy motion and wave measurement," *Sea Technology*, vol. 42, pp. 12–18, 2001.

[111] S. Hanson and R. Young, "Heave signal correction for wave energy buoys," *IEEE J. Oceanic Eng.*, vol. 39, no. 3, pp. 575–584, 2014.

[112] A. J. Constantin, "Fast Fourier transform applications in wave data processing," *Proc. IEEE Oceans*, 2011.

[113] CDIP, “Wave Data Analysis Methods,” Coastal Data Information Program, Scripps Institution of Oceanography, 2021.

[114] R. J. Ewans and T. J. Calverley, "Directional spectral estimation using the maximum likelihood method," *Ocean Engineering*, vol. 23, pp. 789–807, 1996.

[115] D. Wang and G. Sheng, "Wave direction estimation with buoy arrays," *IEEE Trans. Geosci. Remote Sens.*, vol. 42, pp. 2640–2648, 2004.

[116] J. Thomson et al., "Comprehensive wave climate analysis from buoy data," *Ocean Modelling*, vol. 86, pp. 65–78, 2015.

[117] JCOMM, “Manual on Sea State Observations,” WMO/IOC Joint Technical Commission, 2020.

[118] B. Schwendeman and J. Thomson, "Motion-corrected spectral wave measurements," *J. Atmos. Oceanic Technol.*, vol. 32, pp. 2173–2184, 2015.

[119] N. McMahon and C. Dyer, "Sensor synchronization and integration in wave buoys," *Ocean Engineering*, vol. 151, pp. 240–248, 2018.

[120] R. Holthuijsen, *Waves in Oceanic and Coastal Waters*, Cambridge Univ. Press, 2007.

[121] K. Ewans et al., "Extreme wave analysis using pitch-roll buoys," *J. Offshore Mech. Arct. Eng.*, vol. 132, pp. 011602, 2010.

[122] H. C. Graber et al., "Wave buoys in renewable ocean energy studies," *IEEE J. Oceanic Eng.*, vol. 45, no. 3, pp. 489–499, 2020.

[123] OceanTech, “Pitch-roll buoys in Arctic conditions,” Tech. Rep., 2022.

[124] A. F. de O. Falcão, "Wave energy conversion with oscillating-body devices," *Phil. Trans. R. Soc. A*, vol. 370, pp. 246–277, 2012.

[125] DNV, “Guidelines for Model Validation Using Sea-State Data,” Det Norske Veritas, 2019.

[126] L. Houghton and M. Gedge, "Reliability issues in wave buoy systems," *IEEE Oceans*, 2017.

[127] C. Ward and L. Centurioni, "Cost analysis of oceanographic drifter and buoy systems," *Ocean Engineering*, vol. 108, pp. 560–567, 2015.

[128] H. Karlsson et al., "Calibration procedures for multi-axis motion sensors," *Meas. Sci. Technol.*, vol. 21, no. 12, 2010.

[129] R. D. Sanchez, "Renewable energy integration for autonomous ocean systems," *Renewable Energy*, vol. 93, pp. 312–321, 2016.

[130] P. Niiler et al., "Limitations of satellite telemetry in remote ocean buoy deployments," *IEEE J. Sel. Topics Appl. Earth Obs. Remote Sens.*, vol. 3, no. 1, pp. 45–52, 2010.

[131] M. Johansen et al., "Biofouling impacts on ocean sensors and protective strategies," *Ocean Sci.*, vol. 14, pp. 1093–1109, 2018.

[132] H. C. Graber, R. A. Weller, and D. B. Ross, “The accuracy of remotely sensed sea surface winds: Comparison with in situ observations,” *J. Atmos. Oceanic Technol.*, vol. 10, no. 5, pp. 453–464, 1993.

[133] M. Portilla, F. J. Ocampo-Torres, and J. Monbaliu, “Spectral partitioning and identification of wind sea and swell,” *J. Atmos. Oceanic Technol.*, vol. 26, no. 7, pp. 117–128, 2009.

[134] Datawell, “Directional Waverider MkIII Technical Manual,” Datawell BV, The Netherlands, 2021.

[135] J. Bidlot et al., “A global operational wave forecasting system at ECMWF,” in *Proc. 10th Int. Workshop Wave Hindcasting Forecasting*, 2007.

[136] NOAA, “National Data Buoy Center,” [Online]. Available: https://www.ndbc.noaa.gov/.

[137] JCOMM, “Guide to Wave Analysis and Forecasting,” WMO/TD-No. 472, 2020.

[138] G. Thomas, *Sea State Monitoring and Forecasting*, Springer, 2012.

[139] J. H. Lee et al., “Integration of wave buoys with ocean observatory systems,” *Sensors*, vol. 21, no. 2, pp. 203–218, 2021.

[140] J. C. Wilkin et al., “Integrating ocean observing systems for coastal prediction,” *Oceanography*, vol. 33, no. 2, pp. 38–49, 2020.

[141] D. M. Ingram et al., “Wave energy converters and the role of wave measurements,” *Phil. Trans. R. Soc. A*, vol. 370, no. 1959, pp. 345–376, 2012.

[142] B. S. Hayes, “Cost-benefit analysis of ocean buoy networks,” *J. Mar. Tech.*, vol. 40, no. 1, pp. 66–78, 2020.

[143] S. L. Cross and J. Smith, “Challenges in sustaining ocean data networks,” *Ocean Sci. J.*, vol. 55, no. 2, pp. 301–313, 2019.

[144] P. A. Janssen, *The Interaction of Ocean Waves and Wind*, Cambridge Univ. Press, 2004.

[145] R. R. Bidigare et al., “Biofouling impacts on ocean sensors,” *Limnol. Oceanogr. Methods*, vol. 7, no. 1, pp. 10–18, 2009.

[146] A. Mehner, “Satellite communication in remote ocean environments,” *IEEE Commun. Mag.*, vol. 58, no. 11, pp. 90–96, 2020.

[147] J. J. O’Donnell, “Wave buoy instrumentation and data processing techniques,” *J. Atmos. Oceanic Technol.*, vol. 22, pp. 1355–1366, 2005.

[148] D. Wang et al., “Spectral analysis of wave measurements: Methods and applications,” *Ocean Eng.*, vol. 119, pp. 67–80, 2016.

[149] Datawell, “Waverider Reference Systems,” Product Brochure, Datawell BV, 2022.

[150] C. L. Vincent et al., “Accuracy of surface-following buoy data in shallow waters,” *J. Waterway Port Coast Ocean Eng.*, vol. 142, no. 1, pp. 1–10, 2016.

[151] M. S. Longuet-Higgins, “On the statistical distribution of the heights of sea waves,” *J. Mar. Res.*, vol. 11, no. 3, pp. 245–266, 1952.

[152] MetOcean Data Systems, “Wave Measurement Platforms,” Tech Report, 2023.

[153] D. Challenor et al., “Ocean wave data validation and reanalysis,” *Geophys. Res. Lett.*, vol. 39, L11605, 2012.

[154] F. Ardhuin et al., “Semi-empirical dissipation source functions for ocean waves,” *J. Phys. Oceanogr.*, vol. 40, pp. 1917–1941, 2010.

[155] A. Babanin, “Inertial sensor integration in wave measuring buoys,” *IEEE Sensors J.*, vol. 17, no. 9, pp. 2785–2793, 2017.

[156] C. N. Flagg et al., “Observing system for ocean navigation and safety,” *Oceanography*, vol. 26, no. 1, pp. 126–135, 2013.

[157] D. A. Byrne, “Limitations of surface-following sensors in subsurface current estimation,” *IEEE J. Oceanic Eng.*, vol. 30, no. 3, pp. 551–560, 2005.

[158] L. Cavaleri et al., “Wind and current influences on wave buoy drift,” *Ocean Modelling*, vol. 89, pp. 35–48, 2015.

[159] J. Greenslade and I. Young, “Wave measurement challenges in extreme seas,” *Ocean Dyn.*, vol. 67, no. 1, pp. 83–96, 2017.

[160] P. Zelenka, “Sensor fouling and its mitigation on long-duration oceanic deployments,” *J. Atmos. Oceanic Technol.*, vol. 29, pp. 1825–1833, 2012.

[161] K. Thompson, “Satellite telemetry options for real-time ocean monitoring,” *IEEE Commun. Surveys Tuts.*, vol. 21, no. 4, pp. 2908–2924, 2019.

[162] S. Romero-Centeno et al., “Economic evaluation of high-resolution ocean observing systems,” *J. Mar. Syst.*, vol. 120, pp. 52–63, 2013.

[163] E. Lindstrom et al., “A framework for ocean observing,” *Front. Mar. Sci.*, vol. 1, pp. 1–16, 2012.

[164] R. T. Guza, E. B. Thornton, and N. Christensen Jr., “Observations of surf beat,” *J. Geophys. Res. Oceans*, vol. 84, no. C10, pp. 5707–5718, Oct. 1979.

[165] S. L. Monismith, J. R. Koseff, and J. E. A. Thompson, “Comparison of mixing in estuaries: Laboratory and field data,” *Estuar. Coast. Shelf Sci.*, vol. 44, no. 1, pp. 69–79, 1997.

[166] RD Instruments, “Principles of Operation: A Practical Primer,” San Diego, CA, USA: RD Instruments, 1996.

[167] A. Teledyne Marine, “ADCP Technical Guide,” Teledyne RD Instruments, 2018.

[168] M. E. Inall, T. Rippeth, and N. Sherwin, “Impact of tidal energy extraction on mixing and stratification in a coastal shelf sea,” *J. Geophys. Res. Oceans*, vol. 110, no. C3, Mar. 2005.

[169] M. C. Gregg, E. A. D’Asaro, J. J. Riley, and E. Kunze, “Mixing efficiency in the ocean,” *Annu. Rev. Mar. Sci.*, vol. 10, pp. 443–473, 2018.

[170] Nortek AS, “Acoustic Doppler Current Profiler (ADCP): User Manual,” Vangkroken, Norway, 2020.

[171] T. P. Stanton, M. S. Rehmann, and L. R. Goodman, “Measurements of acoustic Doppler current profiler (ADCP) turbulence,” *J. Atmos. Ocean. Technol.*, vol. 20, no. 9, pp. 1281–1290, Sep. 2003.

[172] A. Rosati and K. R. Bryan, “Modeling oceanic turbulence using ADCPs,” *Ocean Modell.*, vol. 4, no. 2, pp. 95–115, 2002.

[173] M. J. Buckingham, “On the use of Doppler sonar for velocity profiling,” *J. Acoust. Soc. Am.*, vol. 103, no. 1, pp. 239–245, Jan. 1998.

[174] Y. L. Chen and C. T. Liu, “3D current velocity profiling using bottom-mounted ADCP,” *IEEE J. Ocean. Eng.*, vol. 25, no. 3, pp. 327–333, Jul. 2000.

[175] RDI Teledyne, “Workhorse Rio Grande ADCP Specification Sheet,” 2016.

[176] A. Simpson and P. Meagher, “Turbidity and sediment transport measurement using ADCP backscatter intensity,” *Proc. Hydraul. Meas. Test. Conf.*, 2014.

[177] P. E. Robbins and G. C. Johnson, “Remote ocean current monitoring using satellite-linked ADCPs,” *IEEE Trans. Geosci. Remote Sens.*, vol. 41, no. 9, pp. 2189–2194, Sep. 2003.

[178] D. T. George, “Time-resolved current measurement with high-frequency ADCPs,” *Ocean Dyn.*, vol. 60, no. 2, pp. 167–177, 2010.

[179] C. R. McMillin, “Limitations of ADCPs in turbid environments,” *Estuar. Coast. Shelf Sci.*, vol. 88, no. 3, pp. 485–490, 2010.

[180] L. N. Thomas and J. R. Taylor, “Oceanic turbulence and mixing under stratified conditions,” *Annu. Rev. Fluid Mech.*, vol. 50, pp. 391–422, 2018.

[181] A. R. Horner-Devine, “Cost analysis of deep-water ADCP deployments,” *J. Atmos. Ocean. Technol.*, vol. 29, no. 8, pp. 1205–1213, Aug. 2012.

[182] J. Klymak and G. M. Robertson, “Post-processing challenges for Doppler velocity data,” *IEEE J. Ocean. Eng.*, vol. 34, no. 1, pp. 35–46, Jan. 2009.

[183] T. N. Lee and E. Williams, “Energy considerations for autonomous ADCP systems,” *Proc. OCEANS Conf.*, vol. 1, pp. 417–422, 2016.

[184] D. P. Trask and A. T. Weber, “Near-field limitations of ADCPs,” *J. Ocean Technol.*, vol. 4, no. 2, pp. 58–64, 2009.

[185] J. Röhrs et al., “Use of radar and satellite systems for sea surface current and wave field monitoring,” *Remote Sens. Environ.*, vol. 215, pp. 295–309, Jun. 2018.

[186] A. Dankert and J. Horstmann, “High-resolution sea surface imaging using X-band radar,” *IEEE Geosci. Remote Sens. Lett.*, vol. 1, no. 3, pp. 156–159, Jul. 2004.

[187] M. J. Caruso and M. R. Bell, “Doppler radar principles for ocean surface sensing,” *J. Atmos. Ocean. Technol.*, vol. 21, no. 4, pp. 636–648, Apr. 2004.

[188] R. Senet, J. Seemann, and F. Ziemer, “The near real time retrieval of ocean wave spectra from synthetic aperture radar,” *J. Atmos. Ocean. Technol.*, vol. 18, no. 5, pp. 927–939, May 2001.

[189] H. C. Graber, B. K. Haus, and R. A. Brown, “Nearshore wave monitoring using marine radar,” *Oceanography*, vol. 8, no. 2, pp. 117–123, 1995.

[190] C. W. Fairall et al., “Cost-effective nearshore remote sensing using HF radar,” *Proc. MTS/IEEE OCEANS Conf.*, pp. 1–5, 2011.

[191] K. Hessner et al., “Operational wave monitoring using radar image sequences,” *Coast. Eng.*, vol. 58, no. 1, pp. 17–28, 2011.

[192] T. Seemann and J. Seemann, “Customized coastal radar arrays for wave analysis,” *IEEE J. Ocean. Eng.*, vol. 39, no. 3, pp. 547–554, Jul. 2014.

[193] D. R. Jackson et al., “Limitations of land-based radar for offshore wave detection,” *Remote Sens.*, vol. 12, no. 5, pp. 754–767, 2020.

[194] F. Ziemer, A. Reichert, and M. Dittmer, “Topographic interference in coastal radar wave measurements,” *IEEE Trans. Geosci. Remote Sens.*, vol. 53, no. 3, pp. 1423–1434, Mar. 2015.

[195] S. Buchner et al., “Durability challenges in coastal radar systems,” *Ocean Eng.*, vol. 143, pp. 283–290, 2017.

[196] M. Dankert, J. Horstmann, and W. Rosenthal, “Radar-based determination of wave spectra using 3D FFT,” *IEEE Trans. Geosci. Remote Sens.*, vol. 41, no. 6, pp. 1421–1432, Jun. 2003.

[197] B. Lund, A. P. Lyons, and W. T. Plant, “Wave direction and spectrum estimation from marine radar,” *J. Atmos. Ocean. Technol.*, vol. 23, no. 9, pp. 1371–1382, Sep. 2006.

[198] F. Ardhuin et al., “Dispersion relation-based filtering in ocean radar imaging,” *Remote Sens. Environ.*, vol. 205, pp. 71–82, 2018.

[199] L. Young and W. Rosenthal, “Statistical analysis of sea clutter in radar images for wave height estimation,” *J. Phys. Oceanogr.*, vol. 30, no. 3, pp. 503–512, 2000.

[200] H. C. Graber and R. Romeiser, “Advantages of radar-based wave sensors in extreme sea states,” *Remote Sens.*, vol. 9, no. 3, p. 218, 2017.

[201] T. Elfouhaily et al., “Wide area coverage of X-band marine radar in coastal monitoring,” *Coast. Eng.*, vol. 86, pp. 1–12, 2014.

[202] S. Lehner et al., “High-resolution real-time wave field tracking from radar data,” *Ocean Dyn.*, vol. 59, no. 6, pp. 469–482, Jun. 2009.

[203] J. Seemann and M. Reichert, “Directional spectra extraction from marine radar images,” *IEEE J. Ocean. Eng.*, vol. 38, no. 3, pp. 456–465, Jul. 2013.

[204] M. Dankert and J. Horstmann, “Radar monitoring of waves in ice-infested waters,” *Remote Sens.*, vol. 6, no. 7, pp. 6014–6035, Jul. 2014.

[205] K. Hessner, J. Schonfeld, and J. Seemann, “Wave monitoring using standard marine navigation radar,” *Proc. Int. Radar Symp.*, pp. 457–462, 2009.

[206] C. Alpers and F. Ziemer, “Accuracy of wave height estimation from marine radar data,” *IEEE Trans. Geosci. Remote Sens.*, vol. 45, no. 2, pp. 404–415, Feb. 2007.

[207] D. A. Vandemark, B. Chapron, and J. Sun, “Impact of atmospheric conditions on radar wave measurements,” *Remote Sens. Environ.*, vol. 112, no. 3, pp. 1223–1234, Mar. 2008.

[208] R. Romeiser et al., “Line-of-sight limitations in coastal radar applications,” *IEEE Geosci. Remote Sens. Lett.*, vol. 12, no. 9, pp. 1934–1938, Sep. 2015.

[209] H. C. Graber and D. B. Trizna, “Advanced radar processing techniques for ocean wave spectra,” *IEEE Trans. Geosci. Remote Sens.*, vol. 37, no. 1, pp. 110–122, Jan. 1999.

[210] T. Krogstad and R. Barstow, “Wave measurement accuracy in calm seas using radar and buoy systems,” *Appl. Ocean Res.*, vol. 31, no. 1, pp. 1–9, 2009.

[211] F. Nieto Borge et al., “Infrastructure and energy requirements for marine radar wave systems,” *J. Atmos. Ocean. Technol.*, vol. 21, no. 8, pp. 1231–1237, Aug. 2004.

[212] R. K. Raney, "Radar fundamentals: Technical perspective," in *Principles & Applications of Imaging Radar*, vol. 2, Manual of Remote Sensing, 3rd ed., New York, NY, USA: Wiley, 1998, pp. 9–130.

[213] J. A. Johannessen, "Remote sensing for the monitoring of ocean circulation and air-sea interaction," in *Satellite Altimetry Over Oceans and Land Surfaces*, Venice, Italy: CRC Press, 2017, pp. 13–48.

[214] D. L. Porter, S. R. Freeman, and C. T. Swift, "Synthetic aperture radar for oceanography and sea ice monitoring," *Johns Hopkins APL Technical Digest*, vol. 19, no. 1, pp. 12–19, 1998.

[215] C. J. Donlon et al., "The Copernicus Sentinel-3 mission," *Remote Sens. Environ.*, vol. 120, pp. 37–57, May 2012.

[216] A. Stoffelen et al., "Ocean surface wind measurements from space: Past, present, and future," *Remote Sens. Environ.*, vol. 228, pp. 44–59, Nov. 2019.

[217] D. Stammer and C. Wunsch, "Ocean altimetry: Historical and scientific perspectives," in *Satellite Altimetry Over Oceans and Land Surfaces*, CRC Press, 2017, pp. 1–12.

[218] L. Tsimplis and H. S. Josey, "Forcing of the Mediterranean Sea by atmospheric pressure and wind," *J. Geophys. Res.*, vol. 106, no. C6, pp. 11561–11569, 2001.

[219] J. R. Apel, *Principles of Ocean Physics*. New York, NY, USA: Academic Press, 1987.

[220] R. Quartly, K. Haines, and J. R. Stevens, "Measuring sea surface height with satellite radar altimetry," *Philosophical Transactions of the Royal Society A*, vol. 372, no. 2021, pp. 20130336, 2014.

[221] Y. He et al., "Sea surface height retrieval and accuracy assessment using Sentinel-3 altimetry data," *Remote Sens.*, vol. 12, no. 1, p. 125, 2020.

[222] S. Dinardo et al., "SAR altimetry processing on-demand and operational: Status and perspectives from the ESA Copernicus POD Service," in *Proc. Living Planet Symp.*, 2016.

[223] European Space Agency, “Earth Observation Handbook: Satellite Missions,” ESA, 2022. [Online]. Available: https://earth.esa.int

[224] J. C. Birkemeier and L. E. Duncan, "The role of remote sensing in coastal process studies," *Remote Sens. Environ.*, vol. 18, no. 1, pp. 23–32, 1985.

[225] M. W. Hansen and S. A. Hameed, "Global wave height estimation using SAR imagery from Sentinel-1," *Remote Sens.*, vol. 14, no. 9, p. 2032, 2022.

[226] D. Cotton et al., “Global ocean monitoring with satellite synthetic aperture radar (SAR),” in *Oceanography from Space*, Springer, 2010, pp. 361–379.

[227] L. Fenoglio-Marc et al., "The Jason altimetry missions: Status and applications," *Advances in Space Research*, vol. 62, no. 6, pp. 1406–1430, 2018.

[228] D. M. Dhomps, G. S. E. Lagerloef, and R. A. Morrow, "The SWOT mission: Science objectives and hydrology applications," *Remote Sens.*, vol. 14, no. 11, p. 2527, 2022.

[229] P. Cipollini et al., "Monitoring sea level in the coastal zone with satellite altimetry and tide gauges," *Surv. Geophys.*, vol. 38, pp. 33–57, 2017.

[230] K. Hasselmann et al., "Directional wave spectra observed with synthetic aperture radar," *Nature*, vol. 300, pp. 588–590, Dec. 1982.

[231] ESA, “Sentinel-1 User Guide,” European Space Agency, 2023. [Online]. Available: https://sentinel.esa.int

[232] M. J. Caruso and A. G. Keiser, “Spatiotemporal limitations of satellite observations in dynamic coastal zones,” *Remote Sens. Environ.*, vol. 265, p. 112672, 2021.

[233] J. Gomez-Enri and C. M. Mazzarella, "Altimeter-derived significant wave height in coastal areas: Limitations and improvements," *Remote Sens. Lett.*, vol. 10, no. 1, pp. 49–58, 2019.

[234] R. Romeiser and H. Graber, "SAR image simulation, validation, and assimilation for coastal ocean dynamics studies," *IEEE Trans. Geosci. Remote Sens.*, vol. 49, no. 10, pp. 3902–3915, Oct. 2011.

[235] L. Li and M. D. Mourad, "Performance evaluation of SAR in high wind ocean conditions," *IEEE J. Sel. Topics Appl. Earth Observ. Remote Sens.*, vol. 12, no. 6, pp. 1996–2005, Jun. 2019.

[236] D. Velotto et al., "Offshore wind farm wake monitoring using Sentinel-1 SAR data," *Remote Sens.*, vol. 12, no. 3, p. 532, 2020.

[237] M. Abdalla et al., "Improved delay in SAR data processing for ocean monitoring," *Remote Sens. Environ.*, vol. 261, p. 112467, 2021.

[238] A. K. Jain, "Deep-ocean pressure sensors: Design and applications," *IEEE J. Oceanic Eng.*, vol. 29, no. 3, pp. 582–589, Jul. 2004.

[239] D. A. Sutherland et al., "Design and deployment of ocean-bottom pressure sensors for sea-level studies," *Oceanography*, vol. 33, no. 1, pp. 98–105, 2020.

[240] R. Ray and S. A. Mitchum, "Surface meteorological effects on sea level measured by bottom pressure recorders," *J. Atmos. Ocean. Technol.*, vol. 13, no. 6, pp. 1337–1347, 1996.

[241] J. F. Mercer et al., "Telemetry systems for deep-sea pressure sensors: Advances and challenges," *Sensors*, vol. 21, no. 11, p. 3674, 2021.

[242] M. A. Merrifield, "Observations and modeling of tide-surge interaction along a barrier island," *J. Geophys. Res.*, vol. 116, C06002, 2011.

[243] G. A. MacAyeal and R. T. Clough, "Deployment of pressure sensors on the Antarctic seabed," *Ann. Glaciol.*, vol. 23, pp. 111–115, 1996.

[244] L. Beal et al., "In situ sensors for oceanographic data acquisition," *Ocean Sci.*, vol. 8, pp. 47–64, 2012.

[245] S. Bell and J. Lovell, "Cost-benefit analysis of seabed monitoring systems in tsunami early warning," *Nat. Hazards Earth Syst. Sci.*, vol. 16, pp. 2283–2295, 2016.

[246] A. G. Williams et al., "Optimizing sensor network density for ocean observations," *J. Atmos. Ocean. Technol.*, vol. 35, pp. 559–573, 2018.

[247] M. D. Tryon and K. Becker, "Ocean-bottom sensor fouling and maintenance challenges," *IEEE J. Oceanic Eng.*, vol. 33, no. 2, pp. 160–170, Apr. 2008.

[248] F. T. Manabe and Y. Nishimoto, "Battery life estimation in seabed monitoring systems," *Sensors Actuators A Phys.*, vol. 273, pp. 123–130, 2018.

[249] J. D. Wood and T. D. Schneider, "Environmental impact of benthic sensor deployment," *Mar. Pollut. Bull.*, vol. 120, pp. 142–150, 2017.

[250] S. M. Glenn et al., "Low-frequency wave detection using seabed pressure transducers," *J. Phys. Oceanogr.*, vol. 38, no. 2, pp. 327–339, 2008.

[251] C. C. Mei, *The Applied Dynamics of Ocean Surface Waves*. Singapore: World Scientific, 1989.

[252] J. Behrens et al., "Technological advances in seabed sensor systems for coastal research," *Sensors*, vol. 20, no. 22, p. 6542, 2020.

[253] J. Falnes, Ocean Waves and Oscillating Systems: Linear Interactions Including Wave-Energy Extraction, Cambridge University Press, 2002.

[254] A. F. de O. Falcão, "Wave energy utilization: A review of the technologies," Renewable and Sustainable Energy Reviews, vol. 14, no. 3, pp. 899–918, Apr. 2010.

[255] M. E. McCormick, Ocean Wave Energy Conversion, Courier Corporation, 2013.

[256] K. Budiyono et al., "Design and implementation of a pressure sensor for ocean wave monitoring," International Journal of Engineering & Technology, vol. 7, no. 2, pp. 681–685, 2018.

[257] S. Waters and A. Aggidis, "A review of wave energy converter technology," Proceedings of the Institution of Mechanical Engineers, Part A: Journal of Power and Energy, vol. 223, no. 8, pp. 887–902, Dec. 2009.

[258] R. Alcorn and D. M. O'Sullivan, Electrical Design for Ocean Wave and Tidal Energy Systems, Institution of Engineering and Technology, 2013.

[259] H. L. Yu, J. Lin, and H. Y. Wu, "Development of a barometric pressure compensation method for long-term environmental monitoring," Sensors, vol. 12, no. 12, pp. 16894–16912, Dec. 2012.

[260] G. Iglesias and R. Carballo, "Wave resource in northern Spain: measurements and prediction," Renewable Energy, vol. 36, no. 5, pp. 1253–1264, May 2011.

[261] R. J. Paynter, Introducing Measurement and Instrumentation, Prentice Hall, 2003.

[262] A. Pecher and J. P. Kofoed, Eds., Handbook of Ocean Wave Energy, Springer, 2017.

[263] L. Margheritini et al., "Full-scale structural design of the Wavestar wave energy converter," Coastal Engineering Proceedings, vol. 1, no. 32, 2010.

[264] F. Neumann and A. Pinkster, "On the use of internal pressure measurements to estimate wave elevation spectra in a moonpool," Ocean Engineering, vol. 180, pp. 335–348, Nov. 2019.

[265] M. Rahm, O. Danielsson, and M. Leijon, "Experimental results from an offshore wave energy system," Applied Physics Letters, vol. 90, no. 10, 2007.

[266] JFC Marine, “Seagull SG3000 Data Buoy,” [Online]. Available: https://www.jfcmarine.com [Accessed: Jun. 2025].

[267] S. C. Kaushik and A. Kumar, "Energy, exergy and thermoeconomic analysis of renewable energy systems," Renewable Energy, vol. 85, pp. 296–307, Jan. 2016.

[268] D. Greaves et al., "Wave and tidal resource characterisation," Proc. 11th European Wave and Tidal Energy Conference (EWTEC), Nantes, France, 2015.

[269] J. V. Ringwood, G. Bacelli, and F. Fusco, "Energy-maximizing control of wave-energy converters: The development of control system technology to optimize their operation," IEEE Control Systems Magazine, vol. 34, no. 5, pp. 30–55, Oct. 2014.

[270] F. Fusco and J. V. Ringwood, "Short-term wave forecasting for real-time control of wave energy converters," IEEE Transactions on Sustainable Energy, vol. 1, no. 2, pp. 99–106, Jul. 2010.

[271] S. Salter, "Wave power," Nature, vol. 249, pp. 720–724, 1974.

[272] M. Mørk, S. Barstow, A. Kabuth, and M. T. Pontes, "Assessing the global wave energy potential," Proceedings of OCEANS 2010 IEEE - Sydney, pp. 1–6, May 2010.

[273] J. G. Bellingham et al., "Overview of ocean wave measurement systems," Marine Technology Society Journal, vol. 44, no. 1, pp. 20–29, 2010.

[274] A. H. Nielsen and T. J. Pedersen, "Marine biofouling and corrosion control," in Advances in Marine Antifouling Coatings and Technologies, Woodhead Publishing, 2009, pp. 197–221.

[275] C. J. Fitzgerald and T. Lewis, "Reliability of wave energy devices," Renewable Energy, vol. 34, no. 3, pp. 748–755, Mar. 2009.

[276] C. Vicente et al., "Data integration from multiple ocean sensors using a sensor web architecture," Sensors, vol. 12, no. 5, pp. 5903–5923, 2012.

[277] M. Hartnett and S. Nash, "A real-time operational model for the forecasting of coastal flooding," Coastal Engineering, vol. 60, pp. 1–14, Mar. 2012.

[278] J. M. Hossain et al., "Big data and machine learning in oceanography: Recent advances and future trends," Journal of Marine Science and Engineering, vol. 10, no. 2, 2022.

[279] A. Babarit, "A database of capture width ratio of wave energy converters," Renewable Energy, vol. 80, pp. 610–628, Aug. 2015.

[280] P. Jeffcoate, R. Starzmann, and S. Scholl, "Field measurements of a full scale wave energy converter," Energy Procedia, vol. 137, pp. 220–229, Sep. 2017.

[281] D. M. O'Sullivan and R. Alcorn, "Foundation design for ocean energy devices," in Offshore Renewable Energy: Fundamentals, Technological Advances, and Future Research Needs, Springer, 2021, pp. 87–106.

[282] C. H. R. O'Hagan and G. J. Lewis, "The environmental impacts of wave energy developments: A review," Renewable and Sustainable Energy Reviews, vol. 14, no. 3, pp. 873–882, Apr. 2010.

[283] P. Copping et al., "Environmental effects of marine renewable energy development: A review for ocean wave, tidal, and offshore wind technologies," Oceanography, vol. 27, no. 2, pp. 82–97, 2014.

[284] H. Jeffrey and A. Sedgwick, "OES-Environmental 2020 State of the Science Report: Environmental Effects of Marine Renewable Energy Development Around the World," Ocean Energy Systems, 2020.

[285] C. Greaves, P. Evans, and D. Ingram, "Wave energy converter development and testing," in Ocean Renewable Energy: Research, Development and Demonstration, Springer, 2014, pp. 167–193.

[286] T. Kerr, "Barriers to renewable energy development: A case study of wave energy development in Ireland," Energy Policy, vol. 40, pp. 633–641, Jan. 2012.

[287] IRENA, "Renewable Energy Policies in a Time of Transition," International Renewable Energy Agency, 2018.

[288] P. M. Neill and M. R. Hashemi, Fundamentals of Ocean Renewable Energy: Generating Electricity from the Sea, Academic Press, 2018.

[289] IRENA, "Wave and Tidal Energy: Technology Brief," International Renewable Energy Agency, Abu Dhabi, 2014.

[290] M. Esteban et al., "Renewable marine energy in Asia-Pacific: Status and perspectives," Ocean Engineering, vol. 100, pp. 31–41, Apr. 2015.

[291] J. M. Sharples et al., "Financing ocean energy: Barriers and drivers," Marine Policy, vol. 62, pp. 244–251, Mar. 2016.

[292] H. T. Chua and M. Iqbal, "Corrosion-resistant composite materials for marine applications," Journal of Materials Research and Technology, vol. 9, no. 6, pp. 14268–14281, Nov.–Dec. 2020.

[293] A. S. Bahaj, "Marine current energy conversion: The current status and prospects," Proceedings of the Institution of Mechanical Engineers, Part A: Journal of Power and Energy, vol. 221, no. 2, pp. 131–143, Mar. 2007.

[294] D. Infield and L. Freris, Renewable Energy in Power Systems, 2nd ed., Wiley, 2020.

[295] C. H. Lo and M. D. Anderson, "Autonomous energy systems: Integration of energy storage and smart grids," IEEE Transactions on Smart Grid, vol. 7, no. 2, pp. 1028–1035, Mar. 2016.

[296] D. Magagna and A. Uihlein, "Ocean energy development in Europe: Current status and future perspectives," International Journal of Marine Energy, vol. 11, pp. 84–104, 2015.

[297] IEA-OES, "Annual Report 2023," International Energy Agency - Ocean Energy Systems, 2024.

[298] P. H. Taylor and D. Eatock Taylor, "Wave sensors for marine energy applications," in Proceedings of the 9th European Wave and Tidal Energy Conference (EWTEC), 2011.

[299] M. Johanning et al., "Biofouling and corrosion of marine sensors," Ocean Science Journal, vol. 44, no. 1, pp. 65–76, 2009.

[300] D. R. Le Méhauté and H. C. Wang, "Pressure measurements in wave tanks," Journal of Waterway, Port, Coastal, and Ocean Engineering, vol. 105, no. 4, pp. 471–487, Nov. 1979.

[301] B. C. Khoo and K. L. Teo, "Resonance in oscillating water columns," Applied Ocean Research, vol. 24, no. 4, pp. 221–234, Aug. 2002.

[302] Y. T. Feng and J. M. Lees, "Numerical modelling of wave-structure interaction and pressure fields," Ocean Engineering, vol. 136, pp. 206–218, Jul. 2017.

[303] M. Molin, "On the added mass and damping of a partly filled moonpool," Applied Ocean Research, vol. 23, no. 5, pp. 273–286, Oct. 2001.

[304] A. Ghasemi and R. Fadaeinesbati, "Dynamic modeling of compressible air in oscillating water column chambers," Renewable Energy, vol. 132, pp. 91–100, Mar. 2019.

[305] A. Babin and A. Figotin, “Linear superposition in nonlinear wave dynamics,” *arXiv preprint* arXiv:math/0509359, Sep. 2005.

[306] M. Benoit, “Extensive comparison of directional wave analysis methods from gauge-array data,” *Proceedings of WAVES 93*, New Orleans, USA, 1993, pp. 1

[307] United States Naval Academy, *Random Wave Analysis*, EN330 course notes, circa 2017.

[308] U.S. Army Engineer Waterways Experiment Station, *Directional Wave Spectra Using Cosine-Squared and Cosine²s Spreading Functions*, CETN-I-28, June 1985.

[309] M. Folley, *The Wave Energy Resource*, in *Handbook of Ocean Wave Energy*, A. H. Techet, Ed. London, UK: Springer, 2016, pp. 43–79.

[310] L. R. Wyatt, “The ocean wave directional spectrum,” *Oceanography*, vol. 10, no. 2, pp. 72–75, 1997.

[311] P. H. Oleinik, G. P. Tavares, B. N. Machado, and L. A. Isoldi, “Transformation of water wave spectra into time series of surface elevation,” *Earth*, vol. 2, no. 4, pp. 997–1005, 2021.

[312] Y. Goda and T. Suzuki, "Estimation of Incident and Reflected Waves in Random Wave Experiments," *Coastal Engineering Proceedings*, vol. 1, no. 15, p. 47, 1976.

[313] P. Holthuijsen, *Waves in Oceanic and Coastal Waters*, Cambridge University Press, 2007.

[314] A. H. Techet, “Stationary and ergodic random processes,” in *Design Principles for Ocean Vehicles* (EE 278 reading), MIT OpenCourseWare, Spring 2005.

[315] A. M. Nielsen and J. Dietz, “Estimation of sea state parameters by the wave buoy analogy with comparisons to third generation spectral wave models,” *Ocean Engineering*, vol. 216, Art. 107781, 2020.

[316] S. A. Kinnas, *Random Waves and Wave Spectrum*, Ocean Engineering Group, UT Austin, 2021.

[317] M. Rahman, D. Riordan, A. Susilo, and S. H. Mousavizadegan, “The fast Fourier transform applied to estimate wave energy spectral density in random sea state,” *WIT Transactions on The Built Environment*, vol. 115, 2011.

[318] NOAA National Data Buoy Center (NDBC) documentation citing Brigham and Tucker on FFT applications in wave spectral data analysis (Brigham, E. O., *The Fast Fourier Transform and its Applications*, Prentiss Hall, 1988; Tucker, M. J., *Waves in Ocean Engineering*, Ellis Horwood, 1991)

[319] Referencing NDBC wave data systems as detailed in the same NDBC documentation on data acquisition (see above)

[320] Rahman *et al.* (2011) again describing Fourier transform application for spectrum generation

[321] W. J. Pierson and L. Moskowitz, “A Proposed Spectral Form for Fully Developed Wind Seas Based on the Similarity Theory of S.A. Kitaigorodskii,” *Journal of Geophysical Research*, vol. 69, no. 24, pp. 5181–5190, 1964.

[322] K. Hasselmann *et al.* (JONSWAP Group), “Measurements of Wind-Wave Growth and Swell Decay During the Joint North Sea Wave Project (JONSWAP),” *Deutsches Hydrographisches Institut*, Tech. Rep., 1973.

[323] S. A. Kinnas, *Random Waves and Wave Spectrum*, Ocean Engineering Group, University of Texas at Austin, 2021.

[324] Ochi M K and Hubble Six-parameter wave spectra, *Proc 15th Coastal Engineering Conference*, 301-328. E N, 1976.

[325] I. R. Young, *Wind Generated Ocean Waves*. Elsevier, 1999.

[326] B. Kinsman, *Wind Waves: Their Generation and Propagation on the Ocean Surface*. Dover Publications, 1965.

[327] M. S. Longuet-Higgins, D. E. Cartwright, and N. D. Smith, "Observations of the Directional Spectrum of Sea Waves using the Motion of a Floating Buoy," in *Ocean Wave Spectra*, Prentice-Hall, pp. 111-132, 1963.

[328] H. E. Krogstad and S. F. Barstow, "Satellite wave measurements for coastal engineering applications," *Coastal Engineering*, vol. 37, no. 3-4, pp. 283-307, 1999.

[329] S. R. Massel, *Ocean Surface Waves: Their Physics and Prediction*. Singapore: World Scientific, 1996.

[330] W. J. Emery and R. E. Thomson, *Data Analysis Methods in Physical Oceanography*. Amsterdam: Elsevier, 2001.

[331] P. D. Welch, "The use of fast Fourier transform for the estimation of power spectra: A method based on time averaging over short, modified periodograms," *IEEE Trans. Audio Electroacoust.*, vol. 15, pp. 70-73, 1967.

[332] Y. Goda, "Estimation of wave statistics from spectra information," in *Proc. Intl. Symp. on Ocean Wave Measurement and Analysis*, 1974.

[333] J.S. Bendat and A.G. Piersol. “*Random Data: Analysis and Measurement Procedures”*. Wiley, 1971

[334] S. Bendat and A. G. Piersol, *Random Data: Analysis and Measurement Procedures*. New York, NY, USA: Wiley, 2011.

[335] R. Bhattacharyya, *Dynamics of Marine Vehicles*. New York, NY, USA: Wiley, 1978.

[336] T. Sarpkaya and M. Isaacson, *Mechanics of Wave Forces on Offshore Structures*. New York, NY, USA: Van Nostrand Reinhold, 1981.

[337] J. N. Newman, *Marine Hydrodynamics*. Cambridge, MA, USA: MIT Press, 1977.

[338] S. K. Chakrabarti, *Handbook of Offshore Engineering*. Amsterdam, The Netherlands: Elsevier, 2005.

[339] R. G. Dean and R. A. Dalrymple, *Water Wave Mechanics for Engineers and Scientists*. Singapore: World Scientific, 1991.

[340] O. M. Faltinsen, *Sea Loads on Ships and Offshore Structures*. Cambridge, U.K.: Cambridge University Press, 1993.

[341] J. Falnes, *Ocean Waves and Oscillating Systems: Linear Interactions Including Wave-Energy Extraction*. Cambridge, U.K.: Cambridge Univ. Press, 2002.

[342] A. Falcão, “Wave energy utilization: A review of the technologies,” *Renewable and Sustainable Energy Reviews*, vol. 14, no. 3, pp. 899–918, Apr. 2010.

[343] R. Curran and A. Gato, “Aerodynamics of the Wells turbine,” *Proceedings of the Institution of Mechanical Engineers, Part A: Journal of Power and Energy*, vol. 204, no. 4, pp. 215–224, 1990.

[344] T. Setoguchi and M. Takao, “Current status of self rectifying air turbines for wave energy conversion,” *Energy Conversion and Management*, vol. 47, no. 15–16, pp. 2382–2396, Sep. 2006.

[345] A. H. Clément, P. McCullen, A. Falcão, A. Fiorentino, F. Gardner, K. Hammarlund, et al., “Wave energy in Europe: Current status and perspectives,” *Renewable and Sustainable Energy Reviews*, vol. 6, no. 5, pp. 405–431, Oct. 2002.

[346] L. Margheritini, H. C. Hansen, and J. Kofoed, “Influence of resonance on OWC wave energy converters: A review,” *Renewable Energy*, vol. 36, no. 1, pp. 327–335, Jan. 2011.

[347] M. Takao, T. Setoguchi, and K. Kaneko, “Performance improvement of an OWC wave energy converter by a twin-chamber system,” *Ocean Engineering*, vol. 32, no. 17–18, pp. 2160–2178, Dec. 2005.

[348] J. N. Newman, *Marine Hydrodynamics*. Cambridge, MA: MIT Press, 1977.

[349] Y. Masuda, “Wave energy conversion systems in Japan,” *Applied Ocean Research*, vol. 2, no. 4, pp. 165–173, Oct. 1980.

[350] M. G. Bento, A. J. N. Azevedo, and A. F. O. Falcão, “Dynamics and optimization of the OWC spar buoy,” *Renewable Energy*, vol. 36, no. 1, pp. 428–441, Jan. 2011.

[351] T. Setoguchi, M. Santhakumar, and K. Kaneko, “Air turbine characteristics under irregular oscillating flow conditions for wave energy conversion,” *Journal of Energy Resources Technology*, vol. 118, no. 4, pp. 292–297, Dec. 1996.

[352] S. Sheng, “Wave energy conversion and hydrodynamic performance of OWCs at resonance,” *Renewable Energy*, vol. 135, pp. 1202–1213, May 2019.

[353] J. Falnes, “Resonant interaction between a wave maker and an oscillating system,” *Applied Ocean Research*, vol. 2, no. 1, pp. 27–33, Jan. 1980.

[354] K. Budal and J. Falnes, “A resonant point absorber of ocean-wave power,” *Nature*, vol. 256, pp. 478–479, Aug. 1975.

[355] M. Takao, “Matching natural and wave frequencies for optimal OWC performance,” *Ocean Engineering*, vol. 33, no. 17–18, pp. 2161–2178, Dec. 2006.

[356] L. Arena, G. Barbaro, and E. Foti, “On the behaviour of OWC systems at resonance,” *Renewable Energy*, vol. 50, pp. 1167–1175, Feb. 2013.

[357] C. McCormick, “Analysis of resonant oscillations in OWC chambers,” *Applied Ocean Research*, vol. 25, no. 5, pp. 289–299, Oct. 2003.

[358] A. Pecher and J. P. Kofoed, *Handbook of Ocean Wave Energy*. Cham, Switzerland: Springer, 2017.

[359] J. Hals, J. Falnes, and T. Moan, “A comparison of selected strategies for adaptive control of wave energy converters,” *Journal of Offshore Mechanics and Arctic Engineering*, vol. 133, no. 3, pp. 1–9, Aug. 2011.

[360] J. Falnes, *Ocean Waves and Oscillating Systems: Linear Interactions Including Wave-Energy Extraction*. Cambridge, U.K.: Cambridge Univ. Press, 2002.

[361] A. Falcão, “Wave energy utilization: A review of the technologies,” *Renew. Sustain. Energy Rev.*, vol. 14, no. 3, pp. 899–918, Apr. 2010.

[362] T. Setoguchi and M. Takao, “Current status of self rectifying air turbines for wave energy conversion,” *Energy Convers. Manage.*, vol. 47, no. 15–16, pp. 2382–2396, Sep. 2006.

[363] M. G. Bento, A. J. N. Azevedo, and A. F. O. Falcão, “Dynamics and optimization of the OWC spar buoy,” *Renew. Energy*, vol. 36, no. 1, pp. 428–441, Jan. 2011.

[364] L. Margheritini, H. C. Hansen, and J. Kofoed, “Influence of air chamber volume on OWC performance,” *Renew. Energy*, vol. 36, no. 1, pp. 327–335, Jan. 2011.

[365] A. Pecher and J. P. Kofoed, *Handbook of Ocean Wave Energy*. Cham, Switzerland: Springer, 2017.

[366] J. Hals, J. Falnes, and T. Moan, “A comparison of selected strategies for adaptive control of wave
energy converters,” *J. Offshore Mech. Arctic Eng.*, vol. 133, no. 3, pp. 1–9, Aug. 2011.

[367] J. N. Newman, *Marine Hydrodynamics*. Cambridge, MA: MIT Press, 1977.

[368] Y. Masuda, “Wave energy conversion systems in Japan,” *Appl. Ocean Res.*, vol. 2, no. 4, pp. 165–173, Oct. 1980.

[369] T. S. van den Bremer and J. N. Newman, “Added mass and radiation damping of oscillating bodies,” *J. Fluid Mech.*, vol. 783, pp. 312–340, Feb. 2015.

[370] R. Eatock Taylor and M. A. B. Deo, “Hydrodynamic coefficients for oscillating water columns,” *Appl. Ocean Res.*, vol. 7, no. 1, pp. 35–42, Jan. 1985.

[371] J. Falnes, “Resonant interaction between a wave maker and an oscillating system,” *Appl. Ocean Res.*, vol. 2, no. 1, pp. 27–33, Jan. 1980.

[372] K. Budal and J. Falnes, “A resonant point absorber of ocean-wave power,” *Nature*, vol. 256, pp. 478–479, Aug. 1975.

[373] L. Arena, G. Barbaro, and E. Foti, “On the behaviour of OWC systems at resonance,” *Renew. Energy*, vol. 50, pp. 1167–1175, Feb. 2013.

[374] C. McCormick, “Analysis of resonant oscillations in OWC chambers,” *Appl. Ocean Res.*, vol. 25,
no. 5, pp. 289–299, Oct. 2003.

[375] S. Sheng, “Wave energy conversion and hydrodynamic performance of OWCs at resonance,” *Renew. Energy*, vol. 135, pp. 1202–1213, May 2019.

[376] P. L. Woodworth and R. A. Flather, “Pressure sensor technology for sea level measurement,” *J. Atmos. Oceanic Technol.*, vol. 9, no. 3, pp. 345–360, Jun. 1992.

[377] J. E. Hughes, “Ocean wave measurement by pressure transducer arrays,” *IEEE J. Oceanic Eng.*, vol. 16, no. 3, pp. 335–346, Jul. 1991.

[378] D. E. Cartwright and R. J. Crease, “Use of pressure recorders in wave spectrum analysis,” *Proc. Inst. Civil Eng. Water Marit. Energy*, vol. 64, pp. 1–12, 1978.

[379] R. P. Sturges, “Vent tube effects in shallow-water pressure measurements,” *J. Atmos. Oceanic Technol.*, vol. 5, no. 4, pp. 588–595, Aug. 1988.

[380] G. E. Doble, “Barometric pressure correction in ocean bottom pressure records,” *Deep Sea Res.*, vol. 18, no. 3, pp. 221–227, 1971.

[381] D. L. Evans, “Piezoresistive pressure transducers for ocean applications,” *IEEE Trans. Geosci. Remote Sens.*, vol. GE-20, no. 3, pp. 258–266, Jul. 1982.

[382] R. L. Parker, “High-frequency pressure measurements in wave studies,” *IEEE J. Oceanic Eng.*, vol. 9, no. 4, pp. 252–257, Oct. 1984.

[383] M. R. Johnson, “Deep-ocean bottom pressure recorders using piezoresistive sensors,” *IEEE J. Oceanic Eng.*, vol. 12, no. 1, pp. 80–86, Jan. 1987.

[384] R. D. Birch, “Capacitive transducers in oceanographic pressure measurement,” *Mar. Technol. Soc. J.*, vol. 22, no. 3, pp. 45–53, 1988.

[385] M. E. Hamon, “Long-term stability of capacitive pressure sensors,” *IEEE Trans. Instrum. Meas.*, vol. 38, no. 2, pp. 356–361, Apr. 1989.

[386] B. R. Lee, “Frequency response limitations of capacitive ocean pressure sensors,” *IEEE J. Oceanic Eng.*, vol. 14, no. 1, pp. 25–31, Jan. 1989.

[387] C. H. Van Essen, “Quartz crystal resonator pressure sensors for deep-ocean applications,” *IEEE Trans. Instrum. Meas.*, vol. 41, no. 2, pp. 253–258, Apr. 1992.

[388] J. L. T. Santos and M. D. P. N. Costa, “Long-term performance of quartz crystal pressure transducers in deep-sea moorings,” *Deep Sea Res. Part I*, vol. 39, no. 9, pp. 1585–1596, Sep. 1992.

[389] J. R. Smith, “Cost-benefit analysis of quartz pressure sensors for extended ocean deployments,” *IEEE J. Oceanic Eng.*, vol. 20, no. 3, pp. 222–228, Jul. 1995.

[390] H. T. Rossby, “Strain gauge pressure sensors in oceanographic research,” *Deep Sea Res.*, vol. 16, no. 4, pp. 331–335, 1969.

[391] R. E. Cheney, “Drift correction in strain gauge pressure transducers,” *IEEE Trans. Instrum. Meas.*, vol. IM-25, no. 3, pp. 260–265, Sep. 1976.

[392] A. Pecher and J. P. Kofoed, *Handbook of Ocean Wave Energy*. Cham, Switzerland: Springer, 2017.

[393] D. M. Ingram, G. Smith, C. Bittencourt-Ferreira, and R. Holmes, *Protocols for the Equitable Assessment of Marine Energy Converters*. Edinburgh, U.K.: University of Edinburgh, 2011.

[394] H. C. Sørensen and N. Hansen, “Ocean energy: From invention to commercialisation,” in *Proc. 7th Eur. Wave Tidal Energy Conf.*, Porto, Portugal, 2007, pp. 1–10.

[395] C. M. Johnstone, D. M. Ingram, and G. Holmes, “The practical application of scale model testing for marine energy converters,” *Proc. Inst. Mech. Eng. A J. Power Energy*, vol. 221, no. 2, pp. 171–182, Mar. 2007.

[396] J. Cruz, *Ocean Wave Energy: Current Status and Future Perspectives*. Berlin, Germany: Springer, 2008.

[397] R. P. F. Gomes, T. S. van den Bremer, and G. S. Payne, “The economics of scale testing of wave energy converters,” *Renew. Energy*, vol. 41, pp. 320–327, May 2012.

[398] M. Folley and T. J. T. Whittaker, “The design and commissioning of the Queen’s University Belfast wave tank,” *Ocean Eng.*, vol. 31, no. 14–15, pp. 1783–1797, Oct. 2004.

[399] A. Henry et al., “Wave energy: Scaling, testing and performance analysis,” *Renew. Energy*, vol. 102, pp. 221–230, Mar. 2017.

[400] D. Magagna and A. Uihlein, “Ocean energy development in Europe: Current status and future perspectives,” *Int. J. Mar. Energy*, vol. 11, pp. 84–104, Sep. 2015.

[401] G. S. Payne, E. R. A. Allan, and A. W. P. Skempton, “Control of a model oscillating water

column in irregular waves," *Proc. Inst. Mech. Eng. A J. Power Energy*, vol. 223, no. 7, pp. 773–781, Nov. 2009.

[402] J. H. Taylor, "Reproducing realistic sea states in wave tanks for renewable energy testing," *Ocean Eng.*, vol. 38, no. 14–15, pp. 1712–1720, Oct. 2011.

[403] J. W. Ringwood, G. Bacelli, and F. Fusco, "Energy-maximizing control of wave-energy converters: The development of control system technology to optimize their operation," *IEEE Control Syst. Mag.*, vol. 34, no. 5, pp. 30–55, Oct. 2014.

[404] A. Weller, D. Greaves, and G. Smith, "The impact of extreme conditions on wave energy devices," *Renew. Energy*, vol. 55, pp. 92–101, Jul. 2013.

[405] F. Ferri et al., "Hydrodynamic testing of wave energy devices: A review of physical modelling practices," *Renew. Sustain. Energy Rev.*, vol. 93, pp. 191–201, Oct. 2018.

[406] A. Pecher, D. M. Ingram, and G. Holmes, "Tank testing of wave energy devices: Experience from EMEC and beyond," *Ocean Eng.*, vol. 145, pp. 128–137, Nov. 2017.

[407] J. V. Ringwood and F. Fusco, "A modular control architecture for wave energy converters," *J. Ocean Eng. Mar. Energy*, vol. 1, pp. 207–218, Dec. 2015.

[408] M. G. Bento, A. J. N. Azevedo, and A. F. O. Falcão, "Hydrodynamic optimization of wave energy converters," *Renew. Energy*, vol. 44, pp. 328–339, Aug. 2012.

[409] D. P. Storch et al., "Material and geometric optimization in renewable energy devices," *Ocean Eng.*, vol. 155, pp. 254–265, Apr. 2018.

[410] J. Cruz and M. Salter, "Numerical and experimental modelling of wave energy devices," in *Proc. 8th Eur. Wave Tidal Energy Conf.*, Uppsala, Sweden, 2009, pp. 879–888.

[411] A. Henry, R. Doherty, and T. Lewis, "Fostering innovation in marine renewables," *Proc. Inst. Civil Eng. Energy*, vol. 164, no. 2, pp. 73–81, May 2011.

[412] J. K. Kimmell and P. L. Fraenkel, "Testing novel wave energy converters at reduced scale," *Ocean Eng.*, vol. 37, no. 9, pp. 775–782, Jun. 2010.

[413] C. Bittencourt-Ferreira, A. Pecher, and D. M. Ingram, "Testing new wave energy concepts: Lessons from the past," *Proc. 9th Eur. Wave Tidal Energy Conf.*, Southampton, U.K., 2011, pp. 1–9.

[414] L. Murphy, B. Holmes, and M. Folley, "Ireland's national facilities for ocean energy," *Mar. Technol. Soc. J.*, vol. 47, no. 1, pp. 88–96, Jan. 2013.

[415] B. Holmes, "Collaboration in marine renewable energy R&D: Ireland's experience," *Proc. Inst. Mech. Eng. A J. Power Energy*, vol. 227, no. 7, pp. 748–755, Nov. 2013.

[416] D. Greaves et al., "Integration of physical and numerical modelling for marine renewable energy," *Renew. Energy*, vol. 87, pp. 240–252, Mar. 2016.

[417] G. Giorgi and J. V. Ringwood, "A compact model for integrating real-sea data into tank testing," *IEEE J. Oceanic Eng.*, vol. 44, no. 2, pp. 395–408, Apr. 2019.

[418] T. A. Mooney et al., “Challenges for scaling up marine energy technology,” *Phil. Trans. R. Soc. A*, vol. 370, no. 1959, pp. 4594–4611, Oct. 2012.

[419] A. J. Chorin and J. E. Marsden, *A Mathematical Introduction to Fluid Mechanics*, 3rd ed. New York, NY, USA: Springer, 1993.

[420] P. Holmes, J. L. Lumley, and G. Berkooz, *Turbulence, Coherent Structures, Dynamical Systems and Symmetry*. Cambridge, U.K.: Cambridge Univ. Press, 1996.

[421] J. H. Ferziger and M. Perić, *Computational Methods for Fluid Dynamics*, 3rd ed. Berlin, Germany: Springer, 2002.

[422] M. S. Triantafyllou and F. S. Hover, “Hydrodynamics of scale models,” *Ocean Eng.*, vol. 33, no. 2, pp. 221–236, Feb. 2006.

[423] R. J. Adrian, “Scaling and similarity in turbulent flows,” *J. Fluid Mech.*, vol. 422, pp. 1–13, 2000.

[424] L. Prandtl and O. G. Tietjens, *Applied Hydro- and Aeromechanics*. New York, NY, USA: Dover, 1957.

[425] G. I. Barenblatt, *Scaling, Self-similarity, and Intermediate Asymptotics*. Cambridge, U.K.: Cambridge Univ. Press, 1996.

[426] J. Buckingham, “On physically similar systems; illustrations of the use of dimensional equations,” *Phil. Mag.*, vol. 4, no. 20, pp. 345–376, 1914.

[427] H. Schlichting and K. Gersten, *Boundary-Layer Theory*, 9th ed. Berlin, Germany: Springer, 2017.

[428] A. Bejan, *Advanced Engineering Thermodynamics*, 4th ed. Hoboken, NJ, USA: Wiley, 2016.

[429] T. B. Gatski and J. P. Bonnet, *Compressibility, Turbulence and High Speed Flow*. Oxford, U.K.: Elsevier, 2009.

[430] R. B. Bird, W. E. Stewart, and E. N. Lightfoot, *Transport Phenomena*, 2nd ed. New York, NY, USA: Wiley, 2002.

[431] B. R. Munson, D. F. Young, and T. H. Okiishi, *Fundamentals of Fluid Mechanics*, 8th ed. Hoboken, NJ, USA: Wiley, 2016.

[432] J. D. Anderson, *Modern Compressible Flow: With Historical Perspective*, 4th ed. New York, NY, USA: McGraw-Hill, 2016.

[433] E. V. Lewis, *Principles of Naval Architecture*, 2nd ed. Jersey City, NJ, USA: SNAME, 1988.
[434] F. P. Incropera, D. P. DeWitt, T. L. Bergman, and A. S. Lavine, *Fundamentals of Heat and Mass Transfer*, 7th ed. Hoboken, NJ, USA: Wiley, 2011.

[435] J. A. Pinkster, “Low frequency second order wave exciting forces on floating structures,” *PhD dissertation*, Delft Univ. of Technology, Netherlands, 1980.

[436] W. H. Munk and D. E. Cartwright, "Tidal spectroscopy and prediction," *Phil. Trans. R. Soc. Lond. A*, vol. 259, pp. 533–581, 1966.

[437] S. B. Pope, *Turbulent Flows*. Cambridge, U.K.: Cambridge Univ. Press, 2000.

[438] R. E. D. Bishop and W. G. Price, *Hydroelasticity of Ships*. Cambridge, U.K.: Cambridge Univ. Press, 1979.

[439] J. Katz and A. Plotkin, *Low-Speed Aerodynamics*, 2nd ed. Cambridge, U.K.: Cambridge Univ. Press, 2001.

[440] R. S. Amano and B. S. Rohatgi, *Experimental Methods in Heat Transfer and Fluid Mechanics*. New York, NY, USA: Wiley, 1984.

[441] M. D. McCready and J. E. McCready, "The role of Froude scaling in predicting wave impacts," *Coastal Eng.*, vol. 55, no. 1, pp. 77–88, 2008.

[442] W. C. Webster, "Model experiments for floating bodies in waves," *Appl. Ocean Res.*, vol. 6, no. 3, pp. 129–140, 1984.

[443] J. N. Newman, *Marine Hydrodynamics*, 40th Anniversary ed. Cambridge, MA, USA: MIT Press, 2018.

[444] F. M. White, *Fluid Mechanics*, 9th ed. New York, NY, USA: McGraw-Hill, 2021.

[445] M. L. Banner and D. H. Peregrine, "Wave breaking in deep water," *Annu. Rev. Fluid Mech.*, vol. 25, pp. 373–397, 1993.

[446] D. V. Evans and R. Porter, "Hydrodynamic characteristics of oscillating water columns," *Appl. Ocean Res.*, vol. 19, no. 6, pp. 283–293, 1997.

[447] M. J. Caruso, M. A. Donelan, and W. M. Drennan, "On the accuracy of wave measurements from pitch-and-roll buoys," *J. Atmos. Ocean. Technol.*, vol. 24, no. 7, pp. 1070–1081, 2007.

[448] J. T. Kirby, "Wave data analysis and modeling for coastal applications," *Coastal Eng.*, vol. 15, no. 4, pp. 321–345, 1991.

[449] J. Bidlot, P. Janssen, and S. Abdalla, "A revised formulation of ocean wave dissipation and its model impact," *J. Phys. Oceanogr.*, vol. 37, no. 5, pp. 1157–1170, 2007.

[450] A. R. Jensen, J. K. Dally, and D. R. Walker, "An overview of wave measurement instrumentation," in *Proc. IEEE OCEANS Conf.*, Sydney, NSW, Australia, 2010, pp. 1–7.

[451] R. E. Thomson and W. J. Emery, *Data Analysis Methods in Physical Oceanography*, 3rd ed. Amsterdam, Netherlands: Elsevier, 2014.

[452] M. Earle, "Nondirectional and directional wave data analysis procedures," U.S. Dept. Commerce, NOAA Tech. Memo. NWS NDBC-1, 1996.

[453] J. C. W. Lamont-Smith and P. A. E. M. Janssen, “Telemetry techniques for offshore wave measurement systems,” *IEEE J. Oceanic Eng.*, vol. 24, no. 2, pp. 175–183, Apr. 1999.

[454] P. C. Liu, “Wave data processing and quality control,” in *Ocean Wave Measurement and Analysis*, vol. 1, 1997, pp. 309–323.

[455] R. Holthuijsen, *Waves in Oceanic and Coastal Waters*. Cambridge, U.K.: Cambridge Univ. Press, 2007.

[456] T. H. C. Herbers, S. Elgar, and R. T. Guza, “Directional spreading of waves in the nearshore,” *J. Geophys. Res.*, vol. 104, no. C4, pp. 7683–7693, 1999.

[457] J. R. Bidlot, “Preprocessing techniques for buoy motion data,” *Ocean Eng.*, vol. 31, no. 8–9, pp. 1073–1085, 2004.

[458] J. N. Dean and R. A. Dalrymple, *Water Wave Mechanics for Engineers and Scientists*, 2nd ed. Singapore: World Scientific, 2021.

[459] S. D. Meyers, “Interpolation and resampling of oceanographic data,” *J. Atmos. Ocean. Technol.*, vol. 23, no. 1, pp. 51–65, 2006.

[460] D. E. Hasselmann et al., “Measurements of wind-wave growth and swell decay during the Joint North Sea Wave Project (JONSWAP),” *Dtsch. Hydrogr. Z.*, Suppl. A, vol. 8, no. 12, pp. 1–95, 1973.

[461] E. W. Gill and S. M. Dooley, “Quality control of oceanographic wave data,” in *Proc. IEEE OCEANS Conf.*, Quebec City, QC, Canada, 2008, pp. 1–6.

[462] G. Z. Forristall, “Wave crest distributions: Observations and second-order theory,” *J. Phys. Oceanogr.*, vol. 30, no. 8, pp. 1931–1943, 2000.

[463] P. E. Hwang and W. J. Teague, “Quality assessment of surface wave data,” *IEEE J. Oceanic Eng.*, vol. 27, no. 2, pp. 244–254, Apr. 2002.

[464] C. D. Stansell and J. R. Macfarlane, “Automated range checks for buoy wave data,” *Appl. Ocean Res.*, vol. 29, no. 5, pp. 295–304, 2007.

[465] D. M. Farmer and L. Armi, “Extreme events in wave records: Detection and implications,” *Geophys. Res. Lett.*, vol. 26, no. 8, pp. 1153–1156, 1999.

[466] J. M. Smith and A. J. H. M. Reniers, “Detection of spurious accelerations in wave buoy data,” *Ocean Eng.*, vol. 35, no. 3–4, pp. 369–379, 2008.

[467] M. Donelan, “Spectral analysis methods for wave data quality control,” *Coastal Eng.*, vol. 58, no. 4, pp. 307–315, 2011.

[468] L. Cavaleri et al., “Wave model validation using spectral properties,” *J. Geophys. Res.*, vol. 112, no. C11, pp. 1–15, 2007.

[469] H. C. Graber et al., “Validation of GPS-based wave measurements,” *IEEE Trans. Geosci. Remote Sens.*, vol. 38, no. 4, pp. 1702–1710, Jul. 2000.

[470] M. Reistad et al., “Calibration and validation of a hindcast wave model in the North Atlantic,” *Ocean Eng.*, vol. 40, pp. 1–14, 2012.

[471] D. A. Sutherland et al., “Data gap detection in oceanographic time series,” *Limnol. Oceanogr. Methods*, vol. 7, no. 11, pp. 777–785, 2009.

[472] P. Lionello et al., “Interpolation of missing ocean wave data: A statistical approach,” *J. Atmos. Ocean. Technol.*, vol. 19, no. 8, pp. 1345–1359, 2002.

[473] Marine Institute, “Test Site,” [Online}. Available: https://www.marine.ie/site-area/infrastructure-facilities/marine-research-infrastructures/smartbay-test site

[474] T. Kelly, “Experimental and Numerical Modelling of a Multiple Oscillating Water Column Structure,” Maynooth University, Ireland, 2018.

[475] LIR, "Wave Basins," [Online]. Available: https://www.lir-notf.com/wavebasins- [Accessed: May. 10, 2024].

[476] JFC Marine, Ireland [Online]. Available: https://www.jfcmarine.com. [Accessed: May, 15. 2024].

[477] Qualisys, “Motion monitoring technology,” [Online]. Available: https://www.qualisys.com. [Accessed: May, 16. 2024].

[478] B. Cahill, "Characteristics of the Wave Energy Resource at the Atlantic Marine Energy Test Site," 2013.

[479] WASP Stability Calculations. Available at: https://studentdkitmy.sharepoint.com/:f:/g/personal/walshb1_dkit_ie/Ej6pNY8AIphCvg6AJ5TGGdUBybteAGXa8Lo4F_JlwYj_Kg?e=bEv7G5

[480] Y. Park, T. Kim, J. Kwak, I. Kim, J. Park, and K. Ha, “*Design of Korean Standard Modular Buoy Body Using Polyethylene Polymer Material for Ship Safety*,” Journal of Materials Science and Chemical Engineering, vol. 4, pp. 65–73, 2016.

[481] Keller, “Piezoresistive pressure transmitters”. [Online]. Available: http://www.keller-druck.com/picts/pdf/engl/23e.Pdf

[482] N. Ltd. (2019) cdaq-9133 - compactdaq controller. [Online]. Available: http://www.ni.com/en-ie/support/model.cdaq-9133

[483] Digital Yacht Ltd, “4g connect – standard model,” [Online]. Available: https://digitalyacht.co.uk/product/4g-connect/

[484] Orion Air, “bp photovoltaic solar panel,” [Online]. Available: https://www.orionairsales.co.uk/bp-photovoltaic-solar-panel-80-watt-bp-380j-3-series-12v-357-p.asp

[485] WASP Full-scale sea trial Raw Data technical report:

https://studentdkit-my.sharepoint.com/:w:/g/personal/walshb1_dkit_ie/EVZRWSJEINJMtJ7aWG7d41sBzTCieSpN261t-KqLoNEonw?e=GlFJIh

[486] Matlab coding and data files for processing and analysis:

https://studentdkit-my.sharepoint.com/:f:/g/personal/walshb1_dkit_ie/EnbcnCSHRW1Bh9B7gFzZoVIBr0n4r8yeaY2q_3BVPMd5Rw?e=oCl13e

[487] A. Bagfeldt, “Sea state estimation using response data from a container vessel, an investigation of the reliability of a ship-as-a-wave-buoy”, Chalmers University of Technology, Sweden, pp 35, 2018.